Karlsruher Institut für Technologie

Comparison of Different Transmembrane Substrates of Intramembrane Proteases by NMR Spectroscopy

Zur Erlangung des akademischen Grades einer

DOKTORIN DER NATURWISSENSCHAFTEN

(Dr. rer. nat.)

von der KIT-Fakultät für Chemie und Biowissenschaften

des Karlsruher Instituts für Technologie (KIT)

genehmigte

DISSERTATION

von

Dipl.-Chem. Nadja Guschtschin-Schmidt

1. Referentin: Dr. Claudia Muhle-Goll
2. Referentin: Prof. Dr. Anne Ulrich

Tag der mündlichen Prüfung: 27. Oktober 2023

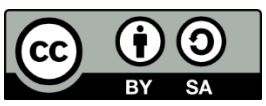

Für Frieda und Artur und mich.

Affidavit/Eidesstattliche Versicherung

Bei der eingereichten Dissertation zu dem Thema:

Comparison of Different Transmembrane Substrates of Intramembrane Proteases by NMR spectroscopy

handelt es sich um meine eigenständig erbrachte Leistung. Ich habe nur die angegebenen Quellen und Hilfsmittel benutzt und mich keiner unzulässigen Hilfe Dritter bedient. Insbesondere habe ich wörtlich oder sinngemäß aus anderen Werken übernommene Inhalte als solche kenntlich gemacht. Die Arbeit oder Teile davon habe ich bislang nicht an einer Hochschule des In- oder Auslands als Bestandteil einer Prüfungs- oder Qualifikationsleistung vorgelegt. Die Richtigkeit der vorstehenden Erklärungen bestätige ich. Die Bedeutung der eidesstattlichen Versicherung und die strafrechtlichen Folgen einer unrichtigen oder unvollständigen eidesstattlichen Versicherung sind mir bekannt.

Ich versichere an Eides statt, dass ich nach bestem Wissen die reine Wahrheit erklärt und nichts verschwiegen habe.

Karlsruhe, 13.09.2023

…… ……

Ort und Datum Nadja Guschtschin-Schmidt

Publications

1. Spitz, Charlotte; Schlosser, Christine; Guschtschin-Schmidt, Nadja; Stelzer, Walter; Menig, Simon; Götz, Alexander et al. (2020): Non-canonical Shedding of TNFα by SPPL2a Is Determined by the Conformational Flexibility of Its Transmembrane Helix. In: iScience 23 (12), S. 101775. DOI: 10.1016/j.isci.2020.101775.

2. Ortner, Martin; Guschtschin-Schmidt, Nadja; Stelzer, Walter; Muhle-Goll, Claudia; Langosch, Dieter (2023): Permissive Conformations of a Transmembrane Helix Allow Intramembrane Proteolysis by γ-Secretase. In: Journal of molecular biology, S. 168218. DOI: 10.1016/j.jmb.2023.168218.
   Martin Ortner and Nadja Guschtschin-Schmidt contributed equally to this work.

Contents

Abstract

In this thesis, two substrates of intramembrane aspartate proteases were investigated. The transmembrane domain (TMD) of Notch1 is a γ-secretase substrate and Notch1 is involved in cell communication, cell-fate decisions during development and neurogenesis. TMD of Tumor necrosis factor α (TNFα) is a substrate of signal peptide peptidase like protease 2a (SPPL2a) and TNFα mediates apoptosis or cell survival as well as is involved in inflammation.

The astonishing intramembrane proteases, which cleave the single-span TMD of substrates within the hydrophobic environment of the lipid bilayer, have been intensively investigated over the last decades. Protease structures and mechanistic aspects have been revealed, but many questions remain unanswered, especially regarding substrate selection. A cryogenic-electron microscopy (cryo-EM) structure of the Notch1–γ-secretase complex has provided ground-breaking mechanistic insights. The helical C-terminal transmembrane domain (TM-C) in Notch1 is unwound and adopts a β-strand, which forms a hybrid β-sheet by interacting with an antiparallel β-sheet in presenilin 1 (PS1), the catalytic subunit of γ-secretase. This stabilizes the active Notch1-PS1 complex and positions them in a cleavage competent orientation.

None of the intramembrane proteases seems to recognize a consensus sequence, nevertheless substrates are cleaved at specific cleavage sites and mutations in the substrate TMD affect their processivity. A flexibility hypothesis has been developed based on mutational results, assuming a flexible substrate TMD for efficient cleavage, but has not been corroborated with structural and dynamic data. This thesis investigates and compares how mutations that alter TMD stability, affect structural and dynamic properties of Notch1 and TNFα, what influence these properties have on processivity, and which substrate requirements can be derived from these influences. A close homologue of Notch1, Notch3, which is cleaved only to 25 % efficiency compared with Notch1, is also included in the analysis.

All structural investigations were carried out in trifluorethanol/water, whose polarity approximately mimics the water containing protease interior. Chemical shifts as well as distance-based NOE data, determined by standard NMR methods, were used to

characterize the secondary structure, and 3D structures were calculated with these data as restraints. Hydrogen deuterium exchange measurements were performed to determine the dynamics and residue-specific stability profiles. Furthermore, a simple model of superimposing the investigated structures on the Notch1-γ-secretase cryo-EM structure or a predicted TNFα-SPPL2a structure was applied to evaluate the interaction between the substrate and enzyme.

The 3D structure revealed an α-helical and slightly bent Notch1 TMD, where the orientation of the N-terminal TMD (TM-N) with respect to the TM-C was restricted to a conical region, when 40 low energy NMR structures were represented in a bundle. Hydrogen bonds stabilized the central TMD around Leu_{1747} and S3 cleavage site together with surrounding residues were characterized by weaker hydrogen bonds and partial unfolding. Notch1$L_{1740\text{-}1743}$ stabilized, while Notch1$G_{1740\text{-}1743}$ destabilized the TM-N, whereas Notch3$_{1642\text{-}1665}$ stabilized the TM-C compare to Notch1.

Superposition of the structural bundles onto the cryo-EM structure of Notch1-γ-secretase complex showed that the investigated Notch1 bundle fitted well in the enzymes active site and the TM-C ends showed towards the antiparallel β-sheet in PS1, indicating an interaction with the enzyme. Due to the straighter TMD and shifted bend in Notch1$L_{1740\text{-}1743}$ and even straighter structure and more shifted bend in Notch3$_{1642\text{-}1665}$ TMD, their TM-Cs clustered more distantly from the β-sheet in PS1, what might hinder the required interaction with PS1 and correlated with reduced cleavability. The conformational less restricted Notch1$G_{1740\text{-}1743}$ TMD might facilitate the access to the active site and the cleavage conform positioning, thereby increasing processivity.

The α-helical structure of TNFα TMD was also slightly bent and the orientation of the TM-N with respect to TM-C limited to a defined cone, when represented as structural bundle. The central part of the TMD was less stable, thus more flexible. At the cleavage sites the helix was disrupted by weaker hydrogen bonds and partial unfolding. While TNFαS34P$_{28\text{-}60}$ was slightly more flexible than TNFα, the entire TMD was more stable in TNFαAGA/LLL$_{28\text{-}60}$, especially in the central part. The investigated TNFα bundle fitted well into the active site of the AlphaFold derived model of SPPL2a. Here, the TM-C ends clustered around the putative antiparallel β-sheet in SPPL2a. TM-C ends in TNFαAGA/LLL$_{28\text{-}60}$ were located more distantly from the β-sheet in SPPL2a because of a straighter TMD and shifted direction of the bend. In TNFαS34P$_{28\text{-}60}$ the bend was even less pronounced and the distribution of orientations in the bundle clustered around the helical

axis, therefore TM-C ends were further away from the β-sheet in SPPL2a but directed closer towards the catalytic aspartates that might enable the formation of a tetrahedral intermediate and facilitating cleavage.

The analysis of my data lead to the conclusion that mutations affect the structural and dynamic properties and thus different mechanistic steps and the processivity. The TMD requires a certain flexibility to enter the interior of the enzyme and translocate to the active site. Furthermore, formation of a hybrid β-sheet is crucial and depends on the stability of the substrate TM-C, the extend and orientation of the bend. Substrate TM-C stability is also important for unfolding of the cleavage site and accessibility of the scissile peptide bond.

In summary, neither the propensity to adopt a β-strand, nor flexibility within the TMD and cleavage sites or the orientation and extend of the TMD bend are exclusively substrate-determining on their own, but can be combined to adjust the cleavage efficiency and create a substrate customised to the biological needs.

Zusammenfassung

In dieser Arbeit wurden zwei Substrate von Aspartat-Intramembran-Proteasen untersucht. Die Transmembrandomäne (TMD) von Notch1 ist ein Substrat von γ-Sekretase und Notch1 an der Zellkommunikation, der Entscheidung über die Zellbestimmung während der Entwicklung und der Neurogenese beteiligt. Die TMD des Tumornekrosefaktors α (TNFα) ist ein Substrat der Signalpeptid Peptidase ähnlichen Protease 2a (SPPL2a) und TNFα, vermittelt Apoptose oder Zellüberleben und ist an Entzündungsreaktionen beteiligt.

Die erstaunlichen Intramembran-Proteasen, die die TMD von Substraten innerhalb der hydrophoben Umgebung der Lipiddoppelschicht spalten, wurden in den letzten Jahrzehnten intensiv untersucht. Protease-Strukturen und mechanistischen Aspekte wurden aufgeklärt, dennoch bleiben viele Fragen unbeantwortet, insbesondere hinsichtlich der Substratauswahl. Eine kryogene Elektronenmikroskopie-Struktur (kryo-EM) des Notch1-γ-Sekretase-Komplexes hat bahnbrechende mechanistische Erkenntnisse geliefert. Die helikale C-terminale Transmembrandomäne (TM-C) in Notch1 ist aufgewunden und bildet einen β-Strang aus, der durch Interaktion mit einem antiparallelen β-Faltblatt in Presenilin 1 (PS1), der katalytischen Untereinheit von γ-Sekretase, ein hybrides β-Faltblatt formt. Diese Wechselwirkung stabilisiert den aktiven Notch1-γ-Sekretase-Komplex und positioniert ihn in einer spaltungsfähigen Orientierung.

Keine der Intramembran-Proteasen scheint eine Konsensussequenz zu erkennen, dennoch werden Substrate an bestimmten Spaltstellen geschnitten und Mutationen in der Substrat Transmembrandomäne (TMD) beeinflussen die Prozessivität. Basierend auf Mutationsergebnissen wurde eine Flexibilitäts-Hypothese entwickelt, die eine flexible Substrat TMD für eine effiziente Spaltung voraussetzt, jedoch nicht durch strukturelle und dynamische Daten bestätigt wurde. Diese Arbeit untersucht, wie Mutationen, die die TMD-Stabilität ändern, die strukturellen und dynamischen Eigenschaften von Notch1 und TNFα beeinflussen, welchen Einfluss diese Eigenschaften auf die Prozessivität haben und welche Substrat-Anforderungen sich von dem Einfluss der strukturellen und dynamischen Eigenschaften ableiten lassen. Ein nahes Homolog von Notch1, das

Transmembran-Protein Notch3, welches im Vergleich zu Notch1 nur mit einer Effizienz von 25 % gespalten wird, wird ebenfalls in die Analyse einbezogen.

Alle Strukturuntersuchungen wurden in Trifluorethanol/Wasser, dessen Polarität annähernd das Innere der wasserhaltigen Protease nachahmt, durchgeführt. Chemische Verschiebungen sowie abstandsbasierte NOE-Daten, die mit Standard-NMR-Methoden bestimmt wurden, wurden zur Charakterisierung der Sekundärstruktur und Berechnung der 3D Strukturen verwendet. Zur Bestimmung der Dynamik und restespezifischen Stabilitätsprofile wurden Wasserstoff/Deuterium-Austausch-Messungen durchgeführt. Um die Wechselwirkung zwischen Substrat und Enzym abschätzen zu können, wurde ein einfaches Modell der Überlagerung der untersuchten Strukturen mit der kryo-EM Struktur des Notch1-γ-Sekretase-Komplexes oder mit der vorhergesagten TNFα-SPPL2a-Komplex Struktur angewendet.

Die 3D Struktur zeigte eine α-helikale und leicht gebogene Notch1 TMD, bei der die Orientierung der N-terminalen TMD (TM-N) bezogen auf die TM-C auf einen konischen Bereich beschränkt war, wenn 40 NMR-Strukturen mit niedrigster Energie in einem Strukturbündel dargestellt wurden. Wasserstoffbrückenbindungen stabilisierten den zentralen Teil der TMD, wobei die S3 Schnittstelle sowie umgebende Reste durch schwächere Wasserstoffbrückenbindungen und eine teilweise Entfaltung gekennzeichnet waren. Notch1$L_{1740\text{-}1743}$ stabilisierte und Notch1$G_{1740\text{-}1743}$ destabilisierte die TM-N, wohingegen Notch3$_{1642\text{-}1665}$ die TM-C stabilisierte.

Die Überlagerung der Strukturbündel mit der kryo-EM Struktur des Notch1-γ-Sekretase-Komplexes zeigte, dass das untersuchte Notch1 Bündel gut in das aktive Zentrum des Enzyms passte und die TM-C Enden in Richtung des antiparallelen β-Faltblattes in PS1 zeigten. Dies lässt auf eine Interaktion mit dem Enzym schließen. Wegen der geraderen TMD und einer geänderten Richtung der Biegung in Notch1$L_{1740\text{-}1743}$ TMD als auch der noch geraderen Struktur und stärker geänderten Richtung der Biegung in Notch3$_{1642\text{-}1665}$ TMD, gruppierten sich die TM-Cs weiter entfernt von dem β-Faltblatt in PS1, was die benötigte Interaktion mit PS1 hindern und mit der verminderten Spaltbarkeit korrelieren könnte. Die konformationell weniger eingeschränkte Notch1$G_{1740\text{-}1743}$ TMD könnte den Zugang zum aktiven Zentrum und die spaltungskonforme Positionierung erleichtern, wodurch die Prozessivität erhöht werden könnte.

Die α-helikale Struktur von TNFα TMD war ebenfalls leicht gebogen und die Orientierung der TM-N im Vergleich zur TM-C auf einen definierten Konus beschränkt, wenn die Strukturen als Bündel dargestellt wurden. Der zentrale Teil der TMD war weniger stabil und daher flexibler. An den Schnittstellen wurde die Helix durch schwächere Wasserstoffbrückenbindungen und einer teilweisen Entfaltung unterbrochen. Während TNFαS34P$_{28-60}$ etwas flexibler war als TNFα WT, war die gesamte TMD in TNFαAGA/LLL$_{28-60}$ stabiler, insbesondere im mittleren Teil. Das untersuchte TNFα Strukturbündel passte gut in das aktive Zentrum des von AlphaFold vorhergesagten Modells von SPPL2a. Hier gruppierten sich die TM-C Enden um das mutmaßliche antiparallele β-Faltblatt in SPPL2a. Die TM-C Enden befanden sich in TNFαAGA/LLL$_{28-60}$ aufgrund einer geraderen TMD und einer geänderten Richtung der Biegung weiter vom β-Faltblatt in SPPL2a entfernt. In TNFαS34P$_{28-60}$ war die Biegung noch weniger ausgeprägt und die Verteilung der Orientierungen im Bündel gruppierte sich um die Helixachse, weshalb sich die TM-C Enden weiter entfernt vom β-Faltblatt, aber näher an den katalytischen Aspartate befanden. Dies könnte die Ausbildung eines tetraedrischen Zwischenprodukts ermöglichen und somit die Spaltung erleichtern.

Die Analyse meiner Daten führte zur Feststellung, dass Mutationen die strukturellen und dynamischen Eigenschaften der TMD und dadurch verschiedene mechanistische Schritte und die Prozessivität beeinflussen. Die TMD erfordert eine gewisse Flexibilität um in das Innere des Enzyms und zum aktiven Zentrum zu gelangen. Des Weiteren ist die Bildung eines hybriden β-Faltblattes von entscheidender Bedeutung für die Effizienz der Spaltung und ist abhängig von der Stabilität der Substrat TM-C sowie der Ausprägung und Ausrichtung der Biegung in der Substrat TMD. Die Stabilität der Substrat TM-C ist ebenfalls wichtig für die Entfaltung der Schnittstelle und die Zugänglichkeit der zu spaltenden Peptidbindung.

Zusammenfassend lässt sich sagen, dass weder die Tendenz zur Ausbildung eines β-Stranges, noch die Flexibilität innerhalb der TMD und der Schnittstellen oder die Ausrichtung und Ausprägung der TMD Biegung für sich genommen ausschließlich substratbestimmend sind, sondern zur Anpassung der Spaltungseffizienz kombiniert und auf die biologischen Ansprüche des Substrats zugeschnitten werden können.

1 Introduction

Intramembrane proteases are highly specialized enzymes and cleave their substrates, transmembrane proteins, within the hydrophobic environment of a membrane. Members of intramembrane protease family are found in all kingdoms of life and fulfil crucial tasks like protein maturation, signal transduction, cellular homeostasis and protein degradation (Beel und Sanders 2008). Malfunction of these fine-tuned processes can lead to neurodegenerative diseases like Alzheimer's disease and Parkinson's disease as well as leukemia or type-II diabetes (Strooper und Annaert 2010; Urban und Dickey 2011). Due to these essential functions and far-reaching consequences, it is of crucial importance to gain insights into the functioning of intramembrane proteases, especially in interaction with their substrates.

Analogous to aqueous proteases, intramembrane proteases are classified according to their catalytic residues in serine, glutamate, aspartate and metalloproteases (Brown et al. 2000; Kühnle et al. 2019). A representative of human intramembrane proteases is the site-2 protease (S2P), a HExxH-type zinc metalloprotease (Brown et al. 2000). Rhomboids are serine proteases containing a catalytic serine-histidine dyad. There are 5 human serine proteases the rhomboid-like proteases (RHBDL1-4) (Lemberg und Freeman 2007) and a presenilin-associated rhomboid-like protease (PARL) (Spinazzi und Strooper 2016). The founding member of glutamate proteases is the Ras and a-factor converting enzyme 1 (Rce1) (Manolaridis et al. 2013). Aspartate proteases are divided in γ-secretase with presenilin PS1 and PS2, the catalytic subunit of γ-secretase, and signal peptide peptidases (SPPs) (Selkoe und Wolfe 2007), containing SPP and SPP-like proteases (SPPL) SPPL2a, SPPL2b, SPPL2c and SPPL3 (Voss et al. 2013).

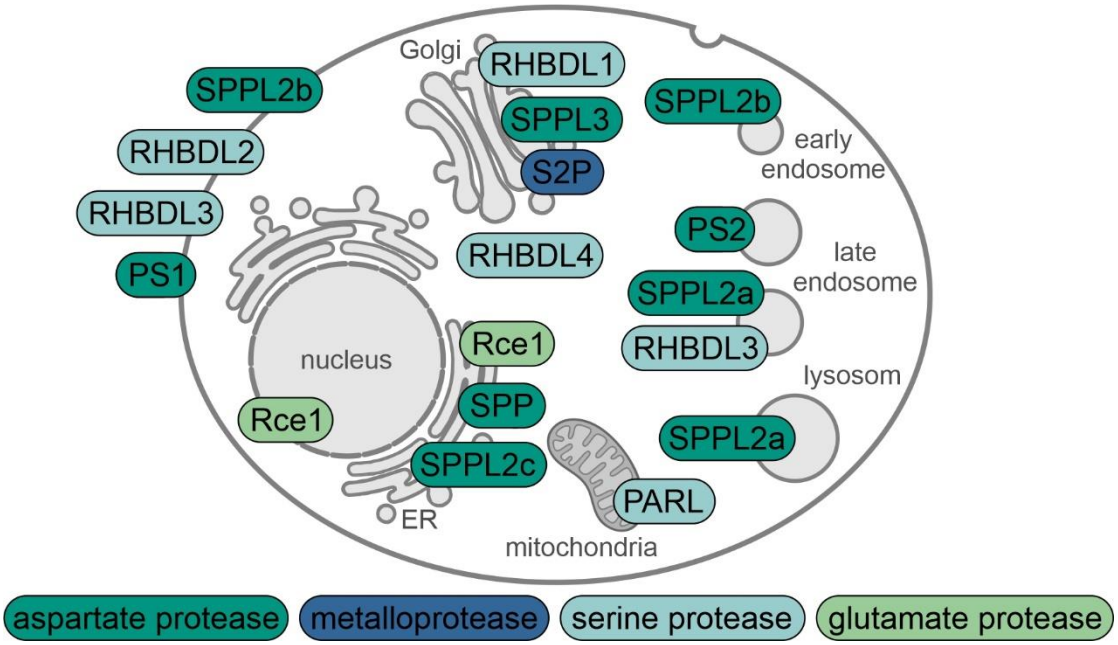

Figure 1.1 Cellular localisation of intramembrane proteases. Shown are the 4 classes of intramembrane proteases and their subcellular localisation.

The members of intramembrane protease family are located in different subcellular compartments (Figure 1.1). SPP, SPPL2c, RHBDL4 and Rce1 resides in the endoplasmic reticulum (ER) and are important for protein maturation and quality control (Friedmann et al. 2004; Niemeyer et al. 2019; Fleig et al. 2012; Manolaridis et al. 2013). In addition Rce1 is found in the inner nuclear membrane (Barrowman et al. 2008). The only mitochondrial intramembrane protease PARL reflects with its function the health of mitochondria (Spinazzi und Strooper 2016). Residing in the Golgi S2P, SPPL3 and RHBDL1 are involved in cholesterol and fatty acid biosynthesis as well as protein maturation (Brown et al. 2000; Voss et al. 2013). In endosomes/lysosomes γ-secretase/PS2 and RHBDL3 are found as well as SPPL2a/b, which are involved in the adaptive immune system (Lohi et al. 2004; Sannerud et al. 2016; Friedmann et al. 2006). RHBDL2 and RHBDL3 reside in the plasma membrane, just like γ-secretase/PS1 that is important for cell signalling (Lohi et al. 2004; Sannerud et al. 2016). Intramembrane proteases located in the plasma membrane or in endosome/lysosome membranes are also involved in protein degradation and so maintain the homeostasis of proteins, the proteostasis (Kühnle et al. 2019). In principle, the intramembrane proteolysis can serve

the purpose of activating or degrading a transmembrane protein independently of the cellular localisation.

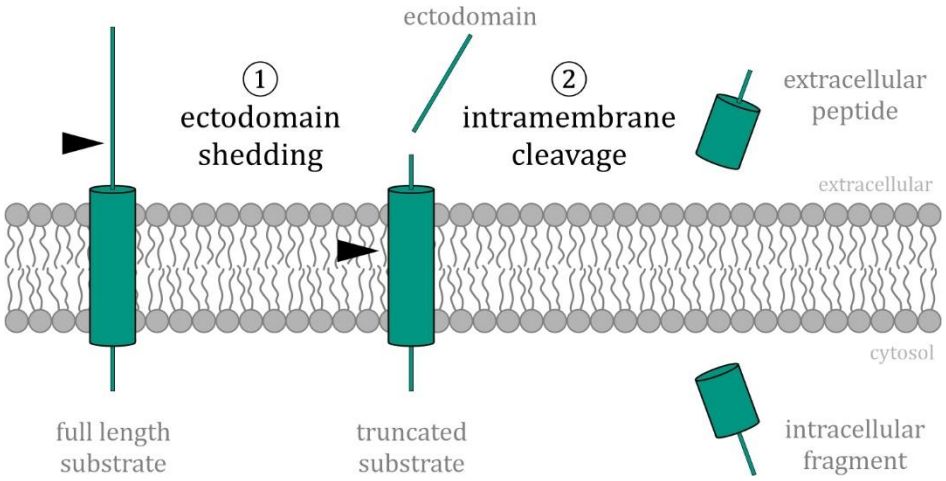

Figure 1.2 Regulated intramembrane proteolysis. In the first step the ectodomain is removed from the full-length substrate and in a second step the truncated membrane bound substrate is cleaved within the membrane by an intramembrane protease to release a small peptide to the extracellular space or lumen and the intracellular fragment into the cytosol.

Regulated intramembrane proteolysis is often a two-step process (Figure 1.2) (Brown et al. 2000). In a first step the large extracellular domain, the ectodomain, is removed by other membrane bound proteases. This process is also referred as ectodomain shedding. In the second step the truncated substrate is subsequently hydrolytically cleaved by an intramembrane protease to release the cleavage products. Depending on the membrane topology of the protease type I transmembrane proteins, where the N-terminus is located in the extracellular space or lumen, or a type II membrane proteins, with the N-terminus located in the cytosol (Figure 1.3), are processed. Some of the intramembrane proteases do not need a prior ectodomain shedding and process substrates with intrinsically short ectodomains or even multipass membrane proteins. Intramembrane proteolysis by aspartate proteases is a very slow process on a timescale of hours, compared to soluble proteases, which cleave their substrates within a fraction of a second. The cleavage rate might be influenced by substrate binding and the individual mechanistic steps (Langosch et al. 2015; Kamp et al. 2015).

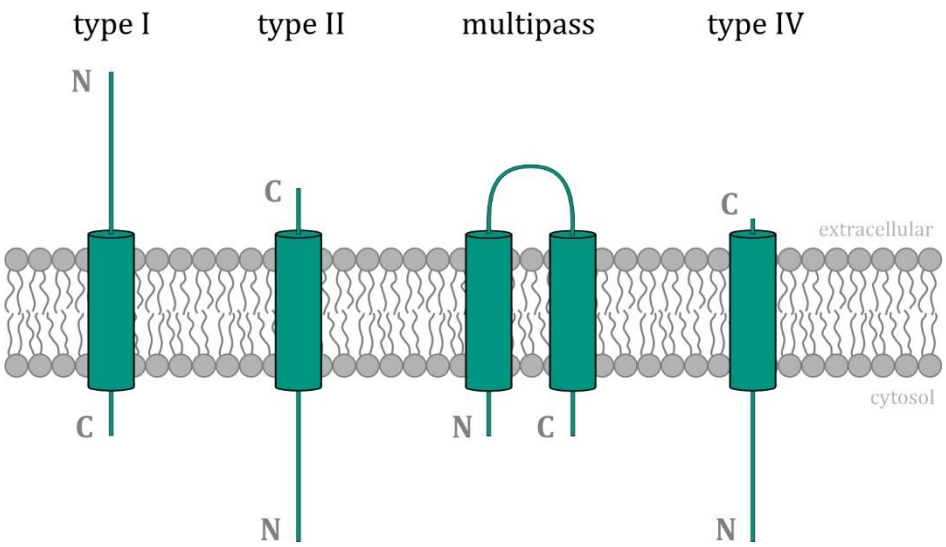

Figure 1.3 Classification of membrane proteins. Transmembrane proteins are classified according to the location of their termini (Spiess 1995). The N-terminus of type I single-span transmembrane proteins is located in the extracellular space or lumen in contrast the N-terminus of type II single-span transmembrane proteins is located in the cytosol. Type IV transmembrane proteins have a N_{in} topology, where the TMD is very close to the C-terminus. Multipass transmembrane proteins, traversing the membrane more than once, can be classified to type I or type II according to the topology of the first TMD.

In the following chapters, the individual intramembrane proteases will be described in more detail with a special emphasis on their structural and mechanistic properties and selected substrates will be presented. Particular attention will be paid to the aspartate proteases PS1 and SPPL2a/b, regarding the presented substrate requirements. Furthermore, insights to nuclear magnetic resonance (NMR) will be given, but limited to the applications of protein structure and dynamic determination required in this thesis.

1.1 Aspartate Proteases

Aspartate proteases in mammals can be divided in two families. The presenilin family consisting of PS1 and PS2, the catalytic subunit of the γ-secretase complex (Steiner und Haass 2000) as well as their closely related homologues SPP and SPPL2a, SPPL2b, SPPL2c and SPPL3, within the SPP/SPPL family (Fluhrer et al. 2009). All members of these two families are composed of 9 transmembrane domains (TMD), containing the catalytic aspartates within an (Y/F)D motif and GxGD motif (x = any amino acid) necessary for proteolytic activity (Wolfe et al. 1999; Weihofen et al. 2002), and a C-terminal PAL motif (Weihofen et al. 2002; Wolfe et al. 1999).

Beside the similarity of this conserved motifs, there are some differences concerning the topology of the membrane embedded aspartate proteases. They have an opposite orientation within the membrane where the N-termini of PS are located in the cytosol, while the N-terminus of SPP/SPPL facing the lumen or extracellular site (Friedmann et al. 2004; Nyborg et al. 2004a). The orientation of catalytic site correlates with the membrane topology of the respective substrates, so that PS only cleaves type-I membrane proteins (N_{out}) and SPP/SPPL are specific towards type-II transmembrane proteins (N_{in}) (Voss et al. 2013; Mentrup et al. 2017).

1.1.1 γ-Secretase

The membrane embedded protease γ-secretase is the founding member of intramembrane proteases (Wolfe et al. 1999). Besides the catalytic subunit PS, 3 other membrane proteins nicastrin (NCT), anterior pharynx-defective 1 (APH1) and presenilin enhancer 2 (PEN2) are essential for γ-secretase activity (Francis et al. 2002; Strooper 2003) (Figure 1.4 (a)).

The single-span transmembrane glycoprotein NCT contains a large extracellular domain. The mobile ectodomain is a substrate receptor (Shah et al. 2005; Petit et al. 2019; Aguayo-Ortiz et al. 2017) with a substrate interaction site, which can bind the N-terminus of the substrate (Bai et al. 2015b). Furthermore the large and bulky NCT ectodomain excludes substrates with a long ectodomain from entering the enzymes active site through steric hindrance, acting as a gatekeeper (Bolduc et al. 2016).

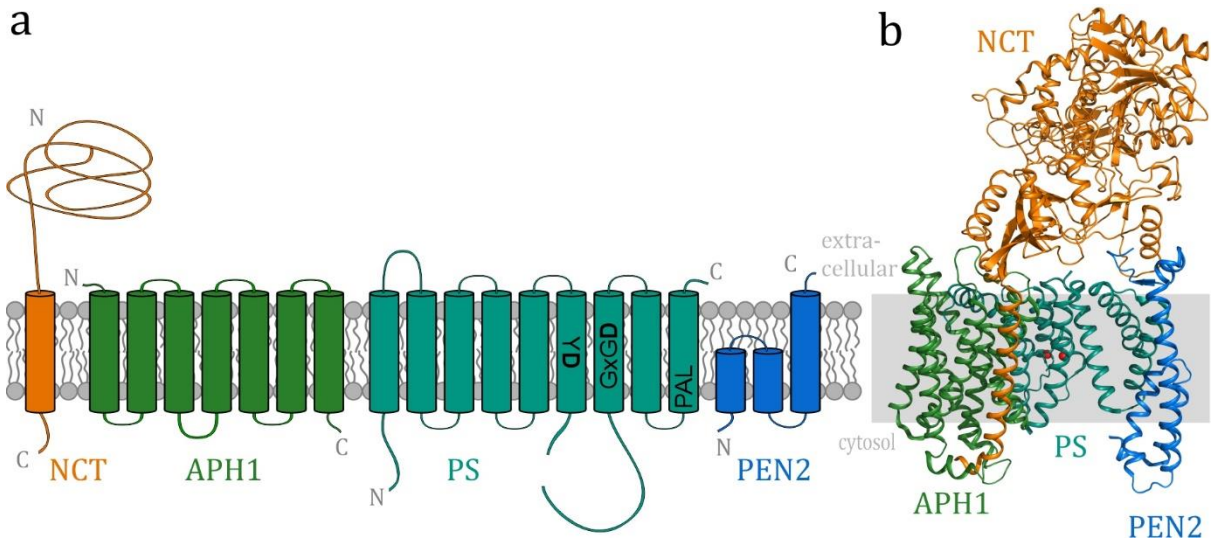

Figure 1.4 Structure of γ-secretase complex. The active γ-secretase complex consists of 4 proteins NCT (orange), APH1 (green), PEN2 (blue) and the catalytic subunit PS (turquoise) schematically shown in (a). The two catalytic aspartates are located within the conserved YD motif in TM6 and the GxGD motif in TM7. The conserved PAL motif is located in TM9. The cryo-EM structure of human γ-secretase ((5A63) (Bai et al. 2015b)) is shown in (b), where the catalytic aspartates are indicated by red dots. The lipid bilayer is depicted in grey.

PEN2 has 3 TMDs and interacts with PS and NCT (Bai et al. 2015b). It is important for the γ-secretase maturation by stabilizing PS (Prokop et al. 2004) and could act as a checkpoint in substrate sorting (Hitzenberger et al. 2020). APH1, with its 7 TMDs, exists in 3 isoforms a, b, c and depending on the combination with PS, the γ-secretase variants are located in different cellular compartments (Meckler und Checler 2016; Sannerud et al. 2016). In general APH1 stabilizes the γ-secretase complex as a scaffold, interacting with PS and the lone TMD of NCT (Watanabe et al. 2022; Bai et al. 2015b).

The subunits of the complex are associated with a 1:1:1:1 stoichiometry and the cryogenic electron microscopy (cryo-EM) structure of the γ-secretase complex (5A63) (Bai et al. 2015b) shows their arrangement (Figure 1.4 (b)). The subunits form an active complex by the assembly of NCT and APH1, stabilizing the holoprotein PS that is autocatalytically cleaved after activation through the final assembly of PEN2 (Kaether et al. 2006).

1.1.1.1 Presenilin

During the assembly into an active γ-secretase complex, the catalytic subunit PS undergoes autoproteolysis and cleaves itself within the large cytosolic loop between transmembrane helix (TM) TM6 and TM7 into a N-terminal fragment (NTF) and C-terminal fragment (CTF) (Thinakaran et al. 1996).

The active site is formed by TM2, TM3, TM5, TM6 and TM7, while one of the catalytic aspartates Asp_{257} is located in the NTF in the middle of TM6 within the YD motif and the other Asp_{385} resides in the CTF at the cytosolic border in TM7 within the GxGD motif (Wolfe et al. 1999). Interestingly, the distance in the cryo-EM structure of C_α atoms in Asp_{257} and Asp_{385} is with about 10 Å longer than the hydrogen bonding distance in aqueous aspartate proteases (Cooper et al. 1990; Bai et al. 2015b), suggesting a conformational change in PS after substrate binding. The PAL motif involved in substrate recognition, is also found at the cytosolic border in TM9 in close proximity to the catalytic aspartates (Sato et al. 2008; Bai et al. 2015b). Within the remarkably flexible PS, TM2 and TM6 as well as the loop between TM6 and TM7 are highly mobile (Bai et al. 2015b).

The binding of a substrate like Notch1 to γ-secretase induces several structural changes both in the enzyme as well as in the substrate. Indicated by the cryo-EM structure of γ-secretase in complex with Notch1 (6IDF) (Yang et al. 2019), the loop between TM1 and TM2 (loop1), TM2 and the cytosolic loop between TM6 and TM7 of PS1 are more ordered in the substrate-bound form compared to free γ-secretase (Bai et al. 2015b; Sun et al. 2015). Loop1 binds to the N-terminal juxtamembrane part of Notch1 and a short Notch1 helix in this part could insert in a hydrophilic pocket of NCT (Takagi-Niidome et al. 2015). Both TM2 and TM3 are extended by 2 or 3 helical turns and TM2 and TM6 are rotated by 15° towards each other.

One of the most important changes occur at the C-terminal part of PS1 NTF and in the cytosolic loop N-terminal of the GxGD motif in PS1 CTF, besides a short helix TM6a two antiparallel β-strands residues 288-290 and 377-381 are formed. This antiparallel β-sheet interacts with Notch1 TMD to stabilize the substrate binding and orient the scissile bond towards the catalytic aspartates, which are now about 6 Å away from the scissile peptide bond. In addition to the structural changes local rearrangements take place in order to realign important parts, like the catalytic aspartates and PAL motif, closer to the substrate.

Similar changes are induced after the binding of another substrate the amyloid precursor protein (APP) to γ-secretase (Zhou et al. 2019), indicating that the structural changes in PS are general features after substrate binding. Interestingly the γ-secretase inhibitor N-[N-(3,5-difluorophenacetyl)-L-alanyl]-S-phenylglycine t-butyl ester (DAPT) induces similar structural changes after binding to the protease (Bai et al. 2015a).

1.1.1.2 Substrates

About 150 substrates of γ-secretase are known (Güner und Lichtenthaler 2020). One of the most important is Notch1 due to its physiological role during development (Wong et al. 1997; Strooper et al. 1999) as well as APP, one of the most studied due to its pathogenesis of Alzheimer's disease (Selkoe 2011; Selkoe 1999).

Notch1

The Notch receptor is a type I transmembrane protein and 4 different Notch receptors, Notch1-4, are found in mammals expressed in a tissue- and cell-type specific manner. While Notch1 and Notch2 are expressed in many tissues, Notch3 is predominantly expressed in vascular smooth muscle cells and pericytes and Notch4 in endothelial cells (Zhang et al. 2023). Notch signalling is involved in cell-to-cell communication, cell-fate decisions during development, hematopoiesis, neuronal maintenance and neurogenesis (Struhl et al. 1993; Artavanis-Tsakonas et al. 1999; Kopan und Ilagan 2009; Bigas und Espinosa 2012). The intramembrane cleavage of Notch1 TMD by γ-secretase activates these processes and malfunction in the intramembrane proteolysis can cause dysregulation and diseases like neurodevelopmental defects and cancer (Wong et al. 2004; Weng et al. 2004). Because of these crucial biological functions and toxicity caused by the inhibition of γ-secretase cleavage of Notch TMD, the development of preventing or treating Alzheimer's disease is impeded (Strooper und Chávez Gutiérrez 2015). Interestingly, not all Notch homologues are equally important for development. While deletion of Notch1 and Notch2 is embryonic lethal, Notch3 and Notch4 are not essential for embryonic development or fertility in mice (Krebs et al. 2003).

The Notch receptor consists of a modular structure with 3 main components an extracellular domain (ECD), TMD and intracellular domain (ICD) (Kopan und Ilagan 2009) (Figure 1.5). The ECD is characterized by 29-36 epidermal growth factor (EGF) repeats, varying in the number among the different homologues, followed by 3 Lin Notch repeats (LNR) and finally by a hydrophobic heterodimerization domain (HD). The LNR and HD

form a negative regulatory region (NRR) that hinders a ligand-independent cleavage of the Notch protein (Sanchez-Irizarry et al. 2004). The ICD is defined by one recombination signal binding protein for immunoglobulin kappa J (RBPJ) associated module (RAM), followed by 7 anchor protein ankyrin repeats (ANK), one translational active domain (TAD) that is absent in Notch3 and Notch4, and one proline, glutamic acid, serine and threonine rich domain (PEST).

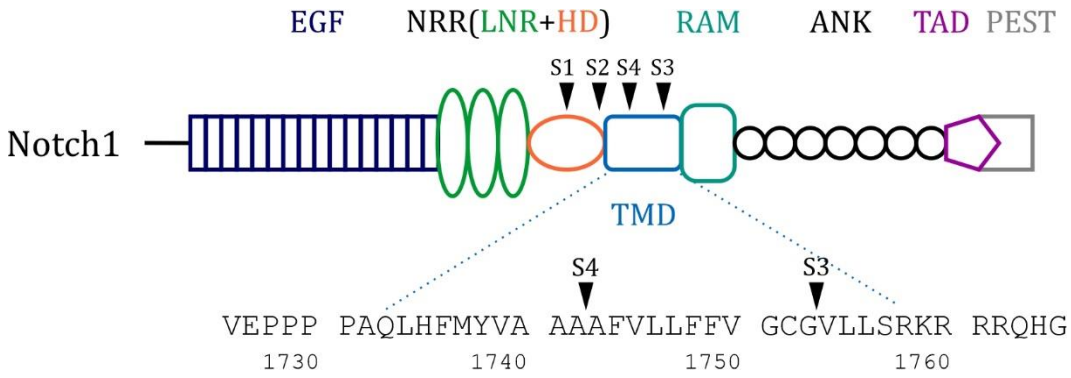

Figure 1.5 Domain organization and cleavage sites of Notch1. The Notch receptor contains an extracellular region, consisting of EGF repeats (dark blue) and the NRR, which comprises LNR modules (green) and the furin-cleaved HD domain (orange). The amino acid sequence of the TMD (blue) is shown below. The intracellular domain consists of RAM (turquoise), ANK (black), TAD (violet) and PEST (grey). Abbreviations are explained in the text. Approximate positions of cleavage sites S1 to S4 are shown in the schematic representation of the domains and the exact cleavage sites S3 and S4 are shown in the amino acid sequence.

The Notch protein is synthesized in the ER and is cleaved by a furin-like convertase at the S1 cleavage site, Arg_{1664}/Glu_{1665} within the HD domain, in the Golgi apparatus during its maturation (Logeat et al. 1998; Gordon et al. 2009). This cleavage produces a heterodimer, where the ECD is attached to the TMD and ICD, is transported to the plasma membrane (Blaumueller et al. 1997). There, a transmembrane ligand from a neighbouring cell can bind to the EGF domain (Cordle et al. 2008), activating the Notch receptor by mechanically extending the NRR and exposing the buried S2 cleavage site, Glu_{1719}/Ala_{1720} in the juxtamembrane region, for cleavage by a disintegrin and metalloproteinase (ADAM) (Gordon et al. 2007; Brou et al. 2000; van Tetering und Vooijs 2011) (Figure 1.6).

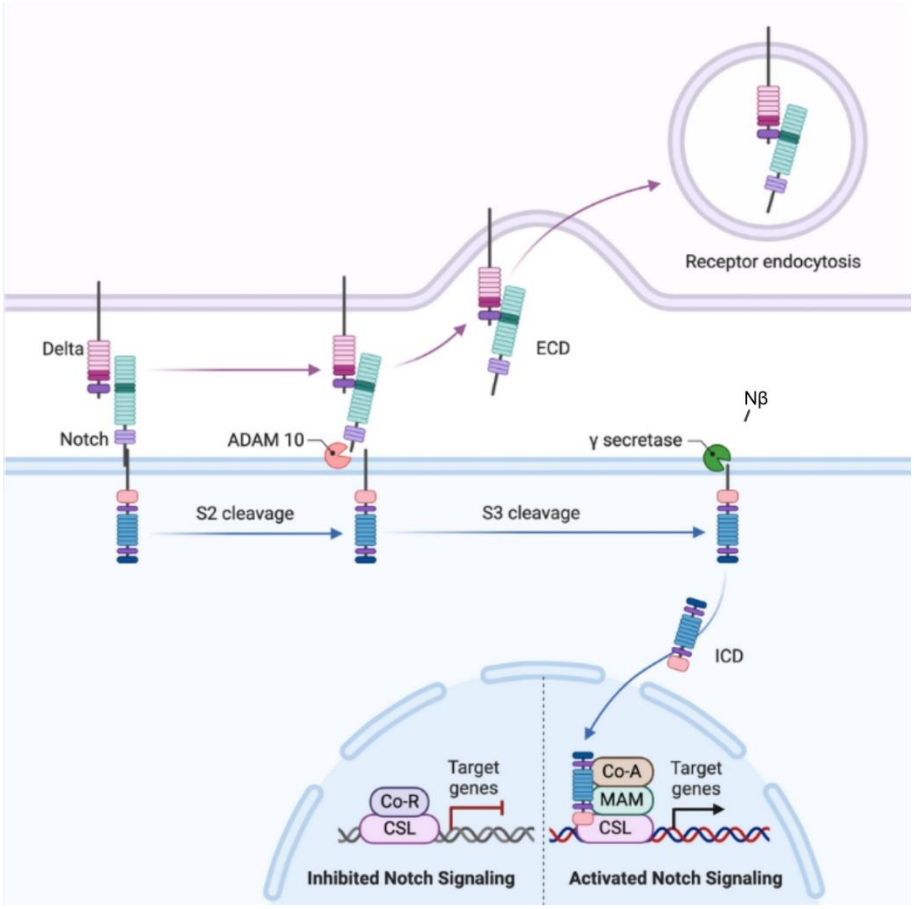

Figure 1.6 Notch signalling pathway. Notch signalling is activated upon ligand (Delta) binding to the heterodimeric Notch receptor, which was previously cleaved at S1 cleavage site by a furin-like protease, where the ECD is still attached to the TMD and ICD and transported to the plasma membrane. The Notch receptor is then cleaved at S2 by ADAM and the released ECD is endocytosed by the ligand-expressing cell. The membrane-bound ICD is cleaved at S3 by γ-secretase to liberate Nβ peptides in extracellular space and release the ICD into the cytosol. The ICD translocates to the nucleus and binds to transcription factor CSL and transcription activator MAML/Co-A, therefore activating the transcription and expression of various downstream target genes. The figure was made in BioRender (https://www.biorender.com).

The released ECD is bound to the ligand and can be phagocytosed by the ligand expressing cell, while the membrane bound fragment is cleaved at the S3 cleavage site Gly_{1753}/Val_{1754} in its TMD by γ-secretase (Figure 1.7) (Vooijs et al. 2004). The intramembrane proteolysis liberates ICD in the cytosol and the membrane bound Notch fragment might be processed by a stepwise and successive cleavage every third residue up to the S4 cleavage site Ala_{1741}/Ala_{1742}, analogous to the processing of APP (Takami et al. 2009; Bhattarai et al. 2022), to release small Notch β peptides (Nβ) into the extracellular space (Okochi et al. 2002; Okochi et al. 2006). The ICD translocates to the nucleus to form a transcriptional

activator complex with CBF1, Su(H), Lag1 (CSL) and mastermind-like (MAML) proteins, which activate the transcription of a number of different Notch1 target genes (Wu et al. 2000; Iso et al. 2003; Kovall 2008). When the ICD PEST domain is phosphorylated by CDK8 and targeted for polyubiquitination and proteasomal degradation, the Notch canonical signalling pathway is terminated (Fryer et al. 2004).

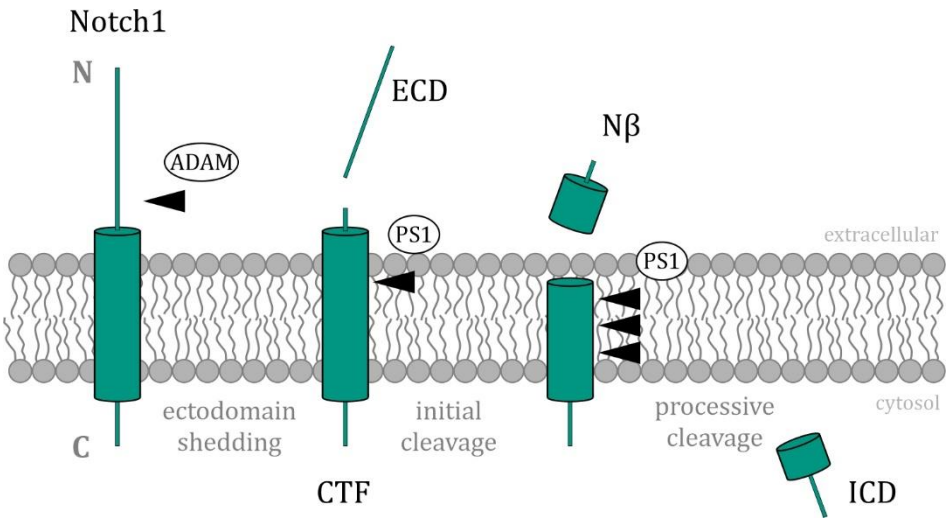

Figure 1.7 Notch1 processing. Notch1 is cleaved by ADAM to release the ECD containing the EGF and NRR domain and the membrane bound CTF is subsequently cleaved by PS1 to liberate Nβ peptide into the extracellular space and the ICD into the cytosol.

APP

Besides Notch, APP is another one of the most prominent γ-secretase substrates, also because of its central role in Alzheimer's disease (Selkoe 1999; Selkoe 2011). APP a type I transmembrane protein containing a large ECD, a TMD and a short ICD, is expressed in various tissues as well as neurons (Puig und Combs 2013). After the synthesis in ER and transport via Golgi to the plasma membrane, APP is processed ether via the non-amyloidogenic or the amyloidogenic pathway (van der Kant und Goldstein 2015) (Figure 1.8). In the non-amyloidogenic pathway, the ectodomain is first shedded by an α-secretase (ADAM10/17) (Lichtenthaler 2011), liberating the soluble NTF sAPPα and the remaining 83 amino acid long membrane bound CTF is cleaved in a second step by γ-secretase to release P3 peptides in the extracellular space/lumen and the ICD into the cytosol (Selkoe 2004). The physiological function of APP and its proteolysis is not known, but P3 peptides could induce the production of inflammatory cytokines and chemokines, sAPPα might be

neuroprotective and APP ICD could translocate to the nucleus analogous to Notch (Szczepanik et al. 2001; Zhou et al. 2011; Kimberly et al. 2001). The amyloidogenic pathway starts with the shedding by a β-secretase, β-site amyloid precursor protein cleaving enzyme (BACE1) (Vassar et al. 2009), to release a soluble NTF sAPPβ and generating a 99 amino acid long membrane bound CTF C99, which is further cleaved by γ-secretase liberating amyloid β-peptides (Aβ) in the extracellular space/lumen and the ICD into the cytosol (Weidemann et al. 2002). The initial γ-secretase cleavage of C99 can occur either at the ε49 cleavage site Leu_{49}/Val_{50}, releasing after stepwise tripeptide trimming (Takami et al. 2009; Bhattarai et al. 2022) the 40 amino acid long Aβ40 peptide or the cleavage occur at the ε48 cleavage site Thr_{48}/Leu_{49} to generate Aβ42 peptide. The ratio of the longer Aβ42 to the shorter Aβ40 is important, since the pathogenic Aβ42 peptide is highly aggregation prone and might deposit in Alzheimer's disease patients brain as plaque, resulting in neurodegeneration and dementia (Haass und Selkoe 2007; Steiner et al. 2018).

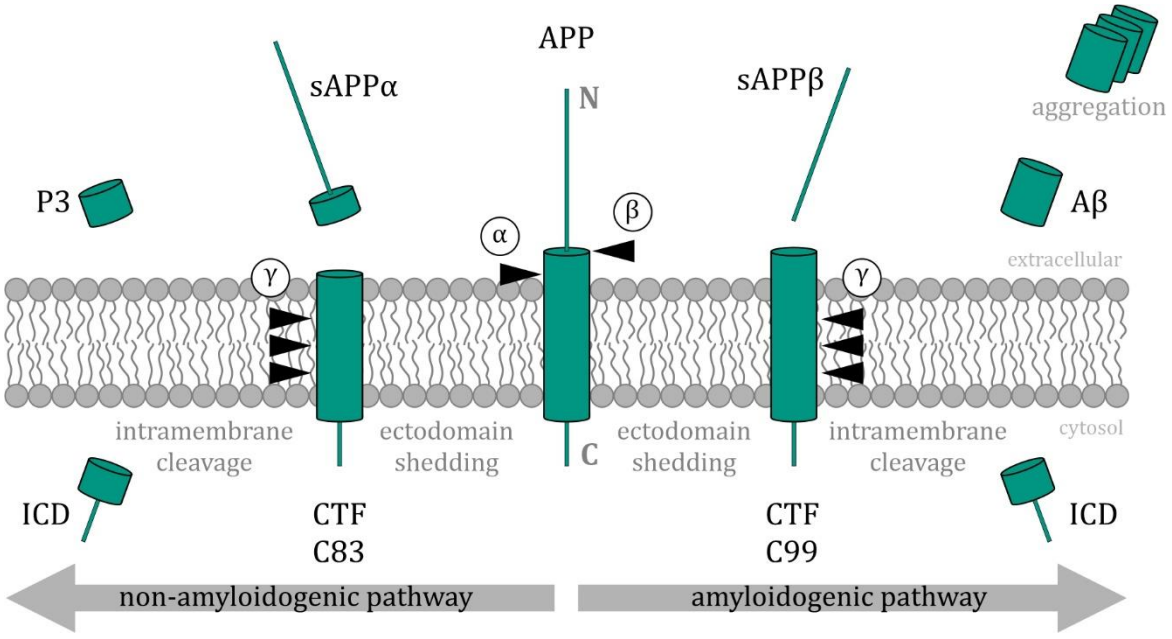

Figure 1.8 APP Processing. There are two possible processing pathways of APP. Processing via the non-amyloidogenic pathway (left side) starts with the release of sAPPα through ectodomain shedding by α-secretase. The membrane bound CTF C83 is cleaved by γ-secretase liberating P3 peptides in the extracellular space and ICD into the cytosol. Ectodomain shedding by β-secretase via the amyloidogenic pathway (right side) releases sAPPβ and the membrane bound CTF C99 is cleaved by γ-secretase to liberate the ICD to the cytosol and aggregation prone Aβ peptides in the extracellular space. The lipid bilayer is depicted in grey.

1.1.1.3 γ-Secretase Cleavage Mechanism

The mechanism of intramembrane proteolysis of the truncated Notch CTF by γ-secretase is considered in detail below, with particular attention to the interaction between Notch1 TMD and PS1.

Exosite Binding and Substrate Entry

The first interaction of Notch1 TMD does not take place directly at the active site, but at the outside of γ-secretase. The recruitment of the substrate is a multi-step gating process and involves the binding to exosites on NCT, PEN2, APH1 and PS1 (Li et al. 2017; Fukumori und Steiner 2016). The first step involves the binding to NCT and/or the binding to PEN2 as well as APH1, guiding the substrate to the exosite on PS1. Here the interaction between PS1 and Notch1 TMD is mainly characterized by charged and polar residues in the C-terminal TMD (TM-C) of Notch1 Ser_{1757} and Arg_{1758} and the loop between TM2 and TM3 (loop2) in PS1 Cys_{158} and Tyr_{159}, orienting the S3 cleavage site towards γ-secretase (Hitzenberger et al. 2020). Notch1 TMD then has the possibility to enter the active site of PS1 through different pathways using the opening between TM2/TM6 or TM6/TM9 (Hitzenberger und Zacharias 2019). Although the entry route is not fully understood and a steric barrier has to be overcome for each of the options, the entry pathway via lateral diffusion through TM2/TM6 seems to be preferred (Yang et al. 2019).

Different substrates differ in their preferences for binding to the exosites and for choosing an entry pathway. This indicates that structural properties rather than the substrate sequence determine the first contact between a substrate and the protease.

Translocation to the Active Site

Regardless which entry pathway is chosen, the substrate TMD requires a certain flexibility to enter the interior of the enzyme and translocate to the active site. Residues as part of a hydrogen bond network can represent mechanical hinges and provide bending and twisting motions (Hayward 1999). Hereby bending is favoured by loose hydrogen bonds on the one side of a helix together with small, sterically not demanding residues on the opposite side and twisting is favoured by a shift from α-helical (i → i+4) to 3_{10}-helical (i → i+3) hydrogen bonds (Hitzenberger et al. 2020). In general, small central amino acids like glycine or alanine destabilize the TMD helix of substrates and increase flexibility, facilitating translocation to PS1 active site (Högel et al. 2018). In contrast large and bulky

residues like leucine stabilize the TMD helix thus decreasing flexibility and impede translocation (Quint et al. 2010).

β-Strand and Hybrid β-Sheet Formation

Binding of Notch1 TMD to γ-secretase induces conformational changes in both the substrate and enzyme in order to stabilize the complex, position the substrate in a cleavage competent orientation and realign important parts of PS1 closer to Notch1 TMD.

The conformation of the Notch1 TMD and juxtamembrane regions bound to γ-secretase in the cryo-EM (Yang et al. 2019) structure differ from the structure of free Notch1 TMD (Deatherage et al. 2017). The unstructured termini in free Notch1 TMD are more ordered after binding to the enzyme. The N-terminal juxtamembrane part forms a short helix, residues 1722-1725, which could insert in a hydrophilic pocket of NCT and a proline-rich region, residues 1726-1733, binds to loop1 (Takagi-Niidome et al. 2015). To enable access to the S3 cleavage site and the scissile peptide bond, Notch1 TM-C helix is unwound after Gly_{1751} in the complex with γ-secretase and residues Leu_{1755} to Arg_{1761} form an extended β-strand (Yang et al. 2019).

The Notch1 TMD extended β-strand, located directly C-terminal after the initial cleavage site, interacts via hydrogen bonds with the antiparallel β-sheet formed in PS1 (Yang et al. 2019). The formation of this hybrid β-sheet stabilizes the active substrate-enzyme complex and positions the substrate in a cleavage competent orientation towards the catalytic residues in PS1. This positioning is further stabilized by main chain hydrogen bonds between Notch1 TMD β-strand and Leu_{432} preceding the PAL motif in the loop connecting TM8 and TM9 as well as Gly_{1753} at the S3 cleavage site and Gly_{384} within the GxGD motif of PS1, directing the cleavage site in close proximity to the catalytic residues (Yang et al. 2019).

Unfolding of Cleavage Site and Tetrahedral Intermediate

After substrate binding to the active site and formation of the hybrid β-sheet a water molecule must coordinate to a catalytic aspartate of PS1 and the scissile peptide bond of the substrate. The active site in PS1 resides in a hydrophilic pore and water molecules could enter this catalytic cavity from the cytosol (Sato et al. 2006).

After a substrate binds to the active site a water molecule could be trapped nearby the catalytic aspartates or enter PS1 from the cytosolic site through a channel formed by the β-strand of the substrate and PS1 CTF (Bhattarai et al. 2020). The formation of a hydrogen

bond between the water molecule and a catalytic aspartate activates the water for a nucleophilic attack to the carbonyl carbon of the scissile amide bond in the substrate (Figure 1.9). The other catalytic aspartate donates a proton to the carbonyl oxygen, generating the tetrahedral intermediate, which then dissociates into the cleavage products (Das et al. 2010).

A partial unfolding of the helix by destabilizing the hydrogen bond between the carbonyl oxygen at the cleavage site and the amide nitrogen of residue (i+4) facilitates the nucleophilic attack and cleavage of the scissile bond.

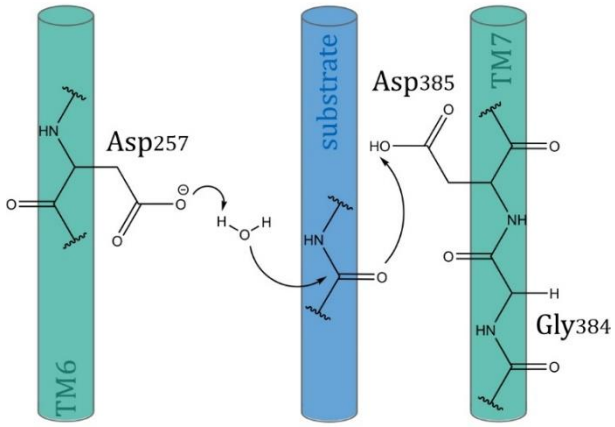

Figure 1.9 Cleavage reaction mechanism. Schematic representation of reaction mechanism. A catalytic aspartate activates a water molecule for nucleophilic attack to the carbonyl carbon of the scissile peptide bond in the substrate (blue). Hydrogen bond between the other catalytic aspartate and the carbonyl oxygen of the scissile peptide bond facilitates nucleophilic attack and stabilizes tetrahedral intermediate, which dissociates in the cleavage products.

1.1.2 SPP/SPPL Proteases

Members of the SPP/SPPL family are active on their own. They do not need additional co-factors for proteolytic activity (Weihofen et al. 2002), unlike PS, which is only active with 3 further proteins (Steiner et al. 2008; Edbauer et al. 2003). Also they do not need an autoproteolytical cleavage of the loop between TM6 and TM7, as PS1 needs during incorporation in the multiprotein complex (Haass und Steiner 2002).

Since the intramembrane proteolysis is a highly regulated process, SPP/SPPL proteases do not have only a degradative function of maintaining membrane proteostasis,

but also influence cellular signalling and membrane traffic (Mentrup und Schröder 2022; Papadopoulou und Fluhrer 2020). In order to fulfil the various tasks, the member of the SPP/SPPL family have different subcellular localisations, where they are able to process a variety of substrates.

In the following, the individual members of the SPP/SPPL family are described in terms of their characteristic properties. Some of the SPP/SPPL substrates are briefly explained to show the spectrum of their wide biological function, thereby the two SPPL2a/b substrates TNFα and Bri2 are presented in more detail.

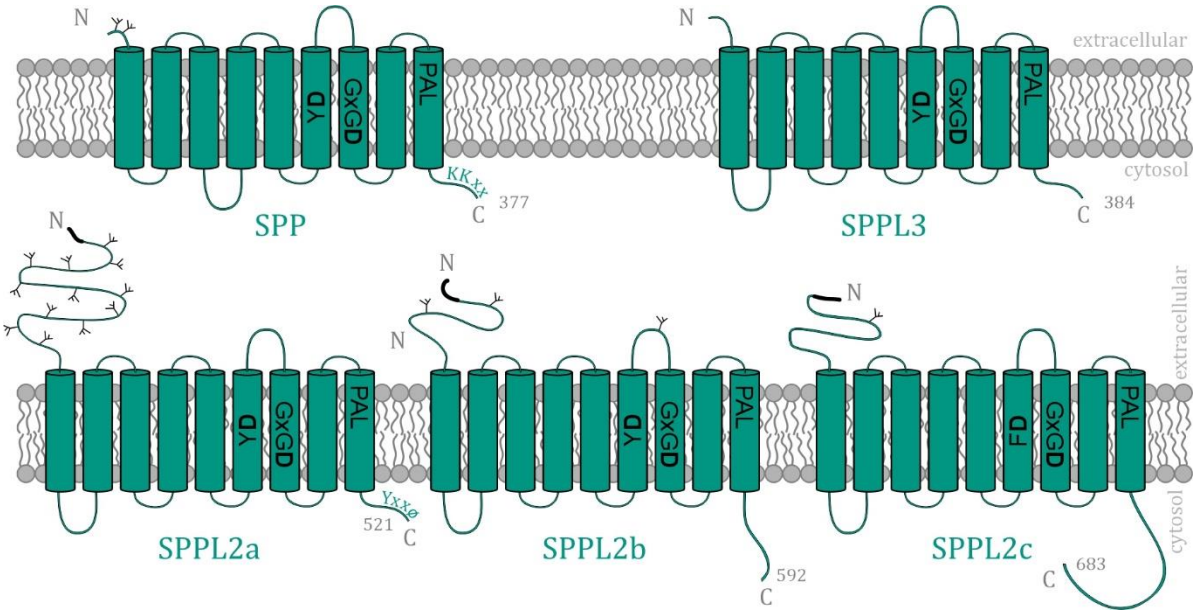

Figure 1.10 Structures of SPP/SPPL proteases. All members share 9 TMDs and characteristic motifs, like GxGD, (Y/F)D and PAL, but they differ in the length of N- and C-termini and glycosylation sites. SPPL2a/b/c contain a N-terminal signal sequence, SPPL2a a C-terminal lysosomal sorting motif and SPP a C-terminal ER retaining signal. In contrast to PS, the N-termini are located in the extracellular space. The lipid bilayer is depicted in grey.

1.1.2.1 SPP

In 2002 SPP, the first discovered protease of this family, was described as an aspartate protease containing 9 TMDs with the characteristic active site motifs, N-terminal glycosylation sites and a C-terminal ER retaining signal KKxx (x = any amino acid) (Friedmann et al. 2004; Weihofen et al. 2002) (Figure 1.10).

Nevertheless SPP is active without further co-factors, a formation of active SPP homodimer and tetramers has been described (Nyborg et al. 2004b; Miyashita et al. 2011;

Nyborg et al. 2006). To extend its substrate spectrum, SPP is able to build complexes with cellular proteins like Derlin1 and E3 ubiquitin ligase TRC8, during ER-associated degradation (ERAD). As a multiprotein complex SPP is able to recognize and cleave substrates like X-box binding protein 1 (XBP1), a regulator of the unfolded protein response (UPS) that would otherwise not be processed by SPP (Chen et al. 2014).

SPP cleavage is involved in signal peptide degradation. Secretory and membrane proteins, destined for the ER, are expressed as pre-proteins and bear an N-terminal signal sequence, which is cleaved by a signal peptidase (SP) during co-translational translocation thorough the ER membrane. Intramembrane proteolysis is performed by SPP releasing the remaining signal peptide from the ER membrane for degradation (Weihofen et al. 2000), where the proteases could act as a proteasome of the membrane (Kopan und Ilagan 2004).

Indirectly SPP controls trafficking by affecting the abundance of key molecules such as soluble N-ethylmaleimide-sensitive factor (NSF) attachment protein receptor (SNARE) proteins (Avci et al. 2019). Peptides, released from the membrane, may induce signal transduction pathways within the cell, as in case of polymorphic human major histocompatibility complex (MHC) class I molecules, important for immune surveillance (Lemberg et al. 2001). SPP is involved in the processing of viral proteins, releasing fragments of signal peptides from newly synthesized viral proteins, to interact with cytosolic target molecules, as in human immunodeficiency virus type 1 (HIV-1) envelope protein gp160 (Martoglio et al. 1997). Further substrates of SPP are tail-anchored (TA) proteins in type-II orientation with an intrinsically short extracellular or luminal C-terminus, such as cytochrome B5A (CYB5A), ribosome-associated membrane protein 4 (RAMP4), heme oxygenase 1 (HO1) and the FK506-binding protein 8 (FKBP8) (Boname et al. 2014; Hsu et al. 2015; Hsu et al. 2019).

With the ability to influence cellular signalling and trafficking the proteolysis by SPP correlates with the progression and malignancy of cancer (Hsu et al. 2019). The SPP-mediated cleavage of HO1 liberates a cytosolic fragment from the ER membrane, which translocates to the nucleus, stimulating proliferation and migration (Hsu et al. 2015). However, ER levels and turnover of the respective peptides can be controlled by intramembrane proteolysis subjecting the released fragments to ERAD (Boname et al. 2014; Hsu et al. 2019).

1.1.2.2 SPPL2 Subfamily: SPPL2a, SPPL2b, SPPL2c

Analysing the human genome in relation to PS identified the SPPL2 subfamily of aspartate proteases consisting of 9 TMDs and the conserved GxGD, (Y/F)D and PAL motifs (Weihofen et al. 2002; Grigorenko et al. 2002). The SPPL2 proteases contain a N-terminal signal sequence and are further N-terminally extended by a hydrophilic extracellular or luminal domain with various glycosylation sites (Figure 1.10) (Friedmann et al. 2004). Additionally, SPPL2b carries a glycosylation site in the luminal loop between TM6 and TM7 (Friedmann et al. 2004). The members of the SPPL2 subfamily have different cellular localisations and thereby different access to substrates. SPPL2a bears a C-terminal tyrosine-based sorting motif Yxxø (x = any amino acid, ø = amino acid with bulky and hydrophobic side chain), targeting to lysosomes and late endosomes, where SPPL2a is mainly found, in a small amount it is additionally present at the plasma membrane (Behnke et al. 2011; Friedmann et al. 2006). SPPL2b lacks this lysosomal target sequence and is predominantly found at the plasma membrane (Behnke et al. 2011; Friedmann et al. 2006). The two homologues SPPL2a and SPPL2b are not only located in different subcellular compartments but differ in the abundance they occur in different tissues. While SPPL2a is expressed in all tissues but only slightly in the brain, the opposite is true for SPPL2b, whose protein levels are high in brain and lower in other tissues (Schneppenheim et al. 2014).

Compared to the other member of the SPPL2 subfamily, one of the catalytic aspartates in SPPL2c is located within a FD motif and the N- and C-termini are most elongated (Friedmann et al. 2004). SPPL2c resides in the ER and early Golgi compartments, where one N-glycosylation site is present in the N-terminal luminal part (Niemeyer et al. 2019). Expression of SPPL2c is highly tissue and cell specific, so it is only found in developing male germ cells in murine and human testis (Niemeyer et al. 2019) and had for long been assumed as a pseudogene due to its intron-less structure (Golde et al. 2009). In addition to SPP, SPPL2c is also able to form high molecular weight complexes in the ER membrane (Schrul et al. 2010; Niemeyer et al. 2019).

Intramembrane cleavage by SPPL2a/b controls the NTF level of the invariant chain (CD74) of MHC class II proteins and thereby strongly impact the adaptive immune system. SPPL2a/b cleave the lectin-like oxidized LDL receptor 1 (LOX1) NTF, removing it from the membrane, and serve as a negative regulator of LOX1 signalling, causing atherosclerosis (Mentrup et al. 2019). Type III multi-span transmembrane proteins are also substrates

for intramembrane proteases, which need a cleavage to open the loop, generating type I and type II oriented membrane stubs that can be further processed. The type III transmembrane foamy virus envelope (FVenv) protein has a long leader peptide (LP18) in type II orientation (Lindemann und Rethwilm 2011) which is a SPPL2a/b substrate for consecutive intramembrane cleavage, but needs a prior shedding ether by a proprotein convertase (PC) or SPPL3 (Voss et al. 2012).

Besides HO1 and RAMP4, SPPL2c cleaves the tail-anchored protein phospholamban (PLN), a regulator of the ER-located sarco/ER Ca^{2+}-ATPase (SERCA) calcium pump. After proteolytic release of the membrane bound PLN to the cytosol, it binds and inhibits SERCA, thus modulating cytoplasmic calcium levels and differentiation of male germ cells (Niemeyer et al. 2019). A further validated SPPL2c substrate is the tail-anchored protein syntaxin 8 (Stx8), a SNARE protein, involved in vesicular transport and thus SPPL2c cleavage might contribute to cellular reorganisation in maturing spermatids (Papadopoulou et al. 2019).

1.1.2.3 SPPL3

SPPL3 is the smallest intramembrane protease of the SPP/SPPL family, lacking the N-terminal signal peptide, and the only one that does not exhibit glycosylation (Figure 1.10) (Friedmann et al. 2004). SPPL3 is expressed in all major tissues (Friedmann et al. 2004). The special thing about SPPL3 is that it cleaves exclusively full-length substrates with large ectodomains without prior shedding, referred to as non-canonical shedding (Voss et al. 2012; Voss et al. 2014).

In the Golgi SPPL3 cleaves glycosidases and glycosyltransferases, like N-acetylglucosaminyltransferase V (GnTV), which modify proteins by adding glycans on their secretory way (Voss et al. 2014). SPPL3 shedding of the ectodomain, containing the catalytic domain of these substrates, results in their deactivation and in a reduced glycosylation activity. Also multipass transmembrane proteins are processed by SPPL3, so SPPL3 cleaves not only the prior truncated foamy virus envelope protein (FVenv), but also acts as non-canonical sheddase for the full-length FVenv (Voss et al. 2012).

The SPPL3 cleavage is crucial for Golgi function and cellular growth control, so deletion studies of SPPL3 in mouse natural killer (NK) cells suggests the control of cell maturation (Hamblet et al. 2016).

1.1.2.4 Substrates of SPPL2a/b

TNFα

In 1962 for the first time a tumor necrotizing activity was described in mice after administration of bacterial endotoxic lipopolysaccharides and attributed in 1975 to tumor necrosis factor (TNFα) (O'Malley et al. 1962; Carswell et al. 1975). Further investigations revealed TNFα as a pleiotropic cytokine and a member of a TNF superfamily. The TNF superfamily consists of 19 ligands and 29 receptors, which are inter alia involved in inflammation, cell growth and apoptosis (Aggarwal et al. 2012). TNFα is primarily found on cell surfaces of macrophages and monocytes but also at lower levels on T lymphocytes, NK cells, dendritic cells, B lymphocytes, cardiomyocytes and fibroblasts (Carswell et al. 1975; Bradley 2008).

TNFα is a type II transmembrane protein with a 25 amino acids long N-terminal intracellular part, a TMD and a conserved C-terminal extracellular domain, the TNF homology domain (THD) (Figure 1.11) (Bodmer et al. 2002). The 150 amino acid long THD domain adopt β-sandwich structure, consisting of two stacked β-sheets, each formed by 5 antiparallel β-strands. Through the THD TNFα is able to trimerize and also bind the TNFα receptor (Bodmer et al. 2002).

The membrane bound TNFα is cleaved between Ala_{76}/Val_{77} by a metalloproteinase TNFα converting enzyme (TACE), a member of the ADAM family, releasing a soluble TNFα (sTNFα) fragment into the extracellular space (Moss et al. 1997; Mohan et al. 2002). After ectodomain shedding by TACE/ADAM, the remaining membrane bound part of TNFα is processed by the intramembrane proteases SPPL2a/b to liberate TNFα ICD into the cytosol and small TNFα C peptides into the extracellular space (Figure 1.12) (Fluhrer et al. 2006; Friedmann et al. 2006).

TNFα canonical shedding by ADAM10/17 liberates a soluble extracellular domain and non-canonical shedding of full-length TNFα (TNFα FL) by SPPL2a releases a slightly larger extracellular soluble domain sTNFαL (Spitz et al. 2020), both independent shedding routes merge in the intramembrane proteolysis of TNFα NTF by SPPL2a/b. Initial cleavage sites of SPPL2a/b cleavage were found at Cys_{49}/Leu_{50} and His_{52}/Phe_{53} as well as consecutive cleavage sites at Ser_{34}/Leu_{35} and Leu_{39}/Val_{40}, some additional minor cleavage sites were also found at Leu_{31}/Phe_{32}, Leu_{35}/Phe_{36}, Ser_{37}/Phe_{38} and outside of the TMD at Val_{55}/Ile_{56} and Gln_{59}/Arg_{60} (Spitz et al. 2020).

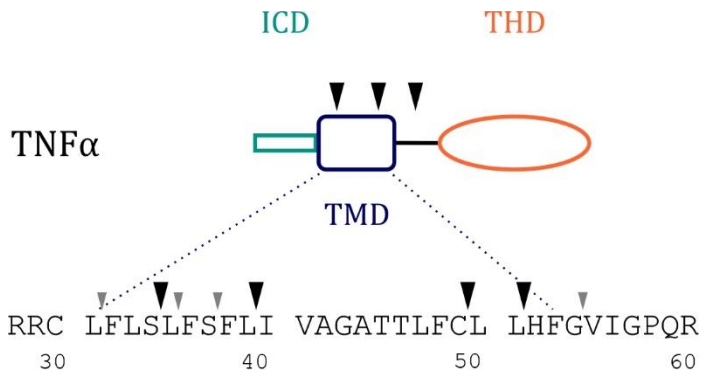

Figure 1.11 Schematic structure and cleavage sites of TNFα. TNFα consists of a short N-terminal intracellular domain (turquoise), a TMD (dark blue) and a homology domain (orange). Main cleavage sites of SPPL2a/b cleavage are indicated by black arrows and minor cleavage sites by small, grey arrows.

In general, TNFα signals through the membrane embedded TNF receptor 1 (TNFR1) triggering cell death and TNF receptor 2 (TNFR2) mediating cell survival (Figure 1.13) (Pimentel-Muiños und Seed 1999). TNFR1, a type I transmembrane protein expressed on nearly all cells, is activated by homotrimeric membrane bound TNFα FL or its homotrimeric soluble form (Eck und Sprang 1989). This activation leads to a trimerization of TNFR1, accordingly the cytoplasmic death domain (DD) serves as a binding platform for various signalling proteins (Banner et al. 1993). Dependent on which signalling proteins are recruited different pathways can be activated leading to caspases induced apoptosis and necroptosis via an signal complex II, or even transcription factor nuclear factor κB (NFκB) mediated expression of proteins associated with cell survival and cell proliferation via signal complex I (Aggarwal et al. 2012; Gough und Myles 2020).

TNFR2 also a type I transmembrane protein with limited expression to particular cells like endothelial cells, immune system cells and nerve cells, bears the same cysteine rich extracellular domain like TNFR1 but lacks the cytosolic DD. This receptor is activated by membrane bound TNFα FL, whereby soluble TNFα has a low affinity towards TNFR2 inducing weak signalling (Grell et al. 1995). After activation and trimerization an adaptor protein binds to the cytosolic domain of TNFR2, forming the signal complex I. Signal complex I promotes, dependent on the assembly of specific signal proteins, proinflammatory effects through NFκB regulated proteins, such as the cytokines interleukin 6 (IL6), IL8, IL18, chemokines, inducible nitric oxide synthase (iNOX), cyclooxygenase 2 (COX2), and lipoxygenase 5 (LOX5), major mediators of inflammation

(Yang et al. 2018; Aggarwal et al. 2012). Besides the production of inflammatory mediators, NFκB triggers transcription of cell survival associated genes and genes with antiapoptotic function (Yang et al. 2018). Starting from the signal complex I, also a further transcription factor activator protein 1 (AP1) can be induced by activating extracellular signal-regulated kinases, resulting in cellular proliferation (Natoli et al. 1997).

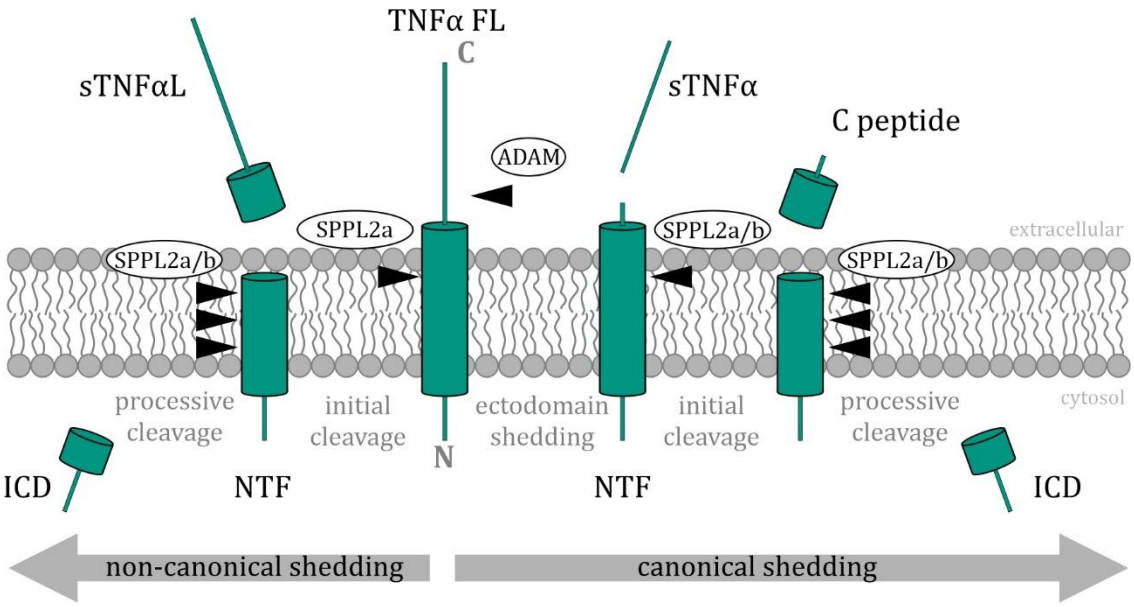

Figure 1.12 TNFα processing. The canonical shedding of TNFα FL by ADAM liberates a sTNFα into the extracellular space and the membrane bound NTF is successively cleaved by SPPL2a/b to release C peptides in the extracellular space and the ICD into the cytosol. TNFα FL initial cleavage of the non-canonical shedding by SPPL2a liberates a slightly larger sTNFαL into the extracellular space and after successive cleavage by SPPL2a/b the ICD is released in the cytosol.

Interestingly TNFα is not only able to induce its own expression through NFκB (Aggarwal 2003), but also to regulate its abundance by reverse signalling. The activated TNFα receptors are cleaved by TACE into a soluble form, which binds to TNFα, reducing its availability to the membrane bound TNFR1 and TNFR2 (van Zee et al. 1992). Independent of the receptor mediated signalling pathways TNFα ICD, bearing a nuclear localisation signal (Domonkos et al. 2001), is able to translocate to the nucleus and activate the expression of IL12 in human dendritic cells (Friedmann et al. 2006).

Cell survival, proliferation and cell death activated by TNFα induced signalling is a finely tuned mechanism and depends on the quantitative balance between TNFR1 and TNFR2, the signalling components and their complexes. Defects in TNFα signalling pathways correlates with autoimmune disorders (Crohn's disease, Sjogren's syndrome,

multiple sclerosis and type I diabetes) (Faustman und Davis 2013), neurologic diseases (depression, Alzheimer disease, Parkinson disease), cardiovascular diseases (rheumatoid arthritis, psoriasis), pulmonary diseases (asthma, chronic bronchitis, acute respiratory distress syndrome), type II diabetes and obesity as well as cancer (Aggarwal et al. 2012).

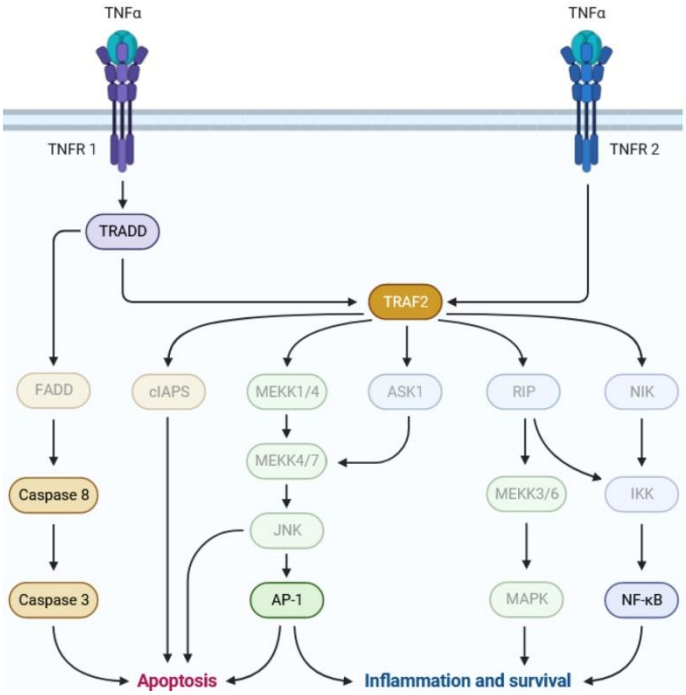

Figure 1.13 TNFα signalling pathway. TNFα can activate different pathways to induce apoptosis, cell survival or inflammation. The figure was made in BioRender (https://www.biorender.com).

Bri2

The Bri family consists of 3 human homologues the integral membrane protein 2A (ITM2A) or Bri1, ITM2B or Bri2 and ITM2C or Bri3 (Vidal et al. 2001). The Bri proteins are expressed in various tissues, with Bri1 being most abundantly expressed in chondro- and osteogenic tissues, skeletal muscle, thymus and brain (Kirchner und Bevan 1999; van den Plas und Merregaert 2004). While Bri2 is expressed in peripheral tissues, like placenta, pancreas and kidney as well as in the brain, Bri3 is primarily expressed in the brain (Vidal et al. 2001). Bri2 affects the APP processing and mutations of bri2 gene cause neurodegenerative diseases like the Familial British Dementia (FBD) (Vidal et al. 1999)and the Familial Danish Dementia (FDD) (Vidal et al. 2000).

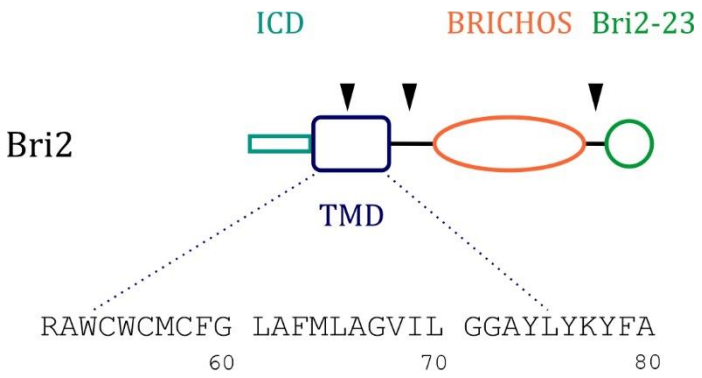

Figure 1.14 Schematic structure and cleavage sites of Bri2. Bri2 consists of a short N-terminal intracellular domain (turquoise), a TMD (dark blue), a BRICHOS domain (orange) and a C-terminal propeptide Bri2-23 (green). Main cleavage sites of SPPL2a/b cleavage are indicated by black arrows.

All Bri proteins have a similar structure. They are type II transmembrane proteins with an N-terminal intracellular domain, a TMD, a linker, a BRICHOS domain and a C-terminal part (Figure 1.20). In the Golgi Bri2 is maturated and cleaved by a furin protease, liberating the 23 amino acid long C-terminal propeptide Bri2-23 that might inhibit Aβ aggregation (Kim et al. 2008). Shifting the reading frame of the bri2 gene by a point mutations leads to the liberation of longer amyloidogenic propeptides, these ABri and ADan peptides aggregate to amyloid fibrils and cause FBD (Vidal et al. 1999) and FDD (Vidal et al. 2000). The remaining N-terminal membrane bound part translocates within the secretory route to the plasma membrane and is cleaved by ADAM10 in the area between residues 76-170, liberating the BRICHOS domain into the lumen/extracellular space, where BRICHOS can also inhibit Aβ aggregation (Willander et al. 2012). The still remaining membrane bound Bri2 NTF is the substrate for intramembrane proteolysis by SPPL2a/b, whereby small C-terminal peptides are secreted and the Bri ICD is released in the cytosol, both with unknown biological function (Martin et al. 2008; Martin et al. 2009).

1.1.2.5 SPP/SPPL Cleavage Mechanism

Unfortunately, there exists no determined protease structure for any of the SPP/SPPL family members and no detailed statement can be made about the cleavage mechanism, as in case of PS, where based on the cryo-EM structures with and without a substrate the individual mechanistic steps could be evaluated.

However, due to the related proteases and similar structural composition with 9 TMDs and catalytic aspartates within the YD motif and GxGD motif (Wolfe et al. 1999; Weihofen et al. 2002), an analogous cleavage mechanism of PS and SPP/SPPL could be assumed. This assumption should base on the previous described mechanistic steps (section 1.1.1.3) of substrate binding to a protease exosite, enzyme entry with translocation to the active site, unfolding of the substrates cleavage site, proteolytic cleavage via a tetrahedral intermediate to the release of cleavage products.

A similarity of cleavage mechanisms is supported by the correspondingly similar substrates requirements with regard to the structural and dynamic properties of the substrates TMD, which are explained in section 1.5.

1.2 Metalloproteases

The metalloprotease S2P is one of the first characterized intramembrane proteases (Sakai et al. 1996; Rawson et al. 1997). S2P consists of 6 TMDs, where the core domain formed by TM2, TM3 and TM4 is highly conserved in all S2P proteins (Feng et al. 2007). The HExxH motif in TM2 and DG motif in TM4 are required for cleavage and allow the coordination of a zinc ion. The zinc ion, supported by His_{54}, His_{58} and Asp_{148}, coordinates a water molecule necessary for proteolytic cleavage. This water molecule is able to access the active site through a solvent channel, lined with polar and charged amino acids (Feng et al. 2007). The crystal structure of an S2P homolog from the archaebacterial species *Methanocaldococcus jannaschii* mjS2P (Figure 1.15) shows a gap between TM1 and TM5/TM6 enabling substrate access to the active site via lateral movement (Feng et al. 2007).

The substrates of S2P are membrane bound transcription factors with a type II transmembrane topology. A precursor of this factors is cleaved by a site 1 protease (S1P) prior to the S2P cleavage. The intramembrane proteolysis releases an ICD, which moves to the nucleus, mediating the transcription of target genes (Sakai et al. 1996; Ye et al. 2000b).

In mammals the S2P cleavage regulates lipid homeostasis and the ER homeostasis (Danyukova et al. 2022). S2P cleavage of the sterol regulatory element binding protein (SREBP) activates this transcription factor and its target genes needed for cholesterol uptake and synthesis (Sakai et al. 1996). A further substrate of S2P is the activating transcription factor 6 (ATF6), after S2P cleavage the cytosolic ATF6 NTF induces the

expression of ER chaperones as a response of ER stress, produced by accumulation of unfolded proteins (Ye et al. 2000b). Several other S2P substrates, ER stress transducers, like old astrocyte specifically induced substance (OASIS), BBF2 human homolog on chromosome 7 (BBF2H7) and CREBH, are known (Rawson 2013).

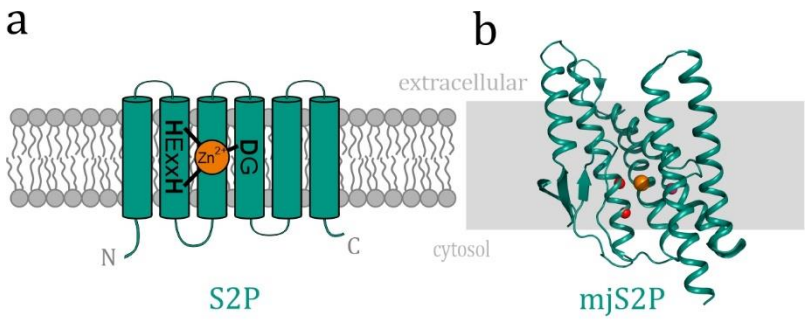

Figure 1.15 Structure of metalloprotease S2P. S2P is shown schematically in (a). Two histidine from HExxH motif in TM2 and aspartic acid from DG motif coordinate a zinc ion. Crystal structure of S2P from *Methanocaldococcus jannaschii* mjS2P ((3B4R), (Feng et al. 2007)) is shown in (b). Histidines are marked as red, zinc ion as orange and aspartic acid as pink dots. The lipid bilayer is depicted in grey.

The membrane bound substrates do not have a consensus sequence, but contain an asparagine or proline next to each other or separated by few amino acids, which are required for S2P cleavage (Ye et al. 2000a). The amino acids at the cleavage site of SREBP are located 3 residues within the membrane at the cytosolic border (Duncan et al. 1998) and are interchangeable without affecting the S2P cleavage. The asparagine-proline sequence enables a partial unwinding of the helix into a more extended conformation, permitting access for the enzyme to the scissile peptide bond (Ye et al. 2000a).

1.3 Serine Proteases

Rhomboids are a large group of intramembrane serine proteases (Urban et al. 2001) and can be categorized into four topological classes, including active and inactive rhomboids (Lemberg und Freeman 2007). The active proteases are subdivided in secretase and presenilin-associated rhomboid-like (PARL)-type subfamilies (Figure 1.16). Bacterial and archaeal rhomboids have a basic core of 6 TMDs (Koonin et al. 2003) and are classified as secretase-B rhomboids. Secretase-A rhomboids, which are also found in eukaryotes, are extended by a C-terminal TMD (6+1). An additional N-terminal TMD (1+6) is fused to PARL-type rhomboids, localized in mitochondria (Esser et al. 2002). Rhomboid-like

proteins that lack certain catalytic residues are inactive rhomboids. Among the inactive rhomboid-like proteins is a highly conserved subfamily classified as inactive rhomboids (iRhoms). iRhoms have a large globular domain inserted in the luminal loop between TM1 and TM2 and may have additional N- or C-terminal domains (Lemberg und Freeman 2007).

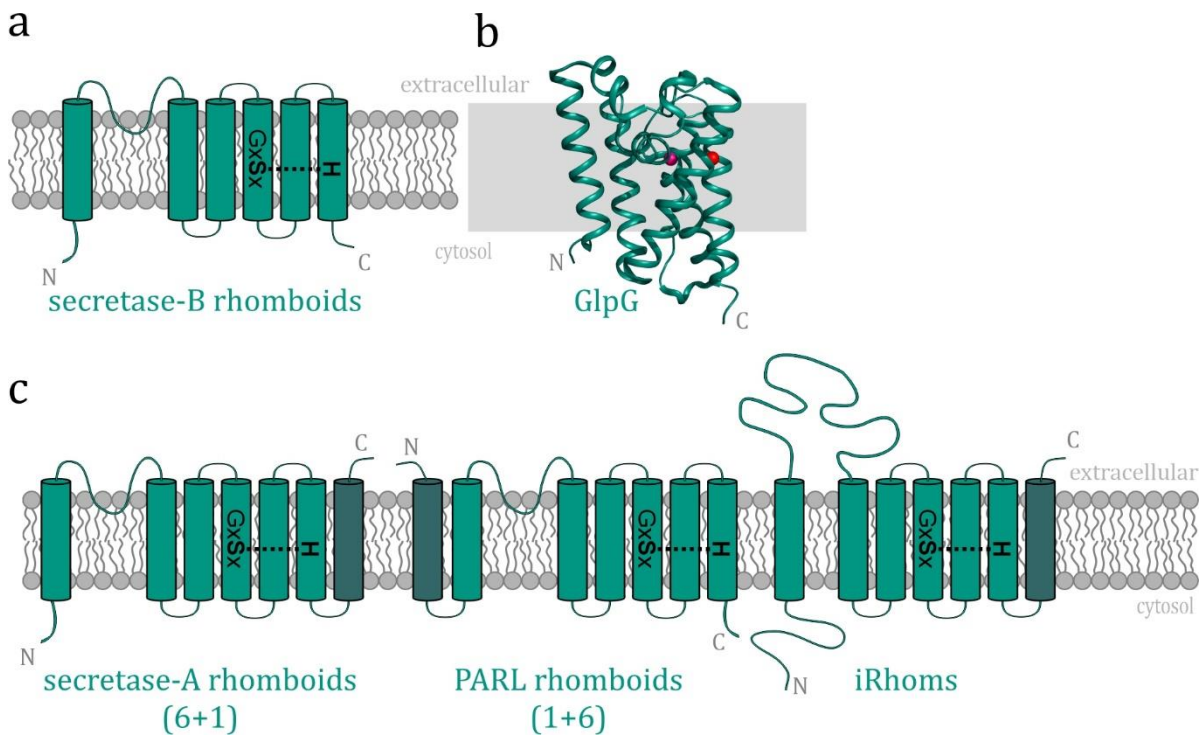

Figure 1.16 Structure of rhomboid proteases. Secretase-B rhomboids with basic 6 TMDs are shown schematically in (a) and the crystal structure of *Escherichia coli* GlpG ((2IC8), (Wang et al. 2006)) with Ser_{201} represented as pink and His_{254} as red dot. Other types of secretase-A rhomboids with (6+1) TMDs, PARL rhomboids with (1+6) TMDs and iRhoms with (6+1) TMDs are depicted schematically in (c).

A GxSx motif, a typical serine protease motif, in TM4 is essential for proteolytic cleavage and forms together with a histidine in TM6 the active site (Lemberg et al. 2005; Urban et al. 2001). Histidine develops a hydrogen bond to serine, activating it directly for nucleophilic attack on the substrate (Wu et al. 2006), thus serine and histidine form the catalytic dyad. The glycine, as part of the serine protease motif, contributes by building an hydrogen bond to a large luminal loop between TM1 and TM2 (loop1) (Wang et al. 2006). At the same height within the TMD as the respective residues in the active site, there is an asparagine residue located in TM2 involved in oxyanion stabilization and relevant for proteolysis (Urban et al. 2001). Loop1 contains a further highly conserved WR motif,

which contributes to several hydrogen bonds (Wu et al. 2006). This motif is important for activity, but not part of the catalytic mechanism and only required in an lipid environment (Lemberg et al. 2005).

Crystal structures of the rhomboid protease GlpG from *Escherichia coli* (Figure 1.16 (b)) (Wang et al. 2006; Wu et al. 2006) reveal deeper insights into the structural details of the whole protease and especially the active site. The TM1-TM3 cross the entire membrane and sticking together with the N-terminal part of TM4. An V-shaped gap between TM1 and TM3 is locked by loop1, which protrudes into the outer leaflet of the membrane (Wang et al. 2006). The TM4-TM6 are shorter than the others and do not travers the entire membrane. Consequently the N-terminus of TM4, containing the catalytic serine, is located 10 Å below the membrane surface at the bottom of a V-shaped cavity that is open towards the extracellular site (Wu et al. 2006). The location of catalytic serine agrees with mapped cleavage sites of rhomboid substrate, which appear several residues within the TMD (Urban et al. 2001; Urban und Freeman 2003). The active site is enclosed by a loop linking TM3 and TM4 (loop3) and in a closed conformation capped by a loop between TM5 and TM6 (loop5) (Wang et al. 2006). In a lateral gating model TM5 is able to perform an slight outward movement or rotation away from the rest of the TMDs, dragging loop5 with it to represent an open conformation (Wu et al. 2006; Xue und Ha 2013).

Disordered loop5 as well as TM5 and interacting residues of TM2, enable an outward bending of TM5, opening the catalytic cavity. Helix destabilizing residues facilitate the unwinding of the top area of a substrate TMD, which is able to enter the active site in this extended conformation between TM2 and TM5 (Cho et al. 2019). Loop5 returns after the substrate has entered the cavity and positions it in a cleavage competent conformation (Cho et al. 2019). Water molecules accessing the catalytic site through the cavity from the extracellular site are controlled by loop5 (Wu et al. 2006). They participate in peptide bond hydrolysis by releasing the cleavage product and restoring the catalytic serine (Cho et al. 2019).

First discovered in *Drosophila melanogaster*, where RHBDL1 activates EGF signalling (Wasserman et al. 2000), rhomboids have important functions in all organisms. As part of the secretory pathway, 4 rhomboid proteases RHBDL1-4 are found in mammals (Lemberg und Freeman 2007). Thrombomodulin, a substrate of RHBDL2, is cleaved as part of the wound healing process (Cheng et al. 2011) just as ephrin-3 a cell adhesion molecule

(Pascall und Brown 2004). RHBDL4 contributes to the ERAD pathway, where it cleaves several ubiquitinated proteins with unstable TMDs (Fleig et al. 2012).

Substrates of the human PARL are the phosphoglyceromutase enzyme (PGAM5) and the PTEN-induced kinase 1 (PINK1) (Meissner et al. 2011). Additionally, further substrates of the mitochondrial protease were found. PALR shows fundamental roles in mitochondrial biology, like metabolism, morphology, apoptosis and therefore also be involved in some diseases like diabetes type II and Parkinson's disease (Spinazzi und Strooper 2016).

Substrates of secretase-like rhomboids are type I transmembrane proteins, whereas PARL-like rhomboids, with its inverted active site, cleave type II membrane proteins (Lemberg und Freeman 2007). These substrates are characterised by small helix-destabilizing residues and limited hydrophobicity in their upper N-terminal TMD (Urban und Freeman 2003). Thus after docking to the protease exosite, unstable regions of the TMD extend, during transition from the lipid-stabilized membrane environment to the opened hydrophilic cavity of the enzyme, reaching the inner active site (Moin und Urban 2012). Although a substrate motif is described (Urban und Freeman 2003; Akiyama und Maegawa 2007), rhomboids tend to recognize less a specific sequence rather than a proteolytic competent conformation. Hence different subclasses of rhomboids may have different substrate requirements.

1.4 Glutamate Proteases

A novel family of glutamate intramembrane proteases was established by the founding member Rce1 (Manolaridis et al. 2013). There are no known human homologues of Rce1 and the orthologues varies in the length showing 7 or 8 TMDs depending on the species. The crystal structure of Rce1 in complex with an antibody Fab fragment from archaea *Methanococcus maripaludis* (Figure 1.17) indicated a large conical cavity, building the active site (Manolaridis et al. 2013). The highly conserved residues Glu_{140} in TM4, His_{173} in TM5, His_{227} and Asn_{231} in TM7 located on the top of the cavity and directing their side chains into the cavity, are proposed to serve as catalytic residues. The catalytic activity depends on Glu_{140} and His_{173}, while mutations in His_{227} or Asn_{231} disrupt cleavage. The large cavity is open towards the cytosol and enables unrestricted access of water, so that a water molecule is located in the cavity and coordinated by Glu_{140} and His_{173}. Through a gap between TM2 and TM4 a substrate might enter the active side by lateral diffusion.

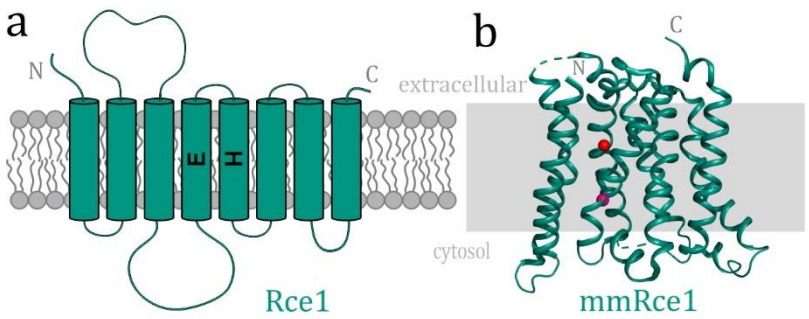

Figure 1.17 Structure of glutamate protease Rce1. Rce1 is shown schematically in (a). Rce1 consists of 8 TMDs with the catalytic glutamic acid in TM4 and catalytic histidine in TM5. Crystal structure of Rce1 from *Methanococcus maripaludis* mmRce1 ((4CAD) (Manolaridis et al. 2013)) is shown without the Fab fragment in (b). Glutamic acid is marked as red and histidine as pink dot. The lipid bilayer is depicted in grey.

The proteolytic mechanism involving cleavage of the 3 C-terminal residues of CaaX proteins, was assessed by a computational docking study of archaeal Rce1 and a farnesylated decapeptide (Manolaridis et al. 2013). The farnesyl group resides between TM2 and TM4, positioning the substrate toward the catalytic residues, such that the glutamate activated water nucleophile attacks the carbonyl carbon of the prenylated cysteine and the resulting tetrahedral oxyanion is stabilized by His_{227} and Asn_{231} until the cleavage products are released (Manolaridis et al. 2013).

Although no Rce1 substrates has yet been found, reporters of Rce1 activity revealed the cleavage of prenylated proteins with a CaaX motif, where C is cysteine, a is an aliphatic amino acid and X any amino acid (Manolaridis et al. 2013). Proteins can be post-translational modified by isoprenylation with a farnesyl (C15) or geranylgeranyl (C20) group, what is important for their localization as well as function, and this modification can be removed by the Rce1 cleavage in the ER (Bracha-Drori et al. 2008; Hampton et al. 2018). The CaaX proteins are important for cell signalling and are implicated in cancer (Wang und Casey 2016; Winter-Vann und Casey 2005).

1.5 Substrate Requirements

Since the discovery of intramembrane proteolysis around the turn of the millennium, the question how these proteases recognize their substrates could not be fully answered. This chapter focuses on the substrate requirements of both aspartate proteases, γ-secretase and SPPL2a/b, and how structural properties affect the behaviour of a potential substrate.

About 150 substrates of γ-secretase and about 30 substrates of the SPP/SPPL family differ in their physiological function, their cleavage fragments and their amino acid sequence (Güner und Lichtenthaler 2020; Mentrup et al. 2017; Mentrup und Schröder 2022). One similarity is that these proteases apparently do not recognize a consensus sequence, but rather cleave their substrates at specific cleavage sites (Langosch et al. 2015; Beel und Sanders 2008). Therefore, there must be some substrate features supporting the substrate on the way through the mechanistic steps towards the cleavage products such as protease binding, entry into the enzyme, translocation to the active site and unfolding of the scissile peptide bond.

1.5.1 Topological Orientation and Basic Anchor

First of all, substrate and protease have to meet in the appropriate topological orientation in the membrane in order to be able to interact. Hence γ-secretase cleaves only type I (N_{out}) transmembrane proteins (Haass und Steiner 2002) and SPPL, due to its inverted topology compared to γ-secretase, cleaves only type II (N_{in}) transmembrane proteins (Martoglio und Golde 2003).

To further orient the substrate within the membrane, many but not all aspartate protease substrates possess several positively charged, basic residues like arginine and lysine in the area C-terminal after the TMD (Yan et al. 2017; Güner und Lichtenthaler 2020; Hemming et al. 2008). This basic anchor might stabilize the right positioning within the membrane by promoting electrostatic interaction of the substrates TM-C end and the mainly negatively charged inner membrane leaflet at the cytosolic membrane border (Ma et al. 2017). At the same time the basic anchor acts as a stop signal for translocation during membrane incorporation (Kopan und Ilagan 2009).

1.5.2 Ectodomain Length

For efficient cleavage by most intramembrane proteases a prior ectodomain shedding is required. γ-secretase substrates with an ectodomain of less than 50 amino acids are

subsequently processed (Struhl und Adachi 2000; Lichtenthaler et al. 2018). Substrates containing a naturally short ectodomain, like the B cell maturation antigen (BCMA) ectodomain with 54 amino acids, can pass the size exclusion of NCT and be processed directly by γ-secretase without prior shedding (Laurent et al. 2015). Concerning the length of the ectodomain, there are also exceptions. So γ-secretase, albeit less efficient, directly cleaves the full-length amyloid precursor-like protein 1 (APLP1), a homologue of APP, but however not APLP2 or APP itself (Schauenburg et al. 2018).

In case of the SPP/SPPL family the situation is more diverse. In general, intramembrane proteolysis is greatly facilitated by prior ectodomain shedding, while an ectodomain size of 60 amino acids is tolerated, cleavage of a substrate with a 90 amino acid long ectodomain is abolished (Martin et al. 2009). SPPL2a is able to process TNFα FL and SPPL2b can also act as non-canonical sheddase depending on the substrate TMD flexibility (Spitz et al. 2020). An exception is SPPL3, this protease cleaves different full-length glycosidases and glycosyltransferases with long extracellular domains and even multipass transmembrane proteins (Voss et al. 2014; Voss et al. 2012; Kuhn et al. 2015). The size exclusion of SPP/SPPL proteases is variable and depends on the substrate/protease combination. Apart from the aspartate protease SPPL3, rhomboids process full-length substrates without prior ectodomain shedding (Lemberg et al. 2005).

1.5.3 Flexible TMD: Flexibility Hypothesis

Early on it was found that the both residues asparagine and proline, which interrupt the TMD helix, in the S2P substrate SREBP are necessary for intramembrane proteolysis (Ye et al. 2000a). Helix-destabilizing or even helix-distorting residues in substrate TMD were also required for SPP cleavage (Lemberg und Martoglio 2002). Shortly afterwards it was shown that rhomboid proteases recognize some destabilization within the substrate TMD of Spitz and mutations in the helix-destabilizing GA motif affect cleavage (Urban und Freeman 2003). The helix containing the GA motif was destabilized, since the small side chains of these amino acids are conformational less restricted than larger residues. The conformational restriction is in glycine even less pronounced compared to alanine due to the lack of a side chain, causing helix packing defects and a higher helical flexibility (Liu und Deber 1998; Högel et al. 2018). Mutating the alanine within the GA motif to glycine destabilizes the helix further and enhances the cleavage. Likewise mutations of alanine to

β-branched residues, such as threonine or isoleucine with a lower α-helical propensity, destabilize the substrates helix and enhance cleavage (Urban und Freeman 2003).

From these initial results, the flexibility hypothesis arose. Helix-destabilizing residues increase the flexibility of the substrates TMD helix and thereby promote intramembrane proteolysis, while helix-stabilizing residues decrease flexibility and reduce cleavage.

When applying to γ-secretase and its substrate APP, the flexibility hypothesis was confirmed as a certain degree of flexibility allows γ-secretase cleavage (Werner et al. 2023). The α-helical APP TMD is bend around a flexible GG motif (Beel et al. 2008; Nadezhdin et al. 2011; Barrett et al. 2012). Mutations concerning the helix stability and thus helix flexibility alter γ-secretase cleavage. As expected, mutating residues Ile_{47} and Thr_{48} to helix-destabilizing glycines increased the cleavage efficiency, while mutations to helix-stabilizing leucines reduced cleavage (Fernandez et al. 2016). Unexpectedly, helix-stabilizing leucine mutant as well as helix-destabilizing glycine mutant of Val_{46} decrease γ-secretase cleavage (Xu et al. 2016). Just as helix-stabilizing leucine and helix-destabilizing proline mutants of Gly_{38}, one of the glycines within the flexible GG motif, also reduce γ-secretase cleavage (Götz et al. 2019b), indicating that besides the TMD flexibility other substrate properties determine cleavage efficiency.

γ-Secretase – Notch1

Nevertheless, the flexibility hypothesis is in principle applicable. The Langosch group was able to show on the Notch1 and γ-secretase pair that mutations in the flexible AAAA motif in Notch1 TMD (Stelzer und Langosch 2019) influence the cleavage efficiency. Replacement of the alanine tetrad by helix-stabilizing leucines led to a significant reduction in TMD flexibility and thus reduced cleavage. Accordingly substitution with helix-destabilizing glycines increased flexibility and also cleavage (Ortner et al. 2023).

SPPL2a/b – TNFα and Bri2

Using the SPPL2b substrate Bri2, Fluhrer et al. were able to show that mutations of the flexibility promoting glycines within the GG motif and 3 other positions in the Bri2 TMD influence cleavage (Fluhrer et al. 2012). Individual mutations of these glycines to alanine resulted only in a slight reduction in cleavage, with exception of position Gly_{60}, which exhibits a significant decrease of cleavage, which is comparable to the extent when all glycines were replaced by alanines (Fluhrer et al. 2012).

In addition, it was demonstrated that not only canonical shedding of a prior truncated substrate is influenced by mutations affecting helix stability, but also non-canonical shedding of TNFα FL by SPPL2a (Spitz et al. 2020). When residues Gly_{43}, within the flexible AGA motif, and Ser_{34} as well as Ser_{37} in TNFα TMD were individually mutated to helix-distorting proline, there is a significant increase in non-canonical shedding, especially in case of Gly_{43}. Interestingly, this flexibility increasing proline mutations enable also the non-canonical shedding by SPPL2b. In contrast, mutations of these residues to alanine or leucine had only minor effect on non-canonical shedding, but replacing the entire AGA motif with helix-stabilizing leucine results in an almost loss of non-canonical cleavage of TNFα by SPPL2a.

In summary, the intrinsic or by mutations influenced TMD stability and thus flexibility of a substrate might facilitate substrate entry and the translocation to active site, but also other substrate determinants influence the cleavage efficiency of intramembrane proteases.

1.5.4 β-Strand Propensity around the Cleavage Site

After the first structure, the cryo-EM structure of the γ-secretase-Notch1 complex was published (Yang et al. 2019), it was clear that the formation of the hybrid β-sheet occurred through interaction between the antiparallel β-sheet in PS1 and the β-strand at the C-terminal end of the Notch1 TMD is crucial for intramembrane proteolysis by aspartate proteases. The hybrid β-sheet stabilizes the enzyme-substrate complex and positions the substrate in a cleavage competent orientation. Deletion of the structural motifs like β-strands in PS1 and Notch1 TMD abolish γ-secretase activity (Sato et al. 2008; Yang et al. 2019). The sheet-forming residues Leu_{1755}/Leu_{1756}/Ser_{1757} in Notch1 TMD are not only sensitive to deletion but also to mutations, so that replacing the Notch1 residues 1754-1757 by a leucine tetrad almost abolish γ-secretase cleavage (Ortner et al. 2023). Further mutations stabilizing the β-strand in Notch1 TMD increase γ-secretase cleavage. Thus, the cleavage is not only enhanced by about 25%, when replacing Leu_{1755} or Leu_{1756} by an amino acid favouring β-sheet formation like valine, but in a certain way also tuneable when both leucines are substituted by β-sheet promoting residues cleavage increased by 50% compared to wild type Notch1 (Notch1 WT). A triple valine mutant including Ser_{1757}, however shows a cleavage efficiency similar to Notch1 WT (Ortner et al. 2023).

The formation of a β-strand is possible in other γ-secretase substrates too. In the cryo-EM complex structure of γ-secretase and APP (Zhou et al. 2019), APP adopts a β-strand conformation in the C-terminal end of the TMD. Many other γ-secretase substrates (Güner und Lichtenthaler 2020) have also β-branched residues following the initial cleavage site.

Unfortunately, there is no structure of a SPPL2-TNFα complex available, but according to the TNFα sequence, both β-branched residues Val_{55} and Ile_{56} at the C-terminal end of the helix might adopt a β-strand.

1.5.5 Unfolding of Cleavage Site

The most transmembrane proteins are α-helical within the hydrophobic environment of the membrane and were stabilized by a network of hydrogen bonds. The helix of the substrate TMD must be destabilized and partially unfold at the corresponding cleavage site in order to be accessible to the protease. Therefore, several substrates (Güner und Lichtenthaler 2020) contain small and partly helix-destabilizing residues within their cleavage site, such as the initial cleavage site of Notch1 Gly_{1753}/Val_{1754} or TNFα Cys_{49}/Leu_{50} and Leu_{51}/His_{52}.

A mutational screen of the Notch1 TM-C revealed that bulky and sterically demanding amino acids at positions Gly_{1753} and Val_{1754} at the cleavage site might hinder the access to the scissile peptide bond and formation of the tetrahedral intermediate, decreasing the γ-secretase cleavage (Ortner et al. 2023).

When mutating the residues Cys_{49} and His_{52} in TNFα TMD to alanines with their small side chain and to helix-distorting prolines, this mutants had only a minor effect of the non-canonical shedding by SPPL2b (Spitz et al. 2020). In contrast bulky leucine mutants might hinder the access for the enzyme and significantly reduce the cleavage efficiency (Spitz et al. 2020).

1.6 NMR Spectroscopy

1.6.1 NMR Basics

NMR uses the magnetic properties of certain nuclei to gain information about the surrounding environment of these nuclei. An NMR spectrum can only be observed for nuclei with a net spin, like ^{1}H, ^{13}C, ^{15}N and ^{31}P with a spin of ½, which are most interesting for protein NMR. Nuclei with a net spin have a magnetic moment μ, defined by the gyromagnetic ratio γ and the nuclear spin angular momentum I, with μ_z and I_z being the z-components of μ and I:

$$\mu = \gamma I \qquad (1.1)$$
$$\mu_z = \gamma I_z$$

The spins of the determined nuclei in a sample are randomly distributed, but if an external magnetic field B_0 is applied along the z-axis, the nuclear spins interact with B_0, what is called the Zeeman effect (Figure 1.18). Spins aligning with the external magnetic field B_0 are lower in energy, while those aligning against B_0 are higher in energy and the energy levels of these states are defined by:

$$E_m = -\gamma I_z B_0 = -m\hbar\gamma B_0 \qquad (1.2)$$

where $\hbar$ is the reduced Planck constant and m the spin quantum number, in the case of I=½ m adopts the values m=+½ for α state and m=-½ for β state. The splitting of the degenerated energy levels, the Zeeman-splitting, is dependent of the applied magnetic field and corresponds to the energy, which is required for the transition between these two α and β states:

$$\Delta E = \hbar\gamma B_0 \qquad (1.3)$$

The number of the nuclei in each state is Boltzmann distributed and the energy separation between these states is small, so that a radio frequency pulse can be used for excitation from the α state to the β state. The excitation frequency that is associated with the energy level difference, is termed as the Lamour frequency ν_0 or the angular frequency ω_0:

$$\nu_0 = -\frac{\gamma}{2\pi} B_0 \tag{1.4}$$

$$\omega_0 = -\gamma B_0 \tag{1.5}$$

The macroscopic magnetization vector consists of the sum of all individual magnetic moments and due to quantum mechanistic effects the single nuclear spins and thus the macroscopic magnetization is not aligned perfectly parallel or antiparallel to the static B_0 field, rather precess around B_0 with the Lamour frequency.

Nuclei with a slightly different chemical environment have slightly different Lamour or resonance frequency and in an NMR experiment all these resonances are simultaneously excited in a defined frequency interval, so that the detected signal is a mixture of all individual frequencies described by a periodic function. The intensity of this periodic function of time, the primary NMR signal, decays due to relaxation effects and is termed as the free induction decay (FID). A mathematical operation the Fourier transformation transfers the FID signal from the time to the frequency domain, separating the detected signal by their frequencies, while the intensities in the spectrum derive from the amplitudes of the overlaid periodic function in the FID (Keeler 2012).

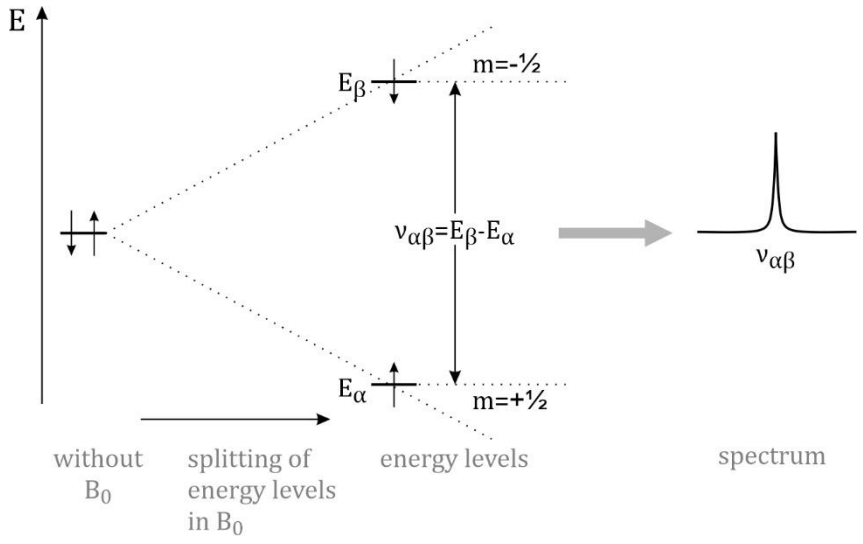

Figure 1.18 Zeeman effect. Zeeman splitting of a nucleus with spin ½ in a static magnetic field B_0. Transition between the energy levels give rise to a single line at the Lamor frequency in a spectrum.

1.6.2 NMR Observables

1.6.2.1 Chemical Shift

The chemical shift gives information about the local structure of the nucleus of interest. When a strong magnetic field is applied to a molecule, the electrons in the molecule, which orbit the nucleus, induce a small local magnetic field B_{loc} at the nucleus. This nucleus experiences the sum of the applied and the induced field changing the energy levels of the nuclear spin states and thus shifting the Lamour frequency by an amount depending on the induced magnetic field. The local magnetic field B_{loc} depends on the orientation of the molecule to the applied magnetic field, due to the anisotropic chemical shielding tensor σ_s:

$$B_{loc} = (1 - \sigma_s)B_0 \tag{1.6}$$

Because of the molecular tumbling in solution, the anisotropy of the chemical shielding tensor is averaged out to a shielding constant σ and the Zeeman splitting then results in:

$$\Delta E = \hbar\gamma B_{loc} = \hbar\gamma(1 - \sigma)B_0 \tag{1.7}$$

Since the resonance frequency depends on the applied magnetic field, the chemical shift scale was initially introduced to achieve comparable resonance frequencies between spectrometer operating at different field strengths. The chemical shift δ describes the frequency separation to a reference frequency ν_{ref}, like tetramethylsilane (TMS), in a way which is independent of the applied magnetic field (Keeler 2012; Cavanagh 2007):

$$\delta[ppm] = 10^6 \frac{\nu - \nu_{ref}}{\nu_{ref}} \tag{1.8}$$

As mentioned above, the chemical shifts depend on the electronic environment of each nucleus for every position in an amino acid distributed over the whole protein and provide a variety of structural information, so that based on the chemical shifts the secondary structure, their classes and locations, dihedral angles Φ and Ψ as well as backbone flexibility via the order parameter S^2 are accessible (Wishart 2011).

The chemical shifts are sensitive to the secondary structure of a protein. The first look at a spectrum provides the information if a protein is folded or has an unstructured conformation. The unstructured conformation is also termed as random coil. Generally,

the chemical shift dispersion of a random coil protein is smaller compared to a folded protein. In an α-helical protein $^{1}H_{\alpha}$ shifts are in a range between 3.5 and 5.5 ppm, amide proton $^{1}H_{N}$ shifts in a range of 6.5 to 10.0 ppm and ^{15}N shifts without glycines in a range between 109 and 130 ppm (Yao et al. 1997; Wishart und Case 2002; Wishart 2011).

Secondary chemical shifts Δδ, the difference between observed chemical shifts δ_{obs} and the corresponding random coil value δ_{rc}, can be used for identification of secondary structure and flexible regions (Szilágyi 1995; Wishart und Case 2002; Wishart 2011):

$$\Delta\delta = \delta_{obs} - \delta_{rc} \tag{1.9}$$

In proteins α-helices and β-sheets are the main secondary structure elements. Within these structure elements the nuclei of specific atom type exhibit characteristic upfield or downfield shifts. Some of these nuclei are influenced by the preceding or following residues, referred to as the nearest-neighbour effect, so the corresponding random coil values have to be adjusted (Wishart 2011). $^{1}H_{\alpha}$ chemical shifts in α-helices are shifted upfield by an average of 0.30 ppm and in β-sheets shifted downfield by an average of 0.46 ppm compared to random coil values, therefore showing negative secondary chemical shifts in an α-helix. In helical structures $^{13}C_{\alpha}$ chemical shifts are shifted downfield by an average of 2.6 ppm and in β-sheets shifted upfield by an average of 1.1 ppm, resulting in positive secondary chemical shift values (Wishart et al. 1991; Wishart und Case 2002; Mulder und Filatov 2010). The opposite is true for $^{13}C_{\beta}$ chemical shifts with negative secondary chemical shift values in helices (Spera und Bax 1991). The $^{1}H_{\alpha}$, $^{13}C_{\alpha}$ and $^{13}C_{\beta}$ shifts are sensitive to backbone Φ and Ψ torsion angles and therefore associated with secondary structure, whereas the ^{15}N and $^{1}H_{N}$ shifts are more sensitive to their environment influenced by pH value, temperature, hydrogen bonds and ring currents of aromatic residues.

The chemical shift index (CSI) simplifies the chemical shift information by using the ^{1}H and ^{13}C backbone chemical shifts and protein sequence to generate a simple graphical output based on the conformation dependent chemical shift tendencies. Therefore, CSI applies a ternary filter converting the upfield secondary chemical shift after a specific threshold value to 1 for β-sheets and the downfield secondary chemical shift to -1 for α-helices, as well as small secondary chemical shifts to 0 for random coil conformation (Wishart 2012). Besides this 3 secondary structure elements, a further development of

the CSI concept, CSI 3.0, enables the identification of up to 11 secondary structure types like coil regions, different β-turns and β-hairpins (Hafsa et al. 2015).

There are characteristic dihedral or torsion angles in helices or β-sheets, which can be determined from scalar couplings and cross-correlated relaxation experiment, are much more easily accessible through chemical shifts. The empirical observation that similar amino acids sequences with similar chemical shifts have similar backbone dihedral angles is used by the program Torsion Angle Likelihood Obtained from Shift (TALOS). TALOS predicts the dihedral angles Φ and Ψ based on ^{1}H, ^{13}C and ^{15}N chemical shifts and a protein database (Cornilescu et al. 1999). To expand the ability to predict backbone dihedral angle, the extension TALOS+ uses a larger database as well as overcomes the limitations of residues lacking chemical shift assignment and additionally reports an estimated backbone order parameter (Shen et al. 2009).

1.6.2.2 Scalar Couplings

Nuclei in different chemical environments can influence the local magnetic field of another nucleus by spin-spin interactions, carrying spin orientation information and magnetization through bonding electrons. This interaction is termed as scalar coupling or J-coupling, and is mediated through maximal 3-4 bonds. When two nuclei with spin of ½ are coupled, the resonance frequency of each spin splits in two lines separated by the field independent coupling constant $^{n}J_{AB}$ measured in Hertz, whereby the *n* describes the number of bonds between coupled nuclei *A* and *B*. The scalar coupling is the reason of characteristic multiplets in an NMR spectrum (Keeler 2012; Cavanagh 2007).

Empirically, a correlation was found between the $^{3}J_{HH}$ scalar coupling of two protons and their dihedral angle by the Karplus curve, which enables the determination of dihedral angles by ^{3}J couplings (Karplus 1963).

1.6.2.3 Nuclear Overhauser Effect

A nucleus with a net spin I acts as a magnetic dipole by generating a magnetic field. Another nucleus with a spin S is influenced by this field and vice versa spin I also feels its magnetic field, termed as the dipole-dipole interaction or dipole-dipole coupling. In contrast to the scalar coupling, dipole-dipole interactions are mediated through space. The dipolar coupling D_{IS} depends on the distance r_{IS} between the nuclei and the orientation of the internuclear vector between these spins with respect to the applied magnetic field B_0:

$$D_{IS} = \frac{h\gamma_I\gamma_S\mu_0}{16\pi^2}\langle\frac{1}{r_{IS}^3}(3\cos^2\theta - 1)\rangle \tag{1.10}$$

with the gyromagnetic ratios γ_I and γ_S of nuclei I and S. The angle θ between the internuclear vector and B_0 is averaged over time indicated by the brackets. The orientation and distance dependent dipolar coupling is averaged out by molecular tumbling in solution, but can be detected in solids or partially aligned media. Although dipolar coupling is not directly measurable, it contributes to the nuclear Overhauser enhancement or effect (NOE).

A fluctuating magnetic field generated by molecular motions constitutes a relaxation mechanism for both spins and the NOE is a cross relaxation effect describing the magnetization transfer between spins by dipolar coupling. For two isolated protons the NOE can be defined as:

$$\sigma_{NOE} = \frac{\hbar\mu_0^2\gamma_H^4\tau_C}{40\pi^2 r^6}\left[\frac{6}{\omega_0^2\tau_C^2}\right] \tag{1.11}$$

with the gyromagnetic ratio of the involved spins γ_H, the permeability of the vacuum μ_0, internuclear distance r, Lamour frequency in this case of protons ω_0 and the correlation time of the tumbling molecule τ_C.

The intensity of NOE cross-peaks in the NMR spectrum are proportional to the internuclear distance by a $1/r^6$ dependency:

$$I_{NOE} \sim a\frac{1}{r^6} \tag{1.12}$$

when a proportional factor a is calibrated by a known or calculated distance, distances of protons up to 5 Å can be determined (Keeler 2012; Cavanagh 2007).

NOE cross-peaks between two protons can only be observed when they are separated by less than 5 Å, so in proteins different types of NOE contacts can be found. There are intraresidual NOEs between nuclei in the same amino acid and interresidual sequential NOEs between an amino acid and the following or preceding residue. Medium range NOEs between 2 to 3 amino acids and long range NOEs of 4 or more residues apart were also found. Characteristic sets of proton distances define secondary structure elements, therefore characteristic NOE pattern can be observed.

Sequential distances between $^1H_\alpha$ atom and ^1H_N atom of the following residue dαN(i, i+1), dβN(i, i+1) between $^1H_\beta$ atom and the following ^1H_N atom as well as dNN(i, i+1) between ^1H_N atoms of the amino acid and the following residues are related to dihedral angles and their distances differ according to the secondary structure (Wüthrich et al. 1991).

Medium range NOEs are particularly useful for identification of helical structures because they correspond to distances between backbone protons that are 2 to 4 residues apart. So distances between $^1H_\alpha$ and ^1H_N atoms dαN(i, i+3), as well as $^1H_\alpha$ and $^1H_\beta$ atoms dαβ(i, i+3), separated by 3 residues are indicative for helices. Additional NOE contact between $^1H_\alpha$ and ^1H_N atoms 2 residues apart are only present in 3_{10} helices furthermore NOEs between $^1H_\alpha$ and ^1H_N separated by 4 residues are only found in α-helices (Wüthrich 1986; Wüthrich et al. 1984; Wagner et al. 1986).

1.6.3 Protein Structure Calculation

The process of protein structure calculation involves two basic steps of generating structural restraints and calculating structures by using these restraints. The restraints derive from NMR data and are primarily distance and dihedral angle restraints, which can be supplemented by chemical shifts and bond lengths. How these restraints are obtained, how they contribute to structure calculation and what the structure calculation output is, is answered in the following.

1.6.3.1 Resonance Assignment

A large number of protons is present in proteins and even in peptides, so that 1D ^1H NMR spectra are not suitable to assign single resonances due to signal overlap. In 2D ^1H-^1H NMR spectra the correlation of two frequencies is determined, so that the peaks are separated and the cross-peaks are caused by different types of spin interaction depending on the NMR experiment that is used.

In 2D homonuclear correlation spectroscopy (COSY), the interaction between spins is based on through-bond J-coupling of protons, separated by not more than 3 bonds, so that the network of connected spins can be examined. The total correlation spectroscopy (TOCSY) determines all cross-peaks from protons of the same spin-system, where one spin system consists of one amino acid. A single cross-section at the shift of one spin should show all spins, which are part of the network of J-couplings to which this spin belongs. In proteins, the cross-section at the proton amide ^1H_N shift shows all proton

spins, which are present in one amino acid. The cross-peaks in COSY or TOCSY spectra are characteristic for the amino acids, therefore proton chemical shifts for each amino acid can be assigned (Wüthrich 1990; Keeler 2012).

In 2D heteronuclear single-quantum correlation (HSQC) experiments spins of different types of nuclei like ^{13}C and ^{15}N interact with protons through one bond heteronuclear coupling to determine the shifts of directly attached nuclei. With HSQC spectra the corresponding ^{13}C and amide ^{15}N chemical shifts can be assigned on the basis of prior proton resonance assignment (Keeler 2012; Cavanagh 2007).

In 2D homonuclear NOE spectroscopy (NOESY), the interaction between spins is based on through-space dipolar coupling of protons. Thereby, identifying the distance between the interacting protons which are less than 5 Å apart. The presence of a cross-peak in NOESY spectra indicates cross-relaxation between the two proton spins and their close proximity to each other, with the intensity of the cross-peak being proportional to the distance. With this information and the knowledge of the amino acid sequence of the investigated protein the sequential assignment of the prior by TOCSY spectra indicated amino acids can be achieved. Through the resonance assignment for the protein backbone and amino acid side chains, a large set of proton-proton distance restraints are obtained. These restraints are one of the most important information required for structure calculation (Wüthrich 1990; Wüthrich 1986; Keeler 2012).

After the resonance assignment of as many cross-peaks as possible in the different kinds of NMR spectra, the chemical shift derived dihedral angle restraints determined by TALOS+ are further used for structure calculation. The input data for protein structure calculation can be supplemented by ^{1}H, ^{13}C and ^{15}N chemical shifts.

1.6.3.2 Structure Calculation with ARIA/CNS

One of the most time-consuming steps in NMR structure calculation is the assignment of the numerous NOE signals. Since misassignment can occur and furthermore several protons can have the same chemical shift leading to ambiguous NOEs. These ambiguous NOE cross-peaks cannot be converted to a distance restraint and be used in structure calculation.

The ambiguous restraints for iterative assignment (ARIA) is a software protocol that integrates ambiguous NOE distance restraints to structure calculation. Therefore, each ambiguous NOE cross-peak is treated as a superposition of all possible assignments. When a cross-peak with a unique assignment provides an upper bond distance of two

protons, then an ambiguous cross-peak can be seen as a superposition of degenerated signals and provide an ambiguous distance restraint. These ambiguous distance restraints can be logically combined to exclude some possibilities during the calculation process and generate unambiguous restraints (Linge et al. 2001).

ARIA defines molecular conformations, based on a chemical shift list and NOE peak list, which are consistent with the observed peaks. Further experimental data like torsion angle, J-coupling, residual dipolar coupling, hydrogen bonds or disulphide bridges can be added, if available. ARIA generates calibrated ambiguous distance restrains from the NOE peak list, merging the distance restraints list and setting up all restraints for automated structure calculation. Explicit assignments are obtained iteratively from chemical shift assignments and successive generation of calculated structures. In each iteration step ARIA detects inconsistent cross-peaks and reduces assignment possibilities. Wrong assignments are found by a violation analysis, where restraints are excluded when distances are outside of defined boundaries. The cut-off is gradually reduced in order to obtain an almost unambiguous assignment after the last iteration. In every cycle NOE assignment, calibration and violation analysis are based on the average distances calculated from lowest energy conformers from the previous cycle, starting with an initially extended structure (Nilges et al. 1997; Nilges und O'Donoghue 1998; Linge et al. 2001; Linge et al. 2003).

Spin diffusion can occur, when magnetization is transferred via indirect pathways, leading to enlarged NOE cross-peak intensities and thus underestimated distances. Simply elongated distance boundaries to overcome this error would lead to a loss of structural information and reduced structure quality. Therefore, spin diffusion correction is applied to ARIA by a relaxation matrix, which determines a correction factor for the distance restraints. The spin diffusion correction requires information of the spectrometer frequency, rotational correlation time and NOE mixing time (Linge et al. 2003, 2004).

The program crystallography and NMR system (CNS) based on simulated annealing with MD simulation, is used to calculate the structures. Simulated annealing is used to find low energy structures of a protein, by raising the temperature of the system and slow cooling to overcome potential energy barriers on the path to the global minimum. When the system is heated the atoms in the protein are no more restricted by forces like chemical bonds or van-der-Waals interactions and are freely moving around like in a

molten state. During the cooling process, these forces are present again together with additional forces caused by the experimental restraints like NOE derived distances or dihedral angles leading to a low-energy conformation, ideally located in the global minimum. The NMR ensembles are represented by the low-energy conformations determined by simulated annealing in the final iteration step (Brünger et al. 1998; Nilges et al. 1988; Brünger et al. 1997).

1.6.3.3 Structure Bundles

The structure calculation of a protein by CNS using the ARIA setup generates NMR structures as an ensemble of different conformations, which are calculated with identical input data but started from different randomized initial conformations (Brünger et al. 1998; Linge et al. 2003). In general, 10 % of the total amount of calculated structures according to their lowest energy, are chosen to visualize the structures in the bundle. The single conformations in these structure bundles are all consistent with the experimentally derived restraints. The spread of the bundles represents the precision or reproducibility of the calculation, however, the quality of the experimental data, but also other factors, influence the accuracy and closeness to a true structure (Zhao und Jardetzky 1994). Towards this definition of accuracy, a structure determined by another method is required for comparison.

On the one hand the structural ensemble might represent different conformational states of a proteins with conformational fluctuation that are important for the biological function (Boehr et al. 2009; Lindorff-Larsen et al. 2005). On the other hand, the structure bundles might reflect limited available information. It is possible that only averaged conformational states could be detected when the acquisition time of NMR spectra is longer than the timescale of conversion between different conformations and the measured data are a mixture of the contributions from each state. Since NOE data can only be used to determine short and medium range distances, but not long range distances, several conformations fulfil the given distance restraints. Furthermore, ambiguous information, such as ambiguous NOEs due to the same chemical shift of several protons, might cause a variability in the calculated structures. Evidently,, random errors like misassignment of NOE cross-peaks or systematic errors such as the inaccuracy of the measurement method could be the reason of different conformations in the structure bundles (Schneidman-Duhovny et al. 2014; Nilges 1997).

The conformation of a structure in the structural bundles is defined by the numerous distances between the hydrogen atoms in the protein determined on the basis of the NOE signals. It should be noted that the direction of the orientation can be caused not only by the presence of NOE signals, but even if NOE signals are missing. A curved helix can be defined by short distances on one side and long distances on the opposite side of the helix. But a curved helix can also be defined by distances that are present on the one side and predominate by the absence of distances of the opposite side, thereby favouring this orientation.

1.6.4 Protein Dynamics: Hydrogen Deuterium Exchange

Protein conformational changes include motions on different time scales from fast femtoseconds vibrations, over picosecond side chain rotation and nanosecond molecular tumbling, to slow domain motions on milliseconds to seconds. All these motions and dynamics are important for the protein function and can be studied by different NMR experiments (Figure 1.19) (Kleckner und Foster 2011).

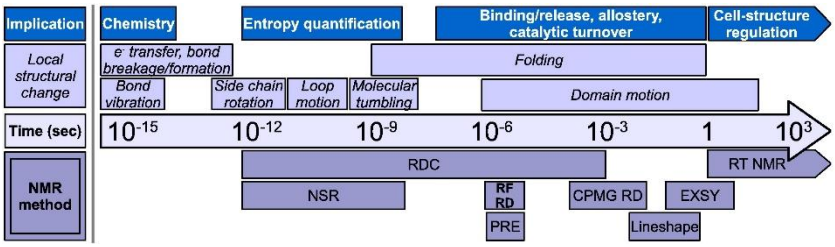

Figure 1.19 Dynamic processes in proteins. Conformational changes of proteins over a broad range of timescales can be studied with a variety of NMR methods, such as real time (RT) NMR, exchange spectroscopy (EXSY), line shape analysis, Carr-Purcell Meiboom-Gill relaxation dispersion (CPMG RD), rotating frame relaxation dispersion (RF RD), nuclear spin relaxation (NSR), residual dipolar coupling (RDC) and paramagnetic relaxation enhancement (PRE). RT NMR can be used to study dynamic behaviour of proteins by hydrogen deuterium exchange. Reprinted from An introduction to NMR-based approaches for measuring protein dynamics, Biochimica et Biophysica Acta (BBA) - Proteins and Proteomics, Volume 1814, Issue 8, 2011, Pages 942-968 (Kleckner und Foster 2011) with permission from Elsevier.

Chemical exchange, the time-dependent exchange between distinct chemical environments or states, can be associated with protein dynamics. The dynamic processes like the exchange between ligand-free and ligand-bound proteins, changes between two

conformations or protonated and deprotonated states, might be described by only two states.

In the slow exchange regime signals from both states are resolved (Figure 1.20), since there is no interconversion between the states during the detection time of the NMR experiment. In the fast exchange regime signals from the two states are averaged to one signal, due to fast interconversion between the states during the detection time. In the intermediate regime the both signals are also averaged to one signal, whose linewidth is additionally broadened (Bain 2003).

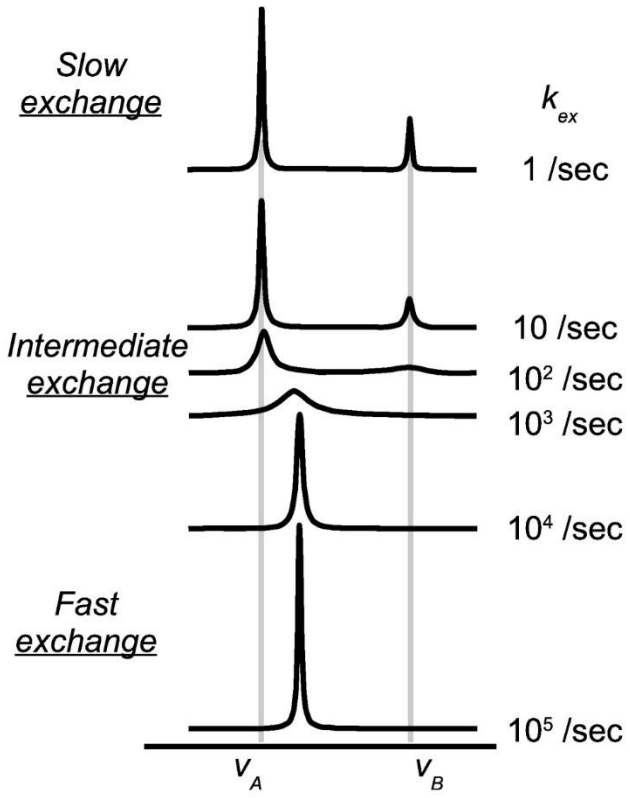

Figure 1.20 Chemical exchange between two states. In the slow exchange regime signals from both states are observed at their distinct chemical shifts. In the fast exchange regime only one signal is observed reflecting the population-weighted averages of chemical shift, intensity and linewidth. In the intermediate exchange regime only one signal with intermediate chemical shift and broadened linewidth. Adjusted reprinted from An introduction to NMR-based approaches for measuring protein dynamics, Biochimica et Biophysica Acta (BBA) - Proteins and Proteomics, Volume 1814, Issue 8, 2011, Pages 942-968 (Kleckner und Foster 2011) with permission from Elsevier.

Protein motions of backbone fluctuations are determined by the exchange properties of hydrogen-bonded amides, which affect protein structure and dynamics. Hydrogen deuterium exchange (HDX) occurs between the ^{1}H hydrogen atoms of the protein and ^{2}H deuterium atoms in the deuterated solvent (Bai et al. 2002; Arrington und Robertson 2002). In general, backbone fluctuations disrupting hydrogen bonds in the secondary structure of proteins facilitate hydrogen exchange. The exchange rate reflects the stability of hydrogen-bonded secondary structure and its response to environmental conditions like pH, temperature and functional interactions (Milne et al. 1998; Mori et al. 1997).

HDX as a slow process, which takes place on seconds, minutes or hours and even longer timescales, is directly detected by series of real-time NMR homonuclear TOCSY or heteronuclear HSQC experiments quantifying the time-dependence of NMR signal intensities (Zeeb und Balbach 2004). Due to the replacement of proton atoms by deuterium atoms, the proton signal decays over time and proton intensities of the amide protons as a function of the acquisition time is fitted to an appropriate model on the basis of an exponential decay.

$$I(t) = I(0) * \exp(-k_{ex} * t) \tag{1.13}$$

The exchange mechanism can be explained by the Linderstrom-Lang model (Hvidt und Nielsen 1966):

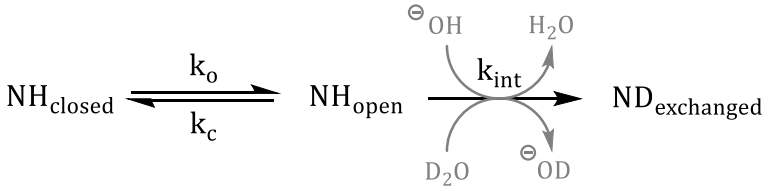

Since exchange is suppressed when amide protons are part of a hydrogen bond network, then a kind of structure opening fluctuation transferring the amide protons from an exchange-protected closed state to an exchange competent open state is required for HDX. The interconversion of the open and closed state is characterized by the rate constants for opening k_o and closing k_c. Once amide protons are in the open state, exchange can take place with the intrinsic solvent-exchange rate k_{int} which depends on the amino acid sequence, temperature and pH (Bai et al. 1993). The pH-dependency is empirically determined and shows minimized k_{int} at pH~2, with higher pH values the exchange mechanism is base-catalysed and k_{int} increases by a factor of 10 for each pH unit

(Bradbury et al. 1977). Changing the pH conditions enables the investigation of a large time window.

In the fast exchange regime (EX1) the intrinsic exchange rate is faster than the rate of closing $k_{int} \gg k_c$, sothat the observed exchange rate k_{ex}, determined by the exponential time-dependent decay of amide proton intensities, only depends on the opening rate and each opening results in an exchange $k_{ex} \approx k_o$. EX1 is used under high pH and denaturating conditions.

In the slow exchange regime (EX2) the intrinsic exchange rate is slower than the rate of closing $k_{int} \ll k_c$, sothat the observed exchange rate k_{ex} now reflects the equilibrium between the open and closed state $k_{ex} \approx k_{int}(k_o/k_c)$ and is characterised by the thermodynamic probability of the protein to be in the open state. EX2 is used under native conditions of folded proteins (Dempsey 2001; Kleckner und Foster 2011).

The protection of amides from exchange indicated by small k_{ex} values correlates to the location within a stable hydrogen bond network of secondary structures like helices, and structure opening backbone fluctuation includes breaking of amide proton hydrogen bonds. This enables exchange of protein protons with solvent deuterium atoms and correlates with a destabilization of the secondary structure around the exchanging proton with unwound secondary structure or random coil conformation.

2 Aim of the Study

Since none of the intramembrane proteases seems to recognize a consensus sequence, but substrates are nevertheless cleaved at specific cleavage sites and mutations affect significantly their processivity, there must be certain properties that define a substrate. Based on mutational results, it was assumed that flexibility of the substrate TMD marks it for efficient cleavage, but this flexibility hypothesis was not confirmed by structural or dynamic data.

Therefore, the structures of WT and mutants will be studied by NMR spectroscopy to reveal if mutations have an influence on flexibility and if this can explain the changed processivity. Mutations will be selected on the basis whether they stabilize or destabilize the TMD helix of γ-secretase substrate Notch1 and SPPL2a/b substrate TNFα, while having simultaneously a significant impact on processivity.

First, to investigate and compare the structural and dynamic properties of substrates and its mutants, standard NMR spectra are acquired and chemical shifts assigned. Chemical shifts and distance-based NOE-data are used to determine secondary structure elements and calculate the 3D structure with these data as restraints. Furthermore, TMD dynamics and residue-specific flexibility profiles are analysed by HDX measurements.

Then to analyse what influence these structural and dynamic properties have on processivity, interactions between the substrate and enzyme are evaluated with a simple superimposing model as well as mechanistic considerations concerning the TMD stability.

Finally, the gained information is used to assume which substrate requirements derived from the structural and dynamic influence on processivity.

3 Material and Methods

3.1 Peptides

The peptides were synthesized by Fmoc chemistry with N-terminal acetylation and C-terminal amidation for more native conditions and removing non-natural charges. The 33 amino acid long peptides TNFα$_{28-60}$, TNFαS34P and TNFαAGA/LLL were purchased from the Core Unit Peptid-Technologien, University of Leipzig, Germany, with a purity of >90 %, judged by mass spectrometry. The 30 amino acid long peptide Notch1$_{1734-1757}$, Notch1L$_{1740-1743}$, Notch1G$_{1740-1743}$ and Notch3$_{1642-1665}$ with added N- and C-terminal lysine triplets for enhanced solubility, were purchased from Peptide Specialty Laboratories, Heidelberg, Germany and purified to >90 % purity as judged by mass spectrometry.
The sequence of the investigated peptides is shown below:

```
                          1740          1750          1760
Notch1 1734-1757     KKKLHFMYVA AAAFVLLFFV GCGVLLSKKK
Notch1L 1740-1743    KKKLHFMYVL LLLFVLLFFV GCGVLLSKKK
Notch1G1 1740-1743   KKKLHFMYVG GGGFVLLFFV GCGVLLSKKK
                               1650          1660
Notch3 1642-1765     KK KPLLPLLVAG AVLLLVILVL GVMVAKKK

                       30          40          50          60
TNFα 28-60        RRC LFLSLFSFLI VAGATTLFCL LHFGVIGPQR
TNFαAGA/LLL       RRC LFLSLFSFLI VLLLTTLFCL LHFGVIGPQR
TNFαS34P          RRC LFLPLFSFLI VAGATTLFCL LHFGVIGPQR
```

3.2 Sample Preparation

Dry peptides were dissolved in hexafluorisopropanol (HFIP) and H_2O (80:20, v:v), 1 mM Tris(2-carboxyethyl)phosphinhydrochlorid (TCEP) was added to reduce potential disulphide bridges and pH was adjusted between 4 to 5 by adding NaOH. The solvent was removed by lyophilisation and the dry peptide film was dissolved in 500 µL trifluorethanol (TFE) and H_2O (80:20, v:v) with renewed addition of TCEP to a final concentration of 1mM. For circular dichroism (CD) measurements protonated TFE was used, deuterated d_2-TFE for chemical shift assignment and structure calculation and

deuterated d_3-TFE as well as D_2O for HDX measurements. The pH was finally adjusted to 6.5 by adding NaOD or DCl and peptide concentration ranged between 2 to 4 mg/mL (500 µM to 1 mM) for NMR measurements and 0.04 to 0.08 mg/mL (10 to 25 µM) for CD measurements.

3.3 NMR Spectra Acquisition

NMR spectra were recorded on a 600 MHz Avance III spectrometer (Bruker BioSpin, Rheinstetten, Germany) equipped with a TCI cryoprobe at a temperature of 300 K, using the NMR experiments and pulse sequences from Table 3.1.

Table 3.1 experiments and pulse sequences. NMR experiments with corresponding pulse sequences used for the chemical shift assignments, structure calculation and hydrogen deuterium exchange measurements.

NMR experiment		pulse sequence	
1D	^{1}H	zggpw5	(Liu et al. 1998)
2D	^{1}H-^{1}H TOCSY	dipsi2gpphpr	(Jeener et al. 1979; Wagner und Berger 1996)
2D	^{1}H-^{1}H NOESY	noesygpphpr	(Jeener et al. 1979; Wagner und Berger 1996)
2D	^{1}H-^{13}C HSQC	hsqcetgp	
2D	^{1}H-^{15}N HSQC	hsqcetf3gpsi	(Kay et al. 1992; Palmer et al. 1991)

3.4 NMR Chemical Shift Assignment

To assign ^{1}H, ^{13}C and ^{15}N resonances of the peptides homonuclear ^{1}H-^{1}H TOCSY (mixing time 60 ms), ^{1}H-^{1}H NOESY (mixing time 200 ms) and natural abundance ^{1}H-^{13}C HSQC and ^{1}H-^{15}N HSQC spectra were acquired. For acquisition and spectral processing TopSpin (Bruker, BioSpin, Rheinstetten, Germany) was used.

CcpNmr Analysis (Vranken et al. 2005) was used for assignment of resonances and integration of NOE peaks. Proton resonances were determined assigning through-bond connections of protons in a spin system. The corresponding ^{13}C and ^{15}N resonances were assigned by through-bond connections between protons and carbon in the ^{1}H-^{13}C HSQC and ^{1}H-^{15}N HSQC spectra. The sequential assignment was achieved by through-space connections of proton between neighbouring amino acids. Resonance assignments are listed in Appendix A. Secondary chemical shifts were determined as the difference between observed and random coil values (Wishart 2011). To account for the influence

of neighbouring amino acids on the chemical shifts, a nearest neighbour correction (Wishart 2011) was applied.

Dihedral restraints for Φ and Ψ backbone dihedral angle, S^2 order parameters and helix probability were derived from chemical shift data using the program TALOS+ (Shen et al. 2009).

3.5 Structure Calculation

All structure calculations were performed with CNS (Brünger et al. 1998) using the ARIA2 setup (Rieping et al. 2007) based on dihedral restraints derived from chemical shift data by TALOS+ (Shen et al. 2009) and distance restraints derived from NOESY peak intensities by CcpNmr Analysis (Vranken et al. 2005). A spin diffusion correction was used for all calculations. Structure statistics are listed in Appendix C. 8 iterations with 400 structures were calculated and 40 lowest energy structures were chosen for visualization. PyMOL (The PyMOL Molecular Graphics System, Version 2.3.1, Schrödinger, LLC) was used to visualize the protein structures.

The atomic coordinates and experimental data have been deposited in the Protein Data Bank PDB (www.pdb.org) and Biological Magnetic Resonance Bank BMRB (https://bmrb.io/) Table 3.2.

Table 3.2 PDB ID and BMRB ID of investigated peptides. Identification number of the deposition of atomic coordinates and experimental data in deposited in the Protein Data Bank PDB and Biological Magnetic Resonance Bank BMRB of Notch1$_{1734\text{-}1757}$ WT, Notch1L$_{1740\text{-}1743}$, Notch1G$_{1740\text{-}1743}$, TNFα$_{28\text{-}60}$ WT, TNFαAGA/LLL$_{28\text{-}60}$ and TNFαS34P$_{28\text{-}60}$.

peptide	PDB ID	BMRB ID
Notch1$_{1734\text{-}1757}$ WT	8OR5	34804
Notch1L$_{1740\text{-}1743}$	8ORY	34806
Notch1G$_{1740\text{-}1743}$	8ORZ	34807
Notch3$_{1642\text{-}1665}$	8OS0	34808
TNFα$_{28\text{-}60}$ WT	7ASY	34567
TNFαAGA/LLL$_{28\text{-}60}$	7ATB	34569
TNFαS34P$_{28\text{-}60}$	7AT7	34568

3.6 Structure Prediction

To predict the structures of the intramembrane protease SPPL2a and SPPL2b in complexes with the substrate TNFα$_{28\text{-}60}$ TMD, the multimer version of AlphaFold2,

accessible through the ColabFold website (https://colab.research.google.com/github/sokrypton/ColabFold/blob/main/AlphaFold2.ipynb) (Mirdita et al. 2022; Jumper et al. 2021; Evans et al. 2021), was used with default settings. The prediction only required the amino acid sequence and no homologous structure as template. The sequences of the human SPPL2a (Q8TCT8) and SPPL2b (Q8TCT7) were taken from the UniProt Database (The UniProt Consortium et al. 2023). The refinement of the final model ensemble was performed by the Amber program implemented within ColabFold (Mirdita et al. 2022). PyMOL (The PyMOL Molecular Graphics System, Version 2.3.1, Schrödinger, LLC) was used to visualize the protein structures.

3.7 Structural Alignment

Notch Peptides

The structural alignment of NMR structures was accomplished using PyMOL (The PyMOL Molecular Graphics System, Version 2.3.1, Schrödinger, LLC). The deflection of the Notch1$_{1734\text{-}1757}$ WT structural bundles was shown by superimposing 40 lowest energy NMR structures onto an average Notch1$_{1734\text{-}1757}$ WT structure along the N-terminal TMD (TM-N) Leu$_{1734}$-Leu$_{1747}$. To compare the orientation of the mutant structural bundles to Notch1$_{1734\text{-}1757}$WT, first the average Notch1L$_{1740\text{-}1743}$ structure was aligned onto the average Notch1$_{1734\text{-}1757}$ TM-N Leu$_{1734}$-Leu$_{1747}$ and then the remaining best energy Notch1L$_{1740\text{-}1743}$ NMR models were superimposed onto its Notch1L$_{1740\text{-}1743}$ average structure along Leu$_{1734}$-Leu$_{1747}$. In case of Notch1G$_{1740\text{-}1743}$ the average structure was first aligned along the backbone atoms of the entire TMD Leu$_{1734}$-Ser$_{1757}$ to the Notch1$_{1734\text{-}1757}$ WT average structure and then the remaining Notch1G$_{1740\text{-}1743}$ NMR models were superimposed onto its average structure along the TM-N Leu$_{1734}$-Val$_{1745}$. An average structure of Notch3$_{1642\text{-}1665}$ WT was aligned with the backbone atoms of residue Leu$_{1644}$-Ile$_{1657}$ along the average Notch1$_{1734\text{-}1757}$ WT structure. The remaining NMR models of Notch3$_{1642\text{-}1665}$ WT were aligned onto its average structure along the TM-N Leu$_{1644}$-Ile$_{1657}$.

The interaction of the investigated Notch1$_{1734\text{-}1757}$ WT to the enzyme-substrate complex was visualized by superimposing the structural bundles onto Notch1 TMD in the cryo-EM structure of γ-secretase (6IDF, (Yang et al. 2019)). An average NMR Notch1$_{1734\text{-}1757}$ WT structure was aligned along the backbone atoms of the entire helix Leu$_{1743}$-Ser$_{1757}$ onto the Cryo-EM Notch1 TMD and the other NMR models were superimposed onto the average Notch1$_{1734\text{-}1757}$ WT structure described above. Distances less than 3 Å of the

heavy backbone atoms between a NMR structure and presenilin TMDs were determined with a PyMOL plugin python script (https://wiki.pymol.org/index.php/Show_contacts).

TNFα Peptides

The deflection of the TNFα$_{28-60}$ WT structural bundles was demonstrated by aligning 40 lowest energy NMR structures on the average TNFα$_{28-60}$ WT structure along the TM-N residues Leu$_{31}$-Gly$_{43}$. To compare the orientation of the mutant bundles to TNFα$_{28-60}$ WT, first the average TNFαAGA/LLL$_{28-60}$ and TNFαS34P$_{28-60}$ structure was aligned with the average TNFα$_{28-60}$ WT TM-N residues Leu$_{31}$ to Gly$_{43}$. Then the 40 lowest energy TNFαAGA/LLL$_{28-60}$ and TNFαS34P$_{28-60}$ NMR models were superimposed onto its average structure along the TM-N residues Leu$_{31}$ to Gly$_{43}$.

The interaction of the investigated TNFα$_{28-60}$ WT to the enzyme-substrate complex was visualized by superimposing the structural bundles onto the predicted AlphaFold TNFα$_{28-60}$ TMD structure in complex with SPPL2a. An average NMR TNFα$_{28-60}$ WT structure was aligned along the backbone atoms of the TM-N residues Leu$_{31}$-Gly$_{43}$ to the AlphaFold TNFα$_{28-60}$ TMD and the other NMR models were superimposed to the average TNFα$_{28-60}$ WT structure described above.

APP Peptides

The deflection of the APP$_{29-51}$ WT (6YHF, (Silber et al. 2020)) structural bundles was shown by superimposing 20 lowest energy NMR structures on the average APP$_{29-51}$ WT structure along the TM-N residues Gly$_{29}$-Gly$_{38}$. To compare the orientation of the mutant bundles to APP$_{29-51}$ WT, first the average G38L and G38P (6YHI and 6YHO, (Silber et al. 2020)) structure was aligned with the average APP$_{29-51}$ WT TM-N residues Gly$_{29}$ to Gly$_{38}$. Then the 20 lowest energy G38L and G38P NMR models were superimposed onto its average structure along the TM-N residues Gly$_{29}$ to Gly$_{38}$.

The interaction of the investigated APP$_{29-51}$ WT to the enzyme-substrate complex was visualized by superimposing the structural bundles onto APP TMD in the cryo-EM structure of γ-secretase (6IYC, (Zhou et al. 2019)). An average APP$_{29-51}$ WT structure was aligned along the backbone atoms of the entire helix Gly$_{29}$-Met$_{51}$ onto the cryo-EM APP TMD and the other NMR models were superimposed onto the average APP$_{29-51}$ WT structure described above.

3.8 Hydrogen Deuterium Exchange

A series of 15 ^{1}H-^{1}H TOCSY (mixing time 30 ms) spectra were acquired sequentially. The acquisition time for one spectrum was 3 h 26 min and the total experimental exchange time was 51.5 hours. Measurements were examined at different pD values pD 3.5 to pD 6.5 to cover a broad time window and access the most exchangeable protons. The pH meter readout pD_{read} was corrected for the pH meter anomaly in deuterated solvents by 0.4 pD units ($pD = pD_{read} + 0.4$) (Glasoe und Long 1960). Cross-peaks of amide protons and H_{α} atoms or H_{β} atoms were integrated and the peak volumes plotted over exchange time. The intensity decay was fitted to an exponential function (3.3) using OriginPro 2022 (OriginLab Corporation, Northamptom, USA) to obtain the experimental exchange rate k_{ex}. With the condition that b the signal intensity at the beginning t = 0 was greater than the offset a, which was set to the value of the spectral noise of 50000 and k_{ex} was positive. To account for the pH/pD dependency of the exchange rate, k_{ex} determined at different pD values was scaled to pD 5 as $k_{ex,s}$ (3.3). The error in the exchange rate determination (3.3) accounted for the error in the fitted parameter k_{ex} Δk_{ex} and the inaccuracy of the pH electrode ΔpD that was set to 0.09. Exchange rates are listed in Appendix B.

$$y(t) = a + b * \exp(-k_{ex} * t) \qquad (3.1)$$
$$b > a \ = 50000$$
$$k_{ex} > 0$$

$$k_{ex,s} = k_{ex} * 10^{(5-pD)} \qquad (3.2)$$

$$\Delta k_{ex,s} = \sqrt{\left(\frac{\partial k_{ex,s}}{\partial k_{ex}}\right)^2 * {\Delta k_{ex}}^2 + \left(\frac{\partial k_{ex,s}}{\partial pD}\right)^2 * \Delta pD^2} \qquad (3.3)$$
$$= \sqrt{(10^{5-pD})^2 * {\Delta k_{ex}}^2 + (k_{ex} * \ln(10) * 10^{5-pD})^2 * \Delta pD^2}$$
$$\Delta \log(k_{ex,s}) = \sqrt{\left(\frac{\partial \log(k_{ex,s})}{\partial k_{ex}}\right)^2 * {\Delta k_{ex}}^2 + \left(\frac{\partial \log(k_{ex,s})}{\partial pD}\right)^2 * \Delta pD^2}$$
$$= \sqrt{\left(\frac{1}{k_{ex}}\right)^2 * {\Delta k_{ex}}^2 + (-\ln(10))^2 * \Delta pD^2}$$

3.9 Circular Dichroism Spectroscopy

CD spectra of the peptides were recorded on a J-815 spectropolarimeter (JASCO, Groß-Umstadt, Germany). The measurements were performed in quartz glass cells (Suprasil, Hellma, Müllheim, Germany) of 1 mm path length between 280 and 180 nm at 0.5 nm intervals. The spectra were acquired at 300 K using a water-thermostated cell holder, with a scan rate of 10 nm/min, 8 s response time and 1 nm bandwidth. 3 scans were averaged and the baseline spectrum, corresponding to the peptide-free sample, subtracted.

CD data were analysed with BeStSel (http://bestsel.elte.hu) web server (Micsonai et al. 2018; Micsonai et al. 2015). The concentrations of the peptide samples were determined from the CD spectra by the absorbance of the peptide bond at 214 nm and the calculated extinction coefficient at 214 nm (Kuipers und Gruppen 2007). The measured ellipticity was converted to the mean residue ellipticity and the secondary structure estimated from the CD spectra.

4 Results

Because of the crucial biological importance of Notch1 and TNFα and their activation by intramembrane proteolysis, it is necessary to elucidate the atomic structure of these aspartate protease substrates. From structural and dynamic properties of substrates, conclusions about the interaction with the proteases could be drawn to estimate what influences the processivity.

In this thesis the secondary structure of Notch1 TMD and TNFα TMD was determined using chemical shift as well as NOE contact data and their 3D structure calculated based on these experimental data. Dynamic studies using HDX measurements completed the characterization of the peptides. Finally, the investigated structure was used to estimate the interaction with the respective protease with a simple model.

4.1 Notch1$_{1734-1757}$ WT TMD

Notch1 a transmembrane receptor protein plays an important role in cell-fate-determination as well as cell communication. Its biological function is activated through the cleavage by γ-secretase. A certain flexibility of a substrate is required for intramembrane proteolysis. To alter the flexibility profile of the Notch1 TMD mutations were inserted and the influence on the 3D structure and TMD dynamics investigated by NMR spectroscopy. In addition, the structural and dynamic effects of a homologue sequence Notch3 were examined.

The NMR experiments were examined in a mixture of TFE and water. TFE is a well-established and widely used solvent to investigate peptides and proteins. The polarity of the TFE/water mixture matches approximately the interior of the enzyme and mimics the water containing cavity of the enzyme's active side (Schutz und Warshel 2001; Buck 1998; Tolia et al. 2006). Simultaneously this mixture was able to solubilize the highly hydrophobic TMD and provides an appropriate solvent for studying hydrophobic peptides in solution by NMR spectroscopy.

All investigated and unlabelled Notch TMDs were analysed in TFE/water (TFE:H_2O, 80:20, v:v) at 300 K and pH 6.5. Formation of disulphide bridges was prevented by adding TCEP to a final concentration of 1 mM. The chosen pH value represents the optimum for γ-secretase activity (Quintero-Monzon et al. 2011).

4.1.1 Sequence

The first clue in the analysis of proteins is the primary structure, the amino acid sequence. The UniProt database (The UniProt Consortium et al. 2023) lists the human Notch1 protein (P46531). Out of these 2555 amino acid long sequence the TMD was determined by DeepTMHMM (https://dtu.biolib.com/DeepTMHMM), an algorithm that detects and predicts the topology of transmembrane proteins (Hallgren et al. 2022). Notch1 harbours a single TMD, which was predicted to be helical, spanning residues 1736 to 1755.

Solution state NMR is limited in protein size to ~30 kDa, considering the slow molecular tumbling of large molecules leads to fast nuclear relaxation and low signal sensitivity, as well as a high signal overlap. Therefore, only a specific region of Notch1 could be examined. The Notch1 TMD sequence for NMR investigations was chosen on the basis of the DeepTMHMM prediction, but with N- and C-terminal added residues, which might be important for positioning in the membrane (Lerch-Bader et al. 2008). The solubility of the highly hydrophobic Notch1 TMD was enhanced by replacing Gln$_{1733}$ and Arg$_{1758}$ in the native sequence by a lysine triplet, therefore the investigated peptide was Notch1$_{1734-1757}$ WT TMD (Figure 4.1).

Notch1$_{native}$ VEPPP PAQLHFMYVA AAAFVLLFFV GCGVLLSRKR RRQHG
1730 1740 1750 1760
Notch1$_{1734-1757}$ KKK**LHFMYVA AAAFVLLFFV GCGVLLS**KKK

Figure 4.1 Notch1$_{1734-1757}$ WT sequence. Native Notch1 sequence of residue 1725-1765 shown in top line, TMD region predicted by DeepTMHMM is underlined. Investigated Notch1$_{1734-1757}$ TMD sequence shown in bold in lower line, with N- and C-terminal appended Lys triplets for enhanced solubility.

Notch1 and its homologues are represented in all kingdoms of life and the protein domains are evolutionary conserved (Hori et al. 2013). To see how the amino acid conservation of the Notch1 TMD is across a wide range of species, a basic local alignment search tool (BLAST) analysis was performed (https://www.ebi.ac.uk/Tools/sss/ncbiblast/). The Notch1 TMD sequence was blasted against UniRef90. Some juxtamembrane areas were added to the query sequence, in total Notch1 residues 1705-1805, to facilitate the similarity search. UniRef90 is a database for similarity searches and clusters proteins of identical or similar function and with 90%

sequence identity (Suzek et al. 2015). All pairwise sequence alignments were analysed using a custom python script written by Martin Ortner (TU Munich). The amino acid conservation from all matched sequences were calculated for each aligned position and the consensus sequence was constructed from the most abundant amino acid at each residue. Surprisingly, the Notch1 TMD was little conserved and showed a significant sequence variability (Figure 4.2).

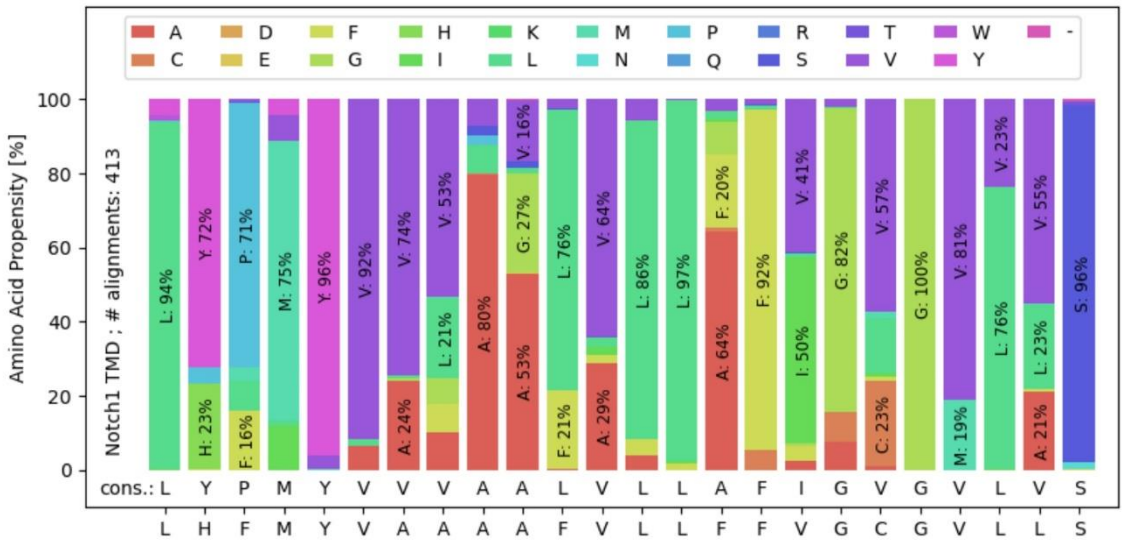

Figure 4.2 Sequence alignment of Notch1 TMD. Notch1 TMD sequence blasted against UniRef90. Evolutionary conservation of each residue was calculated from pairwise alignment.

One of the most conserved Notch1 TMD residues Gly$_{1753}$ was located at the S3 cleavage site and might play an important role together with Gly$_{1751}$ in terms of accessibility of the cleavable bond due to their small side chain volume. Another small amino acid Ser$_{1757}$ was highly conserved and located at the C-terminal end of the TMD. There were also conserved polar residues Met$_{1737}$ and Tyr$_{1738}$ at the N-terminal end of the TMD, which could together with Ser$_{1757}$ ensure the correct positioning in the lipid membrane. At S4 cleavage site the last two residues Ala$_{1742}$ and Ala$_{1743}$ of the alanine tetrad were more conserved than the first two, which were replaced by valine in the consensus sequence. Leu$_{1734}$ at the N-terminal end of the TMD and both Leu$_{1746}$ and Leu$_{1747}$ in the middle of the TMD showed a high level of evolutionary conservation.

4.1.2 Chemical Shifts

Chemical shifts are sensitive to the electronic, chemical and magnetic environments of the investigated nuclei and provide information about the structure and dynamic of molecules. The well resolved ^{1}H-^{1}H NOESY and TOCSY spectra as well as natural abundance ^{1}H-^{13}C HSQC spectrum (Figure 4.3) showed sharp peaks with a good chemical shift dispersion. The amide proton resonances in the range of approximately 7.7 ppm to 8.9 ppm, together with the $^{1}H_{\alpha}$ and $^{13}C_{\alpha}$ resonances in the range of 3.5 ppm to 4.5 ppm and 48 ppm to 68 ppm indicated a folded Notch1$_{1734-1757}$ WT TMD.

All amino acids of the investigated Notch1$_{1734-1757}$ WT TMD were identified in the spectra. Proton resonances were determined assigning through-bond connections of protons in a spin system (Figure 4.3 (a), vertical lines), consisting of all protons in one amino acid. The corresponding ^{13}C resonances were assigned by through-bond connections between protons and carbon atoms in the ^{1}H-^{13}C HSQC spectra (Figure 4.3 (b)). The sequential assignment was achieved by through-space connections of protons between neighbouring amino acids.

On the basis of these assignments the CSI 3.0 identified the whole Notch1$_{1734-1757}$ WT TMD as α-helical (Figure 4.4 (e)). CSI 3.0 is a web server (http://csi3.wishartlab.com) for the prediction of protein secondary structure by comparing experimentally chemical shifts with random coil chemical shifts and generation of a simple graphical output (Hafsa et al. 2015).

This first information about the Notch1$_{1734-1757}$ WT TMD structure by the prediction of CSI 3.0 was confirmed and extended by the secondary structure prediction of TALOS+ (Shen et al. 2009). This program uses an empirical relation between ^{1}H, ^{13}C and ^{15}N chemical shifts and the backbone torsion angles Φ and Ψ not only for the prediction of dihedral angles, but also of the secondary structure and the backbone order parameter S^2. The helical content (Figure 4.4 (c)) revealed a slight destabilization of the α-helix around Gly$_{1753}$/Val$_{1754}$ the initial cleavage site S3. Additionally, the chemical shift derived order parameter S^2 (Figure 4.4 (d)), which is a measure for the restriction of internal N_H bond vector motions, indicated with marginally smaller values higher internal motion around S3 and thus a less rigid helical area.

a

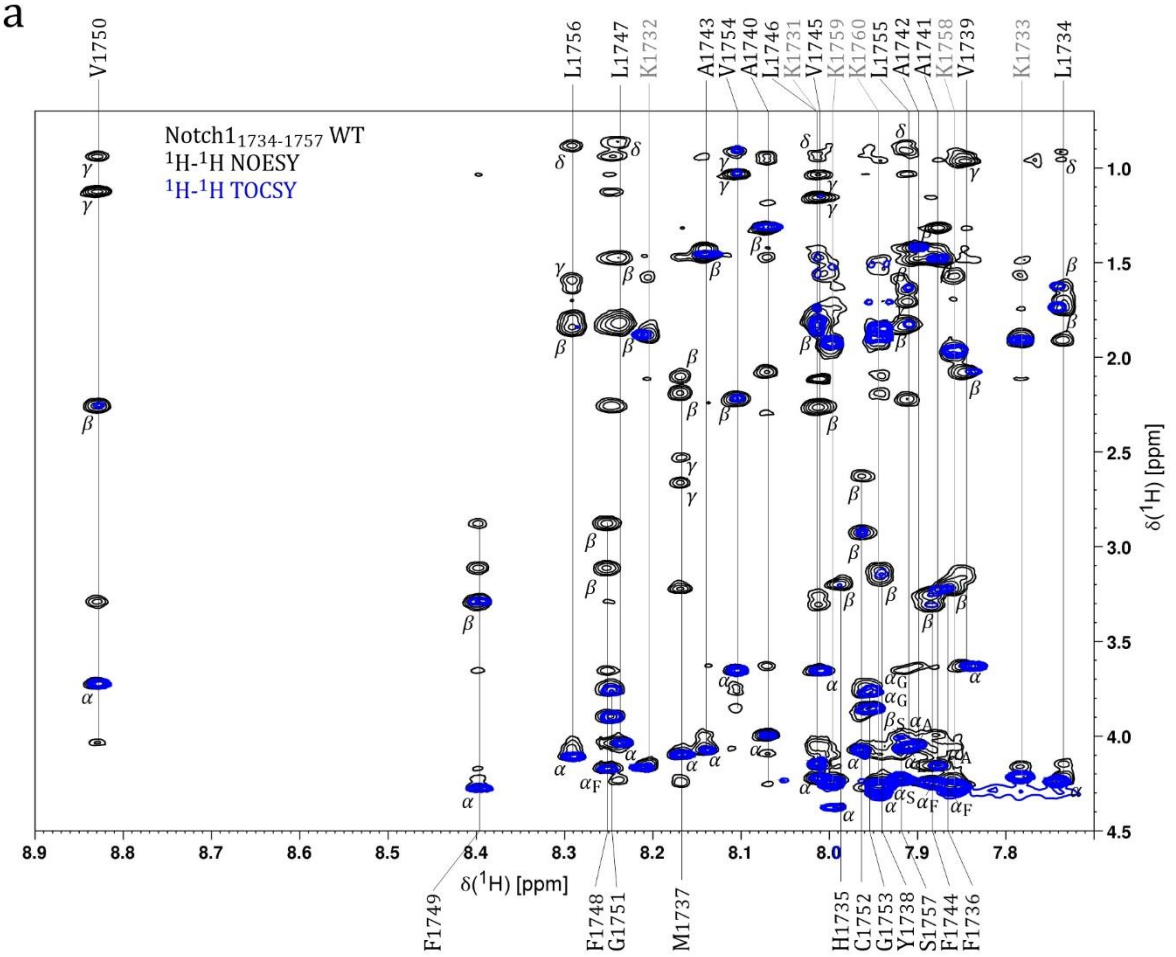
Notch1$_{1734-1757}$ WT
^{1}H-^{1}H NOESY
^{1}H-^{1}H TOCSY
V1750
L1756
L1747
K1732
A1743
V1754
A1740
L1746
K1731
V1745
K1759
K1760
L1755
A1742
A1741
K1758
V1739
K1733
L1734
δ(^{1}H) [ppm]
F1749
F1748
G1751
M1737
H1735
C1752
G1753
Y1738
S1757
F1744
F1736

b

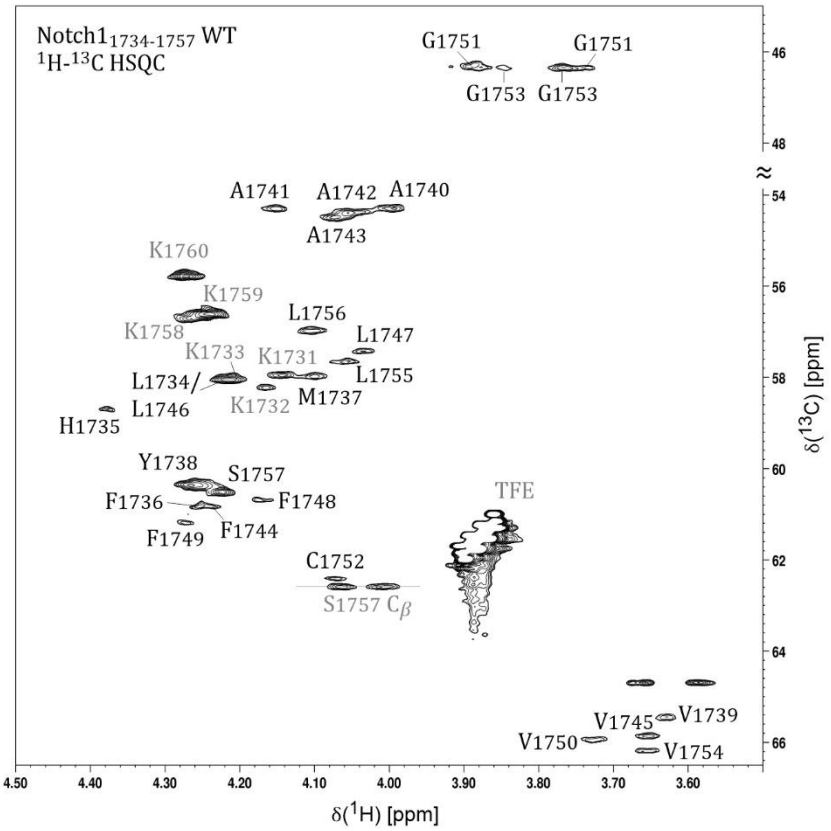
Notch1$_{1734-1757}$ WT
^{1}H-^{13}C HSQC
G1751
G1753
A1741
A1742
A1740
A1743
K1760
K1759
K1758
L1756
L1747
K1733
K1731
L1755
L1734/
L1746
K1732
M1737
H1735
Y1738
S1757
F1736
F1748
F1749
F1744
C1752
S1757 Cβ
TFE
V1745
V1739
V1750
V1754
δ(^{1}H) [ppm]
δ(^{13}C) [ppm]

Figure 4.3 Notch1$_{1734-1757}$ WT NMR spectra. Figure caption refers to the figure on the previous page. Shown are Notch1$_{1734-1757}$ WT ^{1}H-^{1}H NOESY and ^{1}H-^{1}H TOCSY spectra (a) of the H_N-H_α region. The spin systems of the individual residues are indicated by vertical lines. The respective protons are identified by small Greek letters and supplemented by the corresponding amino acid in the range of low spectral dispersity. Residues marked in grey are not part of the native sequence. The ^{1}H-^{13}C HSQC spectrum (b) shows the H_α-C_α region and the respective residues are marked.

In ^{1}H-^{1}H NOESY spectra the peak intensities depend on the distance between the corresponding protons and characteristic NOE contacts provide information about the secondary structure. A continuous series of interresidual NOE cross-peaks dNN(i, i+2), dαN(i, i+3), as well as dαβ(i, i+3) identify a helical structure (Wüthrich 1986). In α-helices there are additional dαN(i, i+4) NOE contacts, while dαN(i, i+2) cross-peaks occur only in 3_{10} helices (Wüthrich et al. 1991; Wagner et al. 1986). Sequential NOE contacts dNN(i, i+1) and dαN(i, i+1) are present in both helical types. A helical conformation leads to negative $^{1}H_\alpha$ and $^{13}C_\beta$, as well as positive $^{13}C_\alpha$ secondary chemical shifts (Wishart et al. 1991; Spera und Bax 1991). For more detailed information of secondary chemical shifts and NOE contacts see section 1.6.2.

The helicity of the entire Notch1$_{1734-1757}$ WT TMD was confirmed by secondary chemical shifts (Figure 4.4 (a)) and consecutive characteristic NOE contacts (Figure 4.4 (b)). The blue boxes in the representation of the consecutive NOE contacts indicate unambiguous contacts, while grey boxes present NOE contacts which could not be assigned unambiguously, due to signal overlap. The beginning of the TM-N, residues Leu$_{1734}$ to Ala$_{1740}$, appeared less helical due to the absence of dNN(i, i+2) and increased occurrence of dαN(i, i+2) NOEs.

Slightly reduced secondary chemical shifts and the simultaneous appearance of dαN(i, i+2) and dαN(i, i+4) NOEs around the AAAA motif points to a disruption of a regular α-helix. This might arise from a mixture of random coil/α-helix or 3_{10} helix/α-helix, as an intermediate in folding and unfolding of α-helices (Millhauser 1995). Like the helix probability and order parameter S^2 before, the presence of dαN(i, i+2) and the absence of dNN(i, i+2), dαN(i, i+4) NOEs also indicated a destabilization of the α-helix around the S3 cleavage site at Gly$_{1753}$/Val$_{1754}$.

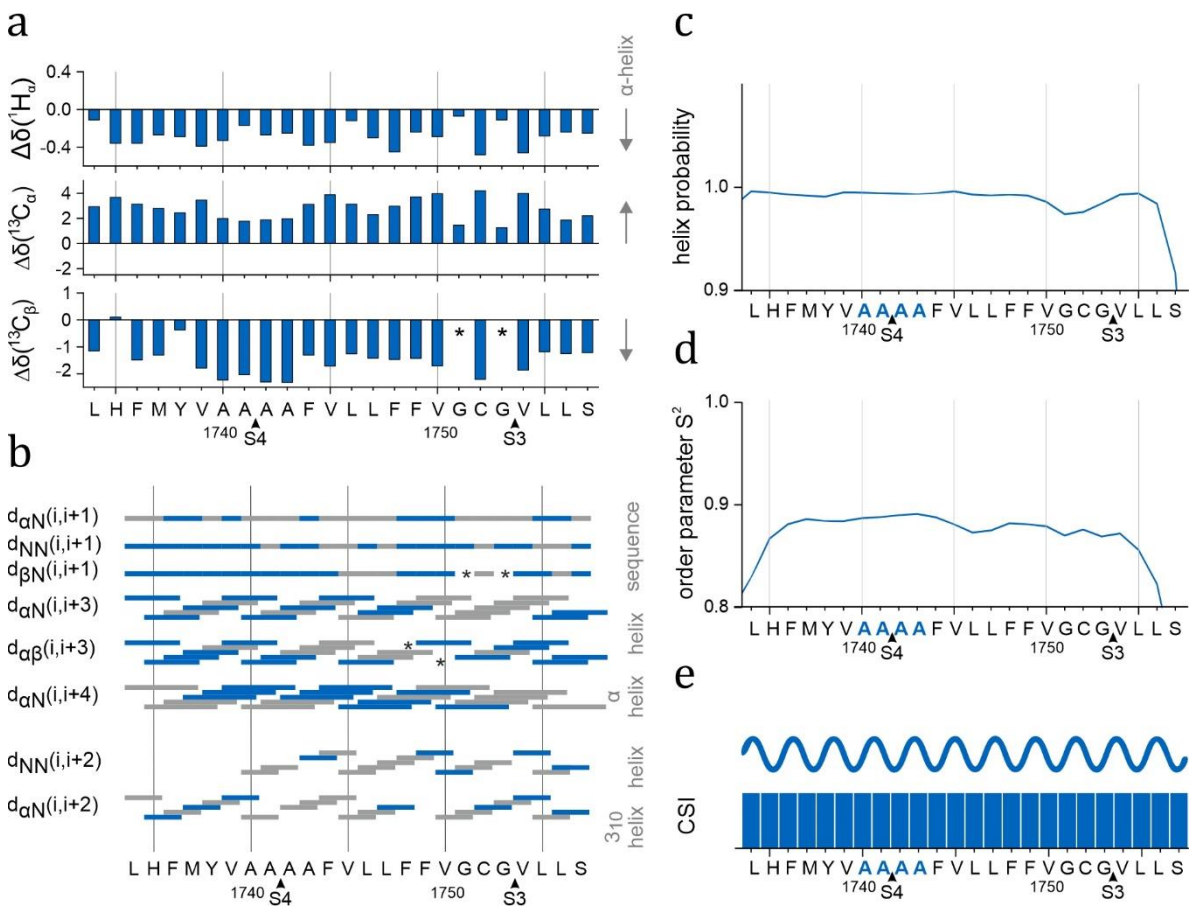

Figure 4.4 Secondary structure characteristics of Notch1$_{1734-1757}$ WT TMD determined by NMR. Secondary chemical shifts (a), the difference between random coil and observed values. Positive $^{13}C_\alpha$ and negative $^{1}H_\alpha$, $^{13}C_\beta$ secondary chemical shifts indicate α-helices. Characteristic NOE contacts (b), where blue boxes indicate unambiguous NOE contacts and grey boxes show NOE contacts that could not be assigned unambiguously due to signal overlap. Asterisks mark glycines without H_β atoms. Helix probability (c) and theoretical order parameter S^2 (d) were predicted with TALOS+ (Shen et al. 2009) on the basis of chemical shifts. An $S^2 = 1$ indicates complete restriction of the internal NH bond vector motion. In the CSI 3.0 output (e) α-helical regions are represented by the blue bars and the wavy line.

4.1.3 3D Structure

The calculation of the 3D structure of Notch1$_{1734-1757}$ TMD was performed with CNS (Brünger et al. 1998) using the ARIA2 setup (Rieping et al. 2007) based on distance restraints derived from ^{1}H-^{1}H NOESY peak intensities and dihedral restraints derived from chemical shifts using TALOS+ (Shen et al. 2009).

The structure determination indicated a fully helical Notch1$_{1734-1757}$ WT TMD (Figure 4.5), consistent with the previous chemical shift and NOE contact data. The average 3D structure of Notch1$_{1734-1757}$ WT TMD (Figure 4.5 (c)) revealed a slight bend in the middle of the helix around residues Leu$_{1746}$/Leu$_{1747}$, which becomes more apparent when NMR structures are superimposed along the TM-N.

When 40 lowest energy NMR structures out of 400 were superimposed along the backbone atoms of the TM-N residues Leu$_{1734}$ to Leu$_{1747}$ the TM-Cs fanned out in a defined cone (Figure 4.5 (a)). This showed that the orientation of the TM-N, with respect to the TM-C was not arbitrary. These bundles do not represent *per se* dynamics. Every single structure is consistent with the experimental data and obeys all given restraints. But whether the distance restraints are not sufficient to determine the extent of bending or rather the calculated structures represent together the ensemble because of true dynamics, cannot be decided at this stage.

Viewing along the bundle of structures from the N-terminus, Ala$_{1742}$, Val$_{1745}$, Phe$_{1749}$ and Cys$_{1752}$ lined the concave side. The bulky amino acids Phe$_{1744}$, Leu$_{1747}$, Phe$_{1748}$ and Val$_{1750}$ were located on the convex side, so the bending was directed away from these space-filling residues. To visualize the location of the concave and convex sites the 2D helical wheel representation of the TMD α-helix residues Phe$_{1736}$ to Val$_{1754}$ was used (Figure 4.5 (d)). The space-filling properties of the amino acids side chains were indicated as transparent surfaces in the bundles of the helix backbone structures (Figure 4.5 (b)).

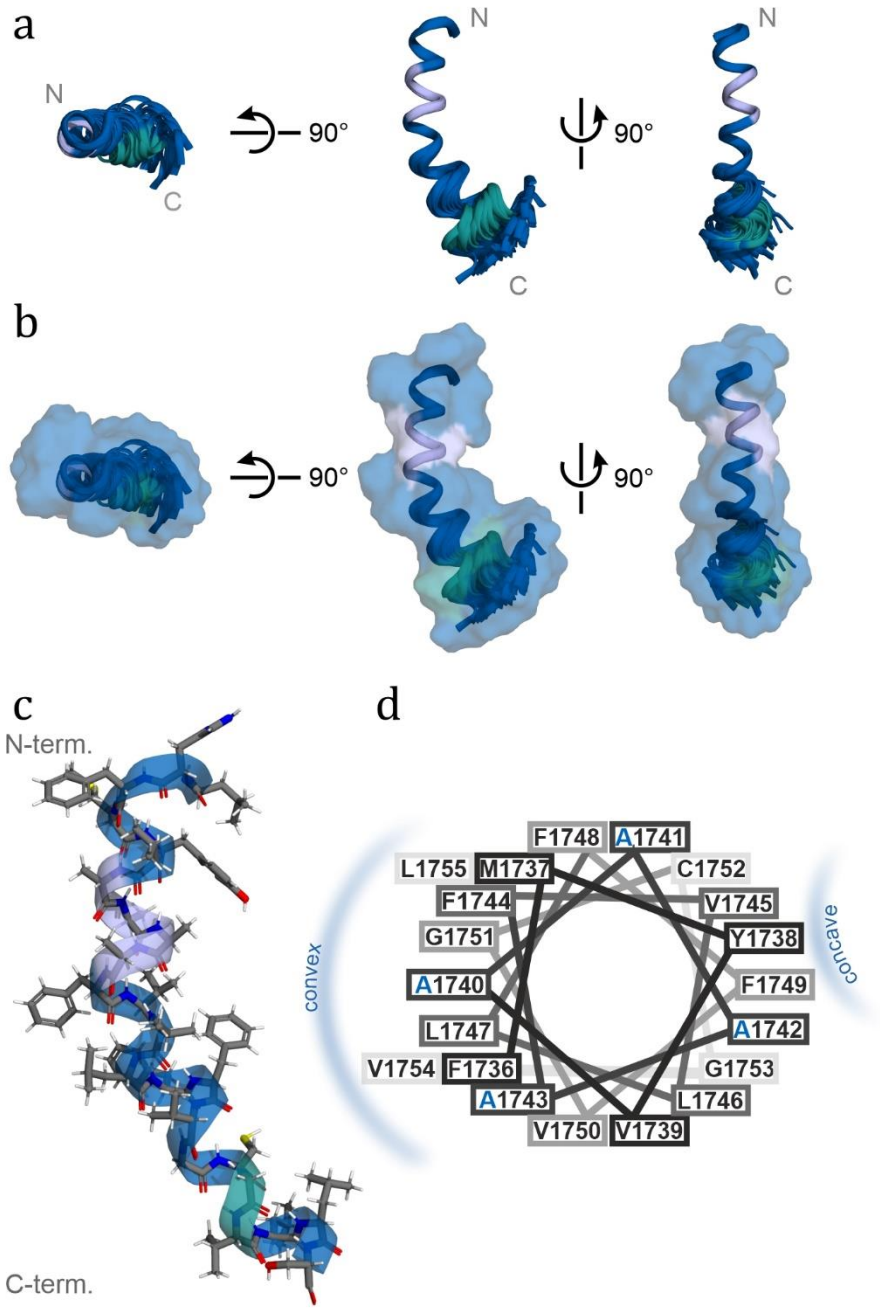

Figure 4.5 3D structure of Notch1$_{1734-1757}$ WT TMD. Structural bundles (a) superimposed on residues Leu$_{1734}$-Leu$_{1747}$. Top and side view of the 40 lowest energy NMR structures out of 400 are shown. Region with four alanine residues is highlighted in light blue. The S3 cleavage site Gly$_{1753}$/Val$_{1754}$ is represented in turquoise. The bundles of helix backbone structure are surrounded by transparent surfaces corresponding to the side chains (b). Average 3D structure (c). In the helical wheel representation (d) the locations of the concave and convex sides of residues Phe$_{1736}$-Val$_{1754}$ are indicated.

4.1.4 Hydrogen Deuterium Exchange

HDX investigated by NMR spectroscopy provides information about protein stability and the accessibility to the solvent. Slow dynamic processes, like HDX, the exchange of hydrogen atoms between the protein and the solvent, with a rate constant ~min^{-1}, are accessible by quantifying the time dependence of signal intensities. ^{1}H atoms of fully protonated proteins are replaced with the ^{2}H deuterium atoms of the solvent and the detected proton signal decays over time. Regions of faster exchange are correlated to regions of less stability and higher flexibility.

To determine slow dynamics, a series of 15 ^{1}H-^{1}H TOCSY spectra of Notch1$_{1734-1757}$ WT TMD in d_3-TFE/D_2O (d_3-TFE:D_2O, 80:20, v:v) at 300 K and 1mM TCEP were measured. The acquisition time for one ^{1}H-^{1}H TOCSY spectrum was set to approximately 3.5 hours and the total experimental exchange time covered 52 hours. Since the exchange rate depends on the pH/pD value and increases 10 fold for each pH unit (Bai et al. 1993; Coales et al. 2010), the Notch1$_{1734-1757}$ WT TMD was examined at different pD values pD 4.5, pD 5.5 and pD 6.5 to cover a broad time window of rate constants and access most of the exchangeable protons. The pH meter readout pD_{read} was corrected for the pH meter anomaly in deuterated solvents by 0.4 pD units ($pD = pD_{read} + 0.4$) (Glasoe und Long 1960). The experimental conditions were chosen in a way to obtain adequate signal and time resolution as well as signal intensity.

No evaluable signals could be detected for the residues at the very N- and C-termini Leu$_{1734}$, Met$_{1737}$ and Ser$_{1757}$ just as both residues Cys$_{1752}$ and Gly$_{1753}$ at the S3 cleavage site, as well as for the non-native lysines at both ends, due to fast exchange. Cross-peaks of amide protons and H_α atoms of the remaining residues, shown at the top of the respective graphs in Figure 4.6, were integrated and the peak volumes plotted over exchange time. In the region where signal overlap of the amide protons occurs due to low spectral resolution, the cross-peaks of $^{1}H_\beta$ atoms were used (Figure 4.6 (b)). The intensity decay was fitted to an exponential function (3.1), where the offset a was set to the value of the spectral noise of 50000.

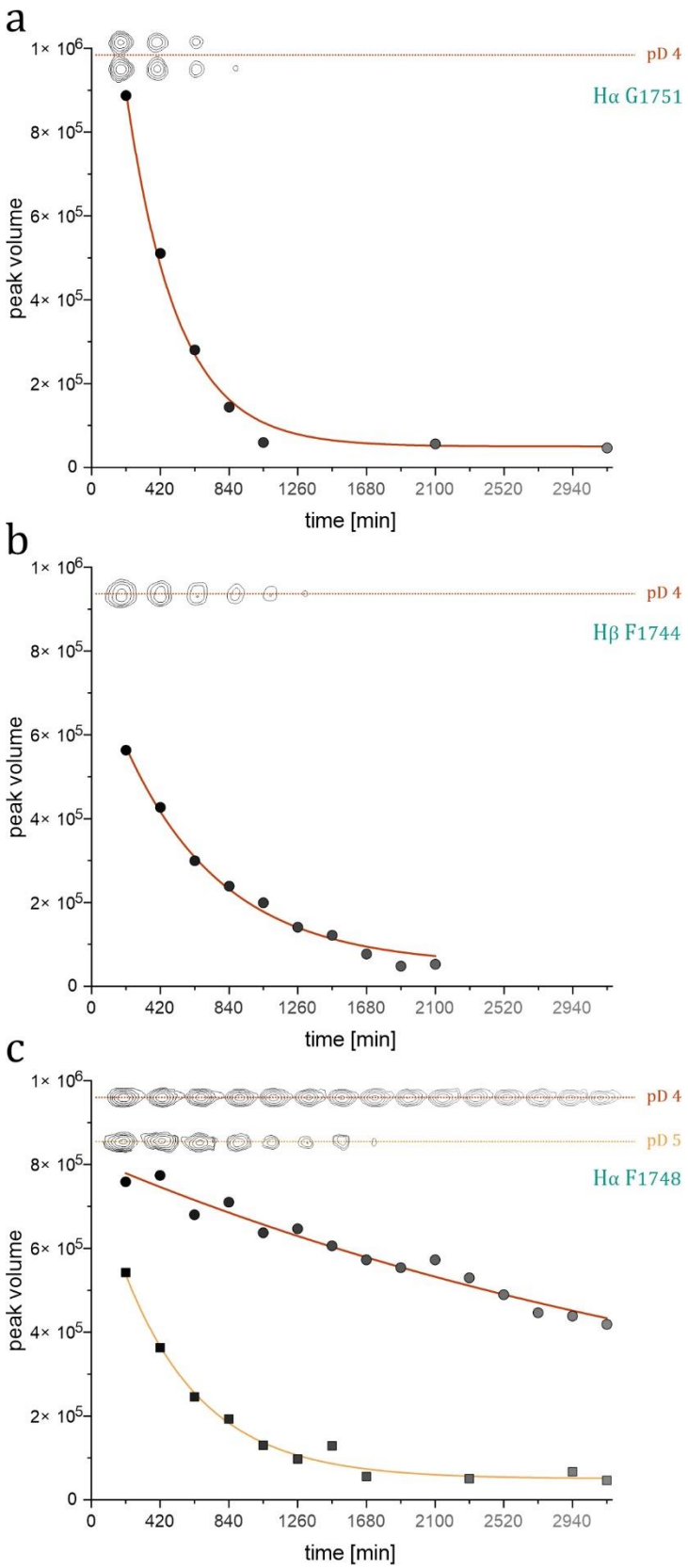

Figure 4.6 Example of HDX peak intensities of Notch1$_{1734-1757}$ residues as a function of time. The integrated cross-peak volumes of Gly$_{1751}$ $^{1}H_N$-$^{1}H_\alpha$ (a), Phe$_{1744}$ $^{1}H_N$-$^{1}H_\beta$ (b) and Phe$_{1748}$ $^{1}H_N$-$^{1}H_\alpha$ (c) as a function of exchange time are represented as dots at pD 4 (red line) and squares at pD 5 (orange line). The individual grey shades indicate different exchange times. The cross-peaks

extracted from the corresponding TOCSY spectra are shown at the top of the diagram. The lines indicate the results of the fitting using equation (2.1).

As long as the exchange was fast enough at a given pD value, the peak intensity decay could be fitted to an exponential function, as in case for the H_α atom of Gly$_{1751}$ (Figure 4.6 (a)) and still for the H_β atom of Phe$_{1744}$ (Figure 4.6 (b)), where the exchange was already slower. If the hydrogen exchange was too slow under the given conditions link for H_α atom of Phe$_{1748}$, the decay in peak intensity could not be fitted appropriate to an exponential function and seems to be linear or even constant (Figure 4.6 (c) red line). The series of ^{1}H-^{1}H TOCSY measurements was repeated at an increased pD value so that the experimental exchange rate k_{ex} could be determined (Figure 4.6 (c) orange line). To account for the pH/pD dependency of the exchange rate, k_{ex} determined at different pD values was scaled to pD 5 as $k_{ex,s}$ (2.2).

The logarithm of the scaled residue-specific exchange rate $k_{ex,s}$ of the exchangeable protons was plotted and its distribution along the Notch1$_{1734-1757}$ TMD referred as "flexibility profile" (Figure 4.7), where the error bars accounted for the error in the fitted parameter k_{ex} and the inaccuracy of the pH electrode.

The determined rate constants of Notch1$_{1734-1757}$ WT TMD residues were in the range of 0.05 min^{-1} (one in 15 minutes) to 0.0002 min^{-1} (one in 3 days), with the smallest exchange rates for Val$_{1745}$, Leu$_{1746}$ and Leu$_{1747}$. Small exchange rates indicate slow exchange of the protons with the deuterated solvent, where the exchange is suppressed mainly by the participation of the amide hydrogen atoms in hydrogen bonds. This also influence exchange of H_α and H_β atoms. Consequently, the α-helix in the middle part of the Notch1$_{1734-1757}$ WT TMD was stabilized by hydrogen bonds.

HDX can only take place if an amide proton is not part of a hydrogen bond as a result of local fluctuation in structure and partial unfolding of the helix, indicating conformational flexibility of the respective residue. As expected, the flexibility of the TMD increased towards the N- and C-termini, where the accelerated HDX of the residues from Gly$_{1751}$ onwards revealed a destabilization of the α-helical TMD and a partial unfolding in the immediate vicinity of the S3 cleavage site.

The TM-C was more stable compared to the TM-N, especially in the first half of the TM-C and confirmed by secondary chemical shifts and characteristic NOE contacts. Within the TM-N the first two alanines of the AAAA motif showed a slightly increased conformational

flexibility compared to the last two alanines, which seemed to correlate with the sequence conservation.

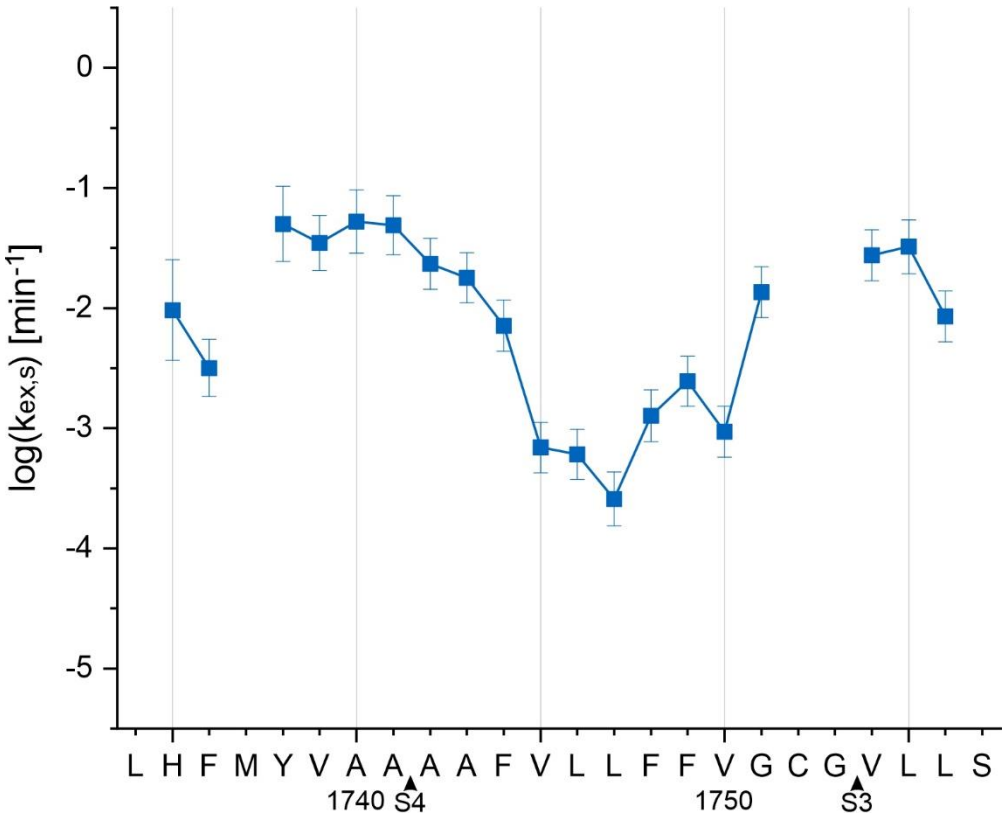

Figure 4.7 Residue-specific HDX rate constants of Notch1$_{1734-1757}$ TMD. Exchange rates of Notch1$_{1734-1757}$ TMD residues were determined in d_3-TFE/D_2O at different pD values (4.5, 5.5 and 6.5) and scaled to pD 5. The error bars account for the error in the fitted parameter k_{ex} and the inaccuracy of the pH electrode. Residues Leu$_{1734}$, Met$_{1737}$ and Ser$_{1757}$ at the N- and C-termini and both residues Cys$_{1752}$ and Gly$_{1753}$ at the S3 cleavage site could not be detected or fitted because of fast exchange at the given conditions. Most stable region of Notch1$_{1734-1757}$ TMD is located around Leu$_{1746}$/Leu$_{1747}$.

4.2 Notch1L$_{1740-1743}$ and Notch1G$_{1740-1743}$ Mutants

In addition to Notch1$_{1734-1757}$ WT TMD, two mutants influencing the flexibility of the TMD were examined. The mutant Notch1L$_{1740-1743}$ was introduced by replacing the AAAA motif with leucines (Figure 4.8) to stabilize the helix (Lyu et al. 1991) and reduce its flexibility. On the other hand the mutant Notch1G$_{1740-1743}$ was introduced by replacing the alanine tetrad by glycines, where glycine destabilizes the helix due to a packing defect of its missing side chains (Högel et al. 2018). To evaluate the influence on the TMD stability,

dynamics and the orientation of the 3D structure Notch1L$_{1740-1743}$ TMD and Notch1G$_{1740-1743}$ TMD were analysed under the same conditions as Notch1$_{1734-1757}$ WT.

	1740	1750	1760
Notch1 WT	KKK**LHFMYVA**	**AAAFVLLFFV**	**GCGVLLS**KKK
Notch1L$_{1740-1743}$	KKK**LHFMYVL**	**LLLFVLLFFV**	**GCGVLLS**KKK
Notch1G1$_{1740-1743}$	KKK**LHFMYVG**	**GGGFVLLFFV**	**GCGVLLS**KKK

Figure 4.8 Notch1$_{1734-1757}$ WT, Notch1L$_{1740-1743}$ and Notch1G$_{1740-1743}$ sequence. Investigated Notch1$_{1734-1757}$ WT and mutant TMD sequence is shown with native sequence in bold and N- and C-terminal appended lysine triplets for enhanced solubility.

4.2.1 Circular Dichroism

Secondary structure, like α-helices, β-sheets or unstructured segments with a specific peptide bond environment, dihedral angles and hydrogen bond patterns, affect the CD spectrum by absorbing characteristically circular polarised light. So α-helices typically show two minima at 222 nm and 208 nm as well as a maximum at 192 nm (Kelly et al. 2005).

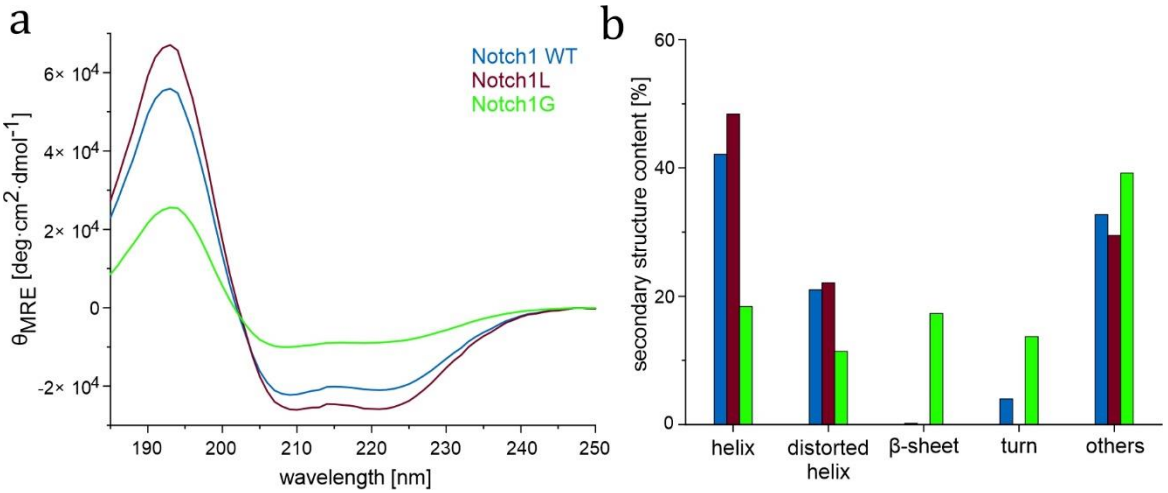

Figure 4.9 CD spectra of Notch1$_{1734-1757}$ WT, Notch1L$_{1740-1743}$, Notch1G$_{1740-1743}$. CD spectra (a) of Notch1$_{1734-1757}$ WT (blue), Notch1L$_{1740-1743}$ (red) and Notch1G$_{1740-1743}$ (green) in TFE/H_2O (80:20, v:v) at pH 6.5 and 300 K. The secondary structure content (b) indicates a helicity of 42 % in Notch1$_{1734-1757}$ WT, 48 % in Notch1L$_{1740-1743}$ and 18 % in Notch1G$_{1740-1743}$. CD spectra were analysed and secondary structure content estimated with BeStSel.

First insights into the influence of mutants on the secondary structure were provided by CD spectra. Similar to the NMR conditions, the CD spectra were recorded in TFE/H_2O (80:20, v:v), 1 mM TCEP at pH 6.5 and 300 K. The concentration of Notch1 WT and both mutants in the CD sample were determined from the CD spectra by the absorbance A_{214} at 214 nm, due to low absorbance at 280 nm (Table 4.1). The corresponding extinction coefficient ε_{214} at 214 nm was calculated using the web server BeStSel (https://bestsel.elte.hu) (Kuipers und Gruppen 2007; Micsonai et al. 2018; Micsonai et al. 2015). The recorded ellipticity was converted to the mean residue ellipticity (Figure 4.9 (a)) and the secondary structure content (Figure 4.9 (b)) was estimated with BeStSel.

Table 4.1 Secondary structure content and concentration of Notch1$_{1734-1757}$ WT and mutants. Secondary structure content of Notch1$_{1734-1757}$ WT, Notch1L$_{1740-1743}$ and Notch1G$_{1740-1743}$ investigated from CD spectra with BeStSel and concentration determination for mean residue ellipticity conversion.

	Notch1 WT	Notch1L$_{1740-1743}$	Notch1G$_{1740-1743}$
extinction coefficient ε_{214} [$M^{-1}cm^{-1}$]	60119	60171	60075
absorbance A_{214}	0.08	0.14	0.14
concentration [µM]	13.4	23.3	23.3
secondary structure content [%]			
helix	42.1	48.4	18.4
distorted helix	21.0	22.1	11.4
β-sheet	0.2	0	17.3
turn	4	0	13.7
others	32.7	29.5	39.2

All CD spectra showed a maximum at 192 nm and two minima at 208 nm and 222 nm, so that all TMDs were predominantly α-helical, but significantly less pronounced in Notch1G$_{1740-1743}$. The helical content in the glycine mutant was only 18 % with a high portion of other secondary structure elements, indicating a distortion of the regular α-helix. In contrast to Notch1G$_{1740-1743}$ the Notch1$_{1734-1757}$ WT and leucine mutant were more helical, where Notch1L$_{1740-1743}$ with a helical content of 48 % appeared more stable than the WT with 42 %.

4.2.2 Chemical Shifts

The ^{1}H-^{1}H NOESY and TOCSY as well as natural abundance ^{1}H-^{13}C and ^{1}H-^{15}N HSQC spectra of both mutants (Figure 4.10) are comparable to the Notch1 WT in terms of resolution and dispersion, with Notch1L$_{1740-1743}$ TMD appeared to have a broader chemical shift distribution than the glycine mutant, suggesting a less structured Notch1G$_{1740-1743}$. All amino acids of the investigated Notch1L$_{1740-1743}$ and Notch1G$_{1740-1743}$ TMDs were identified and ^{1}H, ^{13}C and ^{15}N resonances assigned.

The secondary structure prediction by CSI 3.0 (Hafsa et al. 2015) indicated an entire α-helical TMD from residue Leu$_{1734}$ to Ser$_{1758}$ in Notch1L$_{1740-1743}$ (Figure 4.11 (d)). Whereas the α-helix of Notch1G$_{1740-1743}$ TMD was interrupted by a random coil segment, a part with no secondary structure, reaching from Gly$_{1740}$ to Phe$_{1748}$ and a short random coil segment around Gly$_{1751}$. The destabilization of the Notch1G$_{1740-1743}$ TMD helix was also evident in the helix probability and order parameter S^2 estimated with TALOS+ (Shen et al. 2009) (Figure 4.11 (c)), except here the collapse of the α-helix started a few residue further N-terminal from Tyr$_{1738}$ to Phe$_{1744}$.

In addition, the glycine mutant showed, particular in the helical content a destabilized helix around Gly$_{1753}$/Val$_{1754}$ at the S3 cleavage site. In this region, the otherwise stable Notch1L$_{1740-1743}$ TMD was distorted too.

Replacing the tetra alanine motif with leucine residues led to an overall stabilization of the TMD helix. The Notch1L$_{1740-1743}$ mutant comprised an entire helical TMD ranging from residue Leu$_{1734}$ to Ser$_{1757}$ just like the Notch1$_{1734-1757}$ WT. The consecutive NOE contacts (Figure 4.11 (b)) showed a more stable TM-N. A destabilization of the α-helix around Leu$_{1741}$/Leu$_{1742}$ the S4 cleavage site was indicated by the presence of dαN(i,i+2) NOE contacts and a moderately reduced order parameter S^2. The TM-C helix seemed to have a more labile S3 cleavage site at Gly$_{1753}$/Val$_{1754}$ compared to the Notch1$_{1734-1757}$ WT, due to the lack of dαN(i, i+3) NOE contacts and thus a lower helical content. The beginning of the C-terminal helix appeared marginally more helical because of several helix-typical NOE contacts.

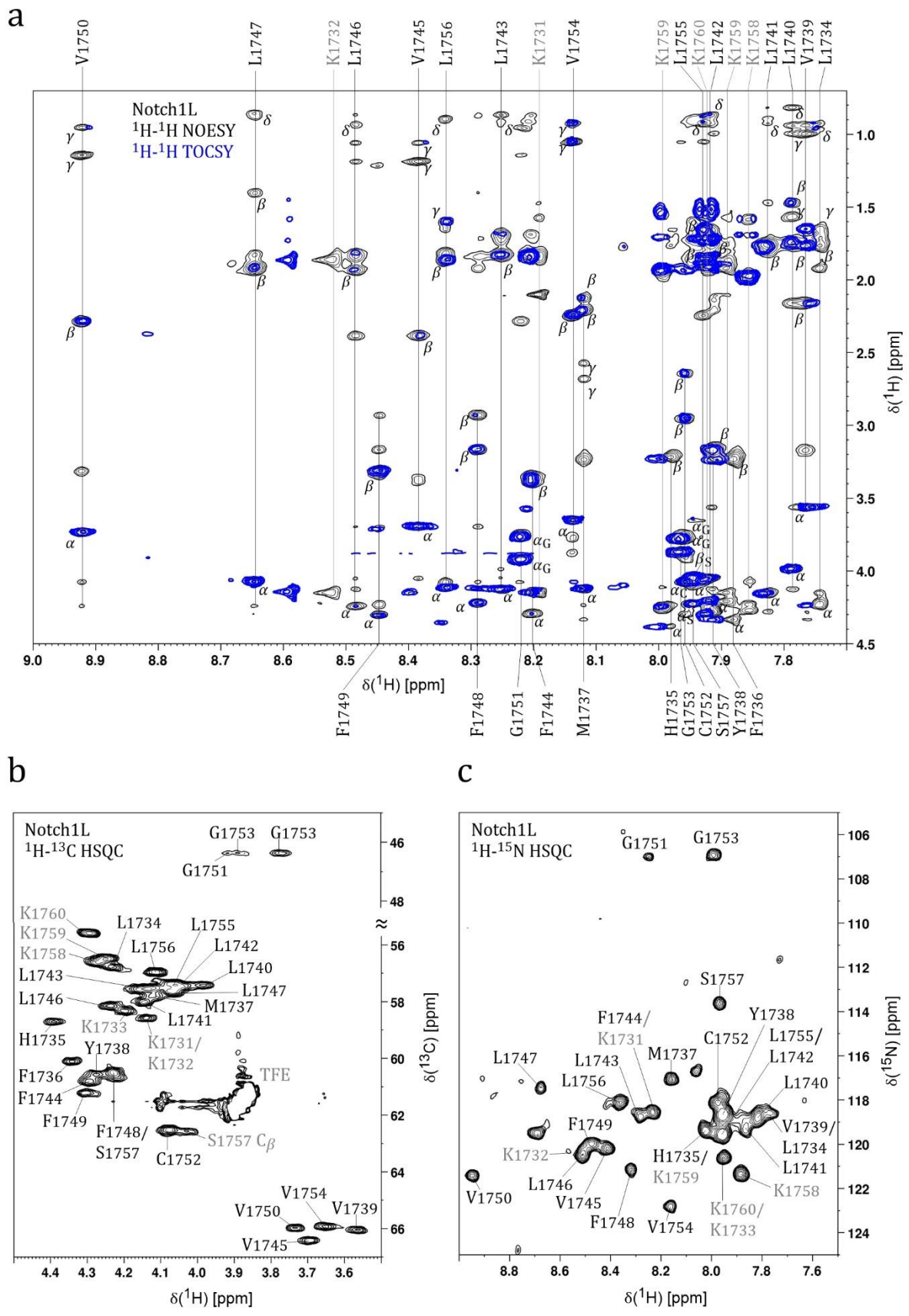
a
Notch1L
^{1}H-^{1}H NOESY
^{1}H-^{1}H TOCSY
δ(^{1}H) [ppm]
b
Notch1L
^{1}H-^{13}C HSQC
δ(^{1}H) [ppm]
δ(^{13}C) [ppm]
TFE
c
Notch1L
^{1}H-^{15}N HSQC
δ(^{1}H) [ppm]
δ(^{15}N) [ppm]

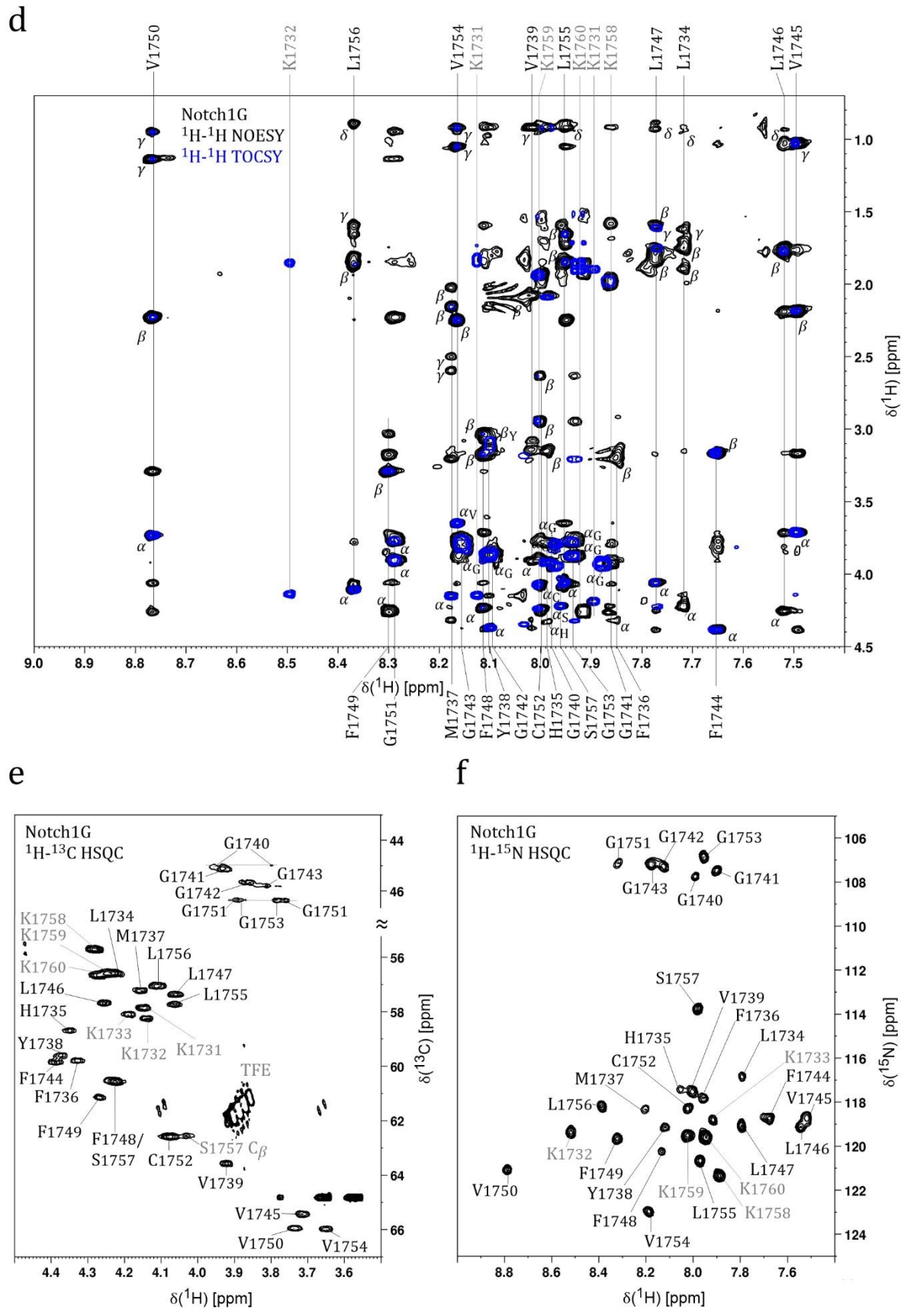
d
Notch1G
^{1}H-^{1}H NOESY
^{1}H-^{1}H TOCSY
δ(^{1}H) [ppm]
e
Notch1G
^{1}H-^{13}C HSQC
δ(^{13}C) [ppm]
δ(^{1}H) [ppm]
f
Notch1G
^{1}H-^{15}N HSQC
δ(^{15}N) [ppm]
δ(^{1}H) [ppm]

Figure 4.10 Notch1$L_{1740-1743}$ and Notch1$G_{1740-1743}$ NMR spectra. Figure caption refers to figures on the previous pages. Shown are Notch1$L_{1740-1743}$ (a) and Notch1$G_{1740-1743}$ (d) ^{1}H-^{1}H NOESY and ^{1}H-^{1}H TOCSY spectra of the H_N-H_α region. The spin systems of the individual residues are indicated by vertical lines. The respective protons are identified by small Greek letters and supplemented by the corresponding amino acid in the range of low spectral dispersity. Residues marked in grey are not part of the native sequence. The ^{1}H-^{13}C HSQC spectrum of Notch1$L_{1740-1743}$ (b) and Notch1$G_{1740-1743}$ (e) shows the H_α-C_α region. The ^{1}H-^{15}N HSQC spectrum of Notch1$L_{1740-1743}$ (c) and Notch1$G_{1740-1743}$ (f) shows the N_H-H_α region. The respective residues are marked.

The introduction of glycines at residue 1740 to 1743 resulted in an undefined region around the mutations and a collapse of the helical structure, which can be determined by the secondary chemical shifts (Figure 4.11 (a)) and the absence of the helix-typical NOE contacts. The findings of the secondary chemical shift and the NOE contacts were supported by the significant decline of the helical content and the order parameter (Figure 4.11 (c)). This gap in the helix divided the TMD in two separate helical segments. The TM-N helix ranging from residue Leu_{1734} to Gly_{1740} was compared to the Notch$1_{1734-1757}$ WT significantly less helical comprising only dαβ(i, i+3) NOE contacts. The TM-C helix was comparable to the Notch$1_{1734-1757}$ WT, in which the presence of dαN(i, i+2) and the absence of dαN(i, i+4) NOE contacts together with the drop in the helical content, indicated a destabilization of the helix around S3 cleavage site.

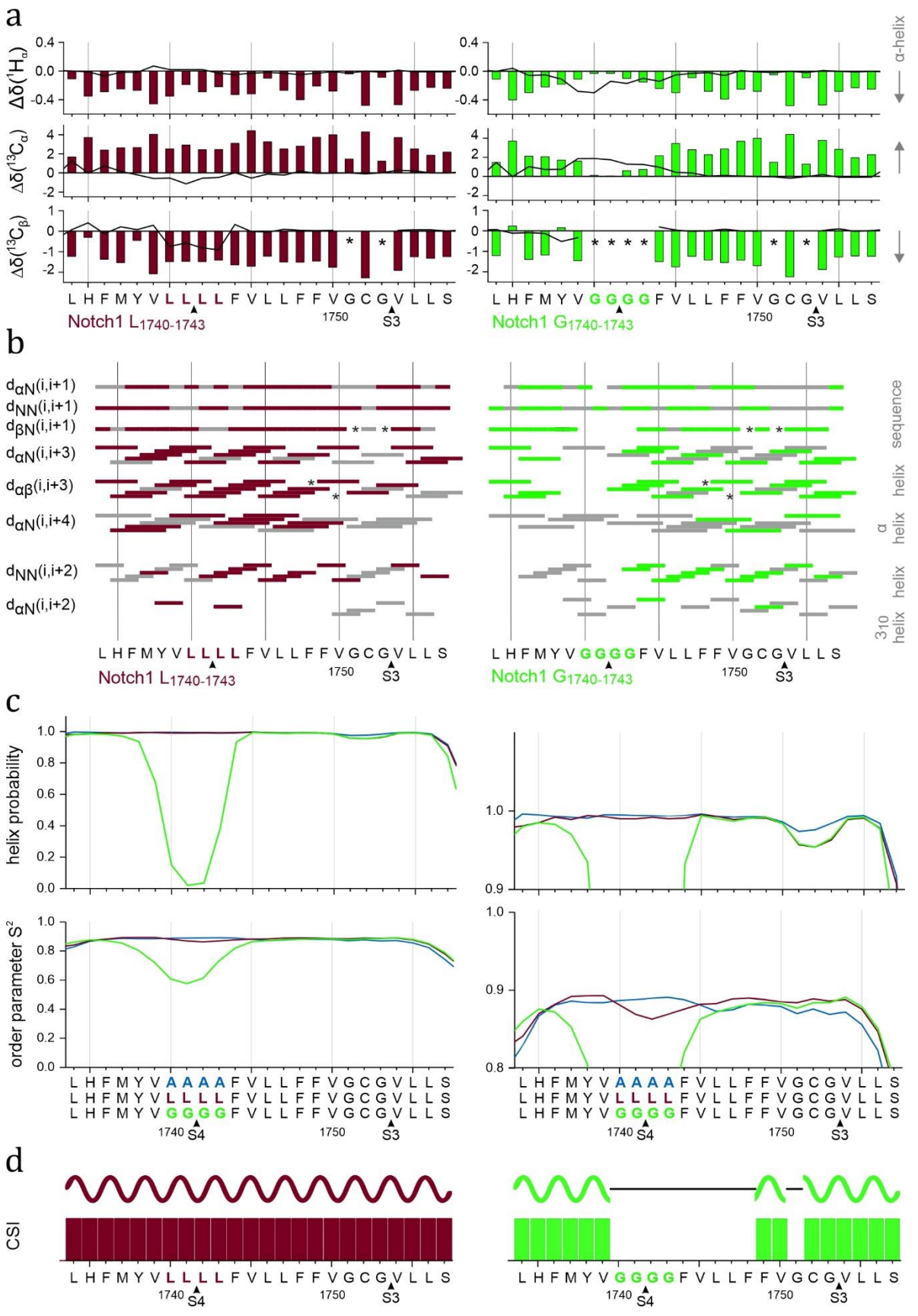
a
Δδ(¹Hα)
Δδ(¹³Cα)
Δδ(¹³Cβ)
α-helix
L H F M Y V L L L L F V L L F F V G C G V L L S
Notch1 L1740-1743
1750
S3
L H F M Y V G G G G F V L L F F V G C G V L L S
Notch1 G1740-1743
b
dαN(i,i+1)
dNN(i,i+1)
dβN(i,i+1)
dαN(i,i+3)
dαβ(i,i+3)
dαN(i,i+4)
dNN(i,i+2)
dαN(i,i+2)
sequence
α helix
3₁₀ helix
c
helix probability
order parameter S²
L H F M Y V A A A A F V L L F F V G C G V L L S
L H F M Y V L L L L F V L L F F V G C G V L L S
L H F M Y V G G G G F V L L F F V G C G V L L S
1740 S4
d
CSI

Figure 4.11 Secondary structure characteristics of Notch1L$_{1740-1743}$ and Notch1G$_{1740-1743}$ TMD determined by NMR. Figure caption refers to the figure on the previous page. Secondary chemical shifts (a), the difference between random coil and observed values of Notch1L$_{1740-1743}$ TMD (red) and Notch1G$_{1740-1743}$ TMD (green). Positive $^{13}C_{\alpha}$ and negative $^{1}H_{\alpha}$, $^{13}C_{\beta}$ secondary chemical shifts indicate α-helices. The black lines show the difference between secondary chemical shifts of the mutants and Notch1$_{1734-1757}$ WT, for example in case of C_{α}, negative values of these differences indicate al less helical Notch1$_{1734-1757}$ WT TMD. Characteristic NOE contacts (b), where coloured boxes indicate unambiguous NOE contacts and grey boxes show NOE contacts that could not be assigned unambiguously due to signal overlap. Asterisks mark glycines without H_{β} atoms. Helix probability and theoretical order parameter S^2 (c) were predicted with TALOS+ (Shen et al. 2009) on the basis of chemical shifts. An $S^2 = 1$ indicates complete restriction of the internal NH bond vector motion. The right panels are an enlarged part of the left panels. In the CSI 3.0 output (Hafsa et al. 2015) (e) α-helical regions are represented by the coloured bars and the wavy line. Areas with no secondary structure are represented by the black line.

4.2.3 3D Structures

The 3D structure of the mutants, calculated analogue to the Notch1$_{1734-1757}$ WT, revealed a less pronounced bend around Leu$_{1746}$/Leu$_{1747}$ in the entire α-helical Notch1L$_{1740-1743}$ TMD (Figure 4.12 (a)). The straighter structure originated from the greater spatial demand of the bulky leucine side chains. To compare the orientation of the individual structures within the Notch1L$_{1740-1743}$ bundles to Notch1$_{1734-1757}$ WT, first the average Notch1L$_{1740-1743}$ structure was aligned with the average Notch1$_{1734-1757}$ WT TM-N residues Leu$_{1734}$ to Leu$_{1747}$. Then the 40 lowest energy Notch1L$_{1740-1743}$ NMR models were superimposed onto its average Notch1L$_{1740-1743}$ structure along the TM-N Leu$_{1734}$ to Leu$_{1747}$ (Figure 4.12 (b)).

Like in the Notch1$_{1734-1757}$ WT bundles, the orientation of the N-terminal helix with respect to the C-terminal part of Notch1L$_{1740-1743}$ bundles was not arbitrary but limited to a specific conical region. If the N-terminus of this bundles pointed out of the plane of the figure, as in Figure 4.12 (b) left-hand representation, and only the Cα atoms of the residue Leu$_{1756}$ at the C-terminus were represented as dots (Figure 4.12 (e)),thus the distribution of the structural bundle could be better compared to the Notch1$_{1734-1757}$ WT. The direction of the bending in the Notch1L$_{1740-1743}$ bundles, indicated by the dotted line in Figure 4.12 (e), was shifted about 60° towards residues Val$_{1750}$/Gly$_{1753}$ (Figure 4.12 (f)).

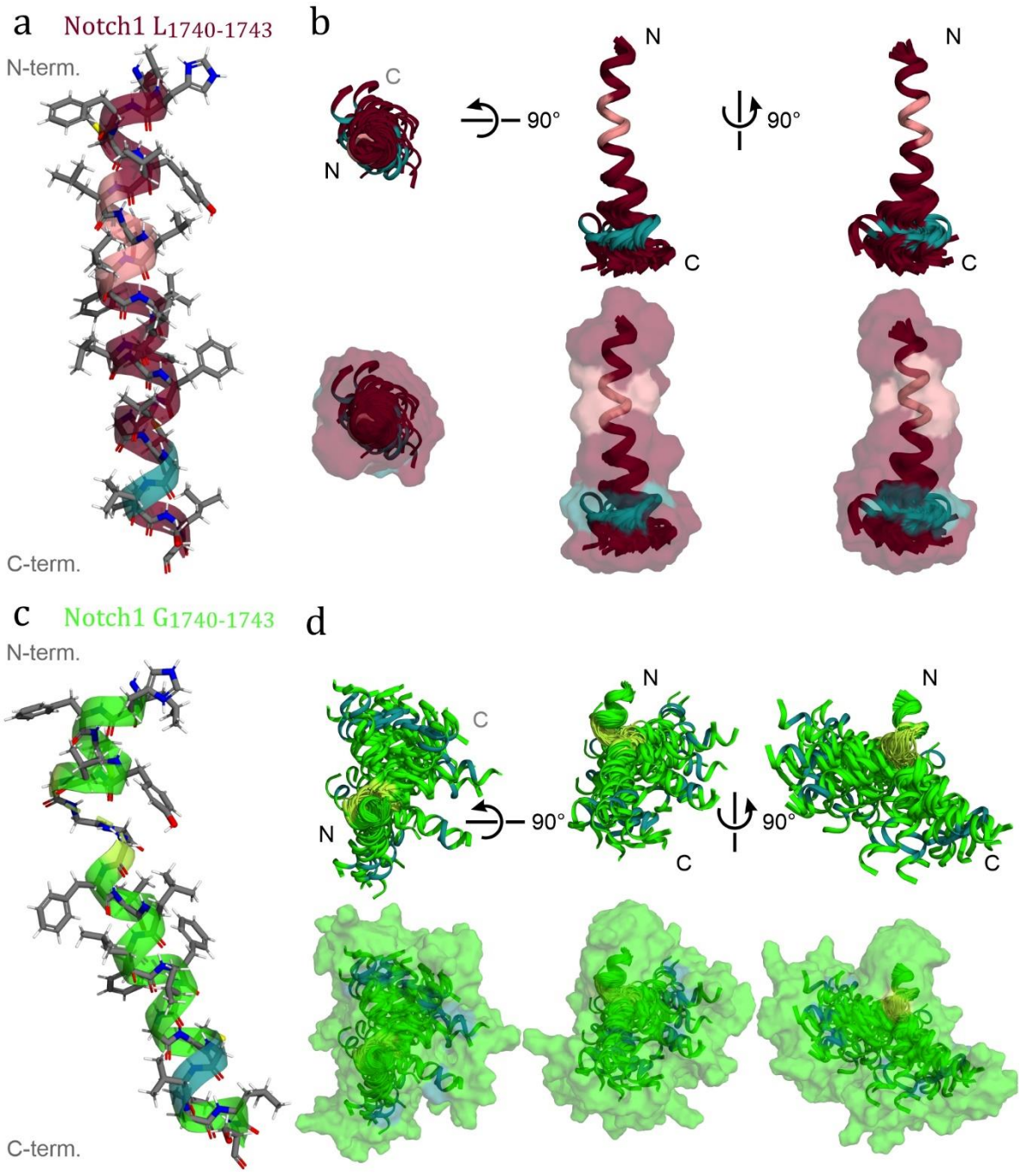
a
Notch1 L1740-1743
N-term.
C-term.
b
C
N
90°
90°
N
C
c
Notch1 G1740-1743
N-term.
C-term.
d
C
N
90°
90°
N
C
e
Leu1756 Cα
f
Notch1 WT
Notch1L1740-1743
Notch1G1740-1743
F1748
A/L/G1741
L1755
M1737
C1752
F1744
V1745
G1751
Y1738
A/L/G1740
F1749
L1747
A/L/G1742
V1754
F1736
G1753
A/L/G1743
L1746
V1750
V1739
convex
concave

Figure 4.12 3D structures of Notch1L$_{1740-1743}$ TMD and Notch1G$_{1740-1743}$ TMD. Figure caption refers to the figure on the previous page. Average 3Dsturcture of Notch1L$_{1740-1743}$ TMD (a) and Notch1G$_{1740-1743}$ TMD (c). Structural bundles of Notch1L$_{1740-1743}$ TMD (b) superimposed on residues Leu$_{1734}$-Leu$_{1747}$ and structural bundles of Notch1G$_{1740-1743}$ TMD (d) aligned on residues Leu$_{1734}$-Val$_{1745}$. Top and side view of the 40 lowest energy NMR structures out of 400 are shown. Region with mutated residues are highlighted in the corresponding light shade. The S3 cleavage site Gly$_{1753}$/Val$_{1754}$ is represented in turquoise. The bundles of helix backbone structure are surrounded by transparent surfaces corresponding to the side chains. The spread of the structural bundles is shown (e) with the N-terminus pointing out of the plane of the figure. The dots correspond to Cα atoms of residue Leu$_{1756}$ in Notch1 WT (blue), Notch1L$_{1740-1743}$ (red) and Notch1G$_{1740-1743}$ (green). The direction of the bent in the bundles is indicated by dotted lines. In the helical wheel representation of residues Phe$_{1736}$ to Val$_{1754}$ (f) the locations of the concave and convex sides in the Notch1 WT 3D structure are indicated.

Due to the small glycine side chains significantly less NOE contacts could be identified, so that only few restraints for the structure calculation were generated and this part of the helix was structurally not defined. The break in the helical structure indicated in the section 4.2.2 was confirmed by the 3D structure, but here only limited to the mutated residues. Hence the Notch1G$_{1740-1743}$ TMD was divided by this unstructured part in two α-helical segments covering residues Leu$_{1734}$-Val$_{1739}$ and Phe$_{1744}$-Ser$_{1757}$ (Figure 4.12 (c)).

Because of the structurally undefined region in the Notch1G$_{1740-1743}$ TMD, the orientation of the TM-N with respect to the TM-C was less restricted and possessed a distinctly wider distribution of the possible orientations, when 40 of the lowest energy structures were aligned over the backbone atoms of the TM-N residues Leu$_{1734}$ to Val$_{1745}$ (Figure 4.12 (d)). To describe the possible orientations in comparison to the Notch1$_{1734-1757}$ WT, the average Notch1G$_{1740-1743}$ structure was superimposed along the entire TMD to the Notch1$_{1734-1757}$ WT structure and the remaining Notch1G$_{1740-1743}$ NMR models were aligned over the TM-N of its average structure. In this representation the TM-N helix was bend towards residue Val$_{1739}$. The TM-C was significantly deflected towards Val$_{1750}$ and in addition to the opposite side towards Phe$_{1748}$/Cys$_{1752}$ (Figure 4.12 (e), (f)). Despite the remarkable wider distribution of the possible bundle orientations, the TM-Cs were not completely arbitrary with respect to the TM-N helix and showed preferred directions.

4.2.4 Hydrogen Deuterium Exchange

The hydrogen deuterium exchange of the mutants was measured analogue to Notch1$_{1734-1757}$ WT (section 4.1.4). To access the main part of the exchangeable protons, Notch1L$_{1740-1743}$ TMD was examined at pD 4.5 and pD 5.5 and Notch1G$_{1740-1743}$ TMD at pD 3.5 and pD 4.5. The experimental exchange rate k_{ex} was scaled to pD 5 as $k_{ex,s}$. The flexibility profiles of the mutants compared to Notch1$_{1734-1757}$ WT (Figure 4.13) revealed a more stable Notch1L$_{1740-1743}$ TMD and a less stable Notch1G$_{1740-1743}$ TMD, especially in the N-terminal part.

No evaluable signals from the lysine triads, as well as for Leu$_{1734}$, Tyr$_{1738}$ and Ser$_{1757}$ at the N- and C-termini and Gly$_{1753}$ at the S3 cleavage site in Notch1L$_{1740-1743}$ TMD could be detected. The identified rate constants ranged from 0.03 min^{-1} (one in 30 minutes) up to 0.000015 min^{-1} (one in 2 months). Residues Tyr$_{1738}$ up to Phe$_{1749}$ were significantly stabilized in Notch1L$_{1740-1743}$ TMD compared to Notch1$_{1734-1757}$ WT. The smaller exchange rate constants indicated a slower exchange of the hydrogen atoms with the solvent and thus the presence of stable hydrogen bonds in which the amide protons participated.

The most stable region of the leucine mutant was located in the middle of the helix around residues Val$_{1745}$/Leu$_{1746}$/Leu$_{1747}$. Like in Notch1$_{1734-1757}$ WT the flexibility increased towards the termini and a destabilization of the helix was evident around the S3 cleavage site. The C-terminal end of Notch1L$_{1740-1743}$, residues Val$_{1750}$ to Ser$_{1757}$, was comparable to Notch1$_{1734-1757}$ WT in terms of stability and flexibility.

Despite the measurement at pD 3.5, which slowed down the exchange, not all signals of the residues at the beginning of TM-N in Notch1G$_{1740-1743}$ TMD could be detected. The determined exchange rate constants lay between 0.2 min^{-1} (one in 5 minutes) and 0.003 min^{-1} (one in 5 hours). In contrast to Notch1L$_{1740-1743}$ TMD, residues from Val$_{1739}$ up to Val$_{1750}$ of Notch1G$_{1740-1743}$ were significantly destabilized compared to the Notch1$_{1734-1757}$ WT (Figure 4.13). The TMD C-terminal from Val$_{1750}$/Gly$_{1751}$ had the same flexibility profiles in both mutants and the Notch1$_{1734-1757}$ WT, so that due to the substitution of the 4 glycines the TM-N in Notch1G$_{1740-1743}$ was conformational more flexible than the TM-C.

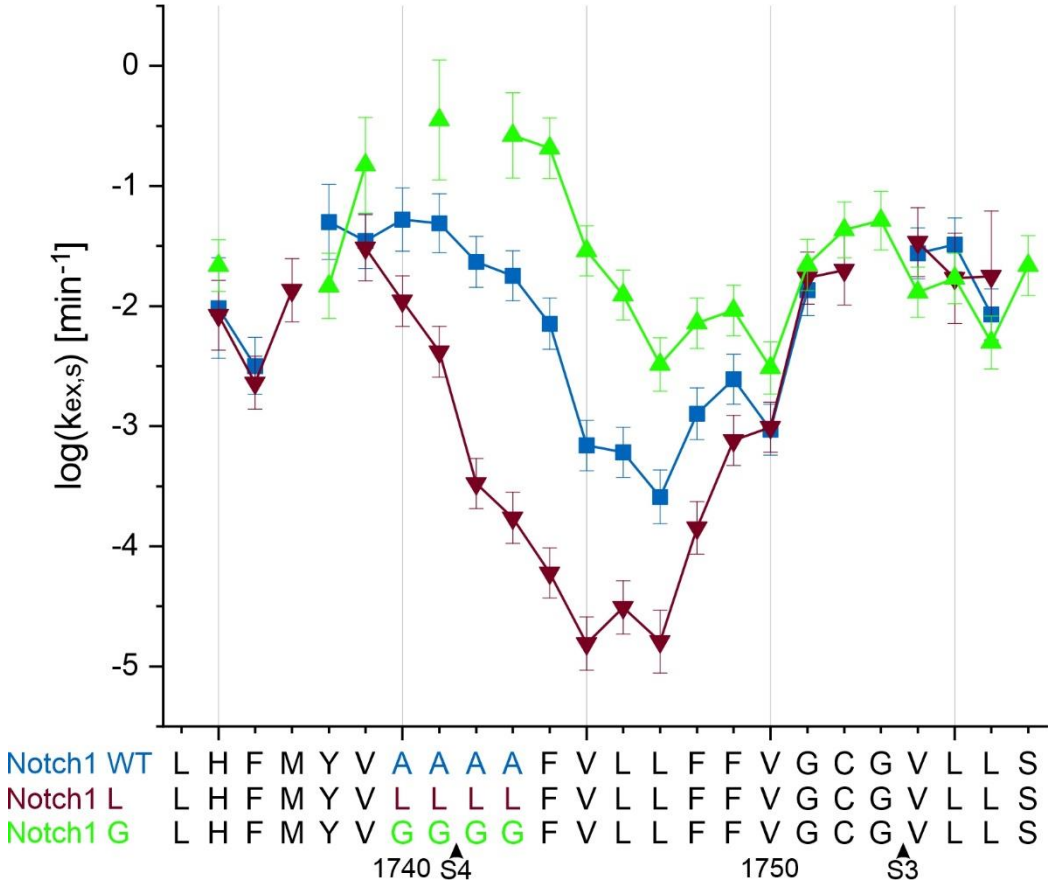

Figure 4.13 Residue-specific HDX rate constants of Notch1L$_{1740-1743}$ TMD and Notch1G$_{1740-1743}$ TMD. Exchange rates of Notch1$_{1734-1757}$ WT (blue), Notch1L$_{1740-1743}$ (red) and Notch1G$_{1740-1743}$ (green) residues were determined in d_3-TFE/D_2O at different pD values (3.5, 4.5, 5.5 and 6.5) and scaled to pD 5. The error bars account for the error in the fitted parameter k_{ex} and the inaccuracy of the pH electrode. Most stable regions of Notch1$_{1734-1757}$ WT are located around Leu$_{1746}$/Leu$_{1747}$.

4.3 Notch3$_{1642-1665}$ TMD

Besides Notch1$_{1734-1757}$ WT and the flexibility modulated mutants, a homologue of the Notch family Notch3$_{1642-1665}$ TMD was investigated. To examine the influence of a homologue sequence on the stability, dynamics and orientation of the 3D structure, the unlabelled Notch3$_{1642-1665}$ TMD was analysed under the same conditions as Notch1$_{1734-1757}$ WT.

4.3.1 Sequence

The human Notch3 protein (Q9UM47) consists of 2321 amino acids, where the TMD was predicted by DeepTMHMM (Hallgren et al. 2022) between residues 1643 and 1663. The investigated sequence should include residues with a specific biological function for stability and membrane insertion, like proline and charged residues at the termini. For enhanced solubility of the highly hydrophobic Notch3 TMD lysine triplets were added to the N- and C-terminal ends, so the analysed peptide was Notch3$_{1642-1665}$ TMD (Figure 4.14).

Figure 4.14 Notch3$_{1642-1665}$ sequence. Native Notch3 sequence of residue 1635-1670 shown in top line, TMD region predicted by DeepTMHMM is underlined. Investigated Notch3$_{1642-1665}$ TMD sequence shown in bold in lower line, with N- and C-terminal appended lysine triplets for enhanced solubility.

The human Notch family comprises of 4 members, who emerged from each other through gene duplication events (Theodosiou et al. 2009). Despite the high conservation of the Notch proteins, resulting from the evolutionary development, the TMD in Notch3 as well as in Notch1 is quite variable. The amino acid conservation of Notch3$_{1642-1665}$ TMD across a wide range of species was visualized by blasting the Notch3 sequence of residues 1613-1713 against UniRef90 and analysing the pairwise alignments with a custom python script written by Martin Ortner (TU Munich) (Figure 4.15 (a)).

Comparable to the glycine position in Notch1 TMD the Gly$_{1651}$ in Notch3, located at the S3 cleavage site, was one of the most conserved residues and appears critical for the accessibility of the cleavable peptide bonds. As Ser$_{1757}$ in Notch1, Ala$_{1665}$, a further small amino acid at the end of the TM-C, was highly conserved in Notch3. At the N-terminal end of the TMD both preserved Pro$_{1642}$ and Pro$_{1645}$ might fix the appropriate orientation of the TMD due to their conformational rigid, cyclic side chain. Interestingly, in the S4 cleavage site of Notch3 TMD at the AGA motif, or more exactly VAGA, small residues were predominantly present, reminiscent of the alanine tetrad in Notch1 TMD. Here too, the last two positions of these tetrad were more conserved, assuming an important role for the overall flexibility of the Notch TMD. Both Leu$_{1654}$ and Leu$_{1655}$ in the middle of the TMD

did not only show a high level of evolutionary conservation within the Notch3 protein, but also at the corresponding position in Notch1 and were therefore crucial for the stability of the Notch TMD in general. While the TM-C within Notch3 TMD seemed to be more conserved than the TM-N, the whole Notch3 TMD sequence seemed slightly more preserved than the Notch1 TMD.

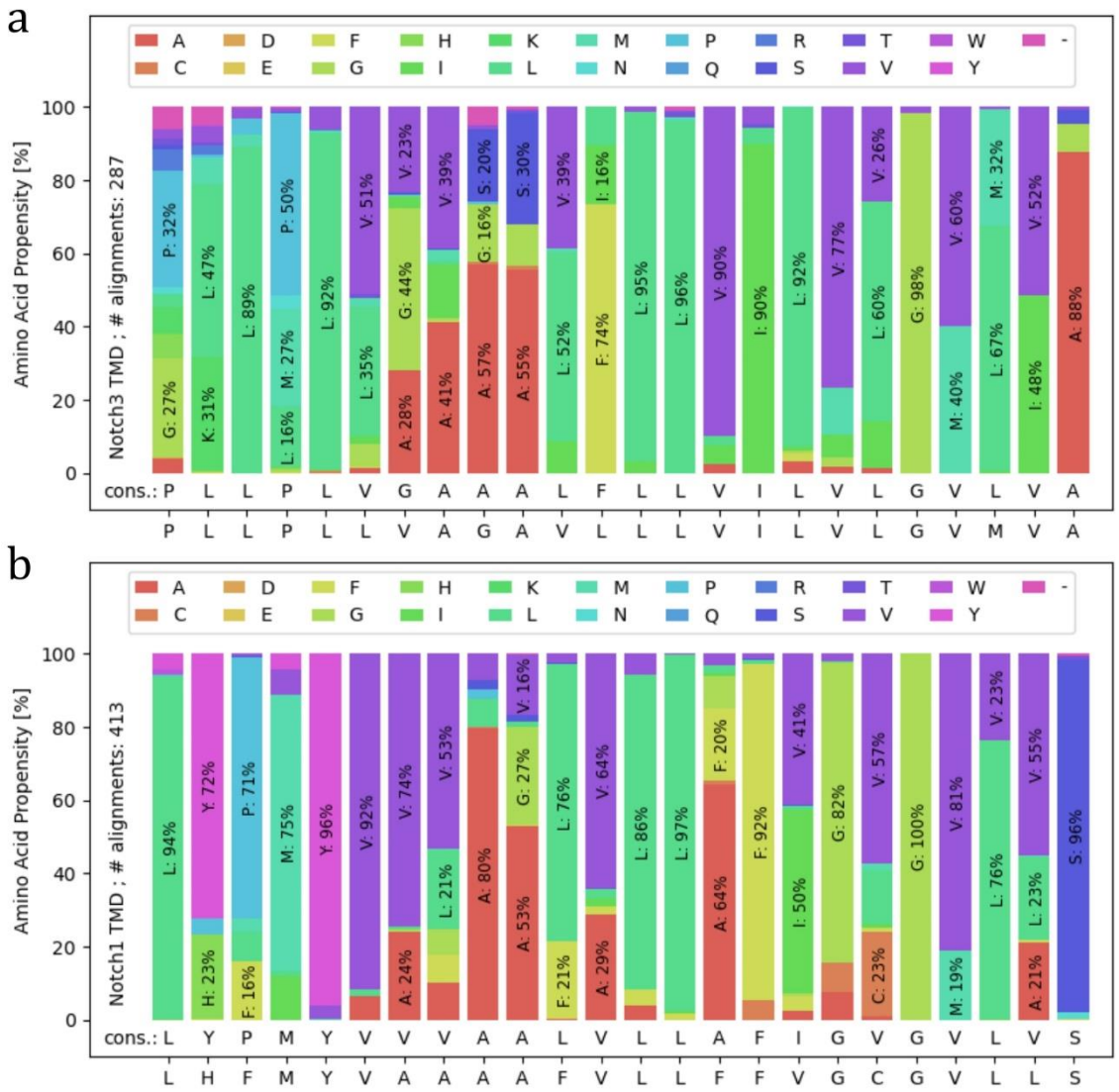

Figure 4.15 Sequence alignment of Notch3 TMD. Notch3 TMD (a) sequence blasted against UniRef90. Evolutionary conservation of each residue was calculated from pairwise alignment. For better comparison of Notch3 TMD with the WT, the sequence alignment of Notch1$_{1734-1757}$ WT TMD (b) is also shown.

4.3.2 Circular Dichroism

The first information regarding the secondary structure of Notch3$_{1642-1665}$ TMD was obtained from CD measurements, which were examined in TFE/H_2O (80:20, v:v) at pH 6.5 and 300 K. The concentration of Notch3$_{1642-1665}$ (Table 4.2), its mean residue ellipticity and the secondary structure content were determined by the BeStSel web server (https://bestsel.elte.hu) (Kuipers und Gruppen 2007; Micsonai et al. 2018) analogue to Notch1$_{1734-1757}$ WT (section 4.2.1).

Table 4.2 Secondary structure content and concentration of Notch1$_{1734-1757}$ WT and Notch3$_{1642-1665}$ TMD. Secondary structure content of Notch1$_{1734-1757}$ WT and Notch3$_{1642-1665}$ TMD investigated from CD spectra with BeStSel and concentration determination for mean residue ellipticity conversion.

	Notch1 WT	Notch3$_{1642-1665}$
extinction coefficient ε_{214} [$M^{-1}cm^{-1}$]	60119	34189
absorbance A_{214}	0.08	0.06
concentration [µM]	13.4	17.9
secondary structure content [%]		
helix	42.1	39.6
distorted helix	21.0	15.8
β-sheet	0.2	4
turn	4	8.9
others	32.7	31.7

The Notch3$_{1642-1665}$ TMD was predominantly α-helical, due to the typical maximum at 192 nm and two minima at 208 nm and 222 nm in the CD spectrum (Figure 4.16 (a)). Compared to Notch1$_{1734-1757}$ WT the maximum at 192 nm was less pronounced, suggesting a slightly less helical TMD in Notch3$_{1642-1665}$. This was also confirmed by the estimated secondary structure content, with a higher percentage of β-sheets and turns.

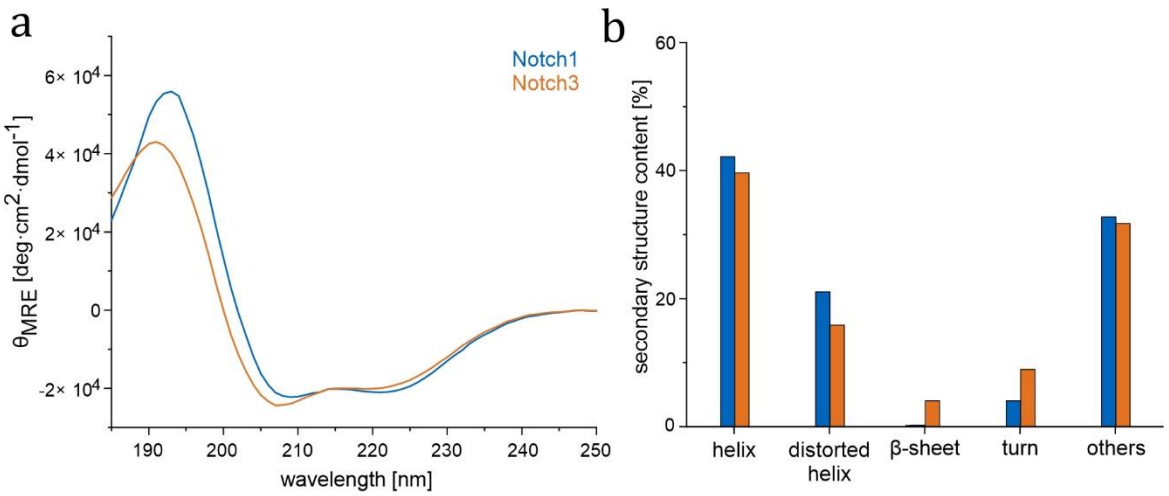

Figure 4.16 CD spectra of Notch1$_{1734-1757}$ WT and Notch3$_{1642-1665}$ TMD. CD spectra (a) of Notch1$_{1734-1757}$ WT (blue) and Notch3$_{1642-1665}$ (orange) in TFE/H_2O (80:20, v:v) at pH 6.5 and 300 K. The secondary structure content (b) indicates a helicity of 42 % in Notch1$_{1734-1757}$ WT, and 40 % in Notch3$_{1642-1665}$. CD spectra were analysed and secondary structure content estimated with BeStSel.

4.3.3 Chemical Shifts

The spectral resolution and dispersion in the Notch3$_{1642-1665}$ ^{1}H-^{1}H NOESY and TOCSY as well as natural abundance ^{1}H-^{13}C and ^{1}H-^{15}N HSQC spectra (Figure 4.17) were comparable to Notch1$_{1734-1757}$ WT, indicating a folded TMD. The amino acids of the Notch3$_{1642-1665}$ TMD were all identified and ^{1}H, ^{13}C and ^{15}N resonances assigned.

The TMD of Notch3$_{1642-1665}$ was determined α-helical by CSI 3.0 from Leu$_{1644}$ to Ala$_{1665}$, while the first two residues remained unstructured (Figure 4.18 (e)). The unstructured beginning of the TM-N was confirmed by the helix probability (Figure 4.18 (c)) and order parameter S^2 (Figure 4.18 (d)) estimated with TALOS+ (Shen et al. 2009), where the stable helix started after the second Pro$_{1645}$. Also secondary chemical shifts (Figure 4.18 (a)) and consecutive NOE contacts (Figure 4.18 (b)) indicated an α-helical Notch3$_{1642-1665}$ TMD starting from residues Pro$_{1645}$/Leu$_{1646}$ to Ala$_{1665}$, which was one and a half turns shorter than Notch1$_{1734-1757}$ WT.

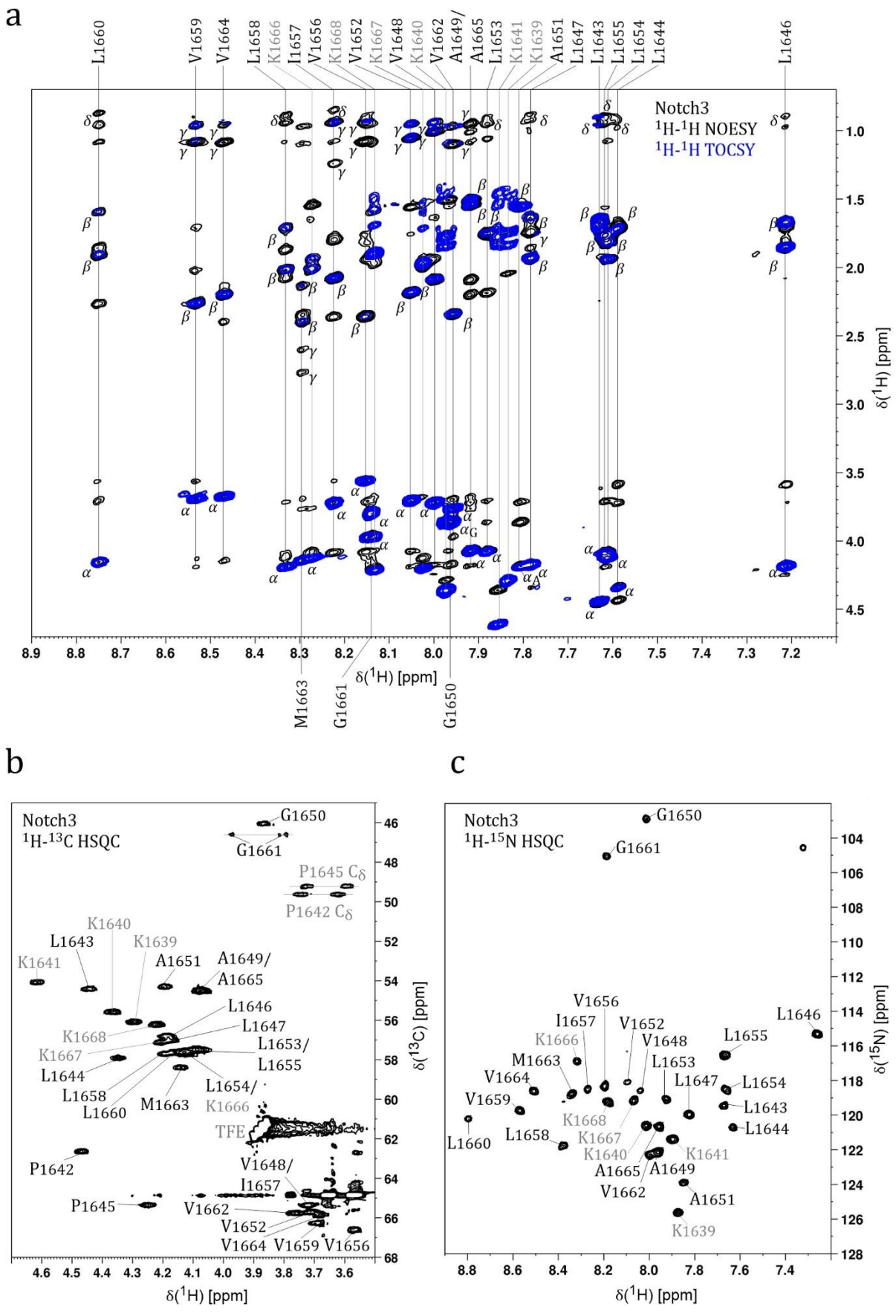
a
Notch3
1H-1H NOESY
1H-1H TOCSY
δ(1H) [ppm]
b
Notch3
1H-13C HSQC
δ(13C) [ppm]
δ(1H) [ppm]
c
Notch3
1H-15N HSQC
δ(15N) [ppm]
δ(1H) [ppm]

Figure 4.17 Notch3$_{1642-1665}$ NMR spectra. Figure caption refers to the figure on the previous page. Shown are Notch3$_{1642-1665}$ ^{1}H-^{1}H NOESY and ^{1}H-^{1}H TOCSY spectra (a) of the H_N-H_α region. The spin systems of the individual residues are indicated by vertical lines. The respective protons are identified by small Greek letters and supplemented by the corresponding amino acid in the range of low spectral dispersity. Residues marked in grey are not part of the native sequence. The ^{1}H-^{13}C HSQC spectrum (b) shows the H_α-C_α region. The ^{1}H-^{15}N HSQC spectrum (c) shows the N_H-H_α region. The respective residues are marked.

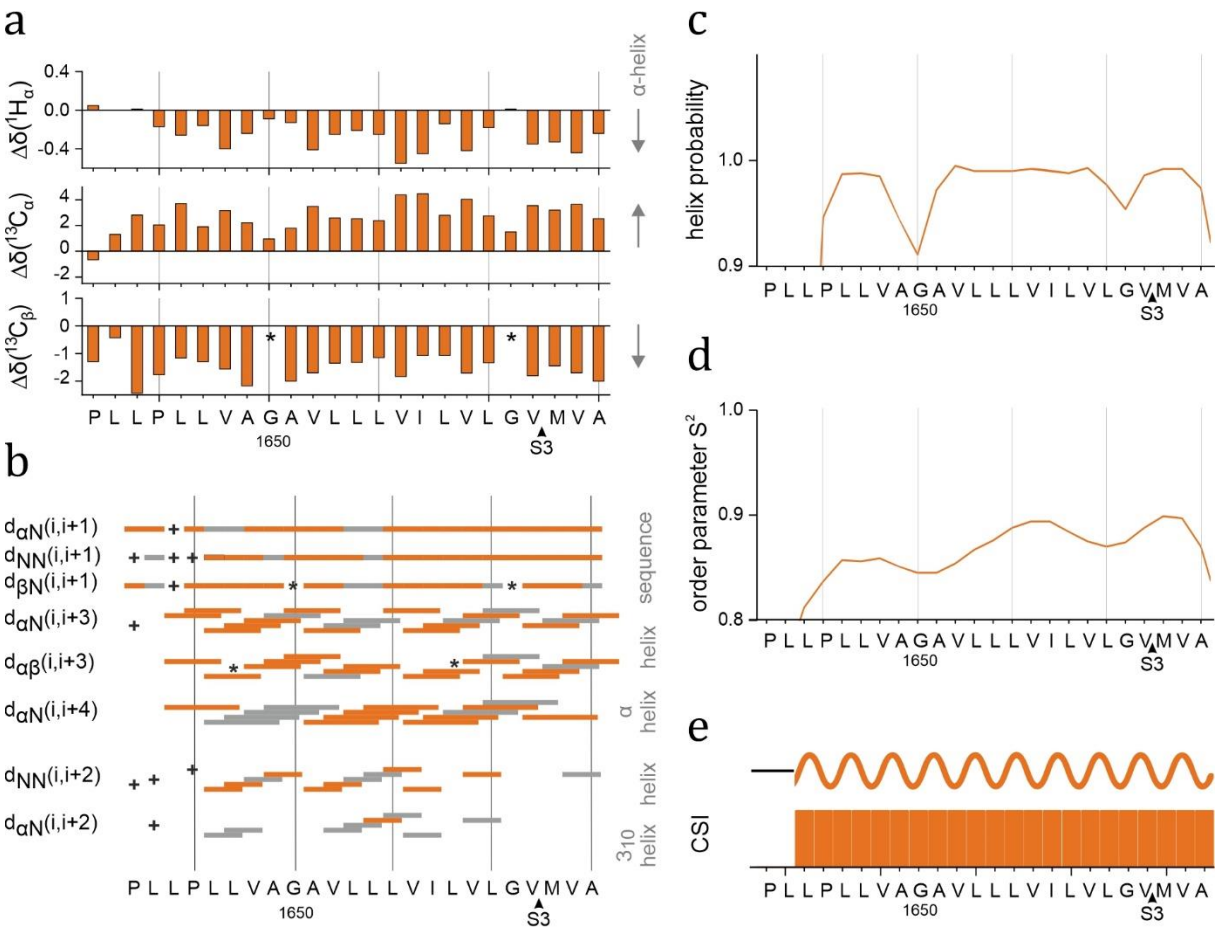

Figure 4.18 Secondary structure characteristics of Notch3$_{1642-1665}$ TMD determined by NMR. Secondary chemical shifts (a), the difference between random coil and observed values. Positive $^{13}C_\alpha$ and negative $^{1}H_\alpha$, $^{13}C_\beta$ secondary chemical shifts indicate α-helices. Characteristic NOE contacts (b), where orange boxes indicate unambiguous NOE contacts and grey boxes show NOE contacts that could not be assigned unambiguously due to signal overlap. Asterisks mark glycines without H_β atoms and plus mark prolines without amid protons. Helix probability (c) and theoretical order parameter S^2 (d) were predicted with TALOS+ (Shen et al. 2009) on the basis of chemical shifts. An $S^2 = 1$ indicates complete restriction of the internal NH bond vector motion. In the CSI 3.0 output (e) α-helical regions are represented by the orange bars and the wavy line. Areas with no secondary structure are represented by the black line.

The destabilization of the S3 cleavage site Val$_{1662}$/Met$_{1663}$ and S4 cleavage sites Ala$_{1649}$/Gly$_{1650}$ could be clearly seen in the reduced values for the helix probability and the order parameter S^2 as well as by reduced secondary chemical shifts.

The TM-N ranging from residues Leu$_{1646}$ to Leu$_{1654}$ was less stable lacking the dαN(i, i+4) NOE contacts compared to the TM-C ranging from Val$_{1656}$ to Ala$_{1665}$ with its helix-typical NOE contacts. In addition, a more flexible TM-N compared to the TM-C was evident from the order parameter S^2.

4.3.4 3D Structure

The 3D structure of the Notch3$_{1642-1665}$ TMD was calculated analogue to Notch1$_{1734-1757}$ WT and presented from Leu$_{1644}$/Pro$_{1645}$ to Ala$_{1665}$ an α-helical TMD. Compared to the Notch1$_{1734-1757}$ WT, the helical part was shorter and the bend in the middle of the helix around residues Leu$_{1654}$/Leu$_{1655}$ less pronounced.

The higher proportion of bulky residues such as leucine or valine are more evenly distributed over the helix (Figure 4.19 (b)), resulting in a straighter structure compared to the Notch1$_{1734-1757}$ WT. Here the abundant aromatic residues tend to gather on one side of the helix, causing a more pronounced bending. Since both Gly$_{1650}$ and Gly$_{1661}$ were located on the same side of the TMD helix, their missing side chains enabled a slight bending of the helix. The slight bend in Notch3$_{1642-1665}$ TMD located residues Leu$_{1646}$, Gly$_{1650}$, Leu$_{1653}$ and Gly$_{1661}$ at the concave site and the residues Val$_{1648}$, Val$_{1652}$, Leu$_{1655}$ and Val$_{1659}$ at the convex side (Figure 4.19 (e)).

The orientation of the Notch3$_{1642-1665}$ structural bundles was compared to Notch1$_{1734-1757}$ WT by first aligning the average Notch3$_{1642-1665}$ NMR structure (Figure 4.19 (c)) with the backbone atoms of residues Leu$_{1644}$ to Ile$_{1657}$ along the average Notch1 WT structure and then superimposing the 40 lowest-energy NMR models of Notch3$_{1642-1665}$ TMD to its average structure along the TM-N residues Leu$_{1644}$ to Ile$_{1656}$. (Figure 4.19 (a)). The orientation of the TM-Ns in Notch3$_{1642-1665}$ bundles compared to the TM-Cs was also not arbitrary and the TM-C helices fanned out in a cone comparable to that of Notch1 WT. The spread of the C_α atoms of Val$_{1664}$, viewed from the N-terminus, corresponds to the distribution of the possible orientation of the Notch3$_{1642-1665}$ bundle (Figure 4.19 (d)). Compared to the Notch1 WT, the direction of the bending in Notch3$_{1642-1665}$ bundles was rotated about 90°.

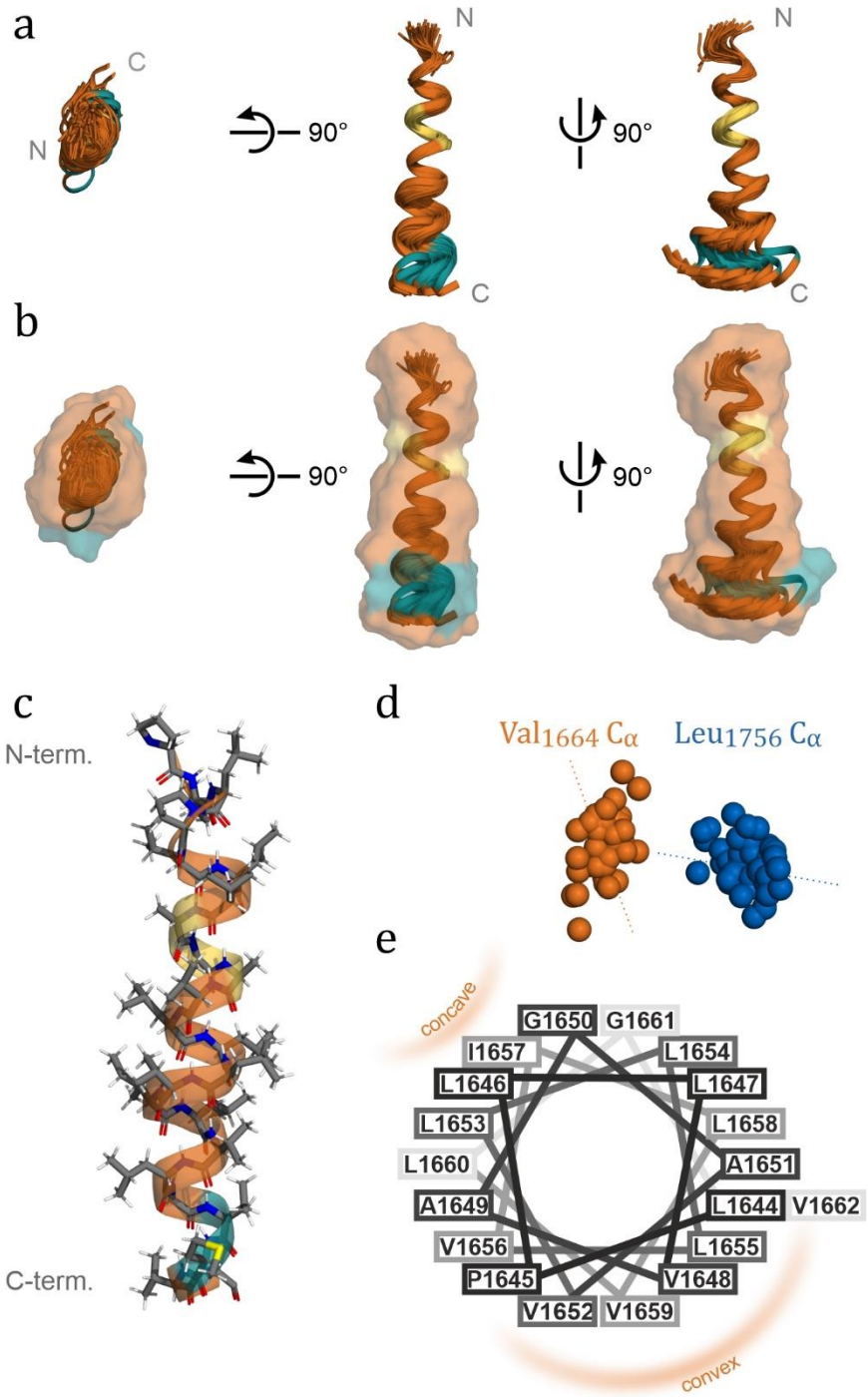

Figure 4.19 3D structure of Notch3$_{1642-1665}$ TMD. Structural bundles (a) superimposed on residues Leu$_{1644}$-Ile$_{1657}$. Top and side view of the 40 lowest energy NMR structures out of 400 are shown. Region with four alanine residues are highlighted in light orange. The S3 cleavage site Val$_{1662}$/Met$_{1663}$ is represented in turquoise. The bundles of helix backbone structure are surrounded by transparent surfaces corresponding to the side chains (b). Average 3D structure (c). The spread of the structural bundles is shown (d) with the N-terminus pointing out of the plane of the figure. The dots correspond to C$_\alpha$ atoms of residue Val$_{1664}$ in Notch3$_{1642-1665}$ (orange) and Leu$_{1756}$ in Notch1 WT (blue). The direction of the bent in the bundles is indicated by dotted

lines. In the helical wheel representation (e) the locations of the concave and convex sides of residues Leu$_{1644}$-Val$_{1662}$ are indicated.

4.3.5 Hydrogen Deuterium Exchange

HDX of Notch3$_{1642-1665}$ TMD was measured analogue to Notch1 WT (section 4.1.4). The ^{1}H-^{1}H TOCSY spectra were acquired at pD 3.5, 4.5, 5.5 and pD 6.5 to cover a large time window of rate constants and to capture most of the exchangeable protons. The experimental exchange rate k_{ex}, determined at different pD values, was scaled to pD 5 as $k_{ex,s}$.

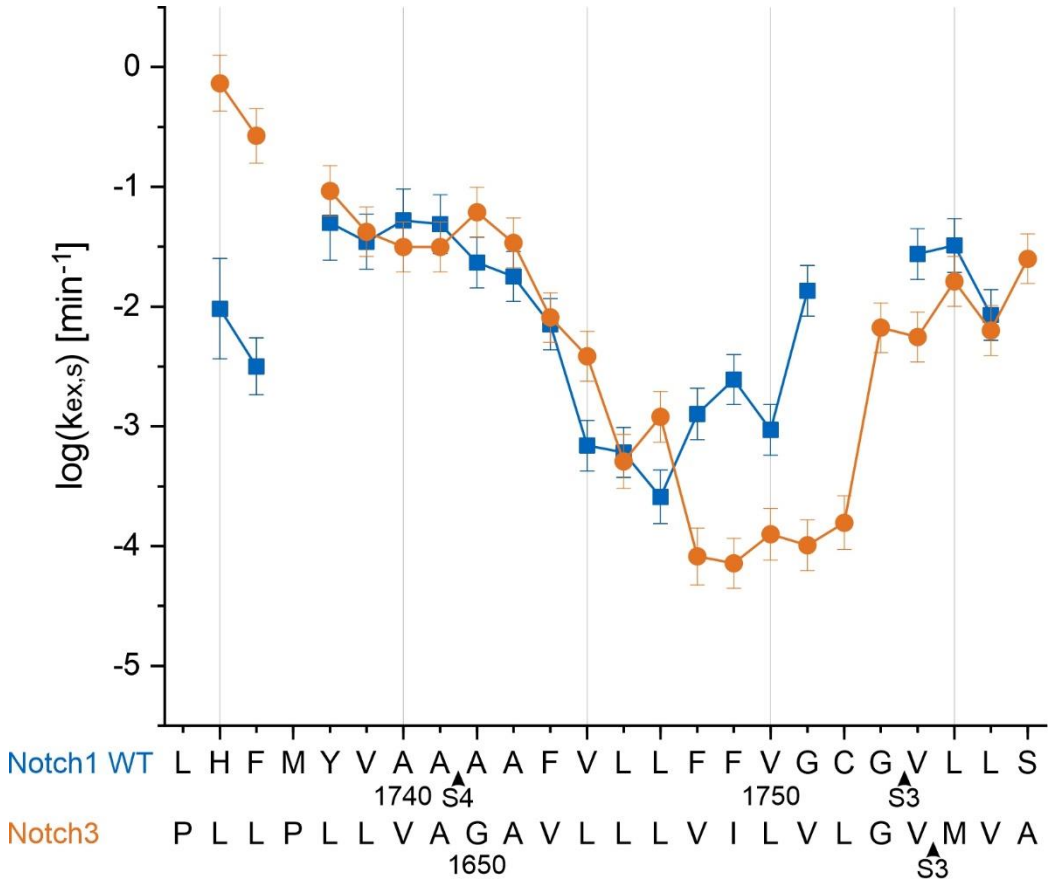

Figure 4.20 Residue-specific HDX rate constants of Notch3$_{1642-1665}$ TMD. Exchange rates of Notch1$_{1734-1757}$ WT (blue) and Notch3$_{1642-1665}$ (orange) residues were determined in d_3-TFE/D_2O at different pD values (3.5, 4.5, 5.5 and 6.5) and scaled to pD 5. The error bars account for the error in the fitted parameter k_{ex} and the inaccuracy of the pH electrode. The most stable region of Notch3$_{1642-1665}$ TMD is located at the beginning of TM-C residues Val$_{1656}$ to Leu$_{1660}$.

Only for the N- and C-terminal lysine triad no evaluable signal could be detected. Since proline lacks an amide proton, the exchange rates both Pro_{1642} and Pro_{1645} could not be determined either. The analysed rate constants were in the range from 0.18 min^{-1} (one per hour) and 0.000012 min^{-1} (one in 2 months).

The flexibility profile (Figure 4.20) showed the most stable area of the $Notch3_{1642-1665}$ TMD at the beginning of the TM-C ranging from residue Val_{1656} to Leu_{1660}. The whole TM-C was not only more stable than the $Notch3_{1642-1665}$ TM-N, but also significantly more stable than TM-C in $Notch1_{1734-1757}$ WT.

Within $Notch3_{1642-1665}$ TM-C residues around the S3 cleavage site Val_{1662}/Met_{1663} exhibited a faster exchange and thus pointed to less stable hydrogen bonds and a partial unfolding.

The TM-N is even less stable than the flexible C-terminal end. In principle, the $Notch3_{1642-1665}$ TM-N is comparable to the TM-N in $Notch1_{1734-1757}$ WT in terms of stability and flexibility. Solely the N-terminal end seems to be more destabilized, since the two Pro have no amide protons and thus could not serve as hydrogen bond donors.

4.4 Comparison of Notch1 WT, Mutants and Notch3

To investigate whether mutations or a homologue sequence affect the helical flexibility, as well as their impact on the overall structure, the 3D TMD structure was determined by NMR spectroscopy.

All experimental data were consistent and described a slightly bend and fully α-helical $Notch1_{1734-1757}$ WT TMD (Figure 4.21), whose central region around residues Leu_{1746}/Leu_{1747} was stabilized by hydrogen bonds (Figure 4.22 (b)). The TM-N was less stable compared to the TM-C and its orientation with respect to the TM-C was restricted to a specific conical area. The S3 cleavage site exhibited greater conformational flexibility due to weaker hydrogen bonds and partial unfolding.

The $Notch1L_{1740-1743}$ TMD was entire helical like $Notch1_{1734-1757}$ WT, while $Notch3_{1642-1665}$ TMD was one and a half helical turns shorter. $Notch1G_{1740-1743}$ TMD had an unstructured region around the mutation and was therefore the least helical of the examined Notch peptides (Figure 4.22 (a) and (c)).

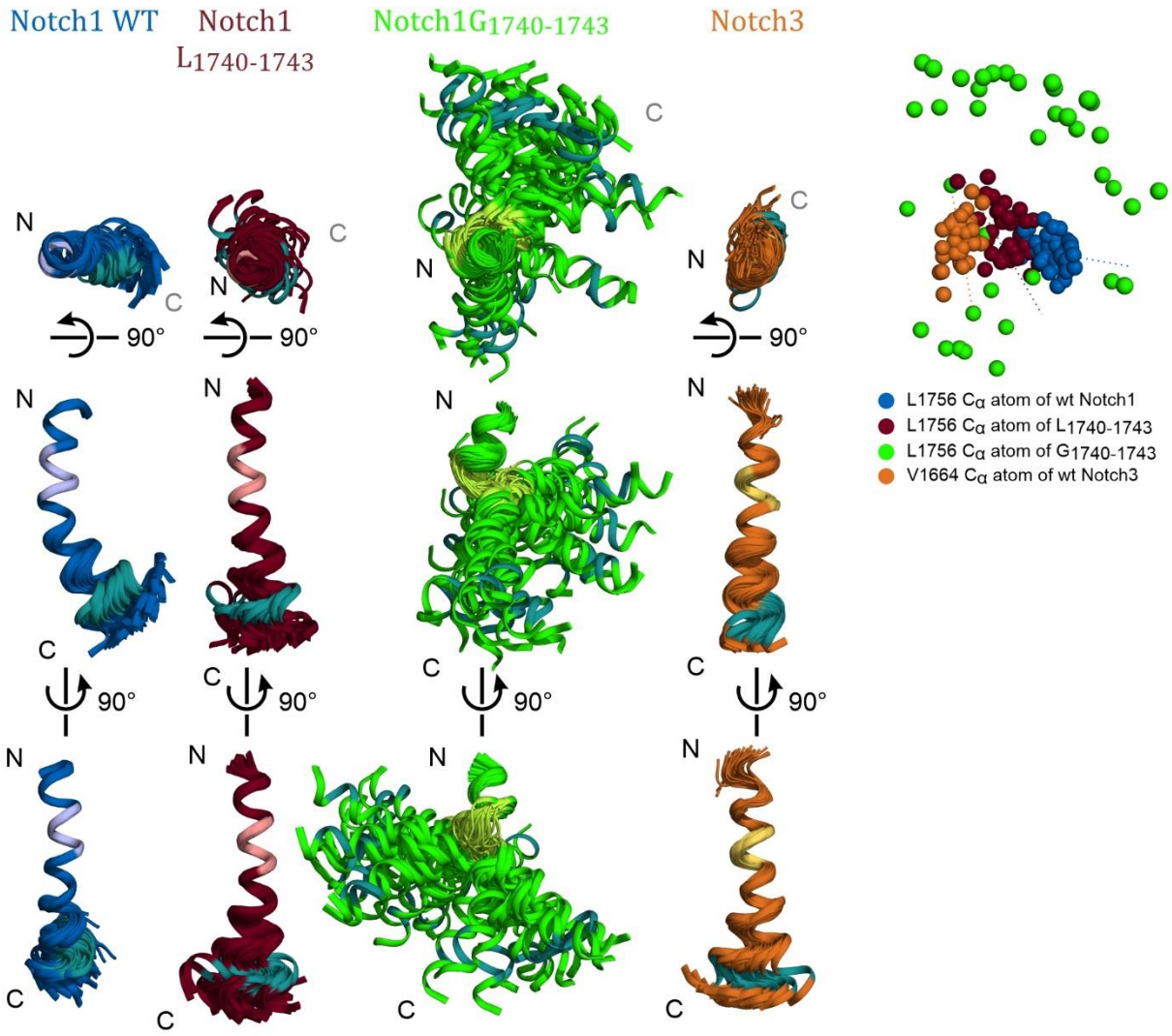

Figure 4.21 Comparison of 3D structures of Notch1 WT, mutants and Notch3. Structural bundles of Notch1$_{1734-1757}$ WT TMD (blue), Notch1L$_{1740-1743}$ TMD (red), Notch1G$_{1740-1743}$ TMD (green) and Notch3$_{1642-1665}$ TMD (orange) aligned on TM-N. Top and side view of the 40 lowest energy NMR structures out of 400 are shown. The alanine tetrad and corresponding mutated residues, as well as AGA motif are coloured more lightly. The S3 cleavage site is represented in turquoise. The spread of the structural bundles is shown in the right column with the N-terminus pointing out of the plane of the figure. The dots correspond to C_α atoms of residue Leu$_{1756}$ in Notch1$_{1734-1757}$ WT (blue), Notch1L$_{1740-1743}$ (red), Notch1G$_{1740-1743}$ (green) and residue Val$_{1664}$ in Notch3$_{1642-1665}$ (orange). The direction of the bend in the bundles is indicated by dotted lines.

In Notch1L$_{1740-1743}$ the bending of the bundle is less pronounced and the direction of the bend turned by about 60°. The helix in Notch3$_{1642-1665}$ TMD is even a little straighter than in Notch1L$_{1740-1743}$ and the direction of the bend shifted further by around 90° (Figure 4.21). The structural bundle of Notch1G$_{1740-1743}$ possessed a distinctly wider distribution

of the possible orientations, and the TM-N with respect to the TM-C was less restricted, but not completely arbitrary showing a preferred direction.

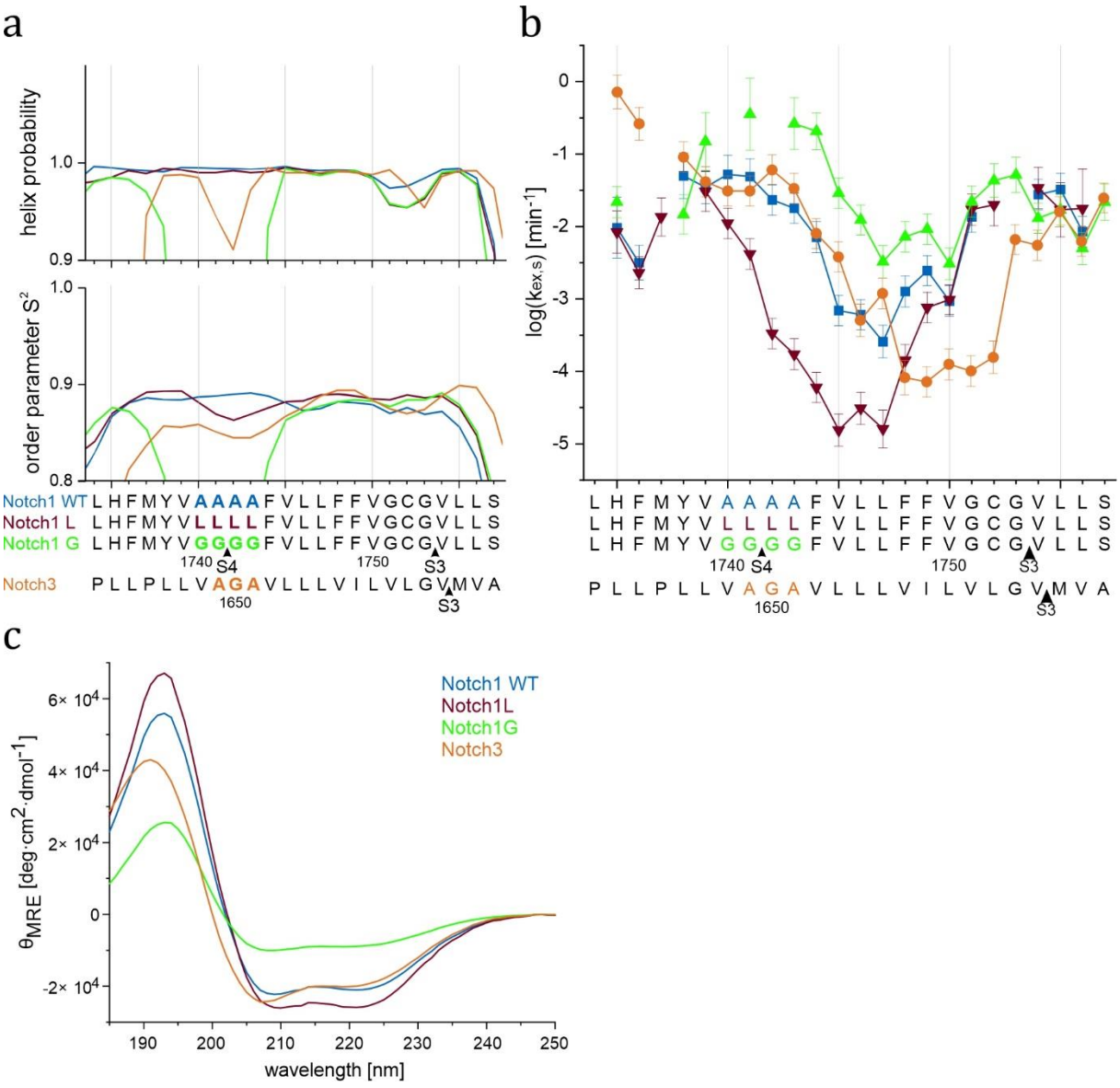

Figure 4.22 Structural and dynamic comparison of Notch1 WT, mutants and Notch3. Helix probability and theoretical order parameter S^2 (a) of $Notch1_{1734-1757}$ WT (blue), $Notch1L_{1740-1743}$ (red), $Notch1G_{1740-1743}$ (green)and $Notch3_{1642-1665}$ (orange) were predicted with TALOS+ (Shen et al. 2009) on the basis of chemical shifts. An $S^2 = 1$ indicates complete restriction of the internal NH bond vector motion. Residue-specific HDX rate constants (b) determined in d_3-TFE/D_2O at different pD values and scaled to pD 5. The error bars account for the error in the fitted parameter k_{ex} ant the inaccuracy of the pH electrode. CD spectra (c) measured in TFE/H_2O at pH 6.5 and 300 K were analysed with BeStSel.

The TM-N of all investigated Notch peptides was generally less stable than the TM-C, with the most stable region located in the middle of the helix, stabilized by hydrogen bonds.

The TM-C flexibility profile of Notch1$_{1734-1757}$ WT and its mutants was similar, whereas the TM-N showed significant differences, such as that the TM-N was stabilized in Notch1L$_{1740-1743}$ TMD and destabilized in Notch1G$_{1740-1743}$ TMD compared to the Notch1$_{1734-1757}$ WT (Figure 4.22 (b)). In contrast to the mutants the TM-N of Notch3$_{1642-1665}$ TMD and Notch1$_{1734-1757}$ WT was similar in terms of stability and flexibility and the TM-C differed, so the TM-C in Notch3$_{1642-1665}$ was significantly stabilized compared to the Notch1$_{1734-1757}$ WT.

The S3 cleavage site was not only destabilized in the Notch1 WT, but also showed a higher conformational flexibility in the mutants and Notch3$_{1642-1665}$ TMD.

4.5 TNFα$_{28-60}$ WT TMD

The transmembrane cytokine TNFα acts as a ligand for the TNFα receptors 1 and 2 and mediates apoptosis or cell survival. Its intramembrane cleavage by SPPL2a/b activates IL12 production, an interleukin important for cell-mediated immune response. A certain substrate flexibility is necessary for proteolytic cleavage, so mutations that changed this flexibility were investigated and the influence on the 3D structure and TMD dynamics analysed by NMR spectroscopy.

The unlabeled TNFα TMDs were measured in TFE/water (TFE:H_2O, 80:20, v:v), a mimetic for the interior of the enzyme, at 300 K and pH 6.5. To prevent the formation of disulphide bridges, 5 mM TCEP was added.

4.5.1 Sequence

Based on the 233 amino acid long sequence, the TMD of the human TNFα (P01375) was predicted by DeepTMHMM (Hallgren et al. 2022) to cover residues Leu$_{31}$ to Leu$_{51}$. Since charged and polar amino acids are involved in the positioning in the membrane and stability of the transmembrane helix (Lerch-Bader et al. 2008), the investigated peptide sequence of TNFα$_{28-60}$ contained juxtamembrane parts with arginine residues (Figure 4.23). These naturally occurring basic amino acids also increased the solubility of the very hydrophobic TNFα$_{28-60}$ TMD.

Figure 4.23 TNFα$_{28-60}$ sequence. Investigated TNFα$_{28-60}$ TMD sequence, where the TMD region predicted by DeepTMHMM is underlined.

The TNF superfamily with its associated receptors evolved early in the animal evolution and is restricted to the metazoan, the kingdom of multicellular animals (Marín 2020). The most conserved regions are extracellular and associated with the induction of cell death (Lu et al. 2016). To evaluate the amino acid conservation of TNFα TMD across a wide range of species, a BLAST analysis was performed. TNFα residues 1-100, containing the TMD and juxtamembrane regions for facilitated similarity search, were blasted against the database UniRef90 and the pairwise alignments were analysed with a custom python script written by Martin Ortner (TU Munich).

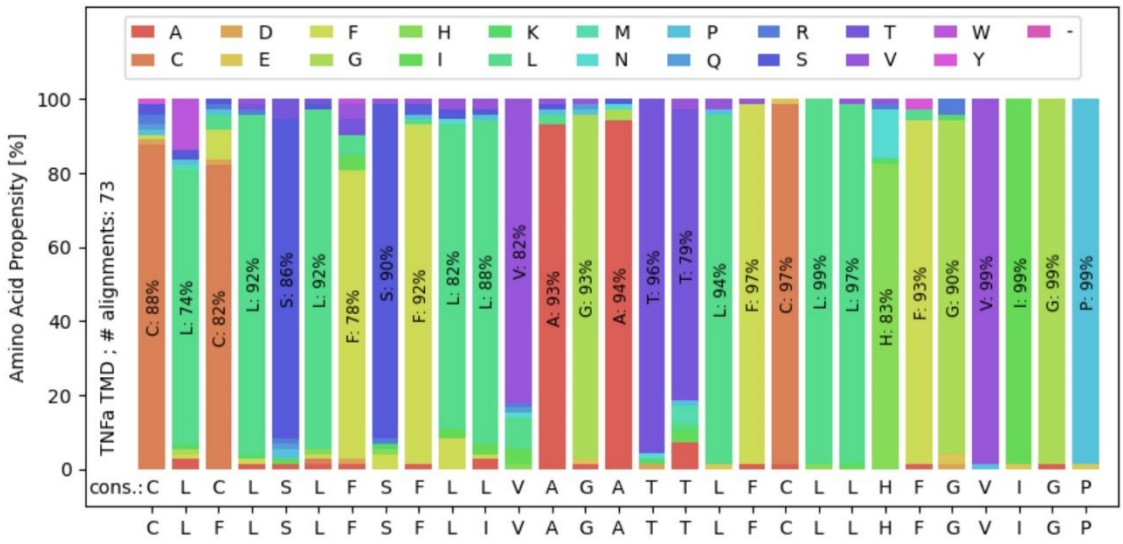

Figure 4.24 Sequence alignment of TNFα TMD. TNFα TMD sequence blasted against UniRef90. Evolutionary conservation of each residue was calculated from pairwise alignment.

The amino acid sequence of TNFα TMD was well conserved (Figure 4.24), although it appears that the TM-N was slightly less conserved compared to the TM-C. The most conserved residues of the TNFα TMD were located around the major initial cleavage sites Cys$_{49}$/Leu$_{50}$ and Leu$_{51}$/His$_{52}$, as well as around residues Val$_{55}$/Ile$_{56}$/Gly$_{57}$/Pro$_{58}$, which were not part of the predicted TMD.

4.5.2 Chemical Shifts

Information derived from the chemical shifts provide structural and dynamic insights of peptides. The ^{1}H-^{1}H NOESY and TOCSY spectra as well as the natural abundance ^{1}H-^{13}C HSQC spectrum (Figure 4.25) were well resolved and showed sharp peaks with good chemical shift dispersion. The amide proton resonances ranging approximately from 9 ppm to 7.5 ppm and the ^{1}H$_{\alpha}$ and ^{13}C$_{\alpha}$ resonances in the range of 3.5 ppm to 4.6 ppm and 44 ppm to 68 ppm, indicated a folded TNFα$_{28\text{-}60}$ WT TMD.

The proton and corresponding ^{13}C resonances were determined. First, assigning the through-bond connections of protons in a spin system (Figure 4.25 (a), vertical lines) and linking them with through-bond connection between protons and carbon atoms in the heteronuclear ^{1}H-^{13}C HSQC spectrum (Figure 4.25(b)). The sequential assignment was done by through-space connections of protons between neighbouring amino acids in the ^{1}H-^{1}H NOESY spectrum.

a

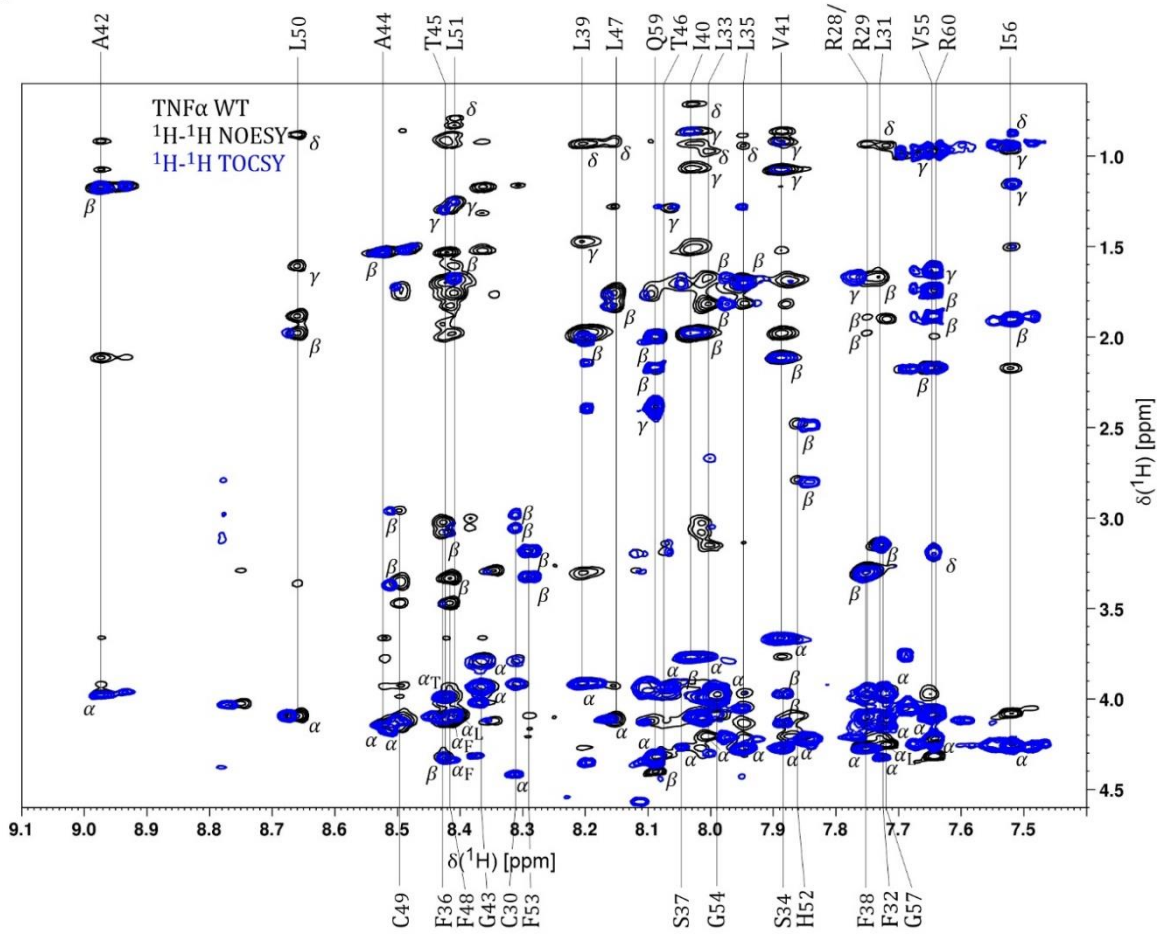
TNFα WT
^{1}H-^{1}H NOESY
^{1}H-^{1}H TOCSY
A42
L50
A44
T45
L51
L39
L47
Q59
T46
I40
L33
L35
V41
R28/
R29
L31
V55
R60
I56
C49
F36
F48
G43
C30
F53
S37
G54
S34
H52
F38
F32
G57
δ(^{1}H) [ppm]

b

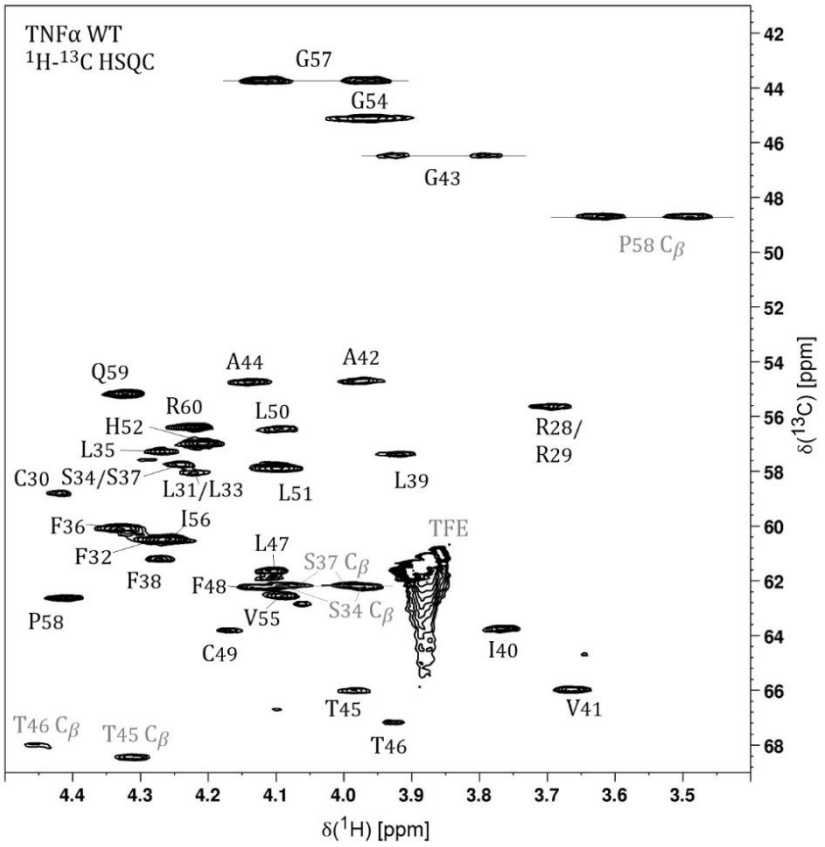
TNFα WT
^{1}H-^{13}C HSQC
G57
G54
G43
P58 Cβ
Q59
A44
A42
R60
L50
H52
L35
C30
S34/S37
L31/L33
L51
L39
R28/
R29
F36
I56
F32
L47
F38
F48
S37 Cβ
S34 Cβ
TFE
P58
V55
C49
I40
T45
V41
T46 Cβ
T45 Cβ
T46
δ(^{1}H) [ppm]
δ(^{13}C) [ppm]

Figure 4.25 TNFα$_{28-60}$ WT ^{1}H-^{1}H NOESY, ^{1}H-^{1}H TOCSY and ^{1}H-^{13}C HSQC spectra. Figure caption refers to the figure on the previous page. Shown are TNFα$_{28-60}$ WT ^{1}H-^{1}H NOESY and ^{1}H-^{1}H TOCSY spectra (a) of the H_N-H_α region. The spin systems of the individual residues are indicated by vertical lines. The respective protons are identified by small Greek letters and supplemented by the corresponding amino acid in the range of low spectral dispersity. The ^{1}H-^{13}C HSQC spectrum (b) shows the H_α-C_α region and the respective residues are marked.

Based on the assigned chemical shifts CSI 3.0 (Hafsa et al. 2015) predicted only a short helical segment in TNFα$_{28-60}$ WT TMD ranging from residue Phe$_{38}$ to His$_{52}$ and a turn around Phe$_{32}$ within the otherwise unstructured sequence (Figure 4.26 (e)). The secondary structure prediction of TALOS+ (Shen et al. 2009), in agreement with the DeepTMHMM prediction, indicated a N-terminal more extended helix covering residues Cys$_{30}$ to His$_{52}$ (Figure 4.26 (c)). Secondary chemical shifts (Figure 4.26 (a)) and consecutive characteristic NOE contacts (Figure 4.26 (b)) confirmed an α-helical TNFα$_{28-60}$ WT TMD ranging from residue Cys$_{30}$/Leu$_{31}$ to His$_{52}$/Phe$_{53}$.

This helical part was divided by the AGA motif, where the secondary chemical shifts as well as the dαβ(i, i+3) NOE contacts were reduced and together with slightly reduced helix probability and order parameter S^2 identified a disturbance of the α-helix. Additional dαN(i, i+2) indicated a 3_{10}-helical contribution as an intermediate in folding and unfolding (Millhauser 1995; Wüthrich 1986).

The TM-N residues Cys$_{30}$/Leu$_{31}$ to Val$_{41}$, and in particular the first half of them up to Phe$_{38}$, were characterized less stable, showing a lower number of dαβ(i, i+3) NOEs and less pronounced secondary chemical shifts. TNFα$_{28-60}$ WT TM-C residues Thr$_{45}$ to His$_{52}$/Phe$_{53}$ formed, compared to the TM-N, a more stable helix by a regular pattern of characteristic NOE contacts and higher secondary chemical shifts. This was in line with the decrease in helical content and the order parameter S^2 around Phe$_{36}$, which showed a destabilization of the TM-N compared to the TM-C, as well as with the trend in the CSI 3.0 prediction an even less stable and up to unstructured TM-N.

The cleavage sites were usually located in destabilized TMD areas since the corresponding peptide bonds are only accessible for cleavage if they were not part of a well-ordered helical structure. Some of the consecutive cleavage sites were located in the destabilized area around Phe$_{36}$. Similar to the helix probability and the order parameter S^2 before, the absence of helix-typical NOE contacts and the presence of dαN(i, i+2) NOEs mapped a destabilization of some cleavage sites such as Ser$_{34}$/Leu$_{35}$, Leu$_{51}$/His$_{52}$ and Gly$_{54}$/Val$_{55}$.

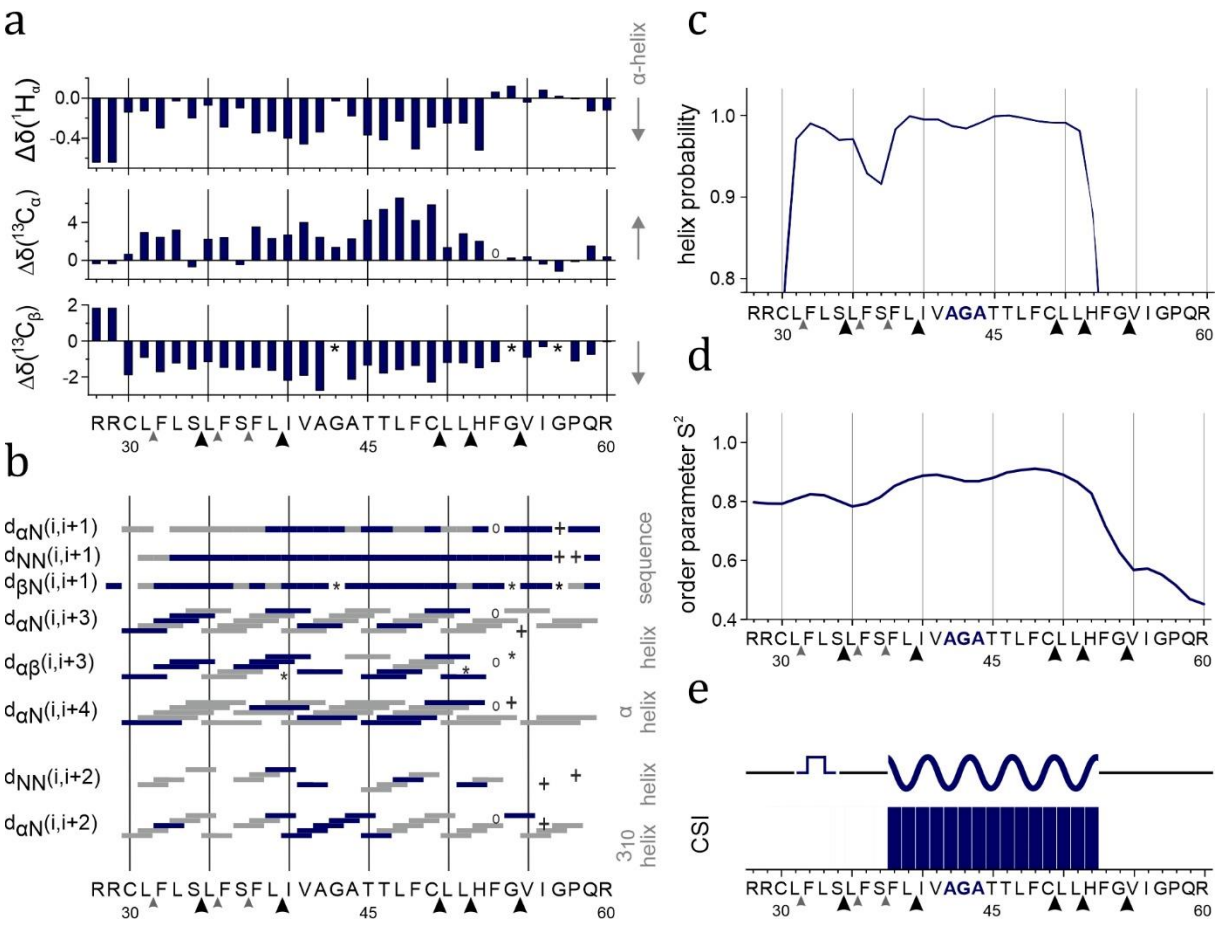

Figure 4.26 Secondary structure characteristics of TNFα$_{28-60}$ WT TMD determined by NMR. Secondary chemical shifts (a), the difference between random coil and observed values. Positive $^{13}C_\alpha$ and negative $^{1}H_\alpha$, $^{13}C_\beta$ secondary chemical shifts indicate α-helices. Characteristic NOE contacts (b), where blue boxes indicate unambiguous NOE contacts and grey boxes show NOE contacts that could not be assigned unambiguously due to signal overlap. Asterisks mark glycines or contacts to glycines without H_β atoms, plus mark prolines or contacts to prolines without amide protons and circles mark Phe$_{53}$, where $^{1}H_\alpha$ resonance could not be observed because of too close proximity to the saturated water resonance at 4.7 ppm. The black arrows show major and small grey arrows minor cleavage sites of the consecutive intramembrane cleavage. Helix probability (c) and theoretical order parameter S^2 (d) were predicted with TALOS+ (Shen et al. 2009) on the basis of chemical shifts. An S^2 = 1 indicates complete restriction of the internal NH bond vector motion. In the CSI 3.0 output (e) α-helical regions are represented by the blue bars and the wavy line. The blue rectangular line indicates a turn. Areas with no secondary structure are represented by the black line.

4.5.3 3D Structure

Chemical shifts, distance restraints derived from ^{1}H-^{1}H NOESY peak intensities and dihedral restraints derived from chemical shifts using TALOS+ (Shen et al. 2009) formed the basis for the calculation of the 3D structure of TNFα$_{28-60}$ WT TMD, performed with CNS (Brünger et al. 1998) and the ARIA2 setup (Rieping et al. 2007).

In agreement with the chemical shift and NOE data, the structure determination revealed a helical part of TNFα$_{28-60}$ WT TMD between Leu$_{31}$ and Phe$_{53}$ (Figure 4.27). The average TNFα$_{28-60}$ 3D structure exhibited a slight bend in the middle of the TMD around the AGA motif (Figure 4.27 (c)).

By superimposing 40 lowest NMR structures out of 400 on the backbone atoms of the TM-N residues Leu$_{31}$ to Gly$_{42}$, the C-terminal helices spread out and their orientation with respect to the TM-N was not arbitrary but limited to a defined elliptical cone (Figure 4.27 (a)). To evaluate the distribution of the possible conformations and the direction of the bend, the bundle was viewed from the N-terminus. Due to the slight bend of the TNFα$_{28-60}$ WT TMD helix residues Phe$_{38}$, Ala$_{42}$, Thr$_{45}$ and Cys$_{49}$ were located at the concave site. On the opposite side of the helix, the convex side, the space-filling residues such as Phe$_{36}$, Ile$_{40}$, Leu$_{47}$and Leu$_{51}$, deflect the TMD toward smaller residues, because of their bulky side chains. The space-consuming properties of the amino acids side chains were indicated as transparent surfaces in the bundle of the helix backbone structures (Figure 4.27 (b)) and the location of the convex and concave sites were visualized by the 2D helical wheel representation of the TMD α-helix residues Ser$_{34}$ to Val$_{55}$ (Figure 4.27 (d)).

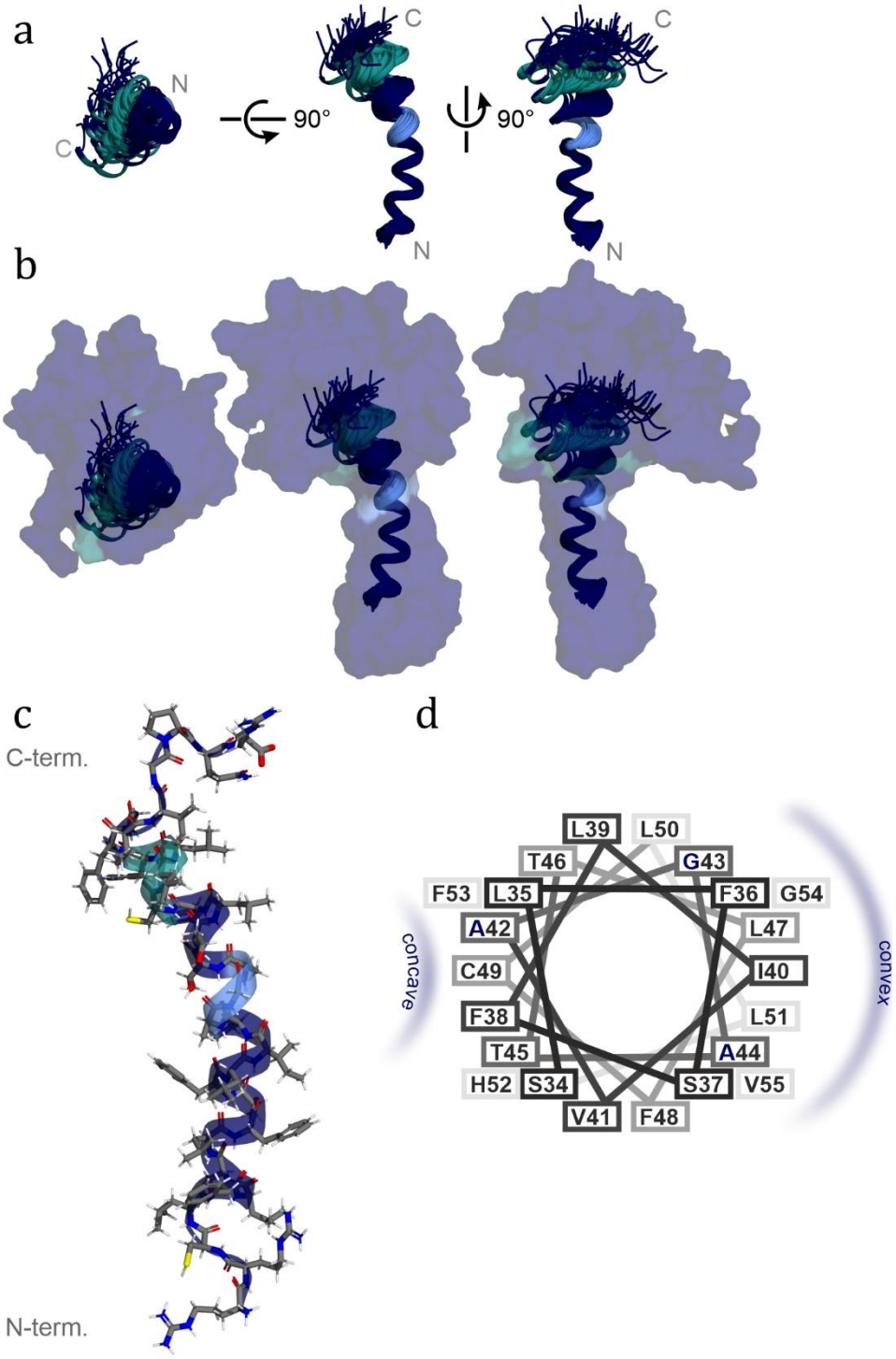

Figure 4.27 3D structure of TNFα$_{28-60}$ WT TMD. Structural bundles of TNFα$_{28-60}$ WT residues Leu$_{31}$-Ile$_{56}$ (a) superimposed on residues Leu$_{31}$-Gly$_{43}$. Top and side view of the 40 lowest energy NMR structures out of 400 are shown. Region with AGA motif is highlighted in light blue. The initial cleavage sites Cys$_{49}$/Leu$_{50}$ and Leu$_{51}$/His$_{53}$ are represented in turquoise. The bundles of helix backbone structure are surrounded by transparent surfaces corresponding to the side

chains of residues Arg$_{28}$-Arg$_{60}$ (b). Average 3D structure (c). In the helical wheel representation (d) the locations of the concave and convex sides of residues Ser$_{34}$-Val$_{55}$ are indicated.

4.5.4 Hydrogen Deuterium Exchange

To examine the dynamics of TNFα$_{28-60}$ TMD 15 ^{1}H-^{1}H TOCSY spectra in d$_3$-TFE/D$_2$O (d$_3$-TFE:D$_2$O, 80:20, v:v) at 300 K and 1mM TCEP were measured. The series of spectra were acquired at pD 3.5, pD 4.5 and pD 5.5 to cover a broad time window of rate constants and access the most exchangeable protons. The experimental exchange rate k_{ex}, investigated at different pD values, was scaled to pD 5 as $k_{ex,s}$.

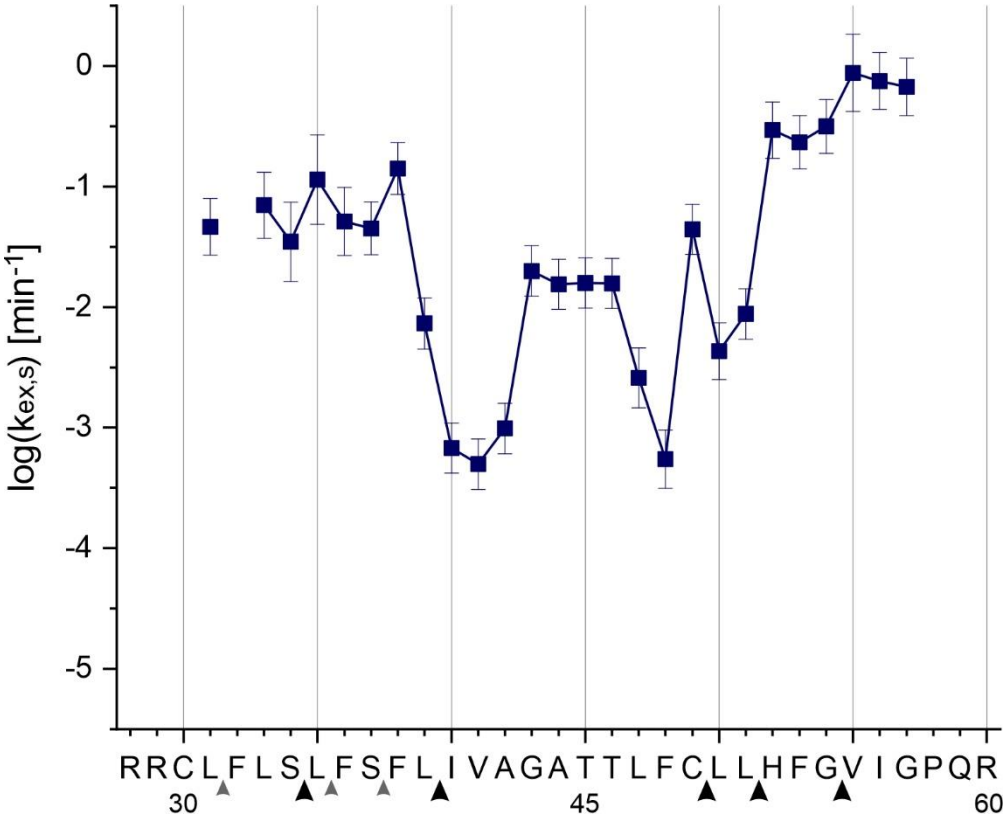

Figure 4.28 Residue specific HDX rate constants of TNFα$_{28-60}$ WT TMD. Exchange rates of TNFα$_{28-60}$ residues were determined in d$_3$-TFE/D$_2$O at different pD values (3.5, 4.5 and 5.5) and scaled to pD 5. The error bars account for the error in the fitted parameter k_{ex} and the inaccuracy of the pH electrode. The most stable region of TNFα$_{28-60}$ WT TMD is located around residues Val$_{41}$ and Phe$_{48}$.

No evaluable signals could be determined for the first three and last two residues of TNFα$_{28-60}$ WT as well as Phe$_{32}$. Because prolines do not have amide protons, the exchange

rate of Pro$_{58}$ could not be determined either. The identified rate constants were in the range of 0.87 min^{-1} (about one per minute) and 0.0005 min^{-1} (one in 35 hours).

The flexibility profile (Figure 4.28) represented a kind of W shape with the most stable regions around residues Val$_{41}$ and Phe$_{48}$ and more flexible N- and C-terminal ends. The most dynamic and flexible area of TNFα$_{28-60}$ WT TMD started after His$_{52}$, which the previous data characterized as non-helical.

The TM-N covering residues Leu$_{31}$ to Val$_{41}$ was linked by a flexible part around AGA motif, residues Gly$_{43}$ to Thr$_{46,}$ to the more stable TM-C ranging from residue Thr$_{45}$ to His$_{52}$. Drops in the flexibility profile mapped cleavage sites revealed faster exchange enabled by less stable hydrogen bonds and a partial unfolding.

4.6 TNFαAGA/LLL$_{28-60}$ and TNFαS34P$_{28-60}$ Mutants

Since the intramembrane proteolysis is affected by the conformational flexibility of the substrate TMD (Fluhrer et al. 2012; Götz et al. 2019b), the influence of two mutations that modulated this flexibility in comparison to the TNFα$_{28-60}$ WT TMD were investigated.

The TNFαAGA/LLL$_{28-60}$ mutant was designed by replacing the central AGA motif with leucines (Figure 4.29) to rigidify and stabilize the TMD helix (Quint et al. 2010). In contrast, the serine to proline substitution at residue 34 in the TNFαS34P$_{28-60}$ mutant was hypothesized to disturb the helical geometry and destabilize the TMD helix (Cordes et al. 2002). To determine the structural and dynamic impacts, TNFαAGA/LLL$_{28-60}$ TMD and TNFαS34P$_{28-60}$ TMD were analysed under the same conditions as TNFα$_{28-60}$ WT.

```
                    30          40          50          60
TNFα28-60           RRC LFLSLFSFLI VAGATTLFCL LHFGVIGPQR
TNFαAGA/LLL         RRC LFLSLFSFLI VLLLTTLFCL LHFGVIGPQR
TNFαS34P            RRC LFLPLFSFLI VAGATTLFCL LHFGVIGPQR
```

Figure 4.29 TNFα$_{28-60}$ WT, TNFαAGA/LLL$_{28-60}$ and TNFαS34P$_{28-60}$ sequence. Investigated TNFα$_{28-60}$ WT and mutant TMD sequence is shown.

4.6.1 Circular Dichroism

The influence of the mutations on the secondary structure were estimated by CD spectra, which were acquired under the same conditions as the NMR spectra in TFE/H_2O (80:20, v:v), 1 mM TCEP at pH 6.5 and 300 K. The concentration of the investigated peptides, needed for the conversion of the recorded ellipticity to the mean residue ellipticity (Figure 4.30), was determined from the CD spectra by the absorbance A_{214} at 214 nm (Table 4.3). The corresponding extinction coefficient ε_{214} at 214 nm and the secondary structure content were calculated using the web server BeStSel (https://bestsel.elte.hu) (Kuipers und Gruppen 2007; Micsonai et al. 2018).

Table 4.3 Secondary structure content and conformation of TNFα$_{28-60}$ WT, TNFαAGA/LLL$_{28-60}$ and TNFαS34P$_{28-60}$ TMD. Secondary structure content of TNFα$_{28-60}$ WT, TNFαAGA/LLL$_{28-60}$ and TNFαS34P$_{28-60}$ TMD investigated from CD spectra with BeStSel and concentration determination for mean residue ellipticity conversion.

	TNFα WT	TNFαAGA/LLL	TNFα S34P
extinction coefficient ε_{214} [$M^{-1}cm^{-1}$]	65002	65052	67643
absorbance A_{214}	0.09	0.07	0.08
concentration [µM]	14.2	13.5	11.1
secondary structure content [%]			
helix	22.5	35.1	29.0
distorted helix	13.2	18.9	18.3
β-sheet	16.6	6.3	10.3
turn	13.8	10.0	10.3
others	33.9	29.7	32.1

TNFα$_{28-60}$ WT and both mutants were helical showing two minima at 208 nm and 222 nm as well as a maximum at 192 nm in the CD spectra (Figure 4.30), but only with a helical content about 30 % or less. Helix-stabilizing properties of the leucine amino acids in TNFαAGA/LLL$_{28-60}$ TMD were evident in the more pronounced maximum and the minima in the CD spectrum compared to the TNFα$_{28-60}$ WT and the highest helical content of 35 %. Surprisingly, the helix-typical minima and the maximum in the CD spectrum of the proline mutant were also more pronounced than in the TNFα$_{28-60}$ WT. The estimated helix proportion of the proline mutant with 29 % is higher than that of the WT with 22%, assuming a stabilized or extended helix in TNFαS34P$_{28-60}$ TMD compared to TNFα$_{28-60}$ WT.

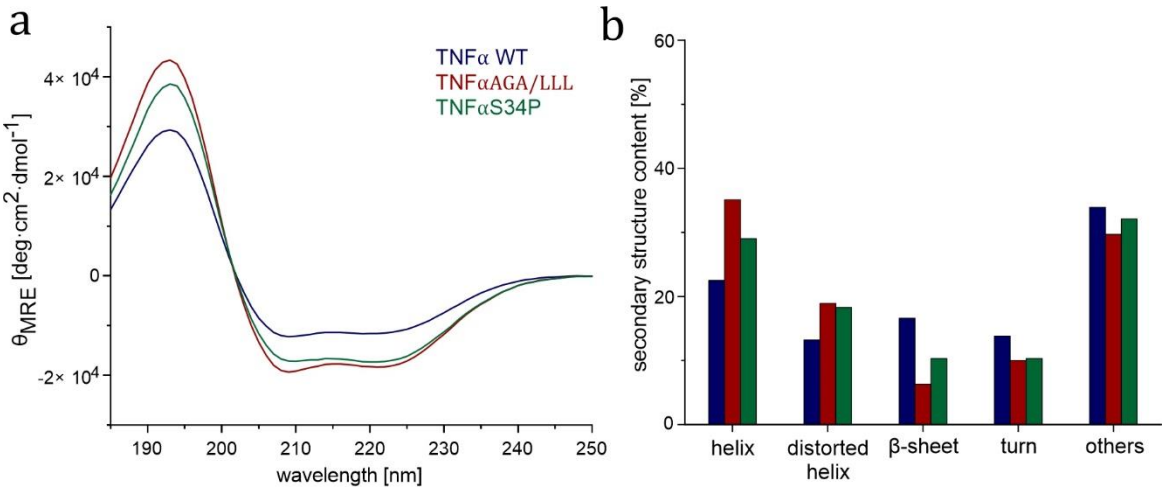

Figure 4.30 CD spectra of TNFα$_{28-60}$ WT, TNFαAGA/LLL$_{28-60}$ and TNFαS34P$_{28-60}$. CD spectra (a) of TNFα$_{28-60}$ WT (blue), TNFαAGA/LLL$_{28-60}$ (red) and TNFαS34P$_{28-60}$ (green) in TFE/H_2O (80:20, v:v) at pH 6.5 and 300 K. The secondary structure content (b) indicates a helicity of 22 % in TNFα$_{28-60}$ WT, 35 % in TNFαAGA/LLL$_{28-60}$ and 29 % in TNFαS34P$_{28-60}$. CD spectra were analysed and secondary structure content estimated with BeStSel.

4.6.2 Chemical Shifts

The ^{1}H-^{1}H NOESY and TOCSY as well as natural abundance ^{1}H-^{13}C spectra of TNFαAGA/LLL$_{28-60}$ and TNFαS34P$_{28-60}$ (Figure 4.31) were comparable in terms of spectral dispersion and resolution to TNFα$_{28-60}$ WT, assuming a folded TMD. All amino acids of both mutants were identified and ^{1}H and ^{13}C resonances assigned.

Similar to the secondary structure prediction of TNFα28-60 WT, CSI 3.0 (Hafsa et al. 2015) denoted a short helical part in TNFαAGA/LLL$_{28-60}$ TMD from Phe$_{38}$ to His$_{52}$ and a turn around Phe$_{32}$ (Figure 4.32 (d)), while the prediction by TALOS+ (Shen et al. 2009) indicated a longer TMD helix starting from Cys$_{30}$ (Figure 4.32 (c)). Secondary chemical shifts (Figure 4.32 (a)) and consecutive NOE contacts (Figure 4.32 (b)) indicated, comparable with the TNFα$_{28-60}$ WT, a helical part of the TNFαAGA/LLL$_{28-60}$ TMD ranging from residues Cys$_{30}$/Leu$_{31}$ to His$_{52}$/Phe$_{53}$.

a

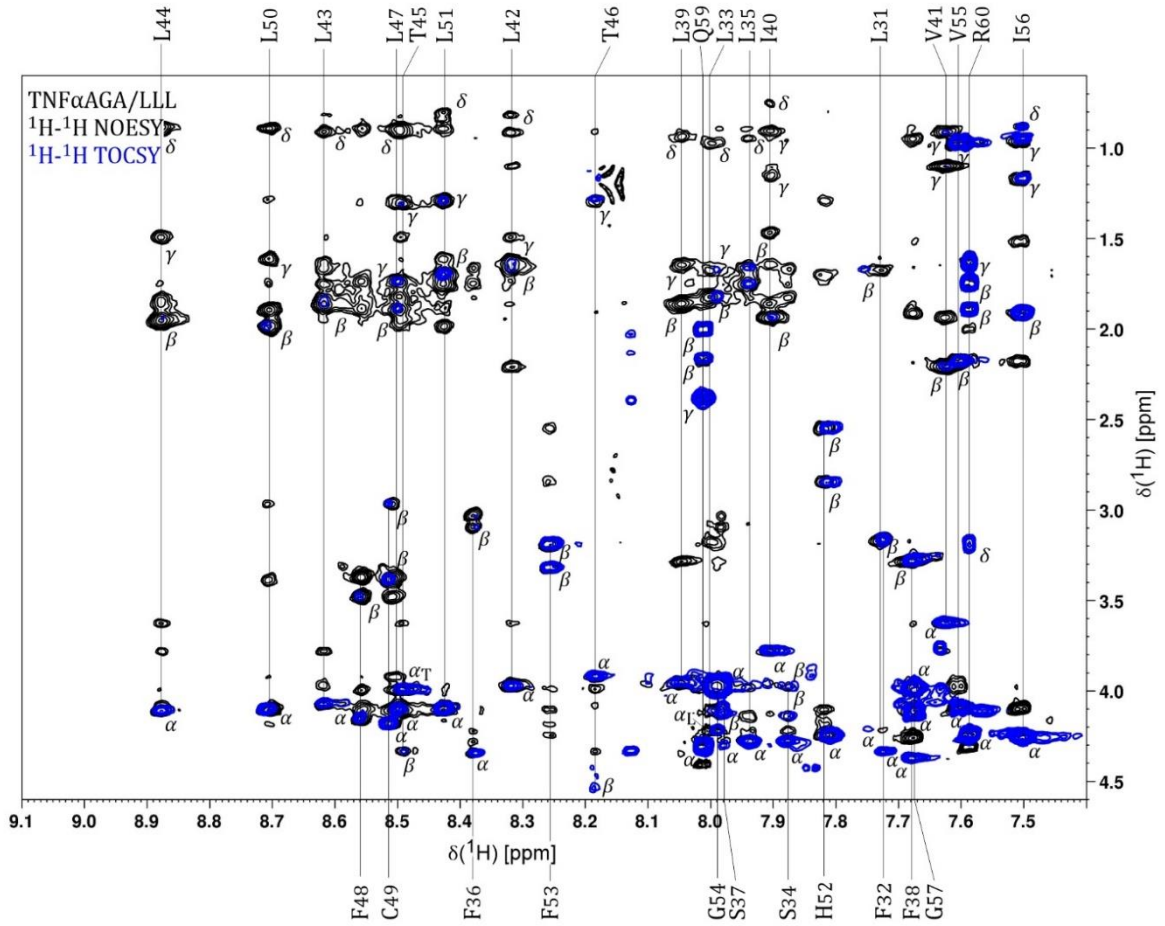
TNFαAGA/LLL
^{1}H-^{1}H NOESY
^{1}H-^{1}H TOCSY
L44 L50 L43 L47 T45 L51 L42 T46 L39 Q59 L33 L35 I40 L31 V41 V55 R60 I56
F48 C49 F36 F53 G54 S37 S34 H52 F32 F38 G57
δ(^{1}H) [ppm]

b

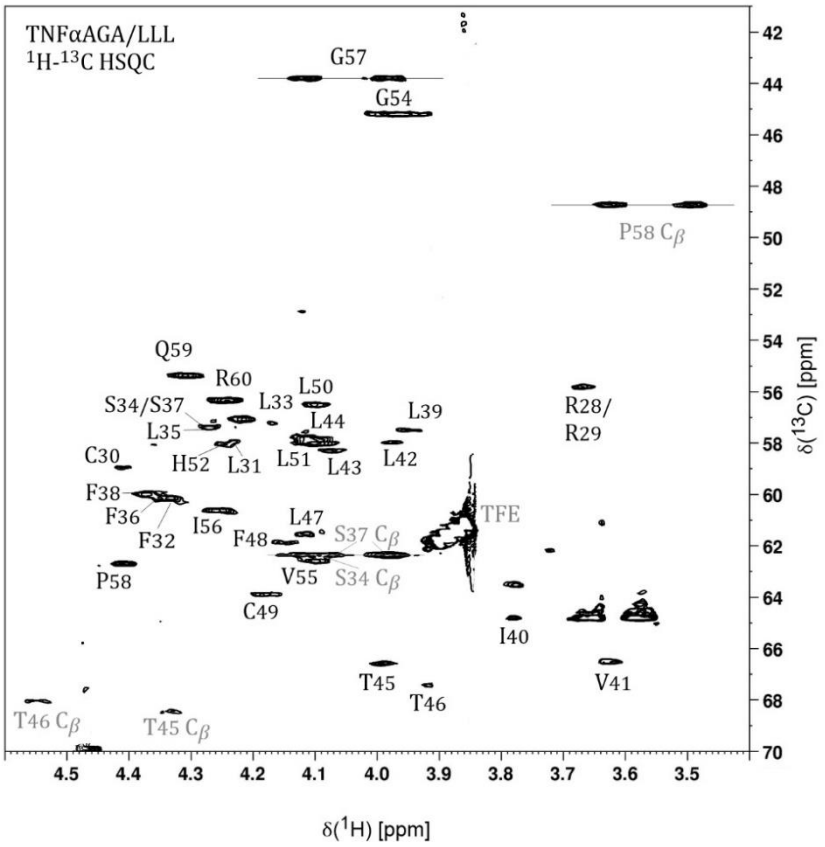
TNFαAGA/LLL
^{1}H-^{13}C HSQC
G57
G54
P58 Cβ
Q59
R60
L50
S34/S37
L33
L44
L39
R28/
R29
L35
C30
H52
L31
L51
L43
L42
F38
F36
F32
I56
L47
F48
S37 Cβ
TFE
P58
V55
S34 Cβ
C49
I40
T45
T46
V41
T46 Cβ
T45 Cβ
δ(^{13}C) [ppm]
δ(^{1}H) [ppm]

c

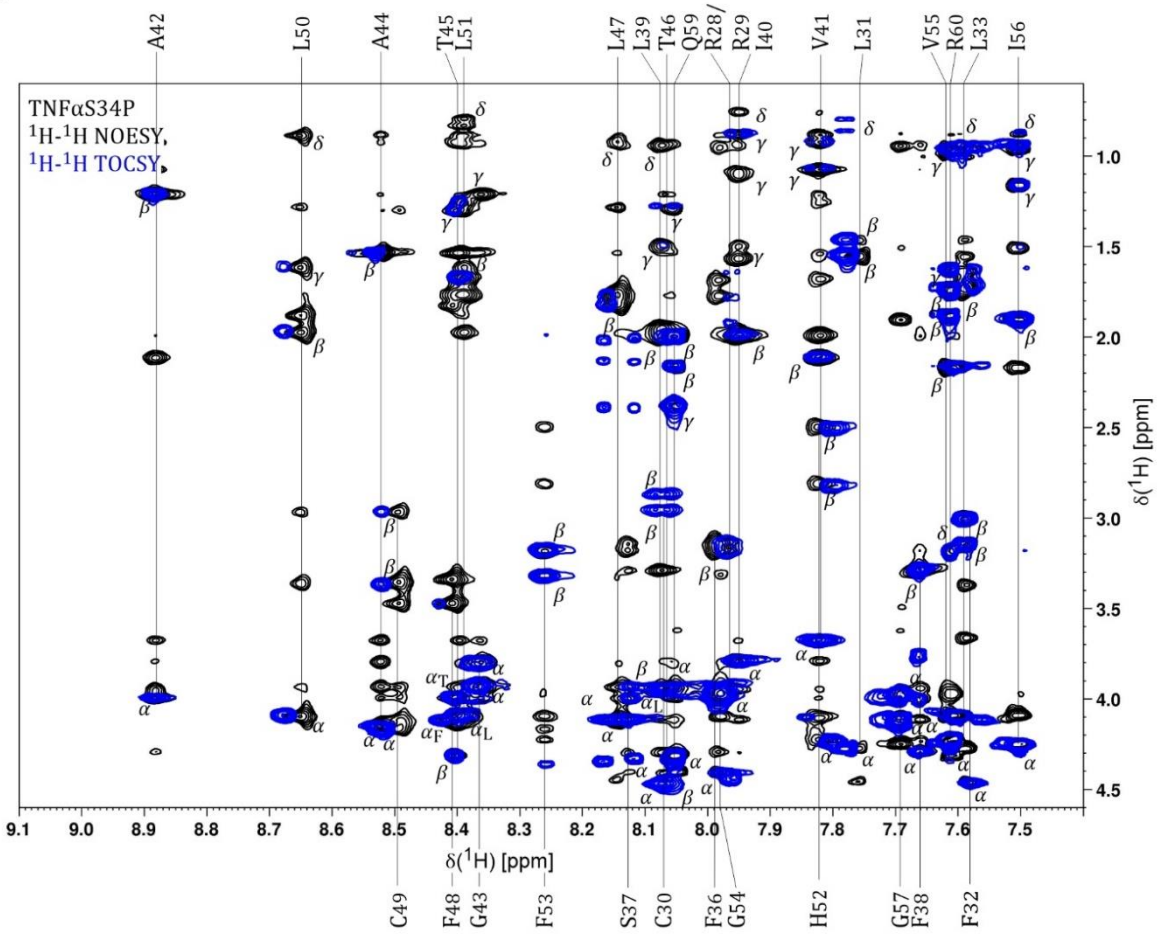
TNFαS34P
^{1}H-^{1}H NOESY,
^{1}H-^{1}H TOCSY,
A42
L50
A44
T45
L51
L47
L39
T46
Q59
R28/
R29
I40
V41
L31
V55
R60
L33
I56
C49
F48
G43
F53
S37
C30
F36
G54
H52
G57
F38
F32
δ(^{1}H) [ppm]

d

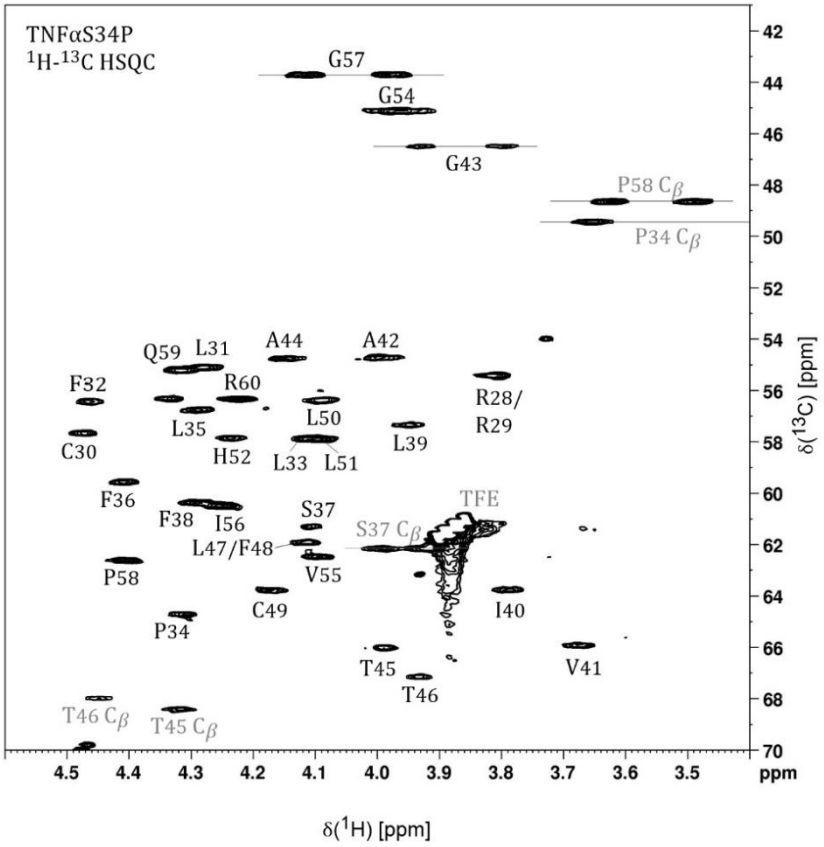
TNFαS34P
^{1}H-^{13}C HSQC
G57
G54
G43
P58 Cβ
P34 Cβ
Q59
L31
A44
A42
F32
R60
R28/
R29
L35
L50
C30
H52
L33
L51
L39
F36
F38
I56
S37
TFE
S37 Cβ
L47/F48
V55
P58
C49
I40
P34
T45
T46
V41
T46 Cβ
T45 Cβ
δ(^{13}C) [ppm]
δ(^{1}H) [ppm]
ppm

Figure 4.31 TNFαAGA/LLL$_{28-60}$ and TNFαS34P$_{28-60}$ NMR spectra. Figure caption refers to figures on the previous pages. Shown are TNFαAGA/LLL$_{28-60}$ (a) and TNFαS34P$_{28-60}$ (c) ^{1}H-^{1}H NOESY and ^{1}H-^{1}H TOCSY spectra of the H_N-H_α region. The spin systems of the individual residues are indicated by vertical lines. The respective protons are identified by small Greek letters and supplemented by the corresponding amino acid in the range of low spectral dispersity. The ^{1}H-^{13}C HSQC spectrum of TNFαAGA/LLL$_{28-60}$ (b) and TNFαS34P$_{28-60}$ (d) shows the H_α-C_α region and the respective residues are marked.

The substitution of the AGA motif by leucine residues led to a stabilization of the central TMD, characterized by the corresponding values for the secondary chemical shifts and fewer dαN(i,i+2) NOE contacts. Analogously to TNFα$_{28-60}$ WT, the TM-C consisting of residues Thr$_{45}$ to His$_{52}$/Phe$_{53}$ formed a more stable helix in the leucine mutant compared to the TM-N, covering residues Cys$_{30}$/Leu$_{31}$ to Val$_{41}$ due to the presence of helix-typical NOE contacts. The order parameter S^2 and the helix probability also identified a less helical and more flexible TM-N compared to the TM-C. Particularly the beginning of the TM-N in TNFαAGA/LLL$_{28-60}$ was less stable around the both residues Ser$_{34}$ and Ser$_{37}$ as evident from the low values of the helical content and indicative of some of the cleavage sites.

Interestingly, in agreement with the CD data, TNFαS34P$_{28-60}$ showed in the secondary structure prediction with CSI 3.0 as well as with TALOS+ an elongated TMD helix with less flexible regions within the cleavage sites. The position of the TMD helix in TNFαS34P$_{28-60}$, covering residues Phe$_{32}$/Leu$_{33}$ to Val$_{55}$/Ile$_{56}$, was shifted by some residues and extended further into the C-terminal region, in contrast to TNFα$_{28-60}$ WT and the leucine mutant.

Since the amino acid proline lacks an amide proton, it is not able to stabilize the helix by the formation of hydrogen bonds with previous residues, so that the helix N-terminal of Pro$_{34}$ was destabilized compared to TNFα$_{28-60}$ WT indicated by the secondary chemical shifts and the loss of NOE contacts in this part.

Additionally, in the proline mutant, the TM-C was more stable than the TM-N and like in the TNFα$_{28-60}$ WT both parts were connected by a disturbed and less stable α-helix region around AGA.

In both mutants the cleavage sites were characterized by a disturbed α-helix and the loss of helix-typical NOE contacts or presence of dαN(i,i+2) contacts.

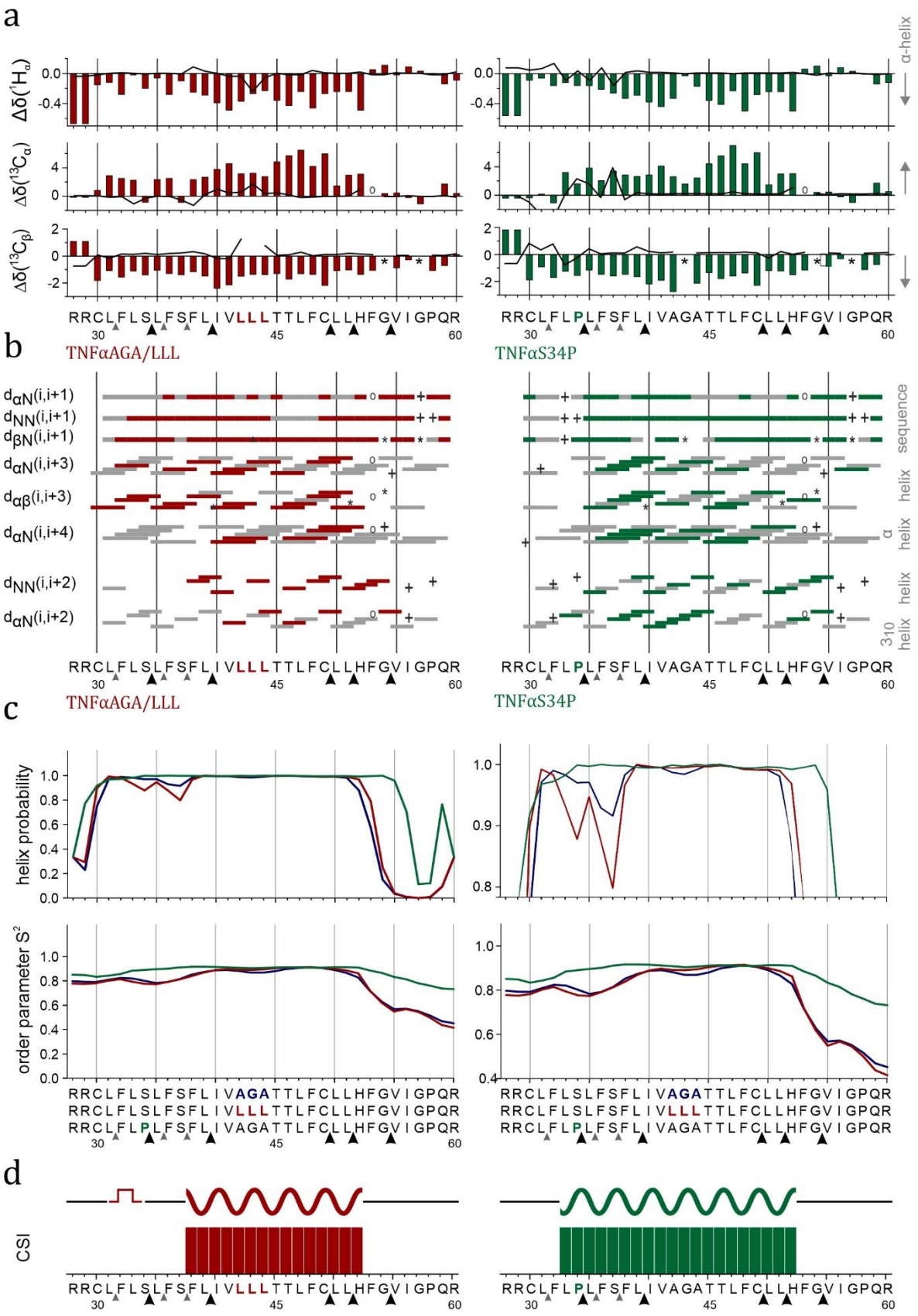
a
b
c
d
TNFαAGA/LLL
TNFαS34P
RRCLFLSLFSFLIVLLLTTLFCLLHFGVIGPQR
RRCLFLPLFSFLIVAGATTLFCLLHFGVIGPQR
helix probability
order parameter S²
CSI
α-helix
sequence
helix
α helix
helix
310 helix

Figure 4.32 Secondary structure characteristics of TNFαAGA/LLL$_{28-60}$ and TNFαS34P$_{28-60}$ TMD determined by NMR. Figure caption refers to the figure on the previous page. Secondary chemical shifts (a), the difference between random coil and observed values of TNFαAGA/LLL$_{28-60}$ TMD (red) and TNFαS34P$_{28-60}$ TMD (green). Positive $^{13}C_{\alpha}$ and negative $^{1}H_{\alpha}$, $^{13}C_{\beta}$ secondary chemical shifts indicate α-helices. The black lines show the difference between secondary chemical shifts of the mutants and TNFα$_{28-60}$ WT, for example in case of C_{α}, negative values of these differences indicate a more helical TNFα$_{28-60}$ WT TMD. Characteristic NOE contacts (b), where coloured boxes indicate unambiguous NOE contacts and grey boxes show NOE contacts that could not be assigned unambiguously due to signal overlap. Asterisks mark glycine or contacts to glycines without H_{β} atoms, plus mark proline or contacts to proline without amide protons and circles mark Phe$_{53}$, where $^{1}H_{\alpha}$ resonance could not be observed because of too close proximity to the saturated water resonance at 4.7 ppm. The black arrows show major and small grey arrows minor cleavage sites of the consecutive intramembrane cleavage. Helix probability and theoretical order parameter S^2 (c) were predicted with TALOS+ (Shen et al. 2009) on the basis of chemical shifts. An $S^2 = 1$ indicates complete restriction of the internal NH bond vector motion. The right panels are an enlarged part of the left panels. In the CSI 3.0 output (Hafsa et al. 2015) (e) α-helical regions are represented by the coloured bars and the wavy line. The red rectangular line indicates a turn. Areas with no secondary structure are represented by the black line.

4.6.3 3D Structure

The 3D structure of the mutants was calculated analogue to TNFα$_{28-60}$ WT (section 4.5.3). The determined TNFαAGA/LLL$_{28-60}$ TMD α-helix ranged from Leu$_{31}$ to Phe$_{53}$ (Figure 4.33 (a)) and showed a less pronounced bend around residues Ala$_{42}$Gly$_{43}$Ala$_{44}$ compared to the TNFα$_{28-60}$ WT, and a straighter helix, due to the bulky leucine side chains and their larger space requirement.

To evaluate the influence of the mutation on the orientation of the TNFαAGA/LLL$_{28-60}$ bundles compared to TNFα$_{28-60}$ WT, first the average TNFαAGA/LLL$_{28-60}$ structure (Figure 4.33 (a)) was aligned with the average TNFα$_{28-60}$ WT TM-N residues Leu$_{31}$ to Gly$_{43}$. Then the 40 lowest energy TNFαAGA/LLL$_{28-60}$ NMR models were superimposed onto its average TNFαAGA/LLL$_{28-60}$ structure along the TM-N residues Leu$_{31}$ to Gly$_{43}$ (Figure 4.33(b)). Here, as in the WT, the orientation of the TM-N in relation to the TM-C was not arbitrary but limited to a comparable conical area, but shifted by 45 ° in the TNFαAGA/LLL$_{28-60}$ bundles in direction of Val$_{41}$ and Phe$_{48}$. Consequently, these residues lined up the concave site, while Leu$_{51}$, Leu$_{47}$, Leu$_{43}$ and Leu$_{39}$ were located at the convex site (Figure 4.33 (f)).

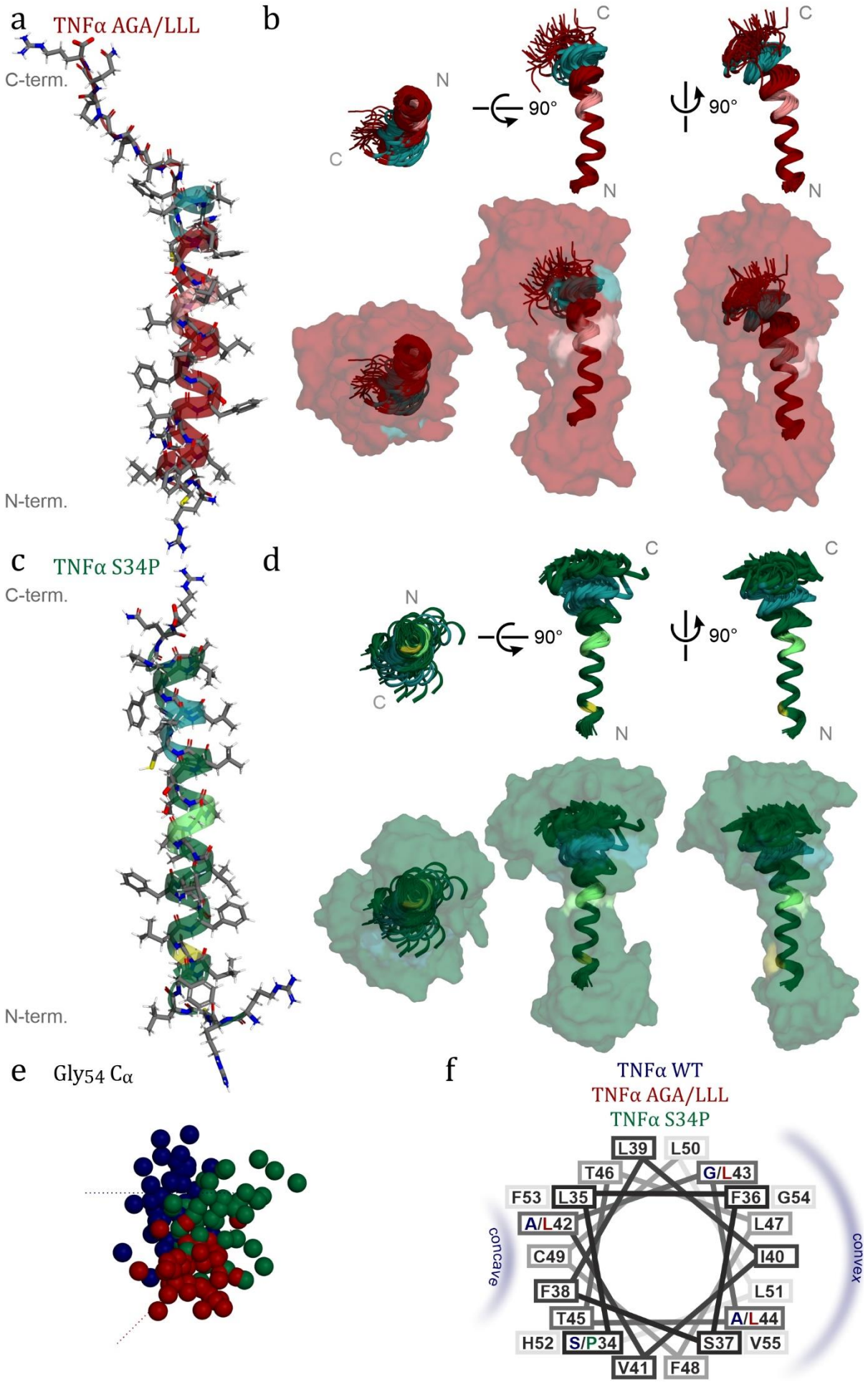
a
TNFα AGA/LLL
C-term.
N-term.
b
C
N
90°
90°
C
N
N
C
C
N
c
TNFα S34P
C-term.
N-term.
d
N
C
90°
90°
C
C
N
N
e
Gly54 Cα
f
TNFα WT
TNFα AGA/LLL
TNFα S34P
L39
L50
T46
G/L43
F53
L35
F36
G54
A/L42
L47
C49
I40
F38
L51
T45
A/L44
H52
S/P34
S37
V55
V41
F48
concave
convex

Figure 4.33 3D structure of TNFαAGA/LLL$_{28-60}$ TMD and TNFαS34P$_{28-60}$ TMD. Figure caption refers to the figure on the previous page. Average 3D structure of TNFαAGA/LLL$_{28-60}$ TMD (a) and TNFαS34P$_{28-60}$ TMD (c). Structural bundles of TNFαAGA/LLL$_{28-60}$ TMD (b) and TNFαS34P$_{28-60}$ TMD (d) residues Leu$_{31}$-Ile$_{56}$ superimposed on residues Leu$_{31}$-Gly$_{43}$. Top and side view of the 40 lowest energy NMR structures out of 400 are shown. Region with AGA motif and mutated residues are highlighted in the corresponding light shade. The initial cleavage sites Cys$_{49}$/Leu$_{50}$ and Leu$_{51}$/His$_{52}$ are represented in turquoise. The bundles of helix backbone structure are surrounded by transparent surfaces corresponding to the side chains of residue Arg$_{28}$-Arg$_{60}$. The spread of the structural bundles is shown (e) with the N-terminus pointing out of the plane of the figure. The dots correspond to C_α atoms of residue Gly$_{54}$ in TNFα$_{28-60}$ WT (blue), TNFαAGA/LLL$_{28-60}$ (red) and TNFαS34P$_{28-60}$ (green). The direction of the bend in the bundles is indicated by dotted lines. In the helical wheel representation (f) the locations of the concave and convex sides of residues Ser$_{34}$-Val$_{55}$ are indicated.

The shift in the direction of the bend, indicated by the dotted lines (Figure 4.33 (e)), could be better recognized if the bundles were rotated in a way that the N-terminus looked out of the plane of the drawing, as illustrated in Figure 4.33 (b) left representation, and only the C_α atoms of Gly$_{54}$ were visualized (Figure 4.33 (e)).

The calculated 3D structure of TNFαS34P$_{28-60}$ TMD identified an α-helix covering residues Phe$_{32}$ to Ile$_{56}$, which was shifted by a helical turn towards the C-terminal end compared to TNFα$_{28-60}$ WT and the leucine mutant (Figure 4.33 (c)). The shift of the helix was already indicated by the secondary chemical shift and NOE contacts and was confirmed by the 3D structure. The incorporation of aromatic NOE contacts and rising the amount of calculated structures to 400 led to a C-terminal elongated helix in TNFαS34P$_{28-60}$ TMD compared to the structure in (Spitz et al. 2020), covering residues Pro$_{34}$ to Phe$_{53}$.

Furthermore, TNFαS34P$_{28-60}$ TMD 3D structure revealed an even less pronounced bend around Ala$_{42}$Gly$_{43}$Ala$_{44}$ than in TNFαAGA/LLL$_{28-60}$ TMD. The orientation of the TM-N in relation to the TM-C was evaluated by first aligning the TNFαS34P$_{28-60}$ average structure to the TNFα$_{28-60}$ WT average structure TM-N residues Leu$_{31}$ to Gly$_{43}$ and then superimposing the 40 lowest energy TNFαS34P$_{28-60}$ NMR models on the average TNFαS34P$_{28-60}$ structure along the TM-N Leu$_{31}$ to Gly$_{43}$ (Figure 4.33 (d)). The orientation of the TM-C compared to the TM-N was not deflected in a particular direction, as a result of its straight TMD, but was more concentrated around the TM-N helix axis.

4.6.4 Hydrogen Deuterium Exchange

The hydrogen deuterium exchange of the mutants was measured analogue to TNFα$_{28-60}$ WT (section 4.5.4). To cover a broad time window of rate constants and access the main part of the exchangeable protons, TNFαAGA/LLL$_{28-60}$ TMD was determined at pD 4.5 and pD 5.5 and TNFαS34P$_{28-60}$ TMD at pD 3.5 and 4.5. The experimental exchange rate k_{ex} was scaled to pD 5 as $k_{ex,s}$. The flexibility profiles of the mutants compared to TNFα$_{28-60}$ WT (Figure 4.34) indicated a more stable TNFαAGA/LLL$_{28-60}$ TMD and a slightly less stable TNFαS34P$_{28-60}$ TMD.

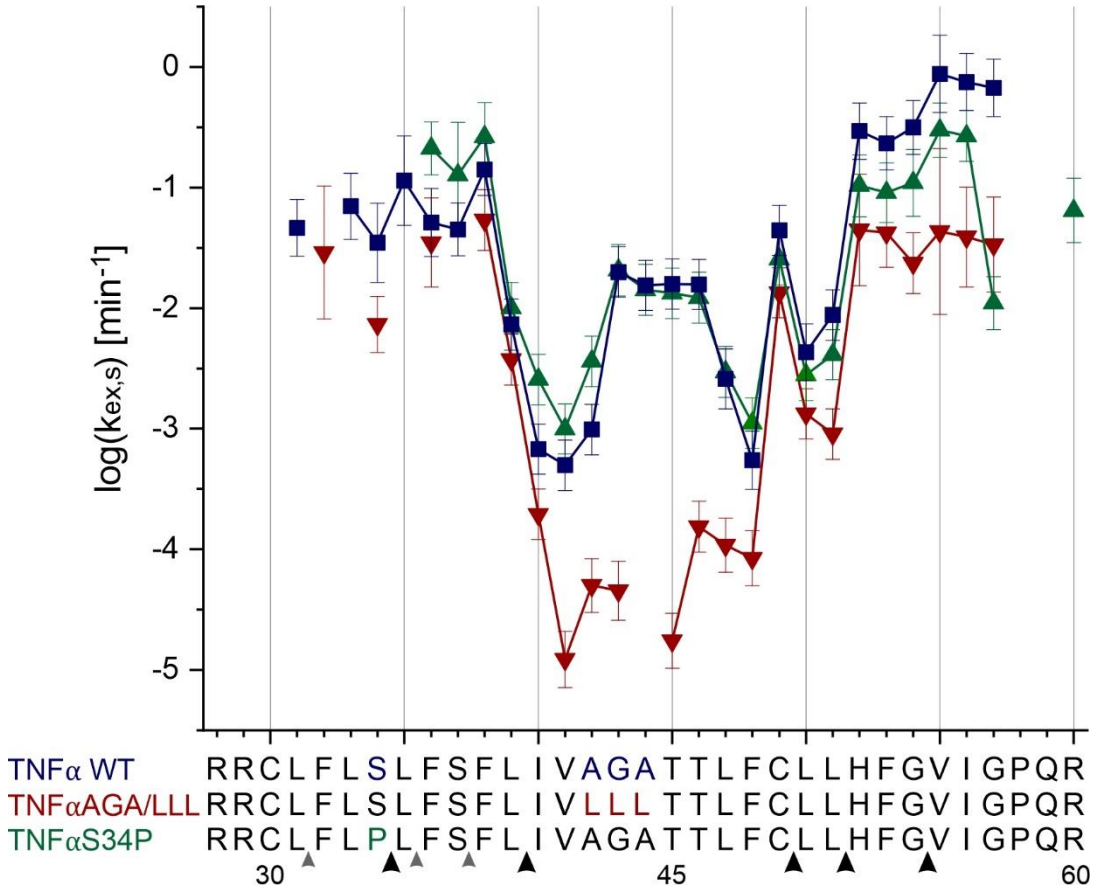

Figure 4.34 Residue specific HDX rate constants of TNFαAGA/LLL$_{28-60}$ TMD and TNFαS34P$_{28-60}$ TMD. Exchange rates of TNFα$_{28-60}$ WT (blue), TNFαAGA/LLL$_{28-60}$ (red) and TNFαS34P$_{28-60}$ (green) residues were determined in d_3-TFE/D_2O at different pD values (3.5, 4.5 and 5.5) and scaled to pD 5. The error bars account for the error in the fitted parameter k_{ex} and the inaccuracy of the pH electrode. The most stable region of TNFαAGA/LLL$_{28-60}$ TMD is located between residues Val$_{41}$ and Phe$_{48}$.

No evaluable signals of some of the residues at the N-terminal end Arg$_{28}$ to Leu$_{31}$, Leu$_{33}$, Leu$_{35}$, Ser$_{37}$, as well as the very C-terminal residues Pro$_{58}$ to Arg$_{60}$ and Leu$_{44}$ in the middle

of the TMD, could be detected in TNFαAGA/LLL$_{28-60}$. The determined exchange rate constants were in the range of 0.054 min^{-1} (one in 20 minutes) and 0.000012 min^{-1} (one in 6 days).

The flexibility profile (Figure 4.34) of TNFαAGA/LLL$_{28-60}$ TMD showed a more stable TM-C compared to the TM-N, whereby the area Val$_{41}$ to Phe$_{48}$, including the mutations, was characterized by significantly more stable hydrogen bonds. The most stable regions were located around Val$_{41}$ and Thr$_{45}$. As in TNFα$_{28-60}$ WT, flexibility increased toward the termini, although these were also more stable in the leucine mutant compared to the WT.

Just like in TNFα$_{28-60}$ WT drops in the flexibility profile not only in TNFαAGA/LLL$_{28-60}$ but also in TNFαS34P$_{28-60}$ indicated cleavage sites.

Measurements at lower pD values, slow down the exchange, but also at pD 3.5 not all signals from TNFαS34P$_{28-60}$ TMD could be detected, no evaluable signals for the first 8 N-terminal residues as well as Pro$_{58}$ and Gln$_{59}$ were found. The remaining exchange rates were in the range of 0.3 min^{-1} (one in 3 minutes) and 0.001 min^{-1} (one in 18 hours).

The course of the flexibility profile in TNFαS34P$_{28-60}$ TMD (Figure 4.34) with the corresponding features was almost identical to TNFα$_{28-60}$ WT. In TNFαS34P$_{28-60}$ TMD residues Phe$_{36}$ to Phe$_{48}$ were slightly less stable and residues C-terminal of Cys$_{49}$ were slightly more stable compared to TNFα$_{28-60}$ WT.

4.7 Comparison of TNFα WT and Mutants

To examine how the mutations influence the helical flexibility and which impact they have to the overall structure, the 3D TMD structures were investigated by NMR spectroscopy.

Much like in the Notch peptides, all experimental data were consistent and showed a slightly bent, α-helical TNFα$_{28-60}$ WT TMD (Figure 4.35). The TM-N was separated by a central and flexible AGA motif from a more stable TM-C and the orientation of the TM-N with respect to the TM-C was limited to a defined cone. The conformational flexible cleavage sites disrupted the helix due to weaker hydrogen bonds and partial unfolding.

The length of the TNFαAGA/LLL$_{28-60}$ TMD helix was as in TNFα$_{28-60}$ WT, while the TNFαS34P$_{28-60}$ TMD helix was shifted by a helical turn towards the C-terminus, causing the TM-N to shorten and the TM-C to elongate.

The bend of the TNFαAGA/LLL$_{28-60}$ bundle was less pronounced resulting in a straighter TMD compared to the TNFα$_{28-60}$ WT and a by 45° shifted direction of the bend. The bend in TNFαS34P$_{28-60}$ TMD was even less pronounced than in the leucine mutant, so

that the distribution of the orientation in the structural bundles clustered around the helical axis (Figure 1.20).

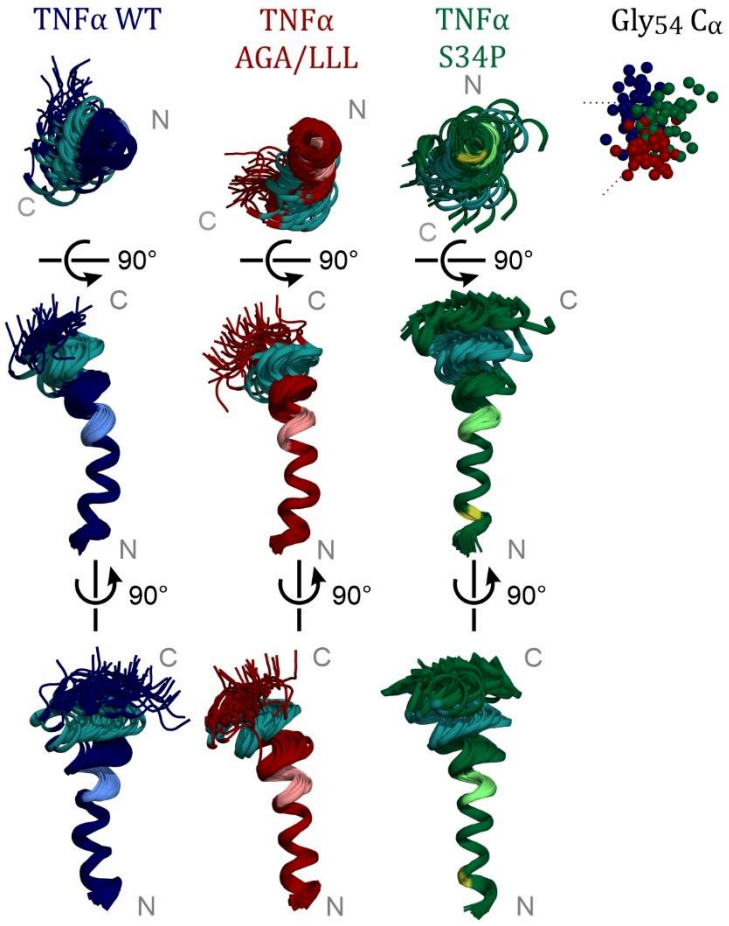

Figure 4.35 Comparison of 3D structures of TNFα WT and mutants. Structural bundles of TNFα$_{28-60}$ WT TMD (blue), TNFαAGA/LLL$_{28-60}$ TMD (red) and TNFαS34P$_{28-60}$ TMD (green) residues Leu$_{31}$-Ile$_{56}$ superimposed on residues Leu$_{31}$-Gly$_{43}$. Top and side view of the 40 lowest energy NMR structures out of 400 are shown. Region with AGA motif and mutated residues are highlighted in the corresponding light shade. The initial cleavage sites Cys$_{49}$/Leu$_{50}$ and Leu$_{51}$/His$_{52}$ are represented in turquoise. The spread of the structural bundles is shown on the right side with the N-terminus pointing out of the plane of the figure. The dots correspond to C$_\alpha$ atoms of residue Gly$_{54}$ in TNFα$_{28-60}$ WT (blue), TNFαAGA/LLL$_{28-60}$ (red) and TNFαS34P$_{28-60}$ (green). The direction of the bend in the bundles is indicated by dotted lines.

Just like in the TNFα$_{28-60}$ WT the TM-N was less stable than the TM-C in both mutants. In TNFαS34P$_{28-60}$ TMD, these helical parts were connected by a less flexible region around Ala$_{42}$Gly$_{43}$Ala$_{44}$, while the entire TNFαAGA/LLL$_{28-60}$ TMD was more stable compared to TNFα$_{28-60}$ WT, especially the mutated area.

Like in the $TNF\alpha_{28\text{-}60}$ WT both mutants possessed conformational flexible cleavage sites, where the α-helix was disrupted.

5 Discussion

Regulated intramembrane proteolysis occurs in the hydrophobic environment of the lipid bilayer, where the transmembrane substrate and enzyme must meet in order to position themselves in a cleavage-competent conformation. For intramembrane cleavage, an interaction between substrate and enzyme is mandatory to access the scissile peptide bond of the substrate. The proteases do not recognize a consensus sequence (Langosch et al. 2015; Beel und Sanders 2008), but cleave their substrates at specific cleavage sites and mutations significantly affect their processivity (Spitz et al. 2020; Götz et al. 2019a; Ortner et al. 2023), according to the flexibility hypothesis (section 1.5.3). Therefore, there must be some determinants, discriminating between a substrate and non-substrate as well as between a good substrate or one that is not efficiently cleaved.

To evaluate the hypothesis that structural features determine the processivity and substrate specificity of intramembrane proteases, substrates of the aspartate proteases γ-secretase and SPPL2a/b were investigated by NMR spectroscopy regarding their 3D structure and dynamic of the TMD. The results indicated that the α-helical TMDs of the investigated peptides and their mutants, which were designed to alter the TMD flexibility, were slightly bent and, in line with the TMD flexibility, the extend and orientation of the bend correlate with the processivity of the corresponding protease.

In the following, the structural and dynamic properties of the substrates TMD and their mutants are discussed in terms of their contribution to the individual mechanistic steps of intramembrane proteolysis and to the substrate requirements.

5.1 Notch1 Intramembrane Cleavage by γ-Secretase

Notch signalling plays fundamental roles in all metazoan (Hori et al. 2013) and is crucially involved in cell-fate determination during development and neurogenesis (Artavanis-Tsakonas et al. 1999; Struhl et al. 1993). γ-secretase cleavage of the Notch1 TMD activates these processes and malfunction in the intramembrane proteolysis can cause dysregulation and diseases like neurodevelopmental defects and cancer (Wong et al. 2004; Weng et al. 2004).

In previous studies, structures of soluble Notch domains, like EGF repeats (Hambleton et al. 2004), NRR (Gordon et al. 2007), ANK and Notch ICD-CSL-MAML transcription factor complex (Nam et al. 2006) were determined, however, only two structures of Notch TMD are available. One of them is a Notch1 TMD NMR-determined structure in DMPC:DHPC bicelles (Deatherage et al. 2017) and the other is a cryo-EM structure of Notch1 TMD in complex with γ-secretase (Yang et al. 2019).

The structure in bicelles mimics the environment of the lipid bilayer and the conformation of Notch1 TMD before the interaction with γ-secretase. The structure in complex with the enzyme represents the active cleavage competent conformation of Notch1 TMD. To achieve a stable substrate-enzyme complex for structure elucidation Pro_{1728} in Notch1 juxtamembrane region and Gln_{112} in PS1 loop1, an area that is thought to have a role in ligand binding (Takagi-Niidome et al. 2015), were mutated to cysteine and cross-linked (Yang et al. 2019). The conformational flexibility of Notch1 TMD was restricted by this cross-linking. The structure of Notch1 TMD in the preceding steps, recognition at the exosite of the protease and transfer to the cleavage competent conformation in the catalytic cavity of γ-secretase is still elusive. During this initial binding and translocation process, the substrate leaves the hydrophobic environment of the lipid bilayer, where its flexibility is restricted by the lateral pressure of the lipids, and enters a new environment of less conformational restriction, the catalytic cavity of γ-secretase that also contains water molecules (Sato et al. 2006).

To mimic the water containing cavity of the protease active site, a mixture of TFE/water, whose polarity approximately matches the interior of the enzyme (Schutz und Warshel 2001; Buck 1998; Tolia et al. 2006), was used in this thesis. The structure of Notch1 TMD in TFE/water provides insights about the dynamic and flexibility of the substrate TMD and thus the accessibility of the cleavable peptide bond and its possible

impact on the processivity during the translocation from the lipid bilayer to the active side of the protease.

Notch1 Mutants and Homologue

Due to the lack of a consensus sequence in the substrate (Beel und Sanders 2008), there should be features other than the amino acid sequence determining a substrate. Based on the flexibility hypothesis that helix stabilizing residues decrease cleavage (section 1.5.3), a mutational screen was performed by our cooperation partners from Munich. They replaced consecutive amino acids of the Notch1 TMD by overlapping sets of 4 leucines and revealed the AAAA motif as the most sensitive region with a significant decrease of about 90% in γ-secretase cleavage, when the alanine tetrad is substituted by leucines (Ortner et al. 2023). This result correlates with findings in APP TMD that mutations in the highly flexible $Val_{36}Gly_{37}Gly_{38}Val_{39}$ hinge influence the TMD flexibility and affect cleavage (Götz et al. 2019b; Barrett et al. 2012). Inspired by these results, not only the $Notch1_{1734\text{-}1757}$ WT TMD, but also the structure and dynamics of the mutant $Notch1L_{1740\text{-}1743}$ TMD, which was assumed to decrease TMD flexibility, were investigated in this thesis.

During this thesis various experimental studies confirmed the flexibility hypothesis for aspartate proteases (Fernandez et al. 2016; Götz et al. 2019a; Götz et al. 2019b), as well as for other proteases (Spitz et al. 2020; Papadopoulou et al. 2022). A further result of the mutational screen performed by our cooperation partner showed an opposite effect of increasing γ-secretase cleavage by mutating the AAAA motif in Notch1 TMD to glycines (Ortner et al. 2023). To assess the effect of the glycine mutation on the structure and dynamic behaviour, this cleavage promoting mutant $Notch1G_{1740\text{-}1743}$ was additionally examined by NMR spectroscopy.

Notably, despite a different sequence the homologue Notch3 shares some structural properties with Notch1 (Theodosiou et al. 2009), such as the flexible part with small amino acids around $Ala_{1649}Gly_{1650}Ala_{1651}$ in its TMD. Compared to Notch1 γ-secretase cleavage was reduced by about 75% in Notch3 (Ortner et al. 2023). To investigate how the homologue influences the interaction with γ-secretase and how this interaction affects the cleavage efficiency, the 3D structure and dynamic was too determined by NMR spectroscopy.

Structural Properties of Notch1 TMD

The slight bend around residues Leu_{1746}/Leu_{1747} in the middle of the entire α-helical $Notch1_{1734-1757}$ WT TMD is only present in the organic solvent determined in this thesis (Figure 5.1, middle structure). In contrast the structure in bicelles (Figure 5.1, left structure) exhibits a straight helix starting at residue Phe_{1732}, where the first turn is located at the water/bilayer interface, just like the residues C-terminal of Ser_{1757} (Deatherage et al. 2015). The helix in both NMR-derived structures is terminated after Ser_{1757} by the cluster of basic residues. Analogue to the investigated $Notch1_{1734-1757}$ WT the helical TMD part in the cryo-EM structure begins at Leu_{1734} (Figure 5.1, right structure), but ends at Val_{1750}, with the last 3 residues in the TMD Leu_{1747}/Phe_{1748}/Phe_{1749} showing a distorted α-helix. From Gly_{1751} the TMD helix in the cryo-EM structure is unwound and adopts a β-strand around Leu_{1755} to Arg_{1761} (Yang et al. 2019).

The tetra alanine motif and S3 cleavage site are approximately in comparable positions within the helical stretches, indicated by the coloured bars in Figure 5.1, when the Notch1 TMD structures in bicelles and TFE/water as well as the cryo-EM structure are displayed in the same orientation. The C-terminal helix packing, however, differs in these structures, from a tight helix in bicelles to a partial unfolded structure in complex with the γ-secretase.

Interestingly, the intrinsic helix-destabilizing properties of Notch1 TMD around the initial cleavage site are already denoted in the bicellar structure by increased ^{15}N relaxations rates for Val_{1754} (Deatherage et al. 2015). This helix disruption can further exert in the investigated $Notch1_{1734-1757}$ WT TMD, culminating in an unfolding beginning at Gly_{1751} in the cryo-EM structure (Yang et al. 2019). Residues C-terminal from Gly_{1751} in $Notch1_{1734-1757}$ WT TMD have already less stable hydrogen bonds and thus allow faster exchange, investigated by HDX measurements in this thesis (Figure 4.7), what correlates with the unfolding of the TM-C in the Notch1 cryo-EM structure. Helix-destabilizing amino acids can promote the transition from a stable helix to a partial unfolding and formation of a β-strand, but it should be noted that the influence of amino acids on helix stability depends on the environment (Li und Deber 1993; Krittanai und Johnson 2000). The helix-destabilizing and β-sheet promoting propensity of valine or isoleucine and even helix-braking propensity of glycine in aqueous solution (Pace und Scholtz 1998) are reversed in the hydrophobic environment of a lipid bilayer (Li und Deber 1994, 1992). Residues such as valine, isoleucine and glycine may promote the formation of a stable Notch1 TMD

α-helix in the membrane but may favour the destabilizing properties upon entry to the water containing cavity of the active site and thus promote instability and unfolding.

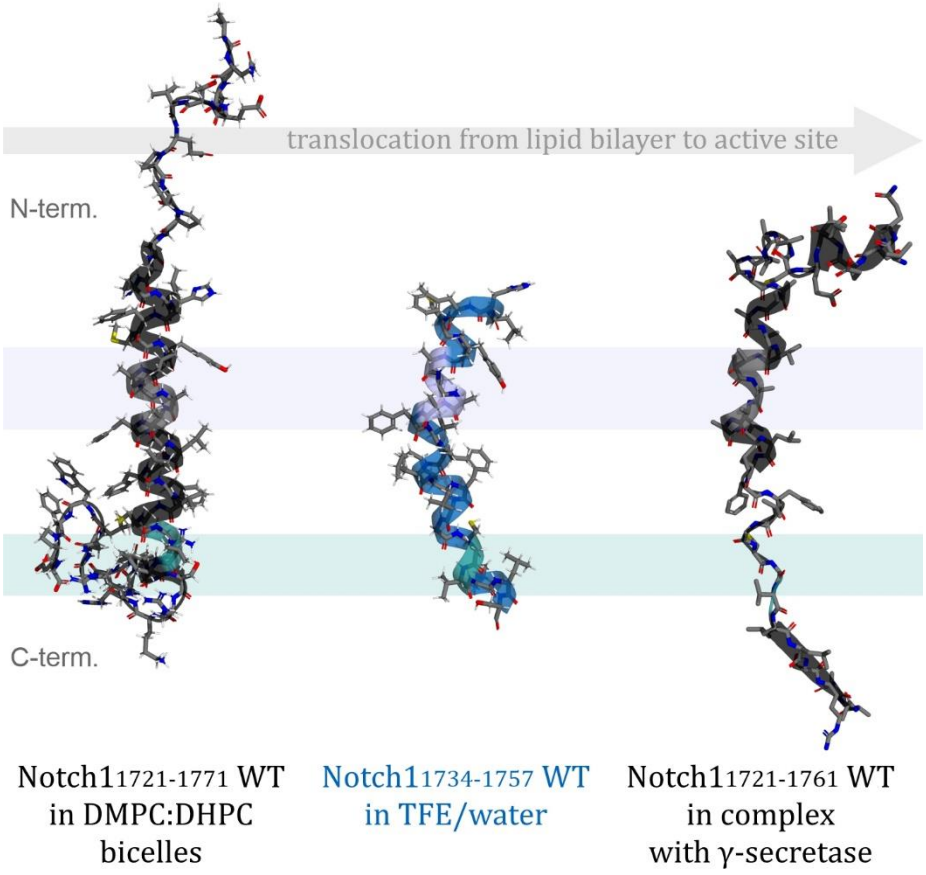

Figure 5.1 NMR and cryo-EM structures of Notch1 WT TMD. Shown are the NMR Notch1$_{1721-1771}$ WT structure in DMPC:DHPC bicelles (5KZO) on the left side, the investigated NMR Notch1$_{1734-1757}$ WT structure in TFE/water in the middle and the cryo-EM Notch1$_{1721-1761}$ WT structure in a complex with γ-secretase (6IDF), where γ-secretase is not shown, on the right side. The region with 4 alanine residues is highlighted in light blue and grey and the S3 cleavage site Gly$_{1753}$/Val$_{1754}$ is represented in turquoise. The coloured bars indicate these regions to compare their position in the different structures.

A hydrogen bond stabilized central part around residue Leu$_{1747}$ in Notch1$_{1734-1757}$ WT TMD as well as a reduced stability towards the termini were determined by HDX measurements (section 4.1.4). The flexibility profile of Notch1$_{1734-1757}$ TMD obtained by NMR HDX measurements here could be confirmed by deuterium hydrogen exchange (DHX) of deuterated Notch1$_{1734-1757}$ TMD also in TFE/water measured by mass spectrometry (Werner et al. 2023; Stelzer und Langosch 2019; Ortner et al. 2023).

In total the TM-N was less stable and thus more flexible than the TM-C not only in TFE/water determined by HDX as well as DHX measurements (Werner et al. 2023; Stelzer und Langosch 2019; Ortner et al. 2023), but also in lipid bicelles (Deatherage et al. 2017).

Compared to Notch1$_{1734\text{-}1757}$ WT, the bend in Notch1L$_{1740\text{-}1743}$ TMD was less pronounced and its direction shifted. Notch3$_{1642\text{-}1665}$ TMD was even little straighter and the direction of the bend shifted even more, while Notch1G$_{1740\text{-}1743}$ TMD showed a wider distribution of possible conformations due to its unstructured central part. In addition, Notch1G$_{1740\text{-}1743}$ destabilized and Notch1L$_{1740\text{-}1743}$ stabilized the TM-N, whereas Notch3$_{1642\text{-}1665}$ stabilized TM-C.

Notch1 Binding to Exosites

In the first step of the proposed cleavage mechanism Notch1 TMD binds to exosites on PEN2, APH1 and NCT (Li et al. 2017; Fukumori und Steiner 2016), in more detail explained in section 1.1.1.3, which guide the substrate to PS1. In silico docking assays revealed an interaction between Ser$_{1757}$ and Arg$_{1758}$ in Notch1 TM-C and Cys$_{158}$ and Tyr$_{159}$ in loop2 of PS1 (Hitzenberger et al. 2020). The high degree of amino acid conservation of the residue Ser$_{1757}$ found in the blast analysis (Figure 4.2) is not only due to the need for appropriate positioning within the lipid bilayer, but could also be based on this initial interaction between Notch1 TMD and PS1. Correct positioning is crucial for the initial contact of Notch1 TMD and PS1. Therefore the presence of basic, positively charged amino acids like arginine or lysine (Xu et al. 2016; Güner und Lichtenthaler 2020), which terminate the substrate TMD helix and place the substrate in the appropriate height within the hydrophobic membrane, might facilitate the first interaction with the enzyme at exosites and subsequent positioning in the active site.

Binding to the exosite is likely to be less affected by the investigated mutants and the homologue Notch3, since the structure within the membrane will adopt a straight helix, comparable to Notch1 TMD in bicelles (Deatherage et al. 2017) due to the lateral pressure of the lipids. The enzyme appears plastic rather than rigid, so structural differences induced by the mutations could evolve after entering the water containing catalytic cavity.

This first binding step not only positions Notch1 in an appropriate orientation towards γ-secretase, but might be decisive whether a transmembrane protein is cleaved as a substrate or rejected from entering the protease remaining a non-substrate. The contact maps, resulting from in silico docking assays, of Notch1, APP and the non-substrate integrin β1 (ITGB1) showed all binding to exosite of PEN2, a checkpoint in substrate

sorting (Hitzenberger et al. 2020). However, only the two substrates Notch1 and APP contacted PS1, albeit at different interaction regions (Figure 5.2), whereas the non-substrate ITGB1 is excluded from interaction with PS1.

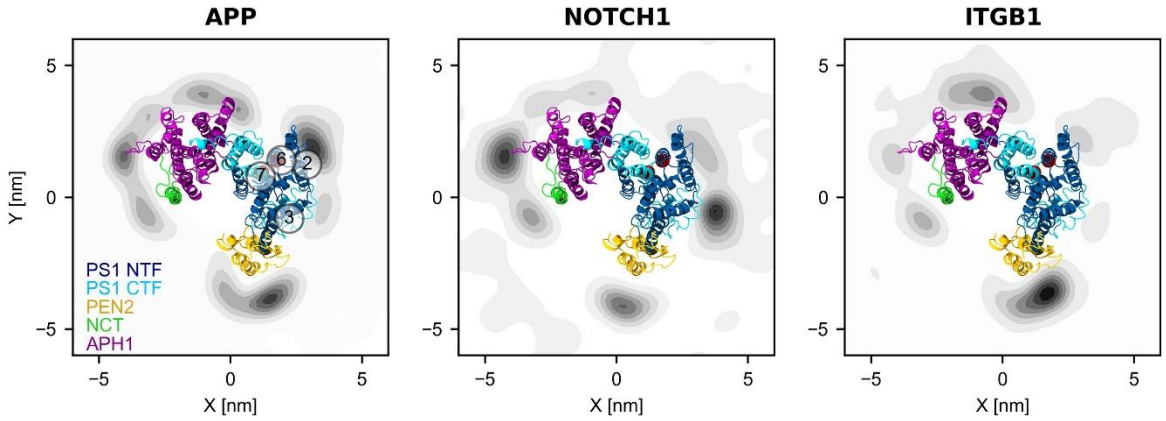

Figure 5.2 Contact densities of substrates and non-substrates with γ-secretase. Exosite binding in POPC found by coarse-grained MD approach of Notch1, APP and ITGB1. Darker grey colour indicates more frequent and/or longer-lasting contacts. PS1 TM2, TM3, TM6 and TM7 are labelled and catalytic aspartates are indicated by spheres. Reprinted from The dynamics of γ-secretase and its substrates, Seminars in Cell & Developmental Biology, Volume 105, 2020, Pages 86-101 (Hitzenberger et al. 2020) with permission from Elsevier.

Translocation

After initial binding to the exosite on PS1, the substrate TMD requires a certain flexibility to enter the interior of the enzyme and translocate to the active site, so the flexible parts of investigated Notch1$_{1734\text{-}1757}$ WT TMD enable translocation into the active site of γ-secretase. The Notch1$_{1734\text{-}1757}$ TMD 3D structure, calculated using chemical shifts data and NOE based distance restraints (section 4.1.3), revealed a slight bend in the middle of the helix (Figure 4.5). The presence of dαN(i, i+2) NOE contacts indicated a shift from α-helical to 3_{10} helical hydrogen bonds favouring twisting motion, what in combination with bending and the flexible parts of the TMD, might facilitate substrate entry and translocation to the active site.

The slight bend in Notch1$_{1734\text{-}1757}$ WT TMD was confirmed by MD simulations showing a certain probability for bending and twisting motions in Notch1 TMD central part (Hitzenberger et al. 2020). However, a highly flexible substrate TMD with a pronounced bend like in APP TMD is not required for γ-secretase cleavage, considering Notch1 TMD

shares a comparable probability for bending and twisting motions with the non-substrate ITGB1 (Hitzenberger et al. 2020).

When the substrate enters the active site of the enzyme, where compared to the membrane it is slightly less conformationally restricted, the influence of mutations acts on the structure. Not only the lateral diffusion but also the translocation could be hampered by the straighter Notch1L$_{1740-1743}$ TMD helix (Figure 4.12) with a more stable TM-N comparted to Notch1$_{1734-1757}$ WT as shown by HDX measurements (Figure 4.13).

In contrast, the TM-N of Notch1G$_{1740-1743}$ was less stable and hence more flexible compared to the Notch1$_{1734-1757}$ WT. The higher flexibility is also noticeable in the 3D structure (Figure 4.12), which is not defined around the glycine mutations due to missing NOE restraints (section 4.2.2). The break in the helix divided the Notch1G$_{1740-1743}$ TMD in two α-helical parts. Because of this significantly more flexible Notch1G$_{1740-1743}$ TMD, the assumption can be made that substrate entry, translocation to the active site, and the achievement of a cleavage competent conformation can occur much faster than in the Notch1$_{1734-1757}$ WT as the cleavage assays of Ortner et al. indicate.

The Notch3$_{1642-1665}$ TMD helix is even slightly straighter than in Notch1L$_{1740-1743}$ TMD (Figure 4.19). While the TM-N of Notch3$_{1642-1665}$ is similar in terms of stability and flexibility to the Notch1$_{1734-1757}$ WT, the TM-C differs and is more stable, evident from more stable hydrogen bonds measured by HDX (section 4.3.5). These two factors, a straighter and less flexible TMD could hinder substrate entry and translocation comparable to Notch1L$_{1740-1743}$ TMD. The flexibility profiles of the mutants and the homologue were confirmed in parallel by DHX of deuterated peptides measured by mass spectrometry (Stelzer und Langosch 2019; Ortner et al. 2023).

Hybrid β-Sheet Formation between PS1 and Notch1

Formation of a hybrid β-sheet between PS1 and Notch1 requires a formation of a β-strand at the TM-C end in Notch1, which is a prior unfolding of the α-helix there. However, α-helix unfolding of the β-strand forming residues cannot be separated from the cleavage site unfolding due to weaker hydrogen bonds in both regions allowing partial helix unfolding. Furthermore, β-strand formation and helix unfolding are not separated processes, but interchange continuously, while the helix starts to unfold and extend the β-strand might develop starting from this extended conformation. For the sake of clarity, the formation of the hybrid β-sheet and the unfolding of the cleavage site are considered separately in the following part.

Once Notch1 has reached the active site of PS1, the binding of Notch1 to PS1 is accompanied by various conformational changes in both the enzyme and the substrate to position the substrate in a cleavage competent orientation and realign important parts of PS1 closer to Notch1 TMD (section 1.1.1.1 and section 1.1.1.3). Briefly, N-terminal juxtamembrane regions in the cryo-EM structure of Notch1 in complex with γ-secretase bind to NCT and loop1 to bring Notch1 TMD in the right orientation closer to the catalytic residues (Yang et al. 2019; Takagi-Niidome et al. 2015). In addition, hydrogen bonds between Notch1 TMD β-strand and Leu_{432} preceding the PAL motif as well as Gly_{1753} at the S3 cleavage site and Gly_{384} within GxGD motif in PS1 further stabilize positioning. Correspondingly, Gly_{1753} is one of the most conserved residues in the Notch1 TMD sequence (Figure 4.2), because of its function to enable access to the cleavage site due to its small size and because it directs the cleavage site in close proximity to the catalytic residues.

Although the above interactions are beneficial for cleavage, the key interaction between Notch1 TMD and PS1 to stabilize the substrate-enzyme complex is the formation of a hybrid β-sheet by hydrogen bonds between the β-strand at the C-terminal end of Notch1 TMD and the antiparallel β-sheet in PS1. Although the TM-C of $Notch1_{1734\text{-}1757}$ WT was more stable than the TM-N, the TMD helix was flexible towards the termini and hydrogen bonds C-terminal of Gly_{1751} in the TM-C of $Notch1_{1734\text{-}1757}$ WT were markedly destabilized (Figure 4.7), favouring unwinding of the helix and formation of a more extended β-strand conformation. Both mutants show hydrogen bond stabilities comparable to $Notch1_{1734\text{-}1757}$ WT TMD at residues C-terminal of the initial cleavage site (Figure 4.22).

No cryo-EM structure of Notch3 TMD exists, but based on the analogy to Notch1 and the residues following the initial cleavage site Val_{1664} and Ala_{1665} as well as the destabilized hydrogen bonds C-terminal of the cleavage site (Figure 4.20), it might be assumed that in Notch3 as well the helix at the C-terminal end of the TMD is unwound and adopts a β-strand. Although the β-strand might be formed with a lower propensity, considering alanine has a low propensity to form β-strands (Street und Mayo 1999) and there are only two residues between the cleaved residue and the basic anchor. This together with the more stable TM-C, compared to $Notch1_{1734\text{-}1757}$ WT, could impede the formation of the β-strand and hybrid β-sheet between Notch3 and PS1, leading to less efficient cleavage.

Notably, the non-substrate ITGB1 showed a clear and constant hydrogen bond stability within the TM-C additionally towards the C-terminus (Julia Flum, data unpublished), which may hinder the unwinding of the helix at the C-terminal end of the TMD and prevent the formation of a β-strand, inhibiting enzyme access to the scissile peptide bond.

Besides the propensity to adopt a β-strand, another determinant influencing the cleavage must be considered, such as the orientation of the TM-N with respect to TM-C, and therefore, the positioning of the β-strand within the active site of PS1.

To evaluate how Notch1 TMD might interact with PS1, the Notch1$_{1734\text{-}1757}$ WT NMR bundle (Figure 4.5 (a)) was superimposed to the cryo-EM structure of Notch1 TMD in complex with γ-secretase. The Notch1$_{1734\text{-}1757}$ WT bundle fitted approximately into the catalytic cavity, but 12/40 structures slightly collided with TM7. To reiterate, the structural bundles do not represent any dynamics but indicate the possible conformational variability that cannot be resolved by the experimentally determined NOE restraints. Leu$_{1756}$ C$_\alpha$ atoms, one of the β-sheet forming residue in the substrate, were chosen to visualize the respective orientation of the structural bundles, reflecting the possible interaction with PS1 (Figure 5.3). Most of Leu$_{1756}$ C$_\alpha$ atoms cluster around the antiparallel β-sheet in PS1 in spatial proximity and thus at a distance possibly promoting the formation of the hybrid β-sheet to stabilize the enzyme-substrate complex and prime the cleavage competent orientation to form the tetrahedral intermediate.

The substrate enzyme interaction of the leucine mutant was compared to the Notch1$_{1734\text{-}1757}$ WT by superimposing the Notch1L$_{1740\text{-}1743}$ NMR bundle (Figure 4.12 (b)) to the Notch1$_{1734\text{-}1757}$ WT NMR structure in the cryo-EM enzyme-substrate complex. Due to a less pronounced bend and shifted orientation by about 60° of the Notch1L$_{1740\text{-}1743}$ bundle compared to Notch1$_{1734\text{-}1757}$ WT, the major part of the TM-C helices was directed towards TM6 of PS1 and therefore 17/40 structures collided with TM2 and the loop between TM6 and TM7. In general, the Notch1L$_{1740\text{-}1743}$ TMD bundle seemed to fit less well into the cavity of the enzyme active site compared to Notch1$_{1734\text{-}1757}$ WT, and additionally the Leu$_{1756}$ C$_\alpha$ atoms were in a less favourable orientation to enable the interaction with PS1 β-sheet forming residues (Figure 5.3).

In case of the Notch1G$_{1740\text{-}1743}$ bundle, the superposition of the NMR structure to the cryo-EM structure was of limited value. The Notch1G$_{1740\text{-}1743}$ NMR bundle (Figure 4.12 (c)) was aligned along the Notch1$_{1734\text{-}1757}$ WT NMR structure in the cryo-EM enzyme-

substrate complex. The major part of the TM-C helices of Notch1G$_{1740-1743}$ was directed towards TM5 and TM7 and as a result of the less defined orientations of TM-N with respect to TM-C 23/40 structures collided with several PS1 TMDs (Figure 5.3). Due to a higher Notch1G$_{1740-1743}$ TMD flexibility caused by the missing side chains of the central glycines and a distinctly higher conformational flexibility of the possible orientations, where the TM-N with respect to the TM-C is less restricted, the access to the active site might be facilitated and thus enhance the processivity.

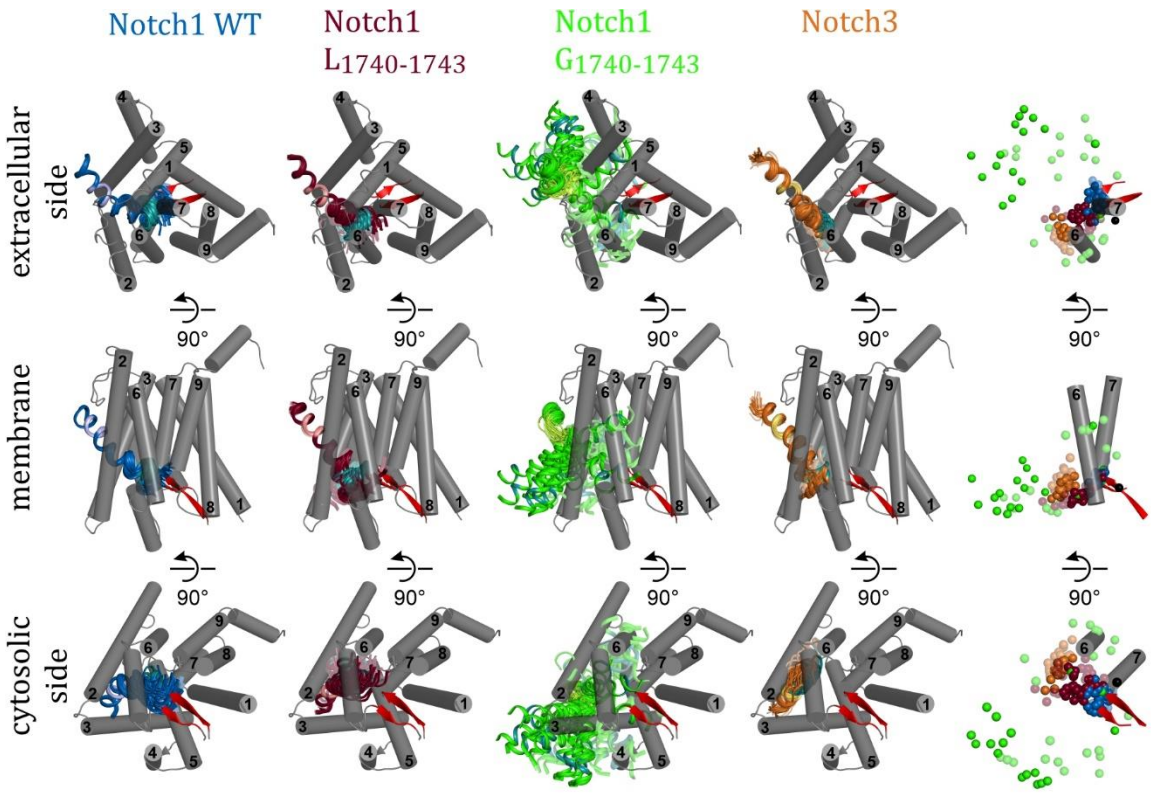

Figure 5.3 Enzyme-substrate complex: Notch and PS1. Extracellular, membrane and cytosolic view of the Notch-PS1 complex. The Notch1$_{1734-1757}$ WT bundles (blue), Notch1L$_{1740-1743}$ (red), Notch1G$_{1740-1743}$ (green) and Notch3$_{1642-1665}$ (orange) are aligned to Notch1 TMD (not shown) in the cryo-EM structure of γ-secretase (6IDF, (Yang et al. 2019)). The alanine tetrad and respective mutated residues as well as AGA motif are coloured more lightly. The S3 cleavage site Gly$_{1753}$/Val$_{1754}$ in Notch1 and Val$_{1662}$/Met$_{1663}$ in Notch3 is represented in turquoise. Of the γ-secretase subunits only PS1 is shown in grey with numbered TMDs. The β-sheet forming residues in the loop between TM6 and TM7 and the N-terminal TM7 are highlighted in red. The right column illustrates the position of Leu$_{1756}$ C$_\alpha$ atoms in Notch1 and Val$_{1664}$ C$_\alpha$ atoms inNotch3 as dots, where the black dot corresponds to Leu$_{1756}$ C$_\alpha$ atom of cryo-EM Notch1 TMD. For clarity only TM6, TM7 and the β-sheet are shown. Structures with distances of less than 3 Å to PS1 and thus colliding with them are displayed transparent.

$Notch3_{1642-1665}$ TMD aligned onto Notch1 WT NMR structure in the cryo-EM enzyme-substrate complex (Figure 5.3) shifted the orientation by about 90° compared to $Notch1_{1734-1757}$ WT. TM-C helices were oriented towards TM2 and 23/40 structures collided slightly with TM2, as well as the loop between TM6 and TM7. The shifted orientation of the $Notch3_{1642-1665}$ bundle moved them further away from the β-sheet forming residues in PS1, and thereby hindering the interaction of the substrate and enzyme (Figure 5.3).

The fact that the TMD helix is bent and the orientation of the bend is affected by mutations (Silber et al. 2020), which could influence the interaction with the enzyme, is also evident in another well-studied γ-secretase substrate APP. Surprisingly, in APP TMD both mutations of residue Gly_{38} to either a helix-stabilizing leucine or a helix-breaking proline (Altmann et al. 1990; Heijne 1991) resulted in reduced cleavage (Götz et al. 2019b), which cannot be explained according to the flexibility hypothesis. The formation of a β-strand in APP TMD was confirmed by the cryo-EM structure of APP in complex with γ-secretase (Zhou et al. 2019). This enables to evaluate the influence of the mutations to the orientation of the substrate TMD within the active site and formation of a hybrid β-sheet between APP and PS1 using the simple model of superimposing NMR structures to the cryo-EM structure.

To compare the γ-secretase interaction of APP and its mutants the APP_{29-51} WT NMR bundle was aligned to the cryo-EM APP TMD. C_α atoms of Met_{51} were chosen to visualize the orientation of the NMR bundle in the active site. The major part of TM-C helices in APP_{29-51} WT bundle pointed towards TM7 and TM2, slightly colliding with TM5 and TM3, so that the TM-C ends are located near by the β-sheet forming residues (Figure 5.4), enabling a stabilizing interaction with the antiparallel β-sheet in PS1. Because of the different extent and orientation of the bend in G38L and G38P, their bundles are directed away from TM7 towards TM6/TM2 and might hinder the formation of the hybrid β-sheet, therefore the cleavage might be reduced in both mutants.

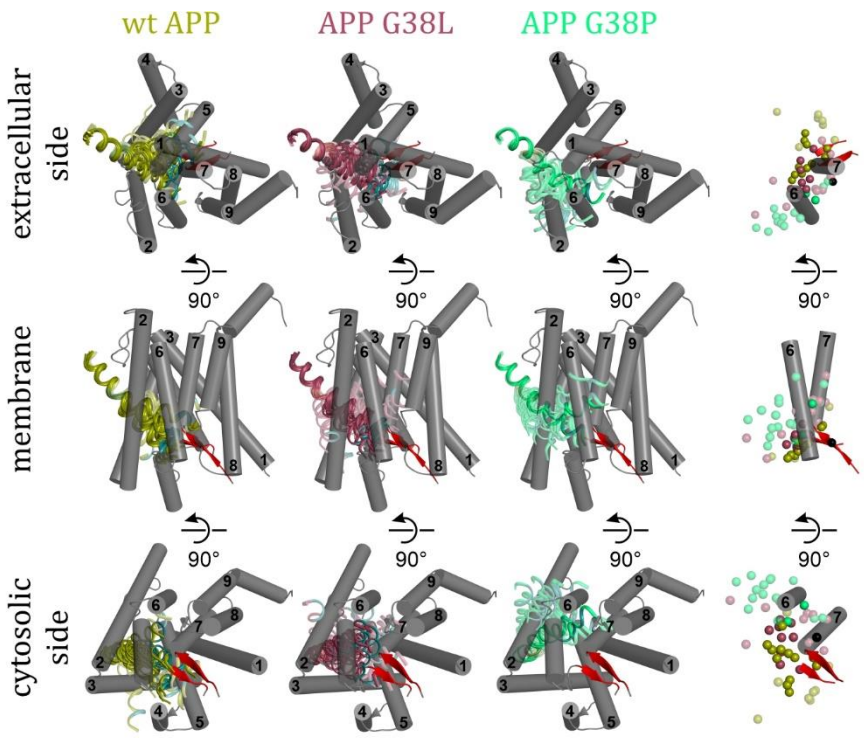

Figure 5.4 Enzyme-substrate complex: APP and PS1. Extracellular, membrane and cytosolic view of the APP-PS complex. The APP_{29-51} WT bundle (olive), G38L (pink) and G38P (light green) are aligned to APP TMD (not shown) in the cryo-EM structure of γ-secretase (6IYC, (Zhou et al. 2019)). The GG motif is highlighted in the corresponding light shade. The ε-cleavage site Leu_{49}/Val_{50} is shown in turquoise. Of the γ-secretase subunits only PS1 is shown in grey with numbered TMDs. Residues forming β-sheets in PS1 are highlighted in red. The right column illustrates the position of Met_{51} C_α atoms as dots. In black is shown Met_{51} C_α atom of cryo-EM APP TMD. For clarity only TM6, TM7 and the β-sheet are shown. Structures within a distance of less than 3 Å to PS TMD and thus colliding with them are displayed transparent.

The intrinsic orientation of the bend in substrate TMD causes the TM-C end within the active site to arrange towards the β-sheet in PS1 allowing interaction with it. When a mutation-induced conformational change in the orientation of the bend results in the TM-C end pointing in another direction, thus impairing the interaction with the β-sheet, then the formation of the hybrid β-sheet between a substrate and enzyme and the influence of mutations in the substrate to this interaction can nonetheless be roughly estimated with this simple overlay method, not only for the Notch1-PS1 but also for the APP-PS1 complex.

Cleavage Site Unfolding in Notch1

After Notch1 TMD adopts a cleavage competent orientation within the active site of PS1, a partial unfolding of the cleavage site is required to enable the enzyme access to the scissile peptide bond. The disruption of a regular α-helix in Notch1$_{1734-1757}$ WT TMD around the initial cleavage site S3 at residues Gly$_{1753}$/Val$_{1754}$ and less pronounced around the S4 cleavage site, located within the alanine tetrad, was indicated by secondary chemical shifts and NOE contacts together with the helix probability and order parameter S^2 (section 4.1.2). A 3_{10} helical contribution in Notch1$_{1734-1757}$ WT TMD, indicated by the presence of dαN(i, i+2) NOE contacts around the cleavage sites (Figure 4.4), points to some instabilities, which most likely induce flexibility. Positions in Notch1 TMD with an enhanced 3_{10} helical content were confirmed by MD simulation (Hitzenberger et al. 2020). Deviations from stable α-helices with weakened α-helical hydrogen bonds between a residue and the fourth residue further C-terminal (i → i+4) are compensated by the formation of 3_{10} helical hydrogen bonds (i → i+3) and thus represent intermediates in the unfolding of α-helices (Kentsis et al. 2004).

This destabilization of the S3 cleavage site in Notch1$_{1734-1757}$ WT TMD was also reflected by faster exchange with larger residue-specific HDX rate constants (Figure 4.22). Furthermore, both mutants and the homologue show the same extend of a destabilized and partial unfolded initial cleavage site. Therefore, exactly this mechanistic step, where the initial cleavage site partially unfolds and the two catalytic aspartates attach together with a water molecule to the scissile peptide bond, forming a tetrahedral cleavage intermediate, is presumably unaffected by the mutants and the homologue. In contrast S4 cleavage site stability is altered by the mutants, so that Notch1L$_{1740-1743}$ impedes the unfolding by stabilizing the helix and Notch1G$_{1740-1743}$ destabilize the cleavage site facilitating the unwinding. These effects might influence the accessibility of γ-secretase to the S4 cleavage site and intramembrane proteolysis of the last cleavage step.

In general, the stability of the helix at the cleavage site and the accessibility to the scissile peptide bond are decisive for proteolytic cleavage. A mutational screen of the Notch1 TM-C revealed that bulky and sterically demanding amino acids at positions Gly$_{1753}$ and Val$_{1754}$ at the initial cleavage site could hinder the access to the scissile peptide bond and formation of the tetrahedral intermediate, decreasing the γ-secretase cleavage (Ortner et al. 2023). Simultaneously, these bulky residues have often a higher propensity to form α-helices (Krittanai und Johnson 2000), and additionally might impede unfolding

and access of PS1. Whereas small amino acids with a low helical propensity could favour unwinding and thus access to the scissile peptide bond.

However, a highly flexible cleavage site is not required but affects γ-secretase cleavage, since the cleavage site in APP TMD is located within the most stable part of the TMD (Götz et al. 2019b), the processivity is decreased compared to the Notch1 TMD bearing a more flexible initial cleavage site (Ortner et al. 2023).

In summary, certain regions within the TMD of Notch1 with their specific structural and dynamic properties influence the individual mechanistic steps of intramembrane proteolysis with γ-secretase. These characteristic structural properties can also be transferred from the substrate Notch1 to other substrates that have analogous effects on proteolysis with γ-secretase. Whether the structural features of the enzyme and substrate and their interaction can be applied to other proteases and their substrates in addition to γ-secretase will be clarified in the next section.

5.2 TNFα Intramembrane Cleavage by SPPL2a

In the following, the structural and dynamic properties of TNFα and two mutants will be discussed again regarding the individual mechanistic steps of intramembrane proteolysis. But before that, the predicted structure of TNFα-SPPL2a/b complex is explained considering no experimentally determined structure of the complex exists.

Structure Prediction of TNFα-SPPL2a/b Complex

Members of the SPP/SPPL family and of the PS family, both belong to intramembrane aspartyl proteases and share the characteristic GxGD, YD and PAL motifs (Weihofen et al. 2002). Given their common characteristics, it stands to reason that they might also share a common cleavage mechanism. Structures of TNFα are only available of the TNFα soluble domain, which forms a homotrimer (Reed et al. 1997; Niu et al. 2022),but there is neither a structure of TNFα TMD nor of the protease SPPL2a or of the complex.

In order to estimate how TNFα interacts with SPPL2a/b and what influence TNFα mutations have on this interaction, the structure of $TNF\alpha_{28\text{-}60}$ in complex with SPPL2a and SPPL2b was predicted by AlphaFold2 (Mirdita et al. 2022). Several models are predicted by AlphaFold and the best 5 are selected according to a predicted local distance difference test (pLDDT) score. A high-confidence structural model of SPPL2a (Figure 5.5 (a)) shows that the 9 TMD helices are arranged analogous to PS1 in the cryo-EM structure (6IDF) (Yang et al. 2019) with similar positions of the catalytic aspartates and an antiparallel β-sheet between TM6 and TM7, but compared to the cryo-EM structure only half of the β-sheet was predicted by AlphaFold. In addition, the N-terminal part of the predicted SPPL2a forms a globular domain, which might represent a kind of extracellular lid and is reminiscent of NCT.

The binding conformation of the predicted $TNF\alpha_{28\text{-}60}$ TMD is analogous to Notch1 TMD in the cryo-EM structure, where $TNF\alpha_{28\text{-}60}$ TMD is located within the catalytic cavity, surrounded by TM2, TM3, TM5, TM6 and TM7 and the C-terminal end is directed towards the antiparallel β-sheet in SPPL2a (Figure 5.5 (a) zoom). Apart from the unstructured C-terminus in SPPL2b, which is not shown in Figure 5.5 (b), the predicted structures of SPPL2a/b differ only in peripheral areas.

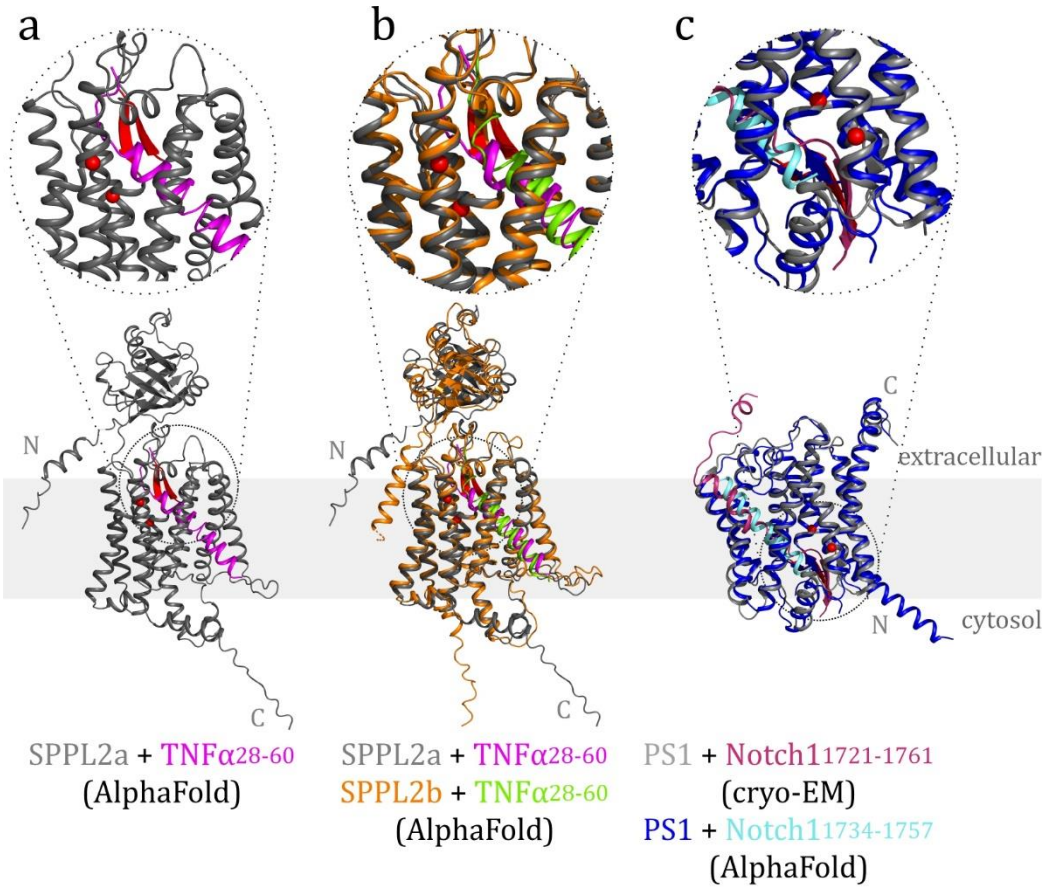

Figure 5.5 Structure of SPPL2a and SPPL2b in complex with TNFα predicted with AlphaFold2. Shown is the predicted structure of SPPL2a (grey) in complex with TNFα$_{28-60}$ TMD (magenta) (a) aligned on the predicted structure of SPPL2b (orange) in complex with TNFα$_{28-60}$ (green) (b). The unstructured C-terminal part in SPPL2b, residues 520-592, is not shown. The cryo-EM structure of PS1 (grey) in complex with Notch1$_{1721-1761}$ (pink) (6IDF) is aligned on the predicted structure of PS1 (blue) in complex with Notch1$_{1734-1757}$ (cyan), here the unstructured N-terminus (1-56) and a part of the large loop between TMD6 and TMD7 (294-373) of predicted PS1 are not shown (c). All structures were predicted with AlphaFold2. C$_\alpha$ atoms of the catalytic aspartates and β-sheet, formed between TM6 and TM7, are marked in red. The areas marked by a circle are shown enlarged above the complex structures. The grey bar indicates schematically the membrane.

To check whether AlphaFold can reflect the crucial structural features in an enzyme-substrate complex, the cryo-EM structure of Notch1$_{1721-1761}$ in complex with γ-secretase was compared with the AlphaFold structure of Notch1$_{1734-1757}$ TMD in complex with PS1 (Figure 5.5 (c)). The position of the β-sheet in PS1 and position of the substrate, directing its C-terminal end towards the β-sheet in PS1 (Figure 5.5 (c) zoom), was predicted analogous to the cryo-EM structure. AlphaFold uses a multiple sequence alignment (MSA)

to get structure information from homologous proteins and pairwise evolutionary correlations to calculate a structure on basis of this information with a neural network (Jumper et al. 2021). Possibly AlphaFold uses the cryo-EM structure of Notch1-PS1 in MSA and therefore the predicted structure is so similar, this could also apply to the prediction of SPPL2a/b. The structure prediction is limited, when there are no ore only few co-evolutionary homologous protein structures. The predicted substrate-enzyme complex structures must be checked for plausibility. It is important to note that the prediction of the substrate TMD alone without enzyme shows only straight helices without structural variation. Nevertheless, and also due to the homology to PS1, the AlphaFold structure of SPPL2a can be used to estimate the interaction of the investigated NMR structures with the enzyme.

The cleavage competent conformation of TNFα TMD is represented by the predicted structure in the enzyme-substrate complex. The structure in a lipid environment, before the first interaction with SPPL2a, can be estimated using the $TNF\alpha_{22\text{-}62}$ TMD structure in POPC bilayer determined by MD simulation (Spitz et al. 2020). Correspondingly, analogous to the investigated Notch1 TMD, the structure of TNFα TMD in TFE/water links the conformation from a hydrophobic lipid environment during the translocation to an active cleavage competent conformation in the catalytic cavity containing water molecules.

TNFα Mutants

Like γ-secretase, SPPL2a also does not recognize a substrate consensus sequence, so presumably structural properties like the substrate TMD flexibility are decisive for intramembrane proteolysis (Hitzenberger et al. 2020; Langosch et al. 2015; Langosch und Steiner 2017). Based on the flexibility hypothesis (section 1.5.3), our cooperation partner from Munich performed mutational investigations on non-canonical shedding of TNFα by SPPL2a. They examined if mutations of Gly_{43} within the flexible AGA motif and mutation in diverse cleavage sites influence proteolysis (Spitz et al. 2020).

While mutations to helix-destabilizing proline (Cordes et al. 2002; Heijne 1991) enhanced non-canonical shedding, substitutions with helix-stabilizing leucines (Quint et al. 2010) had only minor effects on non-canonical shedding, except at the positions of both C-terminal cleavage sites. After mutation of flexibility-promoting Gly_{43} to leucine showed also only a minor effect, the entire AGA motif was replaced with leucines, what significantly reduced non-canonical shedding (Spitz et al. 2020). Based on these

experimental data, two mutants were designed, where the N-terminal Ser_{34} was substituted by proline TNFαS34P$_{28-60}$ and the $Ala_{42}Gly_{43}Ala_{44}$ was replaced by leucine triad TNFαAGA/LLL$_{28-60}$. To investigate how the mutants influence the interaction with SPPL2a/b and how this interaction affects the non-canonical shedding and the cleavage efficiency, the 3D structures and dynamics were determined by NMR spectroscopy in this thesis.

Structural Properties of TNFα TMD

The α-helical TNFα$_{28-60}$ WT TMD investigated in this thesis, covering residues Cys_{30}/Leu_{31} to His_{52}/Phe_{53} indicates a slight bend around $Ala_{42}Gly_{43}Ala_{44}$ (Figure 5.6, blue structure) in organic solvent. The predicted AlphaFold complex structure shows a cleavage competent conformation (Figure 5.6, right structure), where TNFα resides within the active side and has a straight TMD reaching from Arg_{29} to Phe_{53}. The MD simulation of TNFα in POPC bilayer suggests a straight TMD helix in the membrane (Spitz et al. 2020), therefore the structure of TNFα alone without the enzyme was predicted by AlphaFold to obtain a representation analogous to that in Figure 5.1. The predicted TNFα$_{28-60}$ TMD AlphaFold structure shows a straight TMD helix, comparable to the structure simulated in POPC lipids, ranging from Arg_{29} to Phe_{53} (Figure 5.6 left structure).

The area around the central $Ala_{42}Gly_{43}Ala_{44}$ motif in TNFα$_{28-60}$ TMD is characterized by a higher flexibility, especially residues Gly_{43} to Thr_{46} reveal destabilized hydrogen bonds examined by HDX measurements in this thesis (section 4.5.4). The increased occurrence of dαN(i, i+2) NOE contacts in exactly this region indicates a 3_{10} helical contribution and distortion of a regular α-helix (Figure 4.26), which is in line with weakened hydrogen bonds. Surprisingly the AlphaFold prediction was able to reproduce this destabilized central part from Gly_{43} to Thr_{46}, where the secondary structure is not defined (Figure 5.6, right structure), but not in the prediction of TNFα$_{28-60}$ TMD without the enzyme (Figure 5.6, left structure).

The flexible part links the TM-N with a more stable TM-C, where the flexibility increases towards the N- and C-terminal ends. The trends in the flexibility profile of TNFα$_{28-60}$ TMD were confirmed by DHX of deuterated peptides in TFE/water measured by mass spectrometry (Spitz et al. 2020). The most dynamic and flexible region of TNFα$_{28-60}$ TMD starts C-terminal after the initial cleavage site Leu_{51}/His_{52} and was characterized non-helical according to the secondary chemical shifts and NOE contacts (section 4.5.2). Analogous to the Notch1 TMD and its β-strand residues Leu_{1755}/Leu_{1756}/Ser_{1757}, the β-

branched residues Val_{55} and Ile_{56} (Pace und Scholtz 1998) in $TNF\alpha_{28\text{-}60}$ TMD might adopt, together with Gly_{57}, a β-strand without the need of prior unfolding to interact with the antiparallel β-sheet in SPPL2a. A special function of these residues Val_{55}/Ile_{56}/Gly_{57} is also reflected in their high sequence conservation (Figure 4.24).

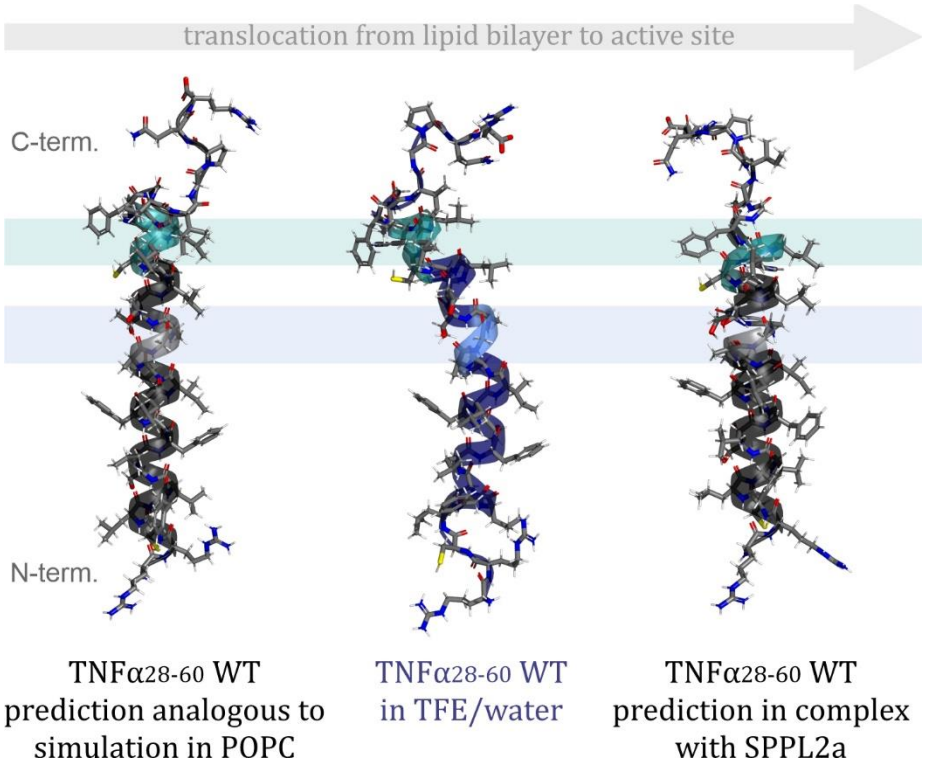

Figure 5.6 NMR and AlphaFold structures of TNFα WT TMD. Shown is a straight $TNF\alpha_{28\text{-}60}$ TMD AlphaFold structure analogous to the MD simulation in POPC bilayer on the left side. The investigated NMR $TNF\alpha_{28\text{-}60}$ WT structure in TFE/water is demonstrated in the middle. AlphaFold $TNF\alpha_{28\text{-}60}$ WT structure in complex with SPPL2a (enzyme not displayed), is shown on the right. Region with AGA motif is highlighted in light blue or grey. The initial cleavage sites Cys_{49}/Leu_{50} and Leu_{51}/His_{52} are represented in turquoise. The coloured bars indicate these regions to compare their position in the different structures.

The cleavage sites in $TNF\alpha_{28\text{-}60}$ TMD are defined by a drop in the flexibility profile (Figure 4.28), which are particularly noticeable at the both C-terminal cleavage sites Cys_{49}/Leu_{50} and Leu_{51}/His_{52}, indicating a faster exchange enabled by less stable hydrogen bonds and partial unfolding. The destabilization within the cleavage sites is also reflected in the predicted $TNF\alpha_{28\text{-}60}$ TMD structure in complex with SPPL2a by a deformed helix with a larger helix radius around the cleavage site (Figure 5.6, right structure). Furthermore, reduced helix probability and order parameter S^2, especially in the case of the N-terminal cleavage sites, as well as reduced secondary chemical shifts and the absence of helix-

typical NOE contacts (Figure 4.26) point to a destabilization of the helix in the cleavage sites, so that the scissile peptide bond becomes accessible to the enzyme.

Compared to TNFα$_{28-60}$ TMD the bend in TNFαAGA/LLL$_{28-60}$ TMD was less pronounced and its orientation shifted. In TNFαS34P$_{28-60}$ TMD the bend was even less pronounced, but the structures in the bundle clustered around the helix axis. In addition, the entire TMD was stabilized in the leucine mutant, especially in the central part, while the flexibility profile in TNFαS34P$_{28-60}$ TMD was similar to TNFα$_{28-60}$ WT TMD.

TNFα Binding to Exosite and Non-Canonical Shedding

Binding to the exosite is probably less affected by the mutations, since TNFα might adopt a straight structure in membrane (Figure 5.6, left structure) like Notch1 TMD in bicelles (Deatherage et al. 2017). Regardless of mutations, however the subsequent step of entering the enzyme is likely to be significantly influenced by the structural and dynamic properties of the substrate (section 1.5.2).

In general, intramembrane aspartyl proteases efficiently cleave substrates with an ectodomain no longer than 50 amino acids, which were truncated in the first step of intramembrane proteolysis or have a naturally short ectodomain (Martin et al. 2009; Lichtenthaler et al. 2018; Güner und Lichtenthaler 2020; Struhl und Adachi 2000). The size exclusion of some substrates might be regulated by the intrinsic steric properties of the protease or a co-factor. For example, in PS1 the extracellular domain of NCT functions as a lid on the enzyme (Figure 5.7 (a)) and acts as a gatekeeper (Bolduc et al. 2016), so that substrates with a long ectodomain are processed only with a low efficiency (Schauenburg et al. 2018).

The extracellular domain of SPPL2a/b (Figure 5.7 (b)), which is smaller compared to NCT, is also positioned like a lid on top of the extracellular site and might exclude substrates with long ectodomains. Nevertheless, TNFα FL is cleaved by SPPL2a but not by SPPL2b (Spitz et al. 2020). Despite the same extracellular domain size, the stricter size exclusion in SPPL2b could be due to an additional glycosylation site between TM6 and TM7, whose glycosidic chain protrudes in the extracellular space (Friedmann et al. 2004; Spitz et al. 2020). Interestingly, TNFαS34P with a slightly more flexible TM-N and a different orientation of the TMD compared to TNFα WT (Figure 4.34 and Figure 4.33), increases not only the non-canonical shedding by SPPL2a but also enables the non-canonical shedding of full-length TNFαS34P (TNFαS34P FL) by SPPL2b (Spitz et al. 2020).

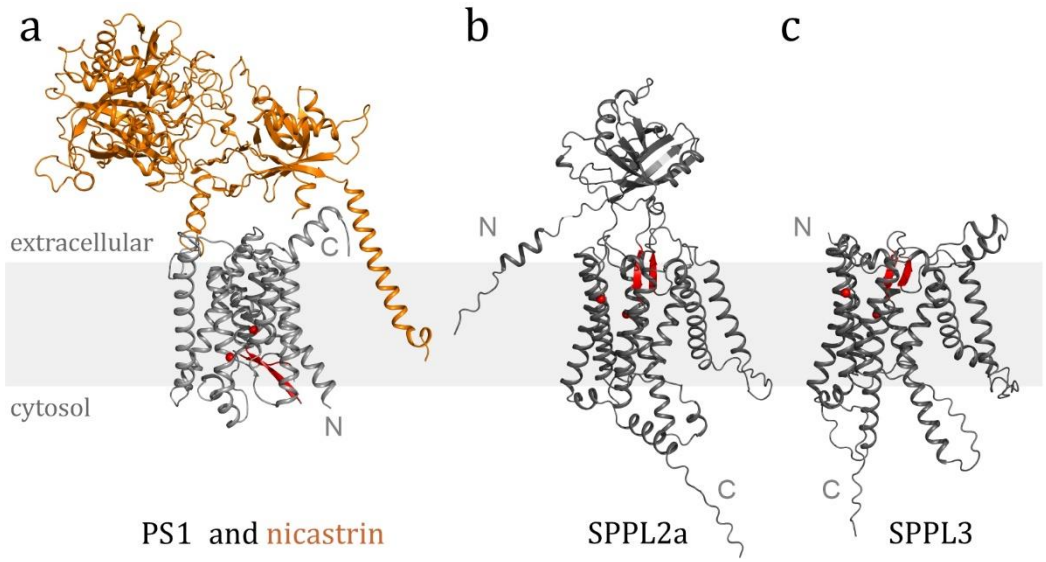

Figure 5.7 Extracellular domains of PS1, SPPL2a and SPPL3. Shown is the cryo-EM structure (a) of PS1 in complex with Notch1$_{1721\text{-}1761}$ (grey) and the co-factor NCT (orange) with a large extracellular domain (6IDF). The predicted AlphaFold structure of SPPL2a in complex with TNFα$_{28\text{-}60}$ (b) shows a smaller and SPPL3 in complex with GnTV$_{13\text{-}38}$ (c) no extracellular domain. The substrates are not shown in the enzyme structures. C_α atoms of the catalytic aspartates and β-sheet, formed between TM6 and TM7, are marked in red. The grey bar indicates schematically the membrane.

Since SPPL3 has no extracellular domain due to its short N-terminus (Friedmann et al. 2004) (Figure 5.7 (c)) and presents no steric hindrance hence substrates are cleaved directly without prior ectodomain shedding (Voss et al. 2013; Voss et al. 2012; Kuhn et al. 2015). Non-canonical shedding correlates with the steric properties of the enzyme and the flexibility of the substrate, such that the lower the steric hindrance by an extracellular domain and the higher the substrates TMD flexibility, the more non-canonical shedding may occur.

Translocation

As already discussed, following the enzyme entry the substrate has to translocate to the active site and reach a cleavage competent orientation. TMD flexibility is thought to affect this process. Mutations of Gly$_{43}$ to helix favouring alanine or leucine, reducing the TMD flexibility, had only minor effects to non-canonical shedding by SPPL2a, considering the flanking alanines with its small side chains might maintain the flexibility of the single mutants in AGA motif.

Mutating the whole AGA motif by rigidifying leucines reduced non–canonical cleavage (Spitz et al. 2020). Leucine mutations stabilized the central part in TNFαAGA/LLL$_{28-60}$ TMD from Val$_{41}$ to Phe$_{48}$ evident from the secondary chemical shifts, NOE data (section 4.6.2) as well as HDX measurements (4.6.4). This might impede the substrate entry and/or the translocation.

In contrast, proline mutation of Gly$_{43}$ as well as Ser$_{34}$ and Ser$_{37}$ not only favour the non-canonical shedding by SPPL2a but also enable the non-canonical shedding by SPPL2b (Spitz et al. 2020). Proline disturbs the helix geometry, since it lacks the amide hydrogen, it cannot form a hydrogen bond to the main chain carbonyl oxygen at residue (i-4) and in addition the bulky cyclic side chain might clash with the previous residue (Cordes et al. 2002). Because of this, the helix in TNFαS34P$_{28-60}$ TMD was shifted by a few residues. Starting from Phe$_{32}$/Leu$_{33}$, the TMD helix was further extended C-terminally to Val$_{55}$/Ile$_{56}$. This C-terminal shift of the TNFαS34P$_{28-60}$ helix demonstrated by secondary chemical shifts, the helix probability and NOE contacts examined in this thesis (section 4.6.2) was confirmed by MD simulations (Spitz et al. 2020). The faster exchange and occurrence of dαN(i, i+2) NOE contacts in the TNFαS34P$_{28-60}$ TM-N indicate a slight destabilization of the hydrogen bonds and a more flexible TM-N compared to TNFα$_{28-60}$ WT, facilitating the translocation to the active site or passing the extracellular domain while entering the enzyme.

Hybrid β-Sheet Formation between SPPL2a and TNFα

As already mentioned, the unfolding of the β-sheet forming residues, as a prerequisite for β-strand formation in the substrate and hybrid β-sheet formation between substrate and enzyme, as well as the unfolding of the initial cleavage site are not separated processes, but will be discussed separately for clarity.

The next step on the mechanistic route is the cleavage competent positioning within the active site. Since the predicted structure of SPPL2a in complex with TNFα TMD is analogous to the cryo-EM structure of PS1 in complex with Notch1 TMD, it stands to reason that the C-terminal end of the TNFα TMD might also adopt a β-strand to interact with the enzyme and position itself in a cleavage competent distance to the catalytic aspartates. The area in the C-terminal end of TNFα$_{28-60}$ WT around residues Val$_{55}$Ile$_{56}$Gly$_{57}$ is already unwound and characterized by weak hydrogen bonds (Figure 4.28). This part is stabilized in TNFαS34P$_{28-60}$ compared to TNFα$_{28-60}$ WT and even more stable in TNFαAGA/LLL$_{28-60}$, possibly affecting the formation of the putative β-strand.

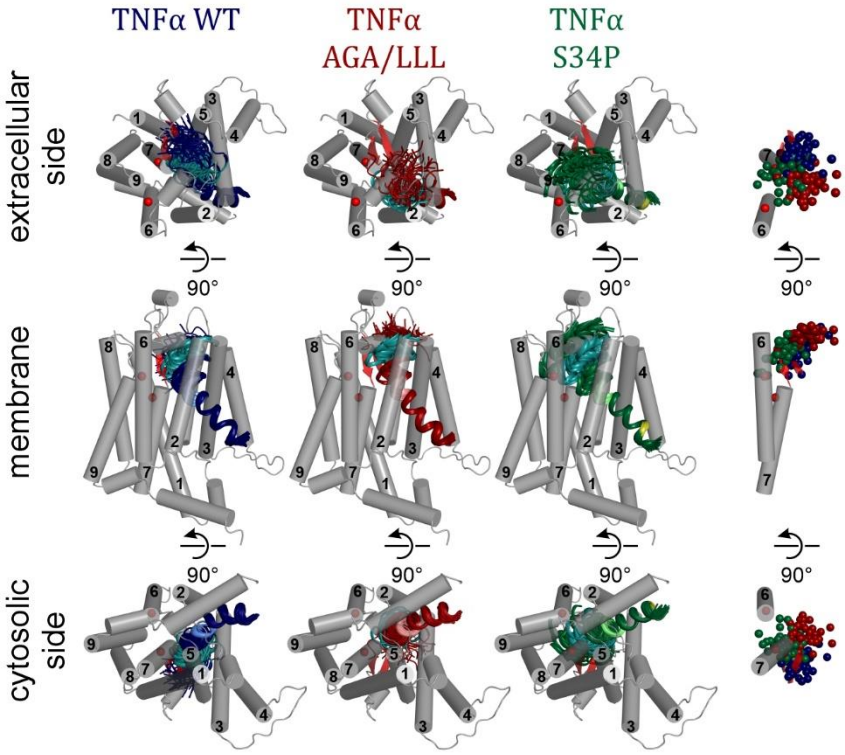

Figure 5.8 Enzyme-substrate complex: TNFα and SPPL2a. Extracellular, membrane and cytosolic view of the TNFα-SPPL2a complex. The TNFα$_{28-60}$ WT bundles (blue), TNFαAGA/LLL$_{28-60}$ (red) and TNFαS34P$_{28-60}$ (green) are aligned to TNFα$_{28-60}$ TMD (not shown) in the AlphaFold structure in complex with SPPL2a. Region with AGA motif and mutated residues are highlighted in the corresponding light shade. The initial cleavage sites Cys$_{49}$/Leu$_{50}$ and Leu$_{51}$/His$_{52}$ are represented in turquoise. SPPL2a is shown in grey with numbered TMDs. The β-sheet forming residues in the loop between TM6 and TM7 and the N-terminal TM7 as well as catalytic aspartates are highlighted in red. The right column illustrates the position of Gly$_{54}$ C$_\alpha$ atom as dots. For clarity the extracellular domain (1-166) and the unstructured C-terminus (512-520) in SPPL2a are not shown and in the right column only TM6 and TM7 are shown.

To further evaluate the interaction of TNFα TMD with SPPL2a, the TNFα$_{28-60}$ WT NMR bundle (Figure 4.27 (a)) was aligned along the TM-N to the AlphaFold structure of TNFα$_{28-60}$ in complex with SPPL2a (Figure 5.8). The TNFα$_{28-60}$ WT NMR bundle fitted well into the catalytic cavity, only 4/40 structures collided slightly with TM3 and TM5. Since the β-branched residues Val$_{55}$ and Ile$_{56}$ (Pace und Scholtz 1998) might adopt, together with one of the surrounding glycines, a β-strand, the residue Gly$_{54}$ was chosen to visualize the deflection of the structures in the bundle. The C$_\alpha$ atoms of Gly$_{54}$ indicated nicely the clustering of the structures in the TNFα$_{28-60}$ WT bundle towards the β-sheet in SPPL2a (Figure 5.8, right column), enabling the formation of the hybrid β-sheet.

To compare the interaction of the leucine mutant with SPPL2a to the interaction with TNFα$_{28-60}$ WT, the TNFαAGA/LLL$_{28-60}$ NMR bundle (Figure 4.33 (b)) was aligned to TNFα$_{28-60}$ WT NMR structure in the AlphaFold enzyme-substrate complex (Figure 5.8). The shifted orientation of the less pronounced bend in TNFαAGA/LLL$_{28-60}$ bundle directed the TM-Cs towards TM2 and TM3 and only few 5/40 structures collided with them. The Gly$_{54}$ C$_\alpha$ atoms were more distant to the β-sheet forming residues in SPPL2a and thus impaired the interaction with the enzyme.

When aligning the TNFαS34P$_{28-60}$ NMR bundle along the TNFα$_{28-60}$ WT NMR structure in the AlphaFold enzyme-substrate complex, the TM-Cs in the TNFαS34P$_{28-60}$ bundle were directed towards TM6 and TM7. As a result of the even straighter structure compared to the leucine mutant, the Gly$_{54}$ C$_\alpha$ atoms moved slightly further away from the β-sheet forming residues but closer to the catalytic aspartates, restricting the formation of a hybrid β-sheet between TNFαS34P$_{28-60}$ and SPPL2a, but could favour the coordination with both aspartates to a tetrahedral intermediate.

To achieve the cleavage competent orientation, two points are important a TM-C destabilization, enabling the helix to unwound and adopt a β-strand as well as the intrinsic orientation of the substrates TM-N with respect to the TM-C defined by the extend and orientation of the bend, so that the interaction with the enzyme is possible.

Cleavage Site Unfolding in TNFα

After the appropriate positioning within the active site, a final step requires partial unfolding of the cleavage site to form a tetrahedral cleavage intermediate and finally release the cleavage products. The two cleavage sites Cys$_{49}$/Leu$_{50}$ and Leu$_{51}$/His$_{52}$ in TNFα$_{28-60}$ WT TM-C have destabilized hydrogen bonds, indicated by the drops in the flexibility profile (Figure 4.28).

N-terminal cleavage sites Ser$_{34}$/Leu$_{35}$ and Leu$_{39}$/Ile$_{40}$ also show destabilized hydrogen bonds N-terminal from Leu$_{39}$ (Figure 4.28). The destabilization in the TM-N cleavage sites is further evident from the NOE contacts and reduced helix probability as well as order parameter S^2 (Figure 4.26). These destabilizations are important, enabling access to the scissile peptide bond by the enzyme.

In both mutants, the stability of the cleavage sites differs only slightly from TNFα$_{28-60}$ WT, except that Leu$_{51}$/His$_{52}$ is more stable in TNFαS34P$_{28-60}$ and even more stable in TNFαAGA/LLL$_{28-60}$ comparted to TNFα$_{28-60}$ WT.

When mutating the residues Cys_{49} and His_{52} in $TNF\alpha_{28-60}$ TMD to alanines with their small side chain and helix-distorting prolines, the mutants had only minor effect of the non-canonical shedding by SPPL2a (Spitz et al. 2020). In contrast, bulky leucines could stabilize the helix, thus impeding cleavage site unfolding and/or might hinder the access for the enzyme and significantly reduce the cleavage efficiency of non-canonical shedding (Spitz et al. 2020).

SPPL2b Substrate Bri2

The concept of a facilitated enzyme entry and translocation by a flexible substrate TMD is also applicable to other substrate-enzyme pairs, like Bri2 and SPPL2b. Mutations of the flexibility promoting glycines decrease intramembrane proteolysis by SPPL2b, where the residue Gly_{60} has an especially high impact of destabilizing the Bri2 TMD (Fluhrer et al. 2012). The extend of the reduced cleavage in Bri2G60A was comparable to the effect when all glycines in the Bri2 TMD were substituted by alanines (Fluhrer et al. 2012). Based on these results $^1H_\alpha$ secondary chemical shifts of $Bri2_{48-82}$ and its mutant $Bri2_{48-82}$G60A were investigated additionally in this thesis (data unpublished). The chemical shift assignment was incomplete most prominent in the TM-N, due to line broadening of H_N resonances caused by unfavourable exchange of amide protons with water, indicating destabilisation in the secondary structure. The same applies to the non-substrate (Martin et al. 2009) $Bri3_{50-87}$, which I also likewise examined.

The $^1H_\alpha$ secondary chemical shifts of $Bri2_{48-82}$ indicated a helical TMD until Tyr_{58} with a destabilized and more flexible part around $Gly_{71}Gly_{72}$ as well as around Gly_{60} (Figure 5.9 (a)). The stabilization of the $Bri2_{48-82}$G60A TMD helix can be assumed from more pronounced helix-typical minima in the CD spectra (Figure 5.9 (b)), so that the stability of the Bri2 TMD is in line with its cleavability by SPPL2b.

That mutations of the flexibility enhancing glycines within the GxxxG motif affect cleavage also applies to GnTV and SPPL3. The helix-distorting proline mutant GnTVG26P increases non-canonical shedding by SPPL3, while the helix stabilizing leucine mutant GnTVG22L decreases non-canonical shedding and the double leucine mutant GnTVG22LG26L even more (Papadopoulou et al. 2022).

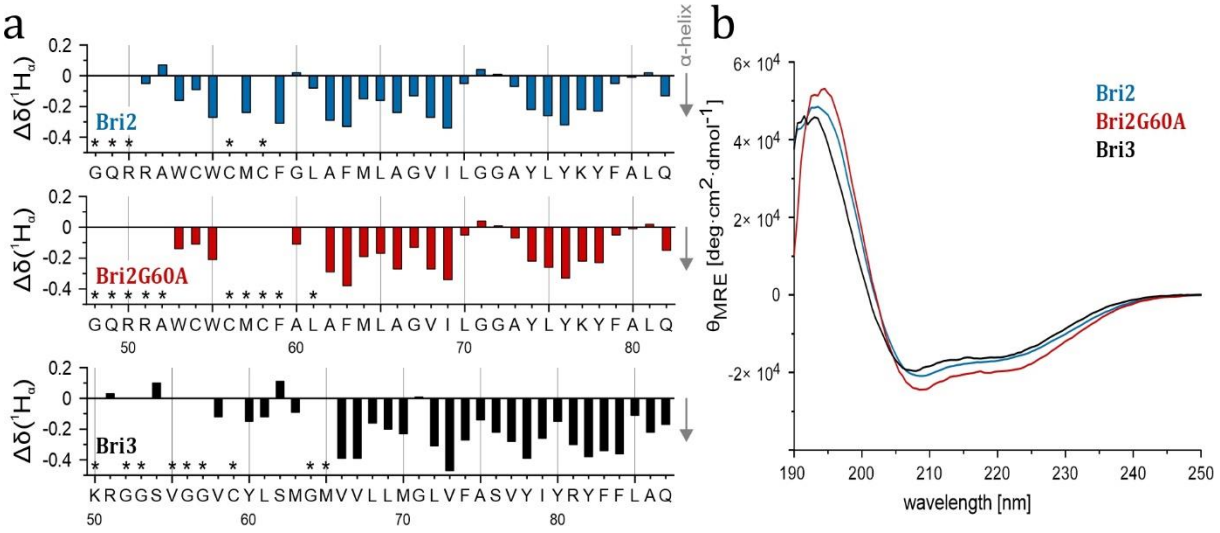

Figure 5.9 Secondary structure characteristics of Bri2, Bri2G60A and Bri3. Shown are $^{1}H_{\alpha}$ secondary chemical shifts (a), the difference between random coil and observed values of $Bri2_{48-82}$ (blue), $Bri2_{48-82}$G60A (red) and $Bri3_{50-87}$ (black). Negative $^{1}H_{\alpha}$ secondary chemical shifts indicate α-helices. Due to low spectral quality residues marked with asterisk could not be assigned. CD spectra (b) in HFIP/H2O (80:20, v:v) at pH 2 ($Bri2_{48-80}$) and pH 5 at 300 K. CD spectra were analysed with BeStSel.

Notably, the non-substrate $Bri3_{50-87}$, one of only two known and verified non-substrates, seems to have a helical TMD to the end of the investigated sequence, indicated by the negative $^{1}H_{\alpha}$ secondary chemical shifts (Figure 5.9 (a)), however, without a destabilization towards the C-terminal end of the TMD such as the SPPL2b substrate Bri2. This stabilization could prevent helix unwinding and thus β-strand formation in the substrate and hybrid β-sheet formation with SPPL2b, possibly resulting in no proper orientation to the catalytic aspartates and abolished cleavage. The stabilization towards the C-terminal end of the TMD is also evident in the γ-secretase non-substrate ITGB1 and could be a common feature of non-substrates.

The characteristic structural properties of proteases and their substrates, required for their interaction and intramembrane proteolysis, are not only limited to single substrate-protease pairs, but can be applied to different proteases and substrates, at least to aspartate proteases. In the following it is summarized how the individual structural motifs within the substrate affecting processivity can be combined to enable, promote or impede proteolysis.

6 Conclusion: Composition of Substrate Requirements

As seen in the previous section, the individual mechanistic steps, starting with exosite binding through substrate entry, translocation, positioning in the active site and hybrid β-sheet formation, towards cleavage site unfolding and the actual hydrolytic cleavage of the peptide bond, are influenced in different ways by the substrates of aspartate proteases and their mutants.

The ability to form a β-strand in the substrate to stabilize a cleavage competent orientation through the formation of a hybrid β-sheet between the substrate and enzyme appears to be a general feature of at least aspartate proteases. The extend and the direction of the bend in substrate TMD must be taken into account, which determines the orientation of the TMD within the active site and thus influence the orientation of the β-strand and formation of the hybrid β-sheet. These two factors might be substrate criterions to distinguish between a substrate and a non-substrate or a good substrate and one that is not efficiently cleaved.

A certain degree of flexibility and accessibility within the substrates cleavage site enables proteolysis by γ-secretase, however, a highly flexible cleavage site is not necessary. Moreover, as previously described, cleavage is influenced by mutations altering the flexibility or accessibility of the cleavage site.

The same is true for the flexibility of the substrates TMD. A certain degree of flexibility allows γ-secretase cleavage, but a highly flexible TMD is not necessary here either.

The basic anchor, positively charged amino acids like arginine or lysine C-terminal of the TMD in substrates, might be involved in the appropriate positioning within the membrane, but since some substrates have several of these residues, while other only have few or none, this substrate criterion is also not required.

The propensity to adopt a β-strand, flexibility within the TMD and cleavage site, orientation and extend of the TMD bend as well as basic residues at the C-terminal end of the TMD, none of these properties are exclusively substrate-determining on their own. They should be viewed more like building blocks in a construction kit, which can be put together depending on the task the substrate has to fulfil, adjusting the cleavage accordingly.

Since none of the mentioned structural features are on their own substrate-decisive, the question is which combination is sufficient for proteolytic cleavage. If a substrate TMD is replaced by a stretch of poly leucine residues, this construct is not cleaved by γ-secretase (Ortner et al. 2023; Werner et al. 2023). Introducing only a flexibility motif, in form of a glycine tetrad analogous to Notch1$G_{1740-1743}$ TMD, to the poly-leucine stretch is not sufficient for cleavage, even if a cleavage site motif with small residues around the cleavage site, consisting of GCG, is added (Ortner et al. 2023). A β-strand motif in the otherwise poly-leucine sequence, consisting of VVVS, is also not sufficient. However, combining the flexibility with the β-strand motif restores γ-secretase cleavage with an efficiency compared to Notch1 WT. The cleavage can further be increased by adding the cleavage site motif or down regulated again by replacing the small glycine to bulkier alanines in the flexibility motif. Analogous considerations also apply to APP TMD (Werner et al. 2023).

The cleavage efficiency can be adjusted by combining the different motifs and tailoring the amino acid within the motif to helix-stabilizing or helix-destabilizing residues, all in context of the orientation of the substrate TMD, to create a substrate customized to the biological needs (Figure 1.20).

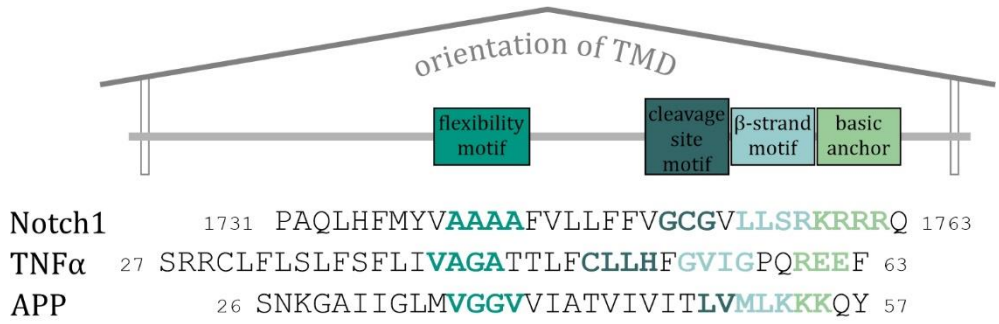

Figure 6.1 Composition of substrate requirements. Shown are the different substrate motifs, all in context of the TMD orientation, in the sequence of Notch1, TNFα and APP, which can be combined to adjust cleavage efficiency.

References

Aggarwal, Bharat B. (2003): Signalling pathways of the TNF superfamily: a double-edged sword. In: *Nature reviews. Immunology* 3 (9), S. 745–756. DOI: 10.1038/nri1184.

Aggarwal, Bharat B.; Gupta, Subash C.; Kim, Ji Hye (2012): Historical perspectives on tumor necrosis factor and its superfamily: 25 years later, a golden journey. In: *Blood* 119 (3), S. 651–665. DOI: 10.1182/blood-2011-04-325225.

Aguayo-Ortiz, Rodrigo; Chávez-García, Cecilia; Straub, John E.; Dominguez, Laura (2017): Characterizing the structural ensemble of γ-secretase using a multiscale molecular dynamics approach. In: *Chem. Sci.* 8 (8), S. 5576–5584. DOI: 10.1039/C7SC00980A.

Akiyama, Yoshinori; Maegawa, Saki (2007): Sequence features of substrates required for cleavage by GlpG, an Escherichia coli rhomboid protease. In: *Molecular microbiology* 64 (4), S. 1028–1037. DOI: 10.1111/j.1365-2958.2007.05715.x.

Altmann, K. H.; Wójcik, J.; Vásquez, M.; Scheraga, H. A. (1990): Helix-coil stability constants for the naturally occurring amino acids in water. XXIII. Proline parameters from random poly (hydroxybutylglutamine-co-L-proline). In: *Biopolymers* 30 (1-2), S. 107–120. DOI: 10.1002/bip.360300112.

Arrington, Cammon B.; Robertson, Andrew D. (2002): Kinetics and thermodynamics of conformational equilibria in native proteins by hydrogen exchange. In: Thomas L. James, Volker Dötsch und Uli Schmitz (Hg.): Methods in Enzymology : Nuclear Magnetic Resonance of Biological Macromolecules Part A, Bd. 323: Academic Press, S. 104–124. Online verfügbar unter https://www.sciencedirect.com/science/article/pii/S0076687900233636.

Artavanis-Tsakonas, S.; Rand, M. D.; Lake, R. J. (1999): Notch signaling: cell fate control and signal integration in development. In: *Science (New York, N.Y.)* 284 (5415), S. 770–776. DOI: 10.1126/science.284.5415.770.

Avci, Dönem; Malchus, Nicole S.; Heidasch, Ronny; Lorenz, Holger; Richter, Karsten; Neßling, Michelle; Lemberg, Marius K. (2019): The intramembrane protease SPP impacts morphology of the endoplasmic reticulum by triggering degradation of morphogenic proteins. In: *The Journal of biological chemistry* 294 (8), S. 2786–2800. DOI: 10.1074/jbc.RA118.005642.

Bai, Xiao-chen; Rajendra, Eeson; Yang, Guanghui; Shi, Yigong; Scheres, Sjors H. W. (2015a): Sampling the conformational space of the catalytic subunit of human γ-secretase. In: *eLife* 4. DOI: 10.7554/eLife.11182.

Bai, Xiao-chen; Yan, Chuangye; Yang, Guanghui; Lu, Peilong; Ma, Dan; Sun, Linfeng et al. (2015b): An atomic structure of human γ-secretase. In: *Nature* 525 (7568), S. 212–217. DOI: 10.1038/nature14892.

Bai, Y.; Milne, J. S.; Mayne, L.; Englander, S. W. (1993): Primary structure effects on peptide group hydrogen exchange. In: *Proteins* 17 (1), S. 75–86. DOI: 10.1002/prot.340170110.

Bai, Yawen; Englander, Joan J.; Mayne, Leland; Milne, John S.; Englander, S.Walter (2002): [15] Thermodynamic parameters from hydrogen exchange measurements. In: Thomas L. James, Volker Dötsch und Uli Schmitz (Hg.): Methods in Enzymology : Nuclear Magnetic Resonance of Biological Macromolecules Part A, Bd. 259: Academic Press, S. 344–356. Online verfügbar unter https://www.sciencedirect.com/science/article/pii/007668799559051X.

Bain, Alex D. (2003): Chemical exchange in NMR. In: *Progress in nuclear magnetic resonance spectroscopy* 43 (3-4), S. 63–103. DOI: 10.1016/j.pnmrs.2003.08.001.

Banner, D. W.; D'Arcy, A.; Janes, W.; Gentz, R.; Schoenfeld, H. J.; Broger, C. et al. (1993): Crystal structure of the soluble human 55 kd TNF receptor-human TNF beta complex: implications for TNF receptor activation. In: *Cell* 73 (3), S. 431–445. DOI: 10.1016/0092-8674(93)90132-a.

Barrett, Paul J.; Song, Yuanli; van Horn, Wade D.; Hustedt, Eric J.; Schafer, Johanna M.; Hadziselimovic, Arina et al. (2012): The amyloid precursor protein has a flexible transmembrane domain and binds cholesterol. In: *Science (New York, N.Y.)* 336 (6085), S. 1168–1171. DOI: 10.1126/science.1219988.

Barrowman, Jemima; Hamblet, Corinne; George, Carolyn M.; Michaelis, Susan (2008): Analysis of prelamin A biogenesis reveals the nucleus to be a CaaX processing compartment. In: *Molecular biology of the cell* 19 (12), S. 5398–5408. DOI: 10.1091/mbc.e08-07-0704.

Beel, A. J.; Sanders, C. R. (2008): Substrate specificity of gamma-secretase and other intramembrane proteases. In: *Cellular and molecular life sciences : CMLS* 65 (9), S. 1311–1334. DOI: 10.1007/s00018-008-7462-2.

Beel, Andrew J.; Mobley, Charles K.; Kim, Hak Jun; Tian, Fang; Hadziselimovic, Arina; Jap, Bing et al. (2008): Structural studies of the transmembrane C-terminal domain of the amyloid precursor protein (APP): does APP function as a cholesterol sensor? In: *Biochemistry* 47 (36), S. 9428–9446. DOI: 10.1021/bi800993c.

Behnke, Jörg; Schneppenheim, Janna; Koch-Nolte, Friedrich; Haag, Friedrich; Saftig, Paul; Schröder, Bernd (2011): Signal-peptide-peptidase-like 2a (SPPL2a) is targeted to lysosomes/late endosomes by a tyrosine motif in its C-terminal tail. In: *FEBS letters* 585 (19), S. 2951–2957. DOI: 10.1016/j.febslet.2011.08.043.

Bhattarai, Apurba; Devkota, Sujan; Bhattarai, Sanjay; Wolfe, Michael S.; Miao, Yinglong (2020): Mechanisms of γ-Secretase Activation and Substrate Processing. In: *ACS Central Science* 6 (6), S. 969–983. DOI: 10.1021/acscentsci.0c00296.

Bhattarai, Apurba; Devkota, Sujan; Do, Hung Nguyen; Wang, Jinan; Bhattarai, Sanjay; Wolfe, Michael S.; Miao, Yinglong (2022): Mechanism of Tripeptide Trimming of Amyloid β-Peptide 49 by γ-Secretase. In: *J. Am. Chem. Soc.* 144 (14), S. 6215–6226. DOI: 10.1021/jacs.1c10533.

Bigas, Anna; Espinosa, Lluis (2012): Hematopoietic stem cells: to be or Notch to be. In: *Blood* 119 (14), S. 3226–3235. DOI: 10.1182/blood-2011-10-355826.

Blaumueller, C. M.; Qi, H.; Zagouras, P.; Artavanis-Tsakonas, S. (1997): Intracellular cleavage of Notch leads to a heterodimeric receptor on the plasma membrane. In: *Cell* 90 (2), S. 281–291. DOI: 10.1016/S0092-8674(00)80336-0.

Bodmer, Jean-Luc; Schneider, Pascal; Tschopp, Jürg (2002): The molecular architecture of the TNF superfamily. In: *Trends in Biochemical Sciences* 27 (1), S. 19–26. DOI: 10.1016/S0968-0004(01)01995-8.

Boehr, David D.; Nussinov, Ruth; Wright, Peter E. (2009): The role of dynamic conformational ensembles in biomolecular recognition. In: *Nat Chem Biol* 5 (11), S. 789–796. DOI: 10.1038/nchembio.232.

Bolduc, David M.; Montagna, Daniel R.; Gu, Yongli; Selkoe, Dennis J.; Wolfe, Michael S. (2016): Nicastrin functions to sterically hinder γ-secretase-substrate interactions driven by substrate transmembrane domain. In: *Proceedings of the National Academy of Sciences of the United States of America* 113 (5), E509-18. DOI: 10.1073/pnas.1512952113.

Boname, Jessica M.; Bloor, Stuart; Wandel, Michal P.; Nathan, James A.; Antrobus, Robin; Dingwell, Kevin S. et al. (2014): Cleavage by signal peptide peptidase is required for

the degradation of selected tail-anchored proteins. In: *J Cell Biol* 205 (6), S. 847–862. DOI: 10.1083/jcb.201312009.

Bracha-Drori, Keren; Shichrur, Keren; Lubetzky, Tsofnat Cohen; Yalovsky, Shaul (2008): Functional analysis of Arabidopsis postprenylation CaaX processing enzymes and their function in subcellular protein targeting. In: *Plant physiology* 148 (1), S. 119–131. DOI: 10.1104/pp.108.120477.

Bradbury, J. H.; Crompton, M. W.; Teh, J. S. (1977): Nuclear-magnetic-resonance study of the histidine residues of S-peptide and S-protein and kinetics of 1H-2H exchange of ribonuclease A. In: *European journal of biochemistry* 81 (2), S. 411–422. DOI: 10.1111/j.1432-1033.1977.tb11966.x.

Bradley, J. R. (2008): TNF-mediated inflammatory disease. In: *The Journal of pathology* 214 (2), S. 149–160. DOI: 10.1002/path.2287.

Brou, C.; Logeat, F.; Gupta, N.; Bessia, C.; LeBail, O.; Doedens, J. R. et al. (2000): A novel proteolytic cleavage involved in Notch signaling: the role of the disintegrin-metalloprotease TACE. In: *Molecular cell* 5 (2), S. 207–216. DOI: 10.1016/S1097-2765(00)80417-7.

Brown, M. S.; Ye, J.; Rawson, R. B.; Goldstein, J. L. (2000): Regulated intramembrane proteolysis: a control mechanism conserved from bacteria to humans. In: *Cell* 100 (4), S. 391–398. DOI: 10.1016/S0092-8674(00)80675-3.

Brünger, A. T.; Adams, P. D.; Clore, G. M.; DeLano, W. L.; Gros, P.; Grosse-Kunstleve, R. W. et al. (1998): Crystallography & NMR system: A new software suite for macromolecular structure determination. In: *Acta crystallographica. Section D, Biological crystallography* 54 (Pt 5), S. 905–921. DOI: 10.1107/S0907444998003254.

Brünger, A. T.; Adams, P. D.; Rice, L. M. (1997): New applications of simulated annealing in X-ray crystallography and solution NMR. In: *Structure* 5 (3), S. 325–336. DOI: 10.1016/S0969-2126(97)00190-1.

Buck, M. (1998): Trifluoroethanol and colleagues: cosolvents come of age. Recent studies with peptides and proteins. In: *Quarterly reviews of biophysics* 31 (3), S. 297–355. DOI: 10.1017/s003358359800345x.

Carswell, E. A.; Old, L. J.; Kassel, R. L.; Green, S.; Fiore, N.; Williamson, B. (1975): An endotoxin-induced serum factor that causes necrosis of tumors. In: *Proceedings of the National Academy of Sciences of the United States of America* 72 (9), S. 3666–3670. DOI: 10.1073/pnas.72.9.3666.

Cavanagh, John (2007): Protein and NMR spectroscopy. Principles and practice. 2.ed. Burlington, MA [etc.]: Elsevier. Online verfügbar unter https://ebookcentral.proquest.com/lib/kxp/detail.action?docID=287969.

Chen, Chia-yi; Malchus, Nicole S.; Hehn, Beate; Stelzer, Walter; Avci, Dönem; Langosch, Dieter; Lemberg, Marius K. (2014): Signal peptide peptidase functions in ERAD to cleave the unfolded protein response regulator XBP1u. In: *The EMBO journal* 33 (21), S. 2492–2506. DOI: 10.15252/embj.201488208.

Cheng, Tsung-Lin; Wu, Yu-Ting; Lin, Hung-Yu; Hsu, Fu-Chih; Liu, Shi-Kai; Chang, Bi-Ing et al. (2011): Functions of rhomboid family protease RHBDL2 and thrombomodulin in wound healing. In: *The Journal of investigative dermatology* 131 (12), S. 2486–2494. DOI: 10.1038/jid.2011.230.

Cho, Sangwoo; Baker, Rosanna P.; Ji, Ming; Urban, Siniša (2019): Ten catalytic snapshots of rhomboid intramembrane proteolysis from gate opening to peptide release. In: *Nat Struct Mol Biol* 26 (10), S. 910–918. DOI: 10.1038/s41594-019-0296-9.

Coales, Stephen J.; E, Sook Yen; Lee, Jessica E.; Ma, Anita; Morrow, Jeffrey A.; Hamuro, Yoshitomo (2010): Expansion of time window for mass spectrometric measurement of amide hydrogen/deuterium exchange reactions. In: *Rapid communications in mass spectrometry : RCM* 24 (24), S. 3585–3592. DOI: 10.1002/rcm.4814.

Cooper, J. B.; Khan, G.; Taylor, G.; Tickle, I. J.; Blundell, T. L. (1990): X-ray analyses of aspartic proteinases. II. Three-dimensional structure of the hexagonal crystal form of porcine pepsin at 2.3 A resolution. In: *Journal of molecular biology* 214 (1), S. 199–222. DOI: 10.1016/0022-2836(90)90156-G.

Cordes, Frank S.; Bright, Joanne N.; Sansom, Mark S. P. (2002): Proline-induced distortions of transmembrane helices. In: *Journal of molecular biology* 323 (5), S. 951–960. DOI: 10.1016/S0022-2836(02)01006-9.

Cordle, Jemima; Redfieldz, Christina; Stacey, Martin; van der Merwe, P. Anton; Willis, Antony C.; Champion, Brian R. et al. (2008): Localization of the delta-like-1-binding site in human Notch-1 and its modulation by calcium affinity. In: *Journal of Biological Chemistry* 283 (17), S. 11785–11793. DOI: 10.1074/jbc.M708424200.

Cornilescu, G.; Delaglio, F.; Bax, A. (1999): Protein backbone angle restraints from searching a database for chemical shift and sequence homology. In: *Journal of biomolecular NMR* 13 (3), S. 289–302. DOI: 10.1023/a:1008392405740.

Danyukova, Tatyana; Schöneck, Kenneth; Pohl, Sandra (2022): Site-1 and site-2 proteases: A team of two in regulated proteolysis. In: *Biochimica et biophysica acta. Molecular cell research* 1869 (1), S. 119138. DOI: 10.1016/j.bbamcr.2021.119138.

Das, Amit; Mahale, Smita; Prashar, Vishal; Bihani, Subhash; Ferrer, J-L; Hosur, M. V. (2010): X-ray snapshot of HIV-1 protease in action: observation of tetrahedral intermediate and short ionic hydrogen bond SIHB with catalytic aspartate. In: *J. Am. Chem. Soc.* 132 (18), S. 6366–6373. DOI: 10.1021/ja100002b.

Deatherage, Catherine L.; Lu, Zhenwei; Kim, Ji-Hun; Sanders, Charles R. (2015): Notch Transmembrane Domain: Secondary Structure and Topology. In: *Biochemistry* 54 (23), S. 3565–3568. DOI: 10.1021/acs.biochem.5b00456.

Deatherage, Catherine L.; Lu, Zhenwei; Kroncke, Brett M.; Ma, Sirui; Smith, Jarrod A.; Voehler, Markus W. et al. (2017): Structural and biochemical differences between the Notch and the amyloid precursor protein transmembrane domains. In: *Science Advances* 3 (4), e1602794. DOI: 10.1126/sciadv.1602794.

Dempsey, Christopher E. (2001): Hydrogen exchange in peptides and proteins using NMR spectroscopy. In: *Progress in nuclear magnetic resonance spectroscopy* 39 (2), S. 135–170. DOI: 10.1016/S0079-6565(01)00032-2.

Domonkos, A.; Udvardy, A.; László, L.; Nagy, T.; Duda, E. (2001): Receptor-like properties of the 26 kDa transmembrane form of TNF. In: *European Cytokine Network* 12 (3), S. 411–419.

Duncan, E. A.; Davé, U. P.; Sakai, J.; Goldstein, J. L.; Brown, M. S. (1998): Second-site cleavage in sterol regulatory element-binding protein occurs at transmembrane junction as determined by cysteine panning. In: *The Journal of biological chemistry* 273 (28), S. 17801–17809. DOI: 10.1074/jbc.273.28.17801.

Eck, M. J.; Sprang, S. R. (1989): The structure of tumor necrosis factor-alpha at 2.6 A resolution. Implications for receptor binding. In: *Journal of Biological Chemistry* 264 (29), S. 17595–17605. DOI: 10.2210/pdb1tnf/pdb.

Edbauer, Dieter; Winkler, Edith; Regula, Joerg T.; Pesold, Brigitte; Steiner, Harald; Haass, Christian (2003): Reconstitution of gamma-secretase activity. In: *Nature cell biology* 5 (5), S. 486–488. DOI: 10.1038/ncb960.

Esser, Karlheinz; Tursun, Baris; Ingenhoven, Martin; Michaelis, Georg; Pratje, Elke (2002): A novel two-step mechanism for removal of a mitochondrial signal sequence involves

the mAAA complex and the putative rhomboid protease Pcp1. In: *Journal of molecular biology* 323 (5), S. 835–843. DOI: 10.1016/s0022-2836(02)01000-8.

Evans, Richard; O'Neill, Michael; Pritzel, Alexander; Antropova, Natasha; Senior, Andrew; Green, Tim et al. (2021): Protein complex prediction with AlphaFold-Multimer. In: *bioRxiv*, 2021.10.04.463034. DOI: 10.1101/2021.10.04.463034.

Faustman, Denise L.; Davis, Miriam (2013): TNF Receptor 2 and Disease: Autoimmunity and Regenerative Medicine. In: *Front. Immunol.* 4, S. 478. DOI: 10.3389/fimmu.2013.00478.

Feng, Liang; Yan, Hanchi; Wu, Zhuoru; Yan, Nieng; Wang, Zhe; Jeffrey, Philip D.; Shi, Yigong (2007): Structure of a site-2 protease family intramembrane metalloprotease. In: *Science (New York, N.Y.)* 318 (5856), S. 1608–1612. DOI: 10.1126/science.1150755.

Fernandez, Marty A.; Biette, Kelly M.; Dolios, Georgia; Seth, Divya; Wang, Rong; Wolfe, Michael S. (2016): Transmembrane Substrate Determinants for γ-Secretase Processing of APP CTFβ. In: *Biochemistry* 55 (40), S. 5675–5688. DOI: 10.1021/acs.biochem.6b00718.

Fleig, Lina; Bergbold, Nina; Sahasrabudhe, Priyanka; Geiger, Beate; Kaltak, Lejla; Lemberg, Marius K. (2012): Ubiquitin-dependent intramembrane rhomboid protease promotes ERAD of membrane proteins. In: *Molecular cell* 47 (4), S. 558–569. DOI: 10.1016/j.molcel.2012.06.008.

Fluhrer, Regina; Grammer, Gudula; Israel, Lars; Condron, Margaret M.; Haffner, Christof; Friedmann, Elena et al. (2006): A gamma-secretase-like intramembrane cleavage of TNFalpha by the GxGD aspartyl protease SPPL2b. In: *Nature cell biology* 8 (8), S. 894–896. DOI: 10.1038/ncb1450.

Fluhrer, Regina; Martin, Lucas; Klier, Bärbel; Haug-Kröper, Martina; Grammer, Gudula; Nuscher, Brigitte; Haass, Christian (2012): The α-helical content of the transmembrane domain of the British dementia protein-2 (Bri2) determines its processing by signal peptide peptidase-like 2b (SPPL2b). In: *The Journal of biological chemistry* 287 (7), S. 5156–5163. DOI: 10.1074/jbc.M111.328104.

Fluhrer, Regina; Steiner, Harald; Haass, Christian (2009): Intramembrane proteolysis by signal peptide peptidases: a comparative discussion of GXGD-type aspartyl proteases. In: *The Journal of biological chemistry* 284 (21), S. 13975–13979. DOI: 10.1074/jbc.R800040200.

Francis, Ross; McGrath, Garth; Zhang, Jianhuan; Ruddy, David A.; Sym, Mary; Apfeld, Javier et al. (2002): aph-1 and pen-2 are required for Notch pathway signaling, gamma-secretase cleavage of betaAPP, and presenilin protein accumulation. In: *Developmental Cell* 3 (1), S. 85–97. DOI: 10.1016/S1534-5807(02)00189-2.

Friedmann, Elena; Hauben, Ehud; Maylandt, Kerstin; Schleeger, Simone; Vreugde, Sarah; Lichtenthaler, Stefan F. et al. (2006): SPPL2a and SPPL2b promote intramembrane proteolysis of TNFalpha in activated dendritic cells to trigger IL-12 production. In: *Nature cell biology* 8 (8), S. 843–848. DOI: 10.1038/ncb1440.

Friedmann, Elena; Lemberg, Marius K.; Weihofen, Andreas; Dev, Kumlesh K.; Dengler, Uwe; Rovelli, Giorgio; Martoglio, Bruno (2004): Consensus analysis of signal peptide peptidase and homologous human aspartic proteases reveals opposite topology of catalytic domains compared with presenilins. In: *The Journal of biological chemistry* 279 (49), S. 50790–50798. DOI: 10.1074/jbc.M407898200.

Fryer, Christy J.; White, J. Brandon; Jones, Katherine A. (2004): Mastermind recruits CycC:CDK8 to phosphorylate the Notch ICD and coordinate activation with turnover. In: *Molecular cell* 16 (4), S. 509–520. DOI: 10.1016/j.molcel.2004.10.014.

Fukumori, Akio; Steiner, Harald (2016): Substrate recruitment of γ-secretase and mechanism of clinical presenilin mutations revealed by photoaffinity mapping. In: *The EMBO journal* 35 (15), S. 1628–1643. DOI: 10.15252/embj.201694151.

Glasoe, Paul K.; Long, F. A. (1960): USE OF GLASS ELECTRODES TO MEASURE ACIDITIES IN DEUTERIUM OXIDE 1,2. In: *J. Phys. Chem.* 64 (1), S. 188–190. DOI: 10.1021/j100830a521.

Golde, Todd E.; Wolfe, Michael S.; Greenbaum, Doron C. (2009): Signal peptide peptidases: a family of intramembrane-cleaving proteases that cleave type 2 transmembrane proteins. In: *Seminars in cell & developmental biology* 20 (2), S. 225–230. DOI: 10.1016/j.semcdb.2009.02.003.

Gordon, Wendy R.; Vardar-Ulu, Didem; Histen, Gavin; Sanchez-Irizarry, Cheryll; Aster, Jon C.; Blacklow, Stephen C. (2007): Structural basis for autoinhibition of Notch. In: *Nature structural & molecular biology* 14 (4), S. 295–300. DOI: 10.1038/nsmb1227.

Gordon, Wendy R.; Vardar-Ulu, Didem; L'Heureux, Sarah; Ashworth, Todd; Malecki, Michael J.; Sanchez-Irizarry, Cheryll et al. (2009): Effects of S1 cleavage on the structure, surface export, and signaling activity of human Notch1 and Notch2. In: *PloS one* 4 (8), e6613. DOI: 10.1371/journal.pone.0006613.

Götz, Alexander; Högel, Philipp; Silber, Mara; Chaitoglou, Iro; Luy, Burkhard; Muhle-Goll, Claudia et al. (2019a): Increased H-Bond Stability Relates to Altered ε-Cleavage Efficiency and Aβ Levels in the I45T Familial Alzheimer's Disease Mutant of APP. In: *Sci Rep* 9 (1), S. 5321. DOI: 10.1038/s41598-019-41766-1.

Götz, Alexander; Mylonas, Nadine; Högel, Philipp; Silber, Mara; Heinel, Hannes; Menig, Simon et al. (2019b): Modulating Hinge Flexibility in the APP Transmembrane Domain Alters γ-Secretase Cleavage. In: *Biophysical Journal* 116 (11), S. 2103–2120. DOI: 10.1016/j.bpj.2019.04.030.

Gough, Portia; Myles, Ian A. (2020): Tumor Necrosis Factor Receptors: Pleiotropic Signaling Complexes and Their Differential Effects. In: *Front. Immunol.* 11, S. 585880. DOI: 10.3389/fimmu.2020.585880.

Grell, M.; Douni, E.; Wajant, H.; Löhden, M.; Clauss, M.; Maxeiner, B. et al. (1995): The transmembrane form of tumor necrosis factor is the prime activating ligand of the 80 kDa tumor necrosis factor receptor. In: *Cell* 83 (5), S. 793–802. DOI: 10.1016/0092-8674(95)90192-2.

Grigorenko, A. P.; Moliaka, Y. K.; Korovaitseva, G. I.; Rogaev, E. I. (2002): Novel class of polytopic proteins with domains associated with putative protease activity. In: *Biochemistry. Biokhimiia* 67 (7), S. 826–835. DOI: 10.1023/a:1016365227942.

Güner, Gökhan; Lichtenthaler, Stefan F. (2020): The substrate repertoire of γ-secretase/presenilin. In: *Seminars in cell & developmental biology* 105, S. 27–42. DOI: 10.1016/j.semcdb.2020.05.019.

Haass, Christian; Selkoe, Dennis J. (2007): Soluble protein oligomers in neurodegeneration: lessons from the Alzheimer's amyloid beta-peptide. In: *Nature reviews. Molecular cell biology* 8 (2), S. 101–112. DOI: 10.1038/nrm2101.

Haass, Christian; Steiner, Harald (2002): Alzheimer disease gamma-secretase: a complex story of GxGD-type presenilin proteases (12). Online verfügbar unter https://reader.elsevier.com/reader/sd/pii/S0962892402023942?token=06767B03C3007C4BA7EA0DABFBBEBC3B6ADA5772456D432488CCE2441763DE43B24BE0F333895FD4F2F892C65CB55D24&originRegion=eu-west-1&originCreation=20230214125757.

Hafsa, Noor E.; Arndt, David; Wishart, David S. (2015): CSI 3.0: a web server for identifying secondary and super-secondary structure in proteins using NMR chemical shifts. In: *Nucleic Acids Res* 43 (W1), W370-7. DOI: 10.1093/nar/gkv494.

Hallgren, Jeppe; Tsirigos, Konstantinos D.; Pedersen, Mads Damgaard; Almagro Armenteros, José Juan; Marcatili, Paolo; Nielsen, Henrik et al. (2022): DeepTMHMM predicts alpha and beta transmembrane proteins using deep neural networks. In: *bioRxiv*, 2022.04.08.487609. DOI: 10.1101/2022.04.08.487609.

Hamblet, Corinne E.; Makowski, Stefanie L.; Tritapoe, Julia M.; Pomerantz, Joel L. (2016): NK Cell Maturation and Cytotoxicity Are Controlled by the Intramembrane Aspartyl Protease SPPL3. In: *J Immunol* 196 (6), S. 2614–2626. DOI: 10.4049/jimmunol.1501970.

Hambleton, Sophie; Valeyev, Najl V.; Muranyi, Andreas; Knott, Vroni; Werner, Jörn M.; McMichael, Andrew J. et al. (2004): Structural and functional properties of the human notch-1 ligand binding region. In: *Structure (London, England : 1993)* 12 (12), S. 2173–2183. DOI: 10.1016/j.str.2004.09.012.

Hampton, Shahienaz E.; Dore, Timothy M.; Schmidt, Walter K. (2018): Rce1: mechanism and inhibition. In: *Critical Reviews in Biochemistry and Molecular Biology* 53 (2), S. 157–174. DOI: 10.1080/10409238.2018.1431606.

Hayward, Steven (1999): Structural principles governing domain motions in proteins. In: *Proteins: Structure, Function, and Bioinformatics* 36 (4), S. 425–435. DOI: 10.1002/(SICI)1097-0134(19990901)36:4<425::AID-PROT6>3.0.CO;2-S.

Heijne, G. von (1991): Proline kinks in transmembrane alpha-helices. In: *Journal of molecular biology* 218 (3), S. 499–503. DOI: 10.1016/0022-2836(91)90695-3.

Hemming, Matthew L.; Elias, Joshua E.; Gygi, Steven P.; Selkoe, Dennis J. (2008): Proteomic profiling of gamma-secretase substrates and mapping of substrate requirements. In: *PLOS Biology* 6 (10), e257. DOI: 10.1371/journal.pbio.0060257.

Hitzenberger, M.; Zacharias, M. (2019): Structural Modeling of γ-Secretase Aβ n Complex Formation and Substrate Processing. In: *ACS Chemical Neuroscience* 10 (3), S. 1826–1840. DOI: 10.1021/acschemneuro.8b00725.

Hitzenberger, Manuel; Götz, Alexander; Menig, Simon; Brunschweiger, Barbara; Zacharias, Martin; Scharnagl, Christina (2020): The dynamics of γ-secretase and its substrates. In: *Seminars in cell & developmental biology* 105, S. 86–101. DOI: 10.1016/j.semcdb.2020.04.008.

Högel, Philipp; Götz, Alexander; Kuhne, Felix; Ebert, Maximilian; Stelzer, Walter; Rand, Kasper D. et al. (2018): Glycine Perturbs Local and Global Conformational Flexibility

of a Transmembrane Helix. In: *Biochemistry* 57 (8), S. 1326–1337. DOI: 10.1021/acs.biochem.7b01197.

Hori, Kazuya; Sen, Anindya; Artavanis-Tsakonas, Spyros (2013): Notch signaling at a glance. In: *J Cell Sci* 126 (Pt 10), S. 2135–2140. DOI: 10.1242/jcs.127308.

Hsu, F-F; Yeh, C-T; Sun, Y-J; Chiang, M-T; Lan, W-M; Li, F-A et al. (2015): Signal peptide peptidase-mediated nuclear localization of heme oxygenase-1 promotes cancer cell proliferation and invasion independent of its enzymatic activity. In: *Oncogene* 34 (18), S. 2360–2370. DOI: 10.1038/onc.2014.166.

Hsu, Fu-Fei; Chou, Yi-Tai; Chiang, Ming-Tsai; Li, Fu-An; Yeh, Chi-Tai; Lee, Wei-Hwa; Chau, Lee-Young (2019): Signal peptide peptidase promotes tumor progression via facilitating FKBP8 degradation. In: *Oncogene* 38 (10), S. 1688–1701. DOI: 10.1038/s41388-018-0539-y.

Hvidt, A.; Nielsen, S. O. (1966): Hydrogen exchange in proteins. In: *Advances in protein chemistry* 21, S. 287–386. DOI: 10.1016/s0065-3233(08)60129-1.

Iso, Tatsuya; Kedes, Larry; Hamamori, Yasuo (2003): HES and HERP families: multiple effectors of the Notch signaling pathway. In: *Journal of Cellular Physiology* 194 (3), S. 237–255. DOI: 10.1002/jcp.10208.

Jeener, J.; Meier, B. H.; Bachmann, P.; Ernst, R. R. (1979): Investigation of exchange processes by two-dimensional NMR spectroscopy. In: *The Journal of Chemical Physics* 71 (11), S. 4546–4553. DOI: 10.1063/1.438208.

Jumper, John; Evans, Richard; Pritzel, Alexander; Green, Tim; Figurnov, Michael; Ronneberger, Olaf et al. (2021): Highly accurate protein structure prediction with AlphaFold. In: *Nature* 596 (7873), S. 583–589. DOI: 10.1038/s41586-021-03819-2.

Kaether, Christoph; Haass, Christian; Steiner, Harald (2006): Assembly, trafficking and function of gamma-secretase. In: *Neurodegener Dis* 3 (4-5), S. 275–283. DOI: 10.1159/000095267.

Kamp, Frits; Winkler, Edith; Trambauer, Johannes; Ebke, Amelie; Fluhrer, Regina; Steiner, Harald (2015): Intramembrane proteolysis of β-amyloid precursor protein by γ-secretase is an unusually slow process. In: *Biophysical Journal* 108 (5), S. 1229–1237. DOI: 10.1016/j.bpj.2014.12.045.

Karplus, Martin (1963): Vicinal proton coupling in nuclear magnetic resonance. Online verfügbar unter https://pubs.acs.org/doi/pdf/10.1021/ja00901a059.

Kay, Lewis; Keifer, Paul; Saarinen, Tim (1992): Pure absorption gradient enhanced heteronuclear single quantum correlation spectroscopy with improved sensitivity. In: *J. Am. Chem. Soc.* 114 (26), S. 10663–10665. DOI: 10.1021/ja00052a088.

Keeler, James (2012): Understanding NMR spectroscopy. Second edition. Reprinted in January 2011. Chichester: John Wiley & Sons, Ltd. Publication.

Kelly, Sharon M.; Jess, Thomas J.; Price, Nicholas C. (2005): How to study proteins by circular dichroism (1751). Online verfügbar unter https://reader.elsevier.com/reader/sd/pii/S1570963905001792?token=572A98DA4690931CC907F658FAAA3495FC3653D455E75A8A47D70EC5F9551774673E1AD60DF540B1BBBADEF97C09CCEB&originRegion=eu-west-1&originCreation=20230519225223.

Kentsis, Alex; Mezei, Mihaly; Gindin, Tatyana; Osman, Roman (2004): Unfolded state of polyalanine is a segmented polyproline II helix. In: *Proteins: Structure, Function, and Bioinformatics* 55 (3), S. 493–501. DOI: 10.1002/prot.20051.

Kim, Jungsu; Miller, Victor M.; Levites, Yona; West, Karen Jansen; Zwizinski, Craig W.; Moore, Brenda D. et al. (2008): BRI2 (ITM2b) inhibits Abeta deposition in vivo. In: *J. Neurosci.* 28 (23), S. 6030–6036. DOI: 10.1523/JNEUROSCI.0891-08.2008.

Kimberly, W. T.; Zheng, J. B.; Guénette, S. Y.; Selkoe, D. J. (2001): The intracellular domain of the beta-amyloid precursor protein is stabilized by Fe65 and translocates to the nucleus in a notch-like manner. In: *Journal of Biological Chemistry* 276 (43), S. 40288–40292. DOI: 10.1074/jbc.C100447200.

Kirchner, J.; Bevan, M. J. (1999): ITM2A is induced during thymocyte selection and T cell activation and causes downregulation of CD8 when overexpressed in CD4(+)CD8(+) double positive thymocytes. In: *J Exp Med* 190 (2), S. 217–228. DOI: 10.1084/jem.190.2.217.

Kleckner, Ian R.; Foster, Mark P. (2011): An introduction to NMR-based approaches for measuring protein dynamics. In: *Biochimica et biophysica acta* 1814 (8), S. 942–968. DOI: 10.1016/j.bbapap.2010.10.012.

Koonin, Eugene V.; Makarova, Kira S.; Rogozin, Igor B.; Davidovic, Laetitia; Letellier, Marie-Claude; Pellegrini, Luca (2003): The rhomboids: a nearly ubiquitous family of intramembrane serine proteases that probably evolved by multiple ancient horizontal gene transfers. In: *Genome biology* 4 (3), R19. DOI: 10.1186/gb-2003-4-3-r19.

Kopan, Raphael; Ilagan, Ma Xenia G. (2004): Gamma-secretase: proteasome of the membrane? In: *Nature reviews. Molecular cell biology* 5 (6), S. 499–504. DOI: 10.1038/nrm1406.

Kopan, Raphael; Ilagan, Maria Xenia G. (2009): The canonical Notch signaling pathway: unfolding the activation mechanism. In: *Cell* 137 (2), S. 216–233. DOI: 10.1016/j.cell.2009.03.045.

Kovall, R. A. (2008): More complicated than it looks: assembly of Notch pathway transcription complexes. In: *Oncogene* 27 (38), S. 5099–5109. DOI: 10.1038/onc.2008.223.

Krebs, Luke T.; Xue, Yingzi; Norton, Christine R.; Sundberg, John P.; Beatus, Paul; Lendahl, Urban et al. (2003): Characterization of Notch3-deficient mice: normal embryonic development and absence of genetic interactions with a Notch1 mutation. In: *genesis* 37 (3), S. 139–143. DOI: 10.1002/gene.10241.

Krittanai, Chartchai; Johnson, W. Curtis (2000): The relative order of helical propensity of amino acids changes with solvent environment. In: *Proteins: Structure, Function, and Bioinformatics* 39 (2), S. 132–141. DOI: 10.1002/(SICI)1097-0134(20000501)39:2<132::AID-PROT3>3.0.CO;2-2.

Kuhn, Peer-Hendrik; Voss, Matthias; Haug-Kröper, Martina; Schröder, Bernd; Schepers, Ute; Bräse, Stefan et al. (2015): Secretome analysis identifies novel signal Peptide peptidase-like 3 (Sppl3) substrates and reveals a role of Sppl3 in multiple Golgi glycosylation pathways. In: *Molecular & cellular proteomics : MCP* 14 (6), S. 1584–1598. DOI: 10.1074/mcp.M115.048298.

Kühnle, Nathalie; Dederer, Verena; Lemberg, Marius K. (2019): Intramembrane proteolysis at a glance: from signalling to protein degradation. In: *J Cell Sci* 132 (16). DOI: 10.1242/jcs.217745.

Kuipers, Bas J. H.; Gruppen, Harry (2007): Prediction of molar extinction coefficients of proteins and peptides using UV absorption of the constituent amino acids at 214 nm to enable quantitative reverse phase high-performance liquid chromatography-mass spectrometry analysis. In: *Journal of Agricultural and Food Chemistry* 55 (14), S. 5445–5451. DOI: 10.1021/jf070337l.

Langosch, D.; Scharnagl, C.; Steiner, H.; Lemberg, M. K. (2015): Understanding intramembrane proteolysis: from protein dynamics to reaction kinetics. In: *Trends in Biochemical Sciences* 40 (6), S. 318–327. DOI: 10.1016/j.tibs.2015.04.001.

Langosch, Dieter; Steiner, Harald (2017): Substrate processing in intramembrane proteolysis by γ-secretase - the role of protein dynamics. In: *Biological Chemistry* 398 (4), S. 441–453. DOI: 10.1515/hsz-2016-0269.

Laurent, Sarah A.; Hoffmann, Franziska S.; Kuhn, Peer-Hendrik; Cheng, Qingyu; Chu, Yuanyuan; Schmidt-Supprian, Marc et al. (2015): γ-Secretase directly sheds the survival receptor BCMA from plasma cells. In: *Nat Commun* 6 (1), S. 7333. DOI: 10.1038/ncomms8333.

Lemberg, M. K.; Bland, F. A.; Weihofen, A.; Braud, V. M.; Martoglio, B. (2001): Intramembrane proteolysis of signal peptides: an essential step in the generation of HLA-E epitopes. In: *Journal of immunology (Baltimore, Md. : 1950)* 167 (11), S. 6441–6446. DOI: 10.4049/jimmunol.167.11.6441.

Lemberg, Marius K.; Freeman, Matthew (2007): Functional and evolutionary implications of enhanced genomic analysis of rhomboid intramembrane proteases. In: *Genome research* 17 (11), S. 1634–1646. DOI: 10.1101/gr.6425307.

Lemberg, Marius K.; Martoglio, Bruno (2002): Requirements for signal peptide peptidase-catalyzed intramembrane proteolysis. In: *Molecular cell* 10 (4), S. 735–744. DOI: 10.1016/s1097-2765(02)00655-x.

Lemberg, Marius K.; Menendez, Javier; Misik, Angelika; Garcia, Maite; Koth, Christopher M.; Freeman, Matthew (2005): Lemberg Freeman_2005 EMBO J_Mechanism of intramembrane proteolysis investigated with purified rhomboid proteases // Mechanism of intramembrane proteolysis investigated with purified rhomboid proteases. In: *The EMBO journal* 24 (3), S. 464–472. DOI: 10.1038/sj.emboj.7600537.

Lerch-Bader, Mirjam; Lundin, Carolina; Kim, Hyun; Nilsson, IngMarie; Heijne, Gunnar von (2008): Contribution of positively charged flanking residues to the insertion of transmembrane helices into the endoplasmic reticulum. In: *Proceedings of the National Academy of Sciences of the United States of America* 105 (11), S. 4127–4132. DOI: 10.1073/pnas.0711580105.

Li, S. C.; Deber, C. M. (1992): Glycine and beta-branched residues support and modulate peptide helicity in membrane environments. In: *FEBS letters* 311 (3), S. 217–220. DOI: 10.1016/0014-5793(92)81106-V.

Li, S. C.; Deber, C. M. (1993): Peptide environment specifies conformation. Helicity of hydrophobic segments compared in aqueous, organic, and membrane environments.

In: *Journal of Biological Chemistry* 268 (31), S. 22975–22978. DOI: 10.1016/S0021-9258(19)49413-1.

Li, S. C.; Deber, C. M. (1994): A measure of helical propensity for amino acids in membrane environments. In: *Nat Struct Mol Biol* 1 (6), S. 368–373. DOI: 10.1038/nsb0694-368.

Li, Shu; Zhang, Wan; Han, Wei (2017): Initial Substrate Binding of γ-Secretase: The Role of Substrate Flexibility. In: *ACS Chemical Neuroscience* 8 (6), S. 1279–1290. DOI: 10.1021/acschemneuro.6b00425.

Lichtenthaler, Stefan F. (2011): α-secretase in Alzheimer's disease: molecular identity, regulation and therapeutic potential. In: *Journal of neurochemistry* 116 (1), S. 10–21. DOI: 10.1111/j.1471-4159.2010.07081.x.

Lichtenthaler, Stefan F.; Lemberg, Marius K.; Fluhrer, Regina (2018): Proteolytic ectodomain shedding of membrane proteins in mammals-hardware, concepts, and recent developments. In: *The EMBO journal* 37 (15). DOI: 10.15252/embj.201899456.

Lindemann, Dirk; Rethwilm, Axel (2011): Foamy virus biology and its application for vector development. In: *Viruses* 3 (5), S. 561–585. DOI: 10.3390/v3050561.

Lindorff-Larsen, Kresten; Best, Robert B.; Depristo, Mark A.; Dobson, Christopher M.; Vendruscolo, Michele (2005): Simultaneous determination of protein structure and dynamics. In: *Nature* 433 (7022), S. 128–132. DOI: 10.1038/nature03199.

Linge, J. P.; O'Donoghue, S. I.; Nilges, M. (2001): Automated assignment of ambiguous nuclear overhauser effects with ARIA. In: *Methods in enzymology* 339, S. 71–90. DOI: 10.1016/s0076-6879(01)39310-2.

Linge, Jens P.; Habeck, Michael; Rieping, Wolfgang; Nilges, Michael (2003): ARIA: automated NOE assignment and NMR structure calculation. In: *Bioinformatics* 19 (2), S. 315–316. DOI: 10.1093/bioinformatics/19.2.315.

Linge, Jens P.; Habeck, Michael; Rieping, Wolfgang; Nilges, Michael (2004): Correction of spin diffusion during iterative automated NOE assignment. In: *Journal of Magnetic Resonance* 167 (2), S. 334–342. DOI: 10.1016/j.jmr.2004.01.010.

Liu, Li-Ping; Deber, Charles M. (1998): Guidelines for membrane protein engineering derived from de novo designed model peptides. In: *Biopolymers* 47 (1), S. 41–62. DOI: 10.1002/(SICI)1097-0282(1998)47:1<41::AID-BIP6>3.0.CO;2-X.

Liu, Maili; Mao, Xi-an; Ye, Chaohui; Huang, He; Nicholson, Jeremy K.; Lindon, John C. (1998): Improved WATERGATE Pulse Sequences for Solvent Suppression in NMR

Spectroscopy. In: *Journal of Magnetic Resonance* 132 (1), S. 125–129. DOI: 10.1006/jmre.1998.1405.

Logeat, F.; Bessia, C.; Brou, C.; LeBail, O.; Jarriault, S.; Seidah, N. G.; Israël, A. (1998): The Notch1 receptor is cleaved constitutively by a furin-like convertase. In: *Proceedings of the National Academy of Sciences of the United States of America* 95 (14), S. 8108–8112. DOI: 10.1073/pnas.95.14.8108.

Lohi, Olli; Urban, Sinisa; Freeman, Matthew (2004): Diverse substrate recognition mechanisms for rhomboids; thrombomodulin is cleaved by Mammalian rhomboids. In: *Current Biology* 14 (3), S. 236–241. DOI: 10.1016/j.cub.2004.01.025.

Lu, Wenshu; Chen, Qiongyu; Ying, Songmin; Xia, Xiaobing; Yu, Zhanru; Lui, Yuan et al. (2016): Evolutionarily conserved primary TNF sequences relate to its primitive functions in cell death induction. In: *J Cell Sci* 129 (1), S. 108–120. DOI: 10.1242/jcs.175463.

Lyu, P. C.; Sherman, J. C.; Chen, A.; Kallenbach, N. R. (1991): Alpha-helix stabilization by natural and unnatural amino acids with alkyl side chains. In: *Proceedings of the National Academy of Sciences of the United States of America* 88 (12), S. 5317–5320. DOI: 10.1073/pnas.88.12.5317.

Ma, Yuanqing; Poole, Kate; Goyette, Jesse; Gaus, Katharina (2017): Introducing Membrane Charge and Membrane Potential to T Cell Signaling. In: *Front. Immunol.* 8, S. 1513. DOI: 10.3389/fimmu.2017.01513.

Manolaridis, Ioannis; Kulkarni, Kiran; Dodd, Roger B.; Ogasawara, Satoshi; Zhang, Ziguo; Bineva, Ganka et al. (2013): Mechanism of farnesylated CAAX protein processing by the intramembrane protease Rce1. In: *Nature* 504 (7479), S. 301–305. DOI: 10.1038/nature12754.

Marín, Ignacio (2020): Tumor Necrosis Factor Superfamily: Ancestral Functions and Remodeling in Early Vertebrate Evolution. In: *Genome Biol Evol* 12 (11), S. 2074–2092. DOI: 10.1093/gbe/evaa140.

Martin, Lucas; Fluhrer, Regina; Haass, Christian (2009): Substrate requirements for SPPL2b-dependent regulated intramembrane proteolysis. In: *Journal of Biological Chemistry* 284 (9), S. 5662–5670. DOI: 10.1074/jbc.M807485200.

Martin, Lucas; Fluhrer, Regina; Reiss, Karina; Kremmer, Elisabeth; Saftig, Paul; Haass, Christian (2008): Regulated intramembrane proteolysis of Bri2 (Itm2b) by ADAM10

and SPPL2a/SPPL2b. In: *Journal of Biological Chemistry* 283 (3), S. 1644–1652. DOI: 10.1074/jbc.M706661200.

Martoglio, B.; Graf, R.; Dobberstein, B. (1997): Signal peptide fragments of preprolactin and HIV-1 p-gp160 interact with calmodulin. In: *The EMBO journal* 16 (22), S. 6636–6645. DOI: 10.1093/emboj/16.22.6636.

Martoglio, Bruno; Golde, Todd E. (2003): Intramembrane-cleaving aspartic proteases and disease: presenilins, signal peptide peptidase and their homologs. In: *Hum Mol Genet* 12 Spec No 2 (suppl_2), R201-6. DOI: 10.1093/hmg/ddg303.

Meckler, Xavier; Checler, Frédéric (2016): Presenilin 1 and Presenilin 2 Target γ-Secretase Complexes to Distinct Cellular Compartments. In: *The Journal of biological chemistry* 291 (24), S. 12821–12837. DOI: 10.1074/jbc.M115.708297.

Meissner, Cathrin; Lorenz, Holger; Weihofen, Andreas; Selkoe, Dennis J.; Lemberg, Marius K. (2011): The mitochondrial intramembrane protease PARL cleaves human Pink1 to regulate Pink1 trafficking. In: *Journal of neurochemistry* 117 (5), S. 856–867. DOI: 10.1111/j.1471-4159.2011.07253.x.

Mentrup, Torben; Fluhrer, Regina; Schröder, Bernd (2017): Latest emerging functions of SPP/SPPL intramembrane proteases. In: *European journal of cell biology* 96 (5), S. 372–382. DOI: 10.1016/j.ejcb.2017.03.002.

Mentrup, Torben; Schröder, Bernd (2022): Signal peptide peptidase-like 2 proteases: Regulatory switches or proteasome of the membrane? In: *Biochimica et biophysica acta. Molecular cell research* 1869 (1), S. 119163. DOI: 10.1016/j.bbamcr.2021.119163.

Mentrup, Torben; Theodorou, Kosta; Cabrera-Cabrera, Florencia; Helbig, Andreas O.; Happ, Kathrin; Gijbels, Marion et al. (2019): Atherogenic LOX-1 signaling is controlled by SPPL2-mediated intramembrane proteolysis. In: *The Journal of experimental medicine* 216 (4), S. 807–830. DOI: 10.1084/jem.20171438.

Micsonai, András; Wien, Frank; Bulyáki, Éva; Kun, Judit; Moussong, Éva; Lee, Young-Ho et al. (2018): BeStSel: a web server for accurate protein secondary structure prediction and fold recognition from the circular dichroism spectra. In: *Nucleic Acids Res* 46 (W1), W315-W322. DOI: 10.1093/nar/gky497.

Micsonai, András; Wien, Frank; Kernya, Linda; Lee, Young-Ho; Goto, Yuji; Réfrégiers, Matthieu; Kardos, József (2015): Accurate secondary structure prediction and fold recognition for circular dichroism spectroscopy. In: *Proceedings of the National*

Academy of Sciences of the United States of America 112 (24), E3095-103. DOI: 10.1073/pnas.1500851112.

Millhauser, G. L. (1995): Views of helical peptides: a proposal for the position of 3(10)-helix along the thermodynamic folding pathway. In: *Biochemistry* 34 (12), S. 3873–3877. DOI: 10.1021/bi00012a001.

Milne, J. S.; Mayne, L.; Roder, H.; Wand, A. J.; Englander, S. W. (1998): Determinants of protein hydrogen exchange studied in equine cytochrome c. In: *Protein science : a publication of the Protein Society* 7 (3), S. 739–745. DOI: 10.1002/pro.5560070323.

Mirdita, Milot; Schütze, Konstantin; Moriwaki, Yoshitaka; Heo, Lim; Ovchinnikov, Sergey; Steinegger, Martin (2022): ColabFold: making protein folding accessible to all. In: *Nat Methods* 19 (6), S. 679–682. DOI: 10.1038/s41592-022-01488-1.

Miyashita, Hiroyuki; Maruyama, Yuusuke; Isshiki, Hayato; Osawa, Satoko; Ogura, Toshihiko; Mio, Kazuhiro et al. (2011): Three-dimensional structure of the signal peptide peptidase. In: *The Journal of biological chemistry* 286 (29), S. 26188–26197. DOI: 10.1074/jbc.M111.260273.

Mohan, Mohita J.; Seaton, Theresa; Mitchell, Justin; Howe, Anne; Blackburn, Kevin; Burkhart, William et al. (2002): The tumor necrosis factor-alpha converting enzyme (TACE): a unique metalloproteinase with highly defined substrate selectivity. In: *Biochemistry* 41 (30), S. 9462–9469. DOI: 10.1021/bi0260132.

Moin, Syed M.; Urban, Sinisa (2012): Membrane immersion allows rhomboid proteases to achieve specificity by reading transmembrane segment dynamics. In: *eLife* 1, e00173. DOI: 10.7554/eLife.00173.

Mori, Susumu; Abeygunawardana, Chitrananda; Berg, Jeremy M.; van Zijl, Peter C. M. (1997): NMR Study of Rapidly Exchanging Backbone Amide Protons in Staphylococcal Nuclease and the Correlation with Structural and Dynamic Properties. In: *J. Am. Chem. Soc.* 119 (29), S. 6844–6852. DOI: 10.1021/ja963351f.

Moss, M. L.; Jin, S. L.; Milla, M. E.; Bickett, D. M.; Burkhart, W.; Carter, H. L. et al. (1997): Cloning of a disintegrin metalloproteinase that processes precursor tumour-necrosis factor-alpha. In: *Nature* 385 (6618), S. 733–736. DOI: 10.1038/385733a0.

Mulder, Frans A. A.; Filatov, Michael (2010): NMR chemical shift data and ab initio shielding calculations: emerging tools for protein structure determination. In: *Chem. Soc. Rev.* 39 (2), S. 578–590. DOI: 10.1039/B811366C.

Nadezhdin, K. D.; Bocharova, O. V.; Bocharov, E. V.; Arseniev, A. S. (2011): Structural and dynamic study of the transmembrane domain of the amyloid precursor protein. In: *Acta Naturae* 3 (1), S. 69–76. Online verfügbar unter https://www.ncbi.nlm.nih.gov/pmc/articles/PMC3347594/.

Nam, Yunsun; Sliz, Piotr; Song, Luyan; Aster, Jon C.; Blacklow, Stephen C. (2006): Structural basis for cooperativity in recruitment of MAML coactivators to Notch transcription complexes. In: *Cell* 124 (5), S. 973–983. DOI: 10.1016/j.cell.2005.12.037.

Natoli, G.; Costanzo, A.; Moretti, F.; Fulco, M.; Balsano, C.; Levrero, M. (1997): Tumor necrosis factor (TNF) receptor 1 signaling downstream of TNF receptor-associated factor 2. Nuclear factor kappaB (NFkappaB)-inducing kinase requirement for activation of activating protein 1 and NFkappaB but not of c-Jun N-terminal kinase/stress-activated protein kinase. In: *Journal of Biological Chemistry* 272 (42), S. 26079–26082. DOI: 10.1074/jbc.272.42.26079.

Niemeyer, Johannes; Mentrup, Torben; Heidasch, Ronny; Müller, Stephan A.; Biswas, Uddipta; Meyer, Rieke et al. (2019): The intramembrane protease SPPL2c promotes male germ cell development by cleaving phospholamban. In: *EMBO reports* 20 (3). DOI: 10.15252/embr.201846449.

Nilges, M. (1997): Ambiguous distance data in the calculation of NMR structures. In: *Folding and Design* 2 (4), S53-7. DOI: 10.1016/S1359-0278(97)00064-3.

Nilges, M.; Clore, G. M.; Gronenborn, A. M. (1988): Determination of three-dimensional structures of proteins from interproton distance data by hybrid distance geometry-dynamical simulated annealing calculations. In: *FEBS letters* 229 (2), S. 317–324. DOI: 10.1016/0014-5793(88)81148-7.

Nilges, M.; Macias, M. J.; O'Donoghue, S. I.; Oschkinat, H. (1997): Automated NOESY interpretation with ambiguous distance restraints: the refined NMR solution structure of the pleckstrin homology domain from beta-spectrin. In: *Journal of molecular biology* 269 (3), S. 408–422. DOI: 10.1006/jmbi.1997.1044.

Nilges, Michael; O'Donoghue, Seán I. (1998): Ambiguous NOEs and automated NOE assignment. In: *Progress in nuclear magnetic resonance spectroscopy* 32 (2), S. 107–139. DOI: 10.1016/S0079-6565(97)00025-3.

Niu, Jiani; Cederstrand, Annika J.; Eddinger, Geoffrey A.; Yin, Boyu; Checco, James W.; Bingman, Craig A. et al. (2022): Trimer-to-Monomer Disruption Mechanism for a

Potent, Protease-Resistant Antagonist of Tumor Necrosis Factor-α Signaling. In: *J. Am. Chem. Soc.* 144 (22), S. 9610–9617. DOI: 10.1021/jacs.1c13717.

Nyborg, Andrew C.; Herl, Lauren; Berezovska, Oksana; Thomas, Anne V.; Ladd, Thomas B.; Jansen, Karen et al. (2006): Signal peptide peptidase (SPP) dimer formation as assessed by fluorescence lifetime imaging microscopy (FLIM) in intact cells. In: *Mol Neurodegeneration* 1 (1), S. 16. DOI: 10.1186/1750-1326-1-16.

Nyborg, Andrew C.; Jansen, Karen; Ladd, Thomas B.; Fauq, Abdul; Golde, Todd E. (2004a): A signal peptide peptidase (SPP) reporter activity assay based on the cleavage of type II membrane protein substrates provides further evidence for an inverted orientation of the SPP active site relative to presenilin. In: *The Journal of biological chemistry* 279 (41), S. 43148–43156. DOI: 10.1074/jbc.M405879200.

Nyborg, Andrew C.; Kornilova, Anna Y.; Jansen, Karen; Ladd, Thomas B.; Wolfe, Michael S.; Golde, Todd E. (2004b): Signal peptide peptidase forms a homodimer that is labeled by an active site-directed gamma-secretase inhibitor. In: *Journal of Biological Chemistry* 279 (15), S. 15153–15160. DOI: 10.1074/jbc.M309305200.

Okochi, Masayasu; Fukumori, Akio; Jiang, Jingwei; Itoh, Naohiro; Kimura, Ryo; Steiner, Harald et al. (2006): Secretion of the Notch-1 Abeta-like peptide during Notch signaling. In: *Journal of Biological Chemistry* 281 (12), S. 7890–7898. DOI: 10.1074/jbc.M513250200.

Okochi, Masayasu; Steiner, Harald; Fukumori, Akio; Tanii, Hisashi; Tomita, Taisuke; Tanaka, Toshihisa et al. (2002): Presenilins mediate a dual intramembranous gamma-secretase cleavage of Notch-1. In: *The EMBO journal* 21 (20), S. 5408–5416. DOI: 10.1093/emboj/cdf541.

O'Malley, W. Edward; Achinstein, Betty; Shear, Murray J. (1962): Action of Bacterial Polysaccharide on Tumors. II. Damage of Sarcoma 37 by Serum of Mice Treated With Serratia Marcescens Polysaccharide, and Induced Tolerance. In: *J Natl Cancer Inst* 29 (6), S. 1169–1175. DOI: 10.1093/jnci/29.6.1169.

Ortner, Martin; Guschtschin-Schmidt, Nadja; Stelzer, Walter; Muhle-Goll, Claudia; Langosch, Dieter (2023): Permissive Conformations of a Transmembrane Helix Allow Intramembrane Proteolysis by γ-Secretase. In: *Journal of molecular biology*, S. 168218. DOI: 10.1016/j.jmb.2023.168218.

Pace, C. N.; Scholtz, J. M. (1998): A helix propensity scale based on experimental studies of peptides and proteins. In: *Biophysical Journal* 75 (1), S. 422–427. DOI: 10.1016/S0006-3495(98)77529-0.

Palmer, Arthur G.; Cavanagh, John; Wright, Peter E.; Rance, Mark (1991): Sensitivity improvement in proton-detected two-dimensional heteronuclear correlation NMR spectroscopy. In: *Journal of Magnetic Resonance (1969)* 93 (1), S. 151–170. DOI: 10.1016/0022-2364(91)90036-S.

Papadopoulou, Alkmini A.; Fluhrer, Regina (2020): Signaling Functions of Intramembrane Aspartyl-Proteases. In: *Front. Cardiovasc. Med.* 7, S. 591787. DOI: 10.3389/fcvm.2020.591787.

Papadopoulou, Alkmini A.; Müller, Stephan A.; Mentrup, Torben; Shmueli, Merav D.; Niemeyer, Johannes; Haug-Kröper, Martina et al. (2019): Signal peptide peptidase-like 2c impairs vesicular transport and cleaves SNARE proteins. In: *EMBO reports* 20 (3), e46451. DOI: 10.15252/embr.201846451.

Papadopoulou, Alkmini A.; Stelzer, Walter; Silber, Mara; Schlosser, Christine; Spitz, Charlotte; Haug-Kröper, Martina et al. (2022): Helical stability of the GnTV transmembrane domain impacts on SPPL3 dependent cleavage. In: *Sci Rep* 12 (1), S. 20987. DOI: 10.1038/s41598-022-24772-8.

Pascall, John C.; Brown, Kenneth D. (2004): Intramembrane cleavage of ephrinB3 by the human rhomboid family protease, RHBDL2. In: *Biochemical and biophysical research communications* 317 (1), S. 244–252. DOI: 10.1016/j.bbrc.2004.03.039.

Petit, Dieter; Hitzenberger, Manuel; Lismont, Sam; Zoltowska, Katarzyna Marta; Ryan, Natalie S.; Mercken, Marc et al. (2019): Extracellular interface between APP and Nicastrin regulates Aβ length and response to γ-secretase modulators. In: *The EMBO journal* 38 (12), e101494. DOI: 10.15252/embj.2019101494.

Pimentel-Muiños, F. X.; Seed, B. (1999): Regulated commitment of TNF receptor signaling: a molecular switch for death or activation. In: *Immunity* 11 (6), S. 783–793. DOI: 10.1016/S1074-7613(00)80152-1.

Prokop, Stefan; Shirotani, Keiro; Edbauer, Dieter; Haass, Christian; Steiner, Harald (2004): Requirement of PEN-2 for stabilization of the presenilin N-/C-terminal fragment heterodimer within the gamma-secretase complex. In: *Journal of Biological Chemistry* 279 (22), S. 23255–23261. DOI: 10.1074/jbc.M401789200.

Puig, Kendra L.; Combs, Colin K. (2013): Expression and function of APP and its metabolites outside the central nervous system. In: *Experimental Gerontology* 48 (7), S. 608–611. DOI: 10.1016/j.exger.2012.07.009.

Quint, Stefan; Widmaier, Simon; Minde, David; Hornburg, Daniel; Langosch, Dieter; Scharnagl, Christina (2010): Residue-specific side-chain packing determines the backbone dynamics of transmembrane model helices. In: *Biophysical Journal* 99 (8), S. 2541–2549. DOI: 10.1016/j.bpj.2010.08.031.

Quintero-Monzon, Omar; Martin, Morgan M.; Fernandez, Marty A.; Cappello, Christina A.; Krzysiak, Amanda J.; Osenkowski, Pamela; Wolfe, Michael S. (2011): Dissociation between the processivity and total activity of γ-secretase: implications for the mechanism of Alzheimer's disease-causing presenilin mutations. In: *Biochemistry* 50 (42), S. 9023–9035. DOI: 10.1021/bi2007146.

Rawson, R. B.; Zelenski, N. G.; Nijhawan, D.; Ye, J.; Sakai, J.; Hasan, M. T. et al. (1997): Complementation cloning of S2P, a gene encoding a putative metalloprotease required for intramembrane cleavage of SREBPs. In: *Molecular cell* 1 (1), S. 47–57. DOI: 10.1016/s1097-2765(00)80006-4.

Rawson, Robert B. (2013): The site-2 protease. In: *Biochimica et biophysica acta* 1828 (12), S. 2801–2807. DOI: 10.1016/j.bbamem.2013.03.031.

Reed, C.; Fu, Z. Q.; Wu, J.; Xue, Y. N.; Harrison, R. W.; Chen, M. J.; Weber, I. T. (1997): Crystal structure of TNF-alpha mutant R31D with greater affinity for receptor R1 compared with R2. In: *Protein engineering* 10 (10), S. 1101–1107. DOI: 10.1093/protein/10.10.1101.

Rieping, Wolfgang; Habeck, Michael; Bardiaux, Benjamin; Bernard, Aymeric; Malliavin, Thérèse E.; Nilges, Michael (2007): ARIA2: automated NOE assignment and data integration in NMR structure calculation. In: *Bioinformatics* 23 (3), S. 381–382. DOI: 10.1093/bioinformatics/btl589.

Sakai, J.; Duncan, E. A.; Rawson, R. B.; Hua, X.; Brown, M. S.; Goldstein, J. L. (1996): Sakai, Goldstein_1996 Cell_Sterol regulated release of SREBP2 from cell membranes requires two sequential cleavages one within a transmembrane segment // Sterol-regulated release of SREBP-2 from cell membranes requires two sequential cleavages, one within a transmembrane segment. In: *Cell* 85 (7), S. 1037–1046. DOI: 10.1016/s0092-8674(00)81304-5.

Sanchez-Irizarry, Cheryll; Carpenter, Andrea C.; Weng, Andrew P.; Pear, Warren S.; Aster, Jon C.; Blacklow, Stephen C. (2004): Notch subunit heterodimerization and prevention of ligand-independent proteolytic activation depend, respectively, on a novel domain and the LNR repeats. In: *Molecular and cellular biology* 24 (21), S. 9265–9273. DOI: 10.1128/MCB.24.21.9265-9273.2004.

Sannerud, Ragna; Esselens, Cary; Ejsmont, Paulina; Mattera, Rafael; Rochin, Leila; Tharkeshwar, Arun Kumar et al. (2016): Restricted Location of PSEN2/γ-Secretase Determines Substrate Specificity and Generates an Intracellular Aβ Pool. In: *Cell* 166 (1), S. 193–208. DOI: 10.1016/j.cell.2016.05.020.

Sato, Chihiro; Morohashi, Yuichi; Tomita, Taisuke; Iwatsubo, Takeshi (2006): Structure of the catalytic pore of gamma-secretase probed by the accessibility of substituted cysteines. In: *J. Neurosci.* 26 (46), S. 12081–12088. DOI: 10.1523/JNEUROSCI.3614-06.2006.

Sato, Chihiro; Takagi, Shizuka; Tomita, Taisuke; Iwatsubo, Takeshi (2008): The C-terminal PAL motif and transmembrane domain 9 of presenilin 1 are involved in the formation of the catalytic pore of the gamma-secretase. In: *J. Neurosci.* 28 (24), S. 6264–6271. DOI: 10.1523/JNEUROSCI.1163-08.2008.

Schauenburg, Linda; Liebsch, Filip; Eravci, Murat; Mayer, Magnus C.; Weise, Christoph; Multhaup, Gerhard (2018): APLP1 is endoproteolytically cleaved by γ-secretase without previous ectodomain shedding. In: *Sci Rep* 8 (1), S. 1916. DOI: 10.1038/s41598-018-19530-8.

Schneidman-Duhovny, Dina; Pellarin, Riccardo; Sali, Andrej (2014): Uncertainty in integrative structural modeling. In: *Current Opinion in Structural Biology* 28, S. 96–104. DOI: 10.1016/j.sbi.2014.08.001.

Schneppenheim, Janna; Hüttl, Susann; Mentrup, Torben; Lüllmann-Rauch, Renate; Rothaug, Michelle; Engelke, Michael et al. (2014): The intramembrane proteases signal Peptide peptidase-like 2a and 2b have distinct functions in vivo. In: *Molecular and cellular biology* 34 (8), S. 1398–1411. DOI: 10.1128/MCB.00038-14.

Schrul, Bianca; Kapp, Katja; Sinning, Irmgard; Dobberstein, Bernhard (2010): Signal peptide peptidase (SPP) assembles with substrates and misfolded membrane proteins into distinct oligomeric complexes. In: *Biochem J* 427 (3), S. 523–534. DOI: 10.1042/BJ20091005.

Schutz, C. N.; Warshel, A. (2001): What are the dielectric "constants" of proteins and how to validate electrostatic models? In: *Proteins* 44 (4), S. 400–417. DOI: 10.1002/prot.1106.

Selkoe, D. J. (1999): Translating cell biology into therapeutic advances in Alzheimer's disease. In: *Nature* 399 (6738 Suppl), A23-31. DOI: 10.1038/399a023.

Selkoe, Dennis J. (2004): Alzheimer disease: mechanistic understanding predicts novel therapies. In: *Annals of internal medicine* 140 (8), S. 627–638. DOI: 10.7326/0003-4819-140-8-200404200-00047.

Selkoe, Dennis J. (2011): Alzheimer's disease. In: *Cold Spring Harb Perspect Biol* 3 (7), a004457. DOI: 10.1101/cshperspect.a004457.

Selkoe, Dennis J.; Wolfe, Michael S. (2007): Presenilin: running with scissors in the membrane. In: *Cell* 131 (2), S. 215–221. DOI: 10.1016/j.cell.2007.10.012.

Shah, Sanjiv; Lee, Sheu-Fen; Tabuchi, Katsuhiko; Hao, Yi-Heng; Yu, Cong; LaPlant, Quincey et al. (2005): Nicastrin functions as a gamma-secretase-substrate receptor. In: *Cell* 122 (3), S. 435–447. DOI: 10.1016/j.cell.2005.05.022.

Shen, Yang; Delaglio, Frank; Cornilescu, Gabriel; Bax, Ad (2009): TALOS+: a hybrid method for predicting protein backbone torsion angles from NMR chemical shifts. In: *Journal of biomolecular NMR* 44 (4), S. 213–223. DOI: 10.1007/s10858-009-9333-z.

Silber, Mara; Hitzenberger, Manuel; Zacharias, Martin; Muhle-Goll, Claudia (2020): Altered Hinge Conformations in APP Transmembrane Helix Mutants May Affect Enzyme-Substrate Interactions of γ-Secretase. In: *ACS Chemical Neuroscience* 11 (24), S. 4426–4433. DOI: 10.1021/acschemneuro.0c00640.

Spera, Silvia; Bax, Ad (1991): Empirical correlation between protein backbone conformation and C.alpha. and C.beta. 13C nuclear magnetic resonance chemical shifts. In: *J. Am. Chem. Soc.* 113 (14), S. 5490–5492. DOI: 10.1021/ja00014a071.

Spiess, M. (1995): Heads or tails--what determines the orientation of proteins in the membrane. In: *FEBS letters* 369 (1), S. 76–79. DOI: 10.1016/0014-5793(95)00551-J.

Spinazzi, Marco; Strooper, Bart de (2016): PARL: The mitochondrial rhomboid protease. In: *Seminars in cell & developmental biology* 60, S. 19–28. DOI: 10.1016/j.semcdb.2016.07.034.

Spitz, Charlotte; Schlosser, Christine; Guschtschin-Schmidt, Nadja; Stelzer, Walter; Menig, Simon; Götz, Alexander et al. (2020): Non-canonical Shedding of TNFα by SPPL2a Is

Determined by the Conformational Flexibility of Its Transmembrane Helix. In: *iScience* 23 (12), S. 101775. DOI: 10.1016/j.isci.2020.101775.

Steiner, H.; Haass, C. (2000): Intramembrane proteolysis by presenilins. In: *Nature reviews. Molecular cell biology* 1 (3), S. 217–224. DOI: 10.1038/35043065.

Steiner, Harald; Fluhrer, Regina; Haass, Christian (2008): Intramembrane proteolysis by gamma-secretase. In: *The Journal of biological chemistry* 283 (44), S. 29627–29631. DOI: 10.1074/jbc.R800010200.

Steiner, Harald; Fukumori, Akio; Tagami, Shinji; Okochi, Masayasu (2018): Making the final cut: pathogenic amyloid-β peptide generation by γ-secretase. In: *Cell Stress* 2 (11), S. 292–310. DOI: 10.15698/cst2018.11.162.

Stelzer, Walter; Langosch, Dieter (2019): Conformationally Flexible Sites within the Transmembrane Helices of Amyloid Precursor Protein and Notch1 Receptor. In: *Biochemistry* 58 (28), S. 3065–3068. DOI: 10.1021/acs.biochem.9b00505.

Street, A. G.; Mayo, S. L. (1999): Intrinsic beta-sheet propensities result from van der Waals interactions between side chains and the local backbone. In: *Proceedings of the National Academy of Sciences of the United States of America* 96 (16), S. 9074–9076. DOI: 10.1073/pnas.96.16.9074.

Strooper, B. de; Annaert, W.; Cupers, P.; Saftig, P.; Craessaerts, K.; Mumm, J. S. et al. (1999): A presenilin-1-dependent gamma-secretase-like protease mediates release of Notch intracellular domain. In: *Nature* 398 (6727), S. 518–522. DOI: 10.1038/19083.

Strooper, Bart de (2003): Aph-1, Pen-2, and Nicastrin with Presenilin generate an active gamma-Secretase complex. In: *Neuron* 38 (1), S. 9–12. DOI: 10.1016/S0896-6273(03)00205-8.

Strooper, Bart de; Annaert, Wim (2010): Novel research horizons for presenilins and γ-secretases in cell biology and disease. In: *Annual review of cell and developmental biology* 26, S. 235–260. DOI: 10.1146/annurev-cellbio-100109-104117.

Strooper, Bart de; Chávez Gutiérrez, Lucía (2015): Learning by failing: ideas and concepts to tackle γ-secretases in Alzheimer's disease and beyond. In: *Annual review of pharmacology and toxicology* 55, S. 419–437. DOI: 10.1146/annurev-pharmtox-010814-124309.

Struhl, G.; Adachi, A. (2000): Requirements for presenilin-dependent cleavage of notch and other transmembrane proteins. In: *Molecular cell* 6 (3), S. 625–636. DOI: 10.1016/S1097-2765(00)00061-7.

Struhl, G.; Fitzgerald, K.; Greenwald, I. (1993): Intrinsic activity of the Lin-12 and Notch intracellular domains in vivo. In: *Cell* 74 (2), S. 331–345. DOI: 10.1016/0092-8674(93)90424-o.

Sun, Linfeng; Zhao, Lingyun; Yang, Guanghui; Yan, Chuangye; Zhou, Rui; Zhou, Xiaoyuan et al. (2015): Structural basis of human γ-secretase assembly. In: *Proceedings of the National Academy of Sciences of the United States of America* 112 (19), S. 6003–6008. DOI: 10.1073/pnas.1506242112.

Suzek, Baris E.; Wang, Yuqi; Huang, Hongzhan; McGarvey, Peter B.; Wu, Cathy H. (2015): UniRef clusters: a comprehensive and scalable alternative for improving sequence similarity searches. In: *Bioinformatics* 31 (6), S. 926–932. DOI: 10.1093/bioinformatics/btu739.

Szczepanik, Ann Marie; Rampe, David; Ringheim, Garth E. (2001): Amyloid-β peptide fragments p3 and p4 induce pro-inflammatory cytokine and chemokine production in vitro and in vivo. In: *Journal of neurochemistry* 77 (1), S. 304–317. DOI: 10.1046/j.1471-4159.2001.00240.x.

Szilágyi, László (1995): Chemical shifts in proteins come of age. In: *Progress in nuclear magnetic resonance spectroscopy* 27 (4), S. 325–442. DOI: 10.1016/0079-6565(95)01011-2.

Takagi-Niidome, Shizuka; Sasaki, Tomoki; Osawa, Satoko; Sato, Takeshi; Morishima, Kanan; Cai, Tetsuo et al. (2015): Cooperative roles of hydrophilic loop 1 and the C-terminus of presenilin 1 in the substrate-gating mechanism of γ-secretase. In: *J. Neurosci.* 35 (6), S. 2646–2656. DOI: 10.1523/JNEUROSCI.3164-14.2015.

Takami, Mako; Nagashima, Yu; Sano, Yoshihisa; Ishihara, Seiko; Morishima-Kawashima, Maho; Funamoto, Satoru; Ihara, Yasuo (2009): gamma-Secretase: successive tripeptide and tetrapeptide release from the transmembrane domain of beta-carboxyl terminal fragment. In: *J. Neurosci.* 29 (41), S. 13042–13052. DOI: 10.1523/JNEUROSCI.2362-09.2009.

The UniProt Consortium; Bateman, Alex; Martin, Maria-Jesus; Orchard, Sandra; Magrane, Michele; Ahmad, Shadab et al. (2023): UniProt: the Universal Protein Knowledgebase in 2023. In: *Nucleic Acids Res* 51 (D1), D523-D531. DOI: 10.1093/nar/gkac1052.

Theodosiou, Athina; Arhondakis, Stilianos; Baumann, Marc; Kossida, Sophia (2009): Evolutionary scenarios of Notch proteins. In: *Mol Biol Evol* 26 (7), S. 1631–1640. DOI: 10.1093/molbev/msp075.

Thinakaran, G.; Borchelt, D. R.; Lee, M. K.; Slunt, H. H.; Spitzer, L.; Kim, G. et al. (1996): Endoproteolysis of presenilin 1 and accumulation of processed derivatives in vivo. In: *Neuron* 17 (1), S. 181–190. DOI: 10.1016/S0896-6273(00)80291-3.

Tolia, Alexandra; Chávez-Gutiérrez, Lucía; Strooper, Bart de (2006): Contribution of Presenilin Transmembrane Domains 6 and 7 to a Water-containing Cavity in the γ-Secretase Complex*. In: *Journal of Biological Chemistry* 281 (37), S. 27633–27642. DOI: 10.1074/jbc.M604997200.

Urban, S.; Lee, J. R.; Freeman, M. (2001): Drosophila rhomboid-1 defines a family of putative intramembrane serine proteases. In: *Cell* 107 (2), S. 173–182. DOI: 10.1016/s0092-8674(01)00525-6.

Urban, Sinisa; Dickey, Seth W. (2011): The rhomboid protease family: a decade of progress on function and mechanism. In: *Genome Biol* 12 (10), S. 231. DOI: 10.1186/gb-2011-12-10-231.

Urban, Sinisa; Freeman, Matthew (2003): Substrate specificity of rhomboid intramembrane proteases is governed by helix-breaking residues in the substrate transmembrane domain. In: *Molecular cell* 11 (6), S. 1425–1434. DOI: 10.1016/s1097-2765(03)00181-3.

van den Plas, Dave; Merregaert, Joseph (2004): In vitro studies on Itm2a reveal its involvement in early stages of the chondrogenic differentiation pathway. In: *Biology of the Cell* 96 (6), S. 463–470. DOI: 10.1016/j.biolcel.2004.04.007.

van der Kant, Rik; Goldstein, Lawrence S. B. (2015): Cellular functions of the amyloid precursor protein from development to dementia. In: *Developmental Cell* 32 (4), S. 502–515. DOI: 10.1016/j.devcel.2015.01.022.

van Tetering, G.; Vooijs, M. (2011): Proteolytic cleavage of Notch: "HIT and RUN". In: *Current molecular medicine* 11 (4), S. 255–269. DOI: 10.2174/156652411795677972.

van Zee, K. J.; Kohno, T.; Fischer, E.; Rock, C. S.; Moldawer, L. L.; Lowry, S. F. (1992): Tumor necrosis factor soluble receptors circulate during experimental and clinical inflammation and can protect against excessive tumor necrosis factor alpha in vitro and in vivo. In: *Proceedings of the National Academy of Sciences of the United States of America* 89 (11), S. 4845–4849. DOI: 10.1073/pnas.89.11.4845.

Vassar, Robert; Kovacs, Dora M.; Yan, Riqiang; Wong, Philip C. (2009): The beta-secretase enzyme BACE in health and Alzheimer's disease: regulation, cell biology, function,

and therapeutic potential. In: *J. Neurosci.* 29 (41), S. 12787–12794. DOI: 10.1523/JNEUROSCI.3657-09.2009.

Vidal, R.; Calero, M.; Révész, T.; Plant, G.; Ghiso, J.; Frangione, B. (2001): Sequence, genomic structure and tissue expression of Human BRI3, a member of the BRI gene family. In: *Gene* 266 (1-2), S. 95–102. DOI: 10.1016/s0378-1119(01)00374-2.

Vidal, R.; Frangione, B.; Rostagno, A.; Mead, S.; Révész, T.; Plant, G.; Ghiso, J. (1999): A stop-codon mutation in the BRI gene associated with familial British dementia. In: *Nature* 399 (6738), S. 776–781. DOI: 10.1038/21637.

Vidal, R.; Revesz, T.; Rostagno, A.; Kim, E.; Holton, J. L.; Bek, T. et al. (2000): A decamer duplication in the 3' region of the BRI gene originates an amyloid peptide that is associated with dementia in a Danish kindred. In: *Proceedings of the National Academy of Sciences of the United States of America* 97 (9), S. 4920–4925. DOI: 10.1073/pnas.080076097.

Vooijs, Marc; Schroeter, Eric H.; Pan, Yonghua; Blandford, Mary; Kopan, Raphael (2004): Ectodomain shedding and intramembrane cleavage of mammalian Notch proteins is not regulated through oligomerization. In: *Journal of Biological Chemistry* 279 (49), S. 50864–50873. DOI: 10.1074/jbc.M409430200.

Voss, Matthias; Fukumori, Akio; Kuhn, Peer-Hendrik; Künzel, Ulrike; Klier, Bärbel; Grammer, Gudula et al. (2012): Foamy virus envelope protein is a substrate for signal peptide peptidase-like 3 (SPPL3). In: *The Journal of biological chemistry* 287 (52), S. 43401–43409. DOI: 10.1074/jbc.M112.371369.

Voss, Matthias; Künzel, Ulrike; Higel, Fabian; Kuhn, Peer-Hendrik; Colombo, Alessio; Fukumori, Akio et al. (2014): Shedding of glycan-modifying enzymes by signal peptide peptidase-like 3 (SPPL3) regulates cellular N-glycosylation. In: *The EMBO journal* 33 (24), S. 2890–2905. DOI: 10.15252/embj.201488375.

Voss, Matthias; Schröder, Bernd; Fluhrer, Regina (2013): Mechanism, specificity, and physiology of signal peptide peptidase (SPP) and SPP-like proteases. In: *Biochimica et biophysica acta* 1828 (12), S. 2828–2839. DOI: 10.1016/j.bbamem.2013.03.033.

Vranken, Wim F.; Boucher, Wayne; Stevens, Tim J.; Fogh, Rasmus H.; Pajon, Anne; Llinas, Miguel et al. (2005): The CCPN data model for NMR spectroscopy: development of a software pipeline. In: *Proteins* 59 (4), S. 687–696. DOI: 10.1002/prot.20449.

Wagner, G.; Neuhaus, D.; Wörgötter, E.; Vasák, M.; Kägi, J. H.; Wüthrich, K. (1986): Nuclear magnetic resonance identification of "half-turn" and 3(10)-helix secondary structure

in rabbit liver metallothionein-2. In: *Journal of molecular biology* 187 (1), S. 131–135. DOI: 10.1016/0022-2836(86)90413-4.

Wagner, R.; Berger, S. (1996): Gradient-Selected NOESY-A Fourfold Reduction of the Measurement Time for the NOESY Experiment. In: *Journal of magnetic resonance. Series A* 123 (1), S. 119–121. DOI: 10.1006/jmra.1996.0222.

Wang, Mei; Casey, Patrick J. (2016): Protein prenylation: unique fats make their mark on biology. In: *Nat Rev Mol Cell Biol* 17 (2), S. 110–122. DOI: 10.1038/nrm.2015.11.

Wang, Yongcheng; Zhang, Yingjiu; Ha, Ya (2006): Crystal structure of a rhomboid family intramembrane protease. In: *Nature* 444 (7116), S. 179–180. DOI: 10.1038/nature05255.

Wasserman, J. D.; Urban, S.; Freeman, M. (2000): A family of rhomboid-like genes: Drosophila rhomboid-1 and roughoid/rhomboid-3 cooperate to activate EGF receptor signaling. In: *Genes & Development* 14 (13), S. 1651–1663.

Watanabe, Hikari; Yoshida, Chika; Hidaka, Masafumi; Ogawa, Tomohisa; Tomita, Taisuke; Futai, Eugene (2022): Specific Mutations in Aph1 Cause γ-Secretase Activation. In: *International Journal of Molecular Sciences* 23 (1), S. 507. DOI: 10.3390/ijms23010507.

Weidemann, Andreas; Eggert, Simone; Reinhard, Friedrich B. M.; Vogel, Markus; Paliga, Krzysztof; Baier, Gottfried et al. (2002): A novel epsilon-cleavage within the transmembrane domain of the Alzheimer amyloid precursor protein demonstrates homology with Notch processing. In: *Biochemistry* 41 (8), S. 2825–2835. DOI: 10.1021/bi015794o.

Weihofen, A.; Lemberg, M. K.; Ploegh, H. L.; Bogyo, M.; Martoglio, B. (2000): Release of signal peptide fragments into the cytosol requires cleavage in the transmembrane region by a protease activity that is specifically blocked by a novel cysteine protease inhibitor. In: *Journal of Biological Chemistry* 275 (40), S. 30951–30956. DOI: 10.1074/jbc.M005980200.

Weihofen, Andreas; Binns, Kathleen; Lemberg, Marius K.; Ashman, Keith; Martoglio, Bruno (2002): Identification of signal peptide peptidase, a presenilin-type aspartic protease. In: *Science (New York, N.Y.)* 296 (5576), S. 2215–2218. DOI: 10.1126/science.1070925.

Weng, Andrew P.; Ferrando, Adolfo A.; Lee, Woojoong; Morris, John P.; Silverman, Lewis B.; Sanchez-Irizarry, Cheryll et al. (2004): Activating mutations of NOTCH1 in human

T cell acute lymphoblastic leukemia. In: *Science (New York, N.Y.)* 306 (5694), S. 269–271. DOI: 10.1126/science.1102160.

Werner, Nadine T.; Högel, Philipp; Güner, Gökhan; Stelzer, Walter; Wozny, Manfred; Aßfalg, Marlene et al. (2023): Cooperation of N- and C-terminal substrate transmembrane domain segments in intramembrane proteolysis by γ-secretase. In: *Commun Biol* 6 (1), S. 177. DOI: 10.1038/s42003-023-04470-5.

Willander, Hanna; Presto, Jenny; Askarieh, Glareh; Biverstål, Henrik; Frohm, Birgitta; Knight, Stefan D. et al. (2012): BRICHOS domains efficiently delay fibrillation of amyloid β-peptide. In: *Journal of Biological Chemistry* 287 (37), S. 31608–31617. DOI: 10.1074/jbc.M112.393157.

Winter-Vann, Ann M.; Casey, Patrick J. (2005): Post-prenylation-processing enzymes as new targets in oncogenesis. In: *Nature reviews. Cancer* 5 (5), S. 405–412. DOI: 10.1038/nrc1612.

Wishart, D. S.; Sykes, B. D.; Richards, F. M. (1991): Relationship between nuclear magnetic resonance chemical shift and protein secondary structure. In: *Journal of molecular biology* 222 (2), S. 311–333. DOI: 10.1016/0022-2836(91)90214-Q.

Wishart, David (2012): Chemical Shift Index. In: Gordon C. K. Roberts (Hg.): Encyclopedia of Biophysics. 1., st Edition. Berlin: Springer Berlin (Encyclopedia of Biophysics), S. 279–280.

Wishart, David S. (2011): Interpreting protein chemical shift data. In: *Progress in nuclear magnetic resonance spectroscopy* 58 (1-2), S. 62–87. DOI: 10.1016/j.pnmrs.2010.07.004.

Wishart, David S.; Case, David A. (2002): [1] - Use of Chemical Shifts in Macromolecular Structure Determination. In: Thomas L. James, Volker Dötsch und Uli Schmitz (Hg.): Methods in Enzymology : Nuclear Magnetic Resonance of Biological Macromolecules Part A, Bd. 338: Academic Press, S. 3–34. Online verfügbar unter https://www.sciencedirect.com/science/article/pii/S0076687902382144.

Wolfe, M. S.; Xia, W.; Ostaszewski, B. L.; Diehl, T. S.; Kimberly, W. T.; Selkoe, D. J. (1999): Two transmembrane aspartates in presenilin-1 required for presenilin endoproteolysis and gamma-secretase activity. In: *Nature* 398 (6727), S. 513–517. DOI: 10.1038/19077.

Wong, Gwendolyn T.; Manfra, Denise; Poulet, Frederique M.; Zhang, Qi; Josien, Hubert; Bara, Thomas et al. (2004): Chronic treatment with the gamma-secretase inhibitor

LY-411,575 inhibits beta-amyloid peptide production and alters lymphopoiesis and intestinal cell differentiation. In: *Journal of Biological Chemistry* 279 (13), S. 12876–12882. DOI: 10.1074/jbc.M311652200.

Wong, P. C.; Zheng, H.; Chen, H.; Becher, M. W.; Sirinathsinghji, D. J.; Trumbauer, M. E. et al. (1997): Presenilin 1 is required for Notch1 and DII1 expression in the paraxial mesoderm. In: *Nature* 387 (6630), S. 288–292. DOI: 10.1038/387288a0.

Wu, L.; Aster, J. C.; Blacklow, S. C.; Lake, R.; Artavanis-Tsakonas, S.; Griffin, J. D. (2000): MAML1, a human homologue of Drosophila mastermind, is a transcriptional co-activator for NOTCH receptors. In: *Nat Genet* 26 (4), S. 484–489. DOI: 10.1038/82644.

Wu, Zhuoru; Yan, Nieng; Feng, Liang; Oberstein, Adam; Yan, Hanchi; Baker, Rosanna P. et al. (2006): Structural analysis of a rhomboid family intramembrane protease reveals a gating mechanism for substrate entry. In: *Nature structural & molecular biology* 13 (12), S. 1084–1091. DOI: 10.1038/nsmb1179.

Wüthrich, K. (1990): Protein structure determination in solution by NMR spectroscopy. In: *Journal of Biological Chemistry* 265 (36), S. 22059–22062. DOI: 10.1016/S0021-9258(18)45665-7.

Wüthrich, K.; Billeter, M.; Braun, W. (1984): Polypeptide secondary structure determination by nuclear magnetic resonance observation of short proton-proton distances. In: *Journal of molecular biology* 180 (3), S. 715–740. DOI: 10.1016/0022-2836(84)90034-2.

Wüthrich, K.; Spitzfaden, C.; Memmert, K.; Widmer, H.; Wider, G. (1991): Protein secondary structure determination by NMR. Application with recombinant human cyclophilin. In: *FEBS letters* 285 (2), S. 237–247. DOI: 10.1016/0014-5793(91)80808-G.

Wüthrich, Kurt (1986): NMR of proteins and nucleic acids. New York: Wiley (Baker lecture series). Online verfügbar unter http://www.loc.gov/catdir/bios/wiley042/86007834.html.

Xu, Ting-Hai; Yan, Yan; Kang, Yanyong; Jiang, Yi; Melcher, Karsten; Xu, H. Eric (2016): Alzheimer's disease-associated mutations increase amyloid precursor protein resistance to γ-secretase cleavage and the Aβ42/Aβ40 ratio. In: *Cell discovery* 2 (1), S. 16026. DOI: 10.1038/celldisc.2016.26.

Xue, Yi; Ha, Ya (2013): Large lateral movement of transmembrane helix S5 is not required for substrate access to the active site of rhomboid intramembrane protease. In: *The*

Journal of biological chemistry 288 (23), S. 16645–16654. DOI: 10.1074/jbc.M112.438127.

Yan, Yan; Xu, Ting-Hai; Melcher, Karsten; Xu, H. Eric (2017): Defining the minimum substrate and charge recognition model of gamma-secretase. In: *Acta Pharmacol Sin* 38 (10), S. 1412–1424. DOI: 10.1038/aps.2017.35.

Yang, Guanghui; Zhou, Rui; Zhou, Qiang; Guo, Xuefei; Yan, Chuangye; Ke, Meng et al. (2019): Structural basis of Notch recognition by human γ-secretase. In: *Nature* 565 (7738), S. 192–197. DOI: 10.1038/s41586-018-0813-8.

Yang, Sujuan; Wang, Julie; Brand, David Douglass; Zheng, Song Guo (2018): Role of TNF-TNF Receptor 2 Signal in Regulatory T Cells and Its Therapeutic Implications. In: *Front. Immunol.* 9, S. 784. DOI: 10.3389/fimmu.2018.00784.

Yao, J.; Dyson, H. J.; Wright, P. E. (1997): Chemical shift dispersion and secondary structure prediction in unfolded and partly folded proteins. In: *FEBS letters* 419 (2-3), S. 285–289. DOI: 10.1016/s0014-5793(97)01474-9.

Ye, J.; Davé, U. P.; Grishin, N. V.; Goldstein, J. L.; Brown, M. S. (2000a): Asparagine-proline sequence within membrane-spanning segment of SREBP triggers intramembrane cleavage by site-2 protease. In: *Proceedings of the National Academy of Sciences of the United States of America* 97 (10), S. 5123–5128. DOI: 10.1073/pnas.97.10.5123.

Ye, J.; Rawson, R. B.; Komuro, R.; Chen, X.; Davé, U. P.; Prywes, R. et al. (2000b): ER stress induces cleavage of membrane-bound ATF6 by the same proteases that process SREBPs. In: *Molecular cell* 6 (6), S. 1355–1364. DOI: 10.1016/s1097-2765(00)00133-7.

Zeeb, Markus; Balbach, Jochen (2004): Protein folding studied by real-time NMR spectroscopy. In: *Methods* 34 (1), S. 65–74. DOI: 10.1016/j.ymeth.2004.03.014.

Zhang, Yan; Wang, Tingting; Wu, Sanlan; Tang, Li; Wang, Jia; Yang, Jinghan; Yao, Shanglong (2023): Notch signaling pathway: a new target for neuropathic pain therapy. In: *J Headache Pain* 24 (1), S. 87. DOI: 10.1186/s10194-023-01616-y.

Zhao, D.; Jardetzky, O. (1994): An assessment of the precision and accuracy of protein structures determined by NMR. Dependence on distance errors. In: *Journal of molecular biology* 239 (5), S. 601–607. DOI: 10.1006/jmbi.1994.1402.

Zhou, Rui; Yang, Guanghui; Guo, Xuefei; Zhou, Qiang; Lei, Jianlin; Shi, Yigong (2019): Recognition of the amyloid precursor protein by human γ-secretase. In: *Science (New York, N.Y.)* 363 (6428). DOI: 10.1126/science.aaw0930.

Zhou, Zhi-dong; Chan, Christine Hui-shan; Ma, Quan-hong; Xu, Xiao-hong; Xiao, Zhi-cheng; Tan, Eng-king (2011): The roles of amyloid precursor protein (APP) in neurogenesis: Implications to pathogenesis and therapy of Alzheimer disease. In: *Cell adhesion & migration* 5 (4), S. 280–292. DOI: 10.4161/cam.5.4.16986.

Abbreviations

µM	micro molar
ADAM	a disintegrin and metalloproteinase
Ala, A	alanine
ANK	ankyrin repeats
AP1	transcription factor activator protein 1
APH1	anterior pharynx-defective 1
APLP1	amyloid precursor-like protein 1
APP	amyloid precursor protein
Arg, R	arginine
ARIA	ambiguous restraints for iterative assignment
Asn, N	asparagine
Asp, D	aspartic acid
ATF6	activating transcription factor 6
Aβ	amyloid β-peptides
B_0	external magnetic field
BACE1	β-site amyloid precursor protein cleaving enzyme
BBF2H7	BBF2 human homolog on chromosome 7
BCMA	B cell maturation antigen
BLAST	basic local alignment search tool
B_{loc}	local magnetic field
BMRB	Biological Magnetic Resonance Bank
CD	circular dichroism
CD74	invariant chain of MHC class II proteins
CNS	crystallography and NMR system
COSY	correlation spectroscopy
COX2	cyclooxygenase 2
cryo-EM	cryogenic electron microscopy
CSI	chemical shift index

CSL	CBF1, Su(H), Lag1
CTF	C-terminal fragment
CYB5A	cytochrome B5A
Cys, C	cysteine
DAPT	N-[N-(3,5-difluorophenacetyl)-L-alanyl]-S-phenylglycine t-butyl ester
DD	death domain
DHX	deuterium hydrogen exchange
D_{IS}	dipolar coupling
ECD	extracellular domain
EGF	epidermal growth factor
ER	endoplasmic reticulum
ERAD	ER-associated degradation
FBD	Familial British Dementia
FDD	Familial Danish Dementia
FID	free induction decay
FKBP8	FK506-binding protein 8
FVenv	foamy virus envelope
Gln, Q	glutamine
Glu, E	glutamic acid
Gly, G	glycine
GnTV	N-acetylglucosaminyltransferase V
$\hbar$	reduced Planck constant
HD	heterodimerization domain
HDX	Hydrogen deuterium exchange
HFIP	hexafluorisopropanol
His, H	histidine
HIV-1	human immunodeficiency virus type 1
HO 1	heme oxygenase 1
HSQC	heteronuclear single-quantum correlation
I	nuclear spin angular momentum
ICD	intracellular domain
IL	interleukin

Ile, I	isoleucine
iNOX	inducible nitric oxide synthase
iRhom	inactive rhomboids
ITGB1	integrin β1
ITM2A	integral membrane protein 2A
K	Kelvin
kDa	kilo Dalton
Leu, L	leucine
LNR	Lin Notch repeats
LOX1	lectin-like oxidized LDL receptor 1
LOX5	lipoxygenase 5
LP	leader peptide
Lys, K	lysine
m	spin quantum number
MAML	mastermind-like protein
Met, M	methionine
MHC	polymorphic human major histocompatibility complex
min	minute
mm	milli meter
mM	milli molar
ms	millisecond
MSA	multiple sequence alignment
NCT	nicastrin
NFκB	nuclear factor κB
NK	natural killer
nm	nano meter
NMR	nuclear magnetic resonance
NOE	nuclear Overhauser enhancement or effect
NOESY	NOE spectroscopy
Notch1 WT	wild type Notch1
NRR	negative regulatory region
NSF	N-ethylmaleimide-sensitive factor
NTF	N-terminal fragment

Nβ	Notch β peptides
OASIS	old astrocyte specifically induced substance
PARL	presenilin-associated rhomboid-like protease
PC	proprotein convertase
PDB	Protein Data Bank
PEN2	presenilin enhancer 2
PEST	proline, glutamic acid, serine and threonine rich domain
PGAM5	phosphoglyceromutase 5
Phe, F	phenylalanine
PINK1	PTEN-induced kinase 1
pLDDT	predicted local distance difference test
PLN	phospholamban
ppm	parts per million
Pro, P	proline
PS	presenilin
RAM	RBPJ associated module
RAMP4	ribosome-associated membrane protein 4
RBPJ	recombination signal binding protein for immunoglobulin kappa J
Rce1	Ras and a-factor converting enzy*me 1*
RHBDL	rhomboid-like proteases
s	second
S1P	site 1 protease
S2P	site-2 protease
sAPPα	soluble APP NTF generated by α-secretase
sAPPβ	soluble APP NTF generated by β-secretase
Ser, S	serine
SERCA	sarco/ER Ca2+-ATPase
SNARE	soluble NSF attachment protein receptor
SPP	signal peptide peptidases
SPPL	SPP-like proteases
SREBP	sterol regulatory element binding protein
sTNFα	soluble TNFα
Stx8	syntaxin 8

TA	tail-anchored
TACE	TNFα converting enzyme
TALOS	Torsion Angle Likelihood Obtained from Shift
TCEP	Tris(2-carboxyethyl)phosphinhydrochlorid
TFE	Trifluorethanol
Thr, T	threonine
TM	transmembrane helix
TM-C	C-terminal TMD
TMD	transmembrane domain
TM-N	N-terminal TMD
TNFR1	TNF receptor 1
TNFR2	TNF receptor 2
TNFα	tumor necrosis factor alpha
TNFα FL	full-length TNFα
TNFαS34P FL	full-length TNFαS34P
TOCSY	total correlation spectroscopy
Tyr, Y	tyrosine
UPS	unfolded protein response
Val, V	valine
XBP1	X-box binding protein 1
γ	gyromagnetic ratio
δ	chemical shift
δ_{obs}	observed chemical shifts
δ_{rc}	random coil chemical shifts
$\Delta\delta$	secondary chemical shifts
μ	magnetic moment
μ_0	permeability of the vacuum
ν_0	Lamour frequency
σ	shielding constant
σ_s	anisotropic chemical shielding tensor
τ_c.	correlation time
ω_0	angular frequency

List of Figures

List of Tables

Appendix

A Resonance Assignment

Table A.1 Chemical shift assignment of Notch1$_{1734\text{-}1757}$ WT. Resonance assignment of ^{1}H-^{1}H NOESY, ^{1}H-^{1}H TOCSY and ^{1}H-^{13}C HSQC spectra.

		H_N	H_α	H_β	C_α	C_β
1731	Lys	-	4.14	1.85	57.93	32.13
1732	Lys	8.21	4.16	1.88	58.21	31.8
1733	Lys	7.78	4.21	1.91	58.03	31.83
1734	Leu	7.74	4.23	1.62,1.74	58.03	41.25
1735	His	7.99	4.37	3.2	58.68	29.11
1736	Phe	7.87	4.26	3.22	60.83	38.11
1737	Met	8.17	4.1	2.18,2.10	57.96	31.59
1738	Tyr	7.94	4.26	3.16,3.13	60.35	37.43
1739	Val	7.85	3.63	2.07	65.44	31.11
1740	Ala	8.07	3.99	1.32	54.28	16.87
1741	Ala	7.88	4.16	1.48	54.28	17.06
1742	Ala	7.9	4.05	1.42	54.37	16.79
1743	Ala	8.14	4.07	1.46	54.47	16.78
1744	Phe	7.89	4.24	3.26,3.31	60.82	38.29
1745	Val	8.01	3.66	2.26	65.86	31.18
1746	Leu	8.01	4.22	1.81	58.03	41.14
1747	Leu	8.24	4.04	1.47,1.82	57.4	40.98
1748	Phe	8.25	4.17	2.88,3.11	60.67	38.13
1749	Phe	8.4	4.27	3.29	61.17	38.17
1750	Val	8.83	3.72	2.25	65.93	31.19
1751	Gly	8.25	3.89,3.74	-	46.34	-
1752	Cys	7.96	4.07	2.93,2.63	62.4	25.79
1753	Gly	7.96	3.85,3.77	-	46.36	-
1754	Val	8.11	3.66	2.22	66.18	31.03
1755	Leu	7.91	4.06	1.83,1.63	57.63	41.22
1756	Leu	8.29	4.1	1.79,1.84	56.96	41.15
1757	Ser	7.92	4.22	4.06,4.01	60.5	62.58
1758	Lys	7.86	4.27	1.97	56.69	31.56
1759	Lys	8	4.24	1.93	56.59	31.86
1760	Lys	7.95	4.27	1.85,1.90	55.76	32.31

Table A.2 Chemical shift assignment of Notch1L$_{1740-1743}$. Resonance assignment of ^{1}H-^{1}H NOESY, ^{1}H-^{1}H TOCSY, ^{1}H-^{13}C HSQC and ^{1}H-^{15}N HSQC spectra.

		H_N	N_H	H_α	H_β	C_α	C_β
1731	Lys	-	118.55	4.15	1.84	58.57	32.09
1732	Lys	8.53	120.31	4.15	1.86	58.57	32.2
1733	Lys	7.9	120.58	4.2	1.91,1.86	58.33	32.22
1734	Leu	7.75	118.59	4.23	1.71,1.76	56.78	41.17
1735	His	7.98	119.39	4.38	3.22	58.7	28.7
1736	Phe	7.89	-	4.33	3.24	60.1	38.23
1737	Met	8.12	117.09	4.12	2.21,2.12	57.8	31.37
1738	Tyr	7.92	118.65	4.28	3.17	60.56	37.35
1739	Val	7.76	118.59	3.56	2.16	66.03	30.82
1740	Leu	7.79	118.77	3.99	1.47,1.75	57.42	40.91
1741	Leu	7.83	119.3	4.15	1.80,1.75	58.02	40.93
1742	Leu	7.92	119.55	4.05	1.73	57.53	40.91
1743	Leu	8.25	118.75	4.12	1.69,1.83	57.54	40.99
1744	Phe	8.2	118.55	4.29	3.39,3.35	60.8	37.96
1745	Val	8.38	120.18	3.69	2.38	66.39	31.19
1746	Leu	8.48	120.44	4.24	1.83,1.93	58.15	41.18
1747	Leu	8.65	117.45	4.07	1.40,1.92	57.63	40.89
1748	Phe	8.29	121.13	4.22	2.93,3.16	60.49	38.08
1749	Phe	8.45	119.96	4.3	3.31	61.21	38.14
1750	Val	8.92	121.41	3.73	2.28	65.96	31.14
1751	Gly	8.22	107.04	3.92,3.75	-	46.34	-
1752	Cys	7.95	118.11	4.07	2.65,2.95	62.5	25.72
1753	Gly	7.96	106.95	3.78,3.87	-	46.34	-
1754	Val	8.14	122.81	3.65	2.24	65.91	30.98
1755	Leu	7.93	119.55	4.07	1.85,1.65	57.42	41.15
1756	Leu	8.34	118.11	4.11	1.86,1.82	56.96	41.08
1757	Ser	7.95	113.66	4.23	4.03	60.49	62.56
1758	Lys	7.86	121.34	4.27	1.98	56.58	31.5
1759	Lys	7.99	119.39	4.25	1.93	56.48	31.73
1760	Lys	7.92	120.58	4.3	1.87,1.93	55.58	31.69

Table A.3 Chemical shift assignment of Notch1G$_{1740-1743}$. Resonance assignment of ^{1}H-^{1}H NOESY, ^{1}H-^{1}H TOCSY, ^{1}H-^{13}C HSQC and ^{1}H-^{15}N HSQC spectra.

		H_N	N_H	H_α	H_β	C_α	C_β
1731	Lys	-	125.96	4.15	1.81,1.85	57.85	32.11
1732	Lys	8.49	119.37	4.14	1.85	58.26	31.76
1733	Lys	7.89	118.82	4.19	1.9	58.1	31.8
1734	Leu	7.72	116.86	4.23	1.75,1.70	56.58	41.19
1735	His	7.99	117.43	4.33	3.15	58.69	29.23
1736	Phe	7.86	117.82	4.31	3.21	59.81	38.2
1737	Met	8.18	118.33	4.15	2.15,2.02	57.23	31.72
1738	Tyr	8.1	119.15	4.37	3.08,3.13	59.61	37.95
1739	Val	8.01	117.54	3.91	2.08	63.58	31.44
1740	Gly	7.98	107.8	3.79,3.93	-	45.01	-
1741	Gly	7.86	107.53	3.93	-	45.14	-
1742	Gly	8.09	107.33	3.85	-	45.69	-
1743	Gly	8.15	107.25	3.77,3.81	-	45.82	-
1744	Phe	7.65	118.74	4.38	3.17	59.86	38.1
1745	Val	7.49	118.74	3.71	2.19	65.43	31.14
1746	Leu	7.52	119.14	4.25	1.77	57.68	41.16
1747	Leu	7.77	119.09	4.06	1.84,1.59	57.37	40.98
1748	Phe	8.11	120.23	4.23	3.03,3.17	60.57	38.05
1749	Phe	8.3	119.65	4.26	3.29	61.14	38.17
1750	Val	8.76	121.05	3.73	2.23	65.96	31.2
1751	Gly	8.29	107.19	3.77,3.91	-	46.38	-
1752	Cys	8	118.31	4.07	2.95,2.64	62.59	25.75
1753	Gly	7.93	106.91	3.78,3.87	-	46.38	-
1754	Val	8.16	122.96	3.65	2.25	65.98	31.01
1755	Leu	7.95	120.65	4.06	1.85,1.65	57.72	41.12
1756	Leu	8.37	118.19	4.11	1.59,1.86	57.05	41.17
1757	Ser	7.96	113.76	4.22	4.03,4.08	60.57	62.56
1758	Lys	7.86	121.33	4.27	1.96,2.00	55.72	31.49
1759	Lys	8	119.51	4.24	1.94	56.58	31.82
1760	Lys	7.91	119.6	4.27	1.85,1.91	56.65	32.28

Table A.4 Chemical shift assignment of Notch3$_{1642\text{-}1665}$. Resonance assignment of ^{1}H-^{1}H NOESY, ^{1}H-^{1}H TOCSY, ^{1}H-^{13}C HSQC and ^{1}H-^{15}N HSQC spectra.

		H_N	N_H	H_α	H_β	C_α	C_β
1639	Lys	-	125.64	4.3	1.84,1.76	56.09	32.45
1640	Lys	7.97	120.63	4.37	1.85,1.77	55.57	32.07
1641	Lys	7.85	121.42	4.62	1.83,1.79	54.08	32.4
1642	Pro	-	-	4.47	1.91,2.24	62.63	30.81
1643	Leu	7.63	119.49	4.45	1.68	54.42	41.97
1644	Leu	7.59	120.73	4.35	1.72	57.92	39.96
1645	Pro	-	-	4.25	2.35,1.80	65.34	30.33
1646	Leu	7.21	115.32	4.19	1.86	56.81	41.23
1647	Leu	7.78	120	4.18	1.94,1.64	57	41.11
1648	Val	8	118.61	3.72	2.09	65.36	31.34
1649	Ala	7.92	122.19	4.08	1.51	54.51	16.93
1650	Gly	7.97	102.9	3.87	-	46.06	-
1651	Ala	7.81	123.92	4.19	1.56	54.3	17.1
1652	Val	8.05	118.11	3.71	2.19	65.68	31.2
1653	Leu	7.88	119.13	4.09	1.76	57.48	41.05
1654	Leu	7.61	118.59	4.13	1.82,1.94	57.62	41.08
1655	Leu	7.61	116.58	4.09	1.76	57.48	41.05
1656	Val	8.15	118.35	3.57	2.36	66.57	31.06
1657	Ile	8.22	118.51	3.72	2.08	65.36	37.22
1658	Leu	8.33	121.8	4.2	1.71,2.02	57.69	41.32
1659	Val	8.53	119.78	3.7	2.27	66.25	31.19
1660	Leu	8.75	120.23	4.16	1.92,1.60	57.64	41.06
1661	Gly	8.14	105.06	3.80,3.97	-	46.6	-
1662	Val	7.95	122.32	3.77	2.34	65.74	31.09
1663	Met	8.29	118.8	4.15	2.13,2.40	58.39	31.45
1664	Val	8.47	118.64	3.68	2.2	65.84	31.2
1665	Ala	7.92	120.71	4.08	1.55	54.51	17.1
1666	Lys	8.28	116.91	4.13	2.01,1.94	57.62	31.76
1667	Lys	8.02	119.22	4.21	1.97	57.1	31.86
1668	Lys	8.13	119.26	4.22	1.91	56.23	32.16

Table A.5 Chemical shift assignment of TNFα$_{28-60}$ WT. Resonance assignment of ^{1}H-^{1}H NOESY, ^{1}H-^{1}H TOCSY and ^{1}H-^{13}C HSQC spectra.

		H_N	H_α	H_β	C_α	C_β
28	Arg	-	3.7	1.97,1.81	55.65	32.72
29	Arg	7.75	3.7	1.97,1.81	55.65	32.72
30	Cys	8.31	4.41	3.05,2.98	58.84	26.12
31	Leu	7.73	4.21	1.66	58.03	41.48
32	Phe	7.73	4.32	3.15	60.13	37.89
33	Leu	8	4.21	1.81,1.67	58.07	41.17
34	Ser	7.88	4.27	3.97,4.13	57.6	62.23
35	Leu	7.95	4.27	1.69	57.31	41.24
36	Phe	8.42	4.33	3.08,3.02	60.12	38.13
37	Ser	8.01	4.27	4.10,3.99	57.6	62.2
38	Phe	7.75	4.27	3.3	61.22	38.13
39	Leu	8.2	3.91	1.47,1.98	57.4	40.76
40	Ile	8.03	3.77	1.98	63.77	36.61
41	Val	7.89	3.66	2.11	65.99	30.98
42	Ala	8.97	3.98	1.16	54.73	16.35
43	Gly	8.36	3.93,3.78	-	46.48	-
44	Ala	8.52	4.14	1.53	54.76	16.97
45	Thr	8.42	3.98	4.31	66.03	68.45
46	Thr	8.07	3.93	4.45	67.19	68.01
47	Leu	8.16	4.11	1.76,1.82	61.66	40.8
48	Phe	8.42	4.11	3.47,3.33	61.92	38.23
49	Cys	8.5	4.16	3.36,2.96	63.83	25.71
50	Leu	8.66	4.09	1.98,1.88	56.46	41.2
51	Leu	8.41	4.09	1.68	57.91	41.18
52	His	7.86	4.21	2.79,2.48	57	27.5
53	Phe	8.29	4.68	3.18,3.32	-	38.45
54	Gly	7.99	3.98	-	45.13	-
55	Val	7.65	4.08	2.17	62.58	31.99
56	Ile	7.52	4.25	1.89	60.5	38.48
57	Gly	7.72	3.98,4.11	-	43.74	-
58	Pro	-	4.41	1.99,2.21	62.66	30.98
59	Gln	8.09	4.32	2.16,1.99	55.2	28.65
60	Arg	7.64	4.22	1.88,1.74	56.39	30.85

Table A.6 Chemical shift assignment of TNFαAGA/LLL$_{28-60}$. Resonance assignment of ^{1}H-^{1}H NOESY, ^{1}H-^{1}H TOCSY and ^{1}H-^{13}C HSQC spectra.

		H_N	H_α	H_β	C_α	C_β
28	Arg	-	3.67	1.82,1.95	55.85	31.98
29	Arg	-	3.67	1.82,1.95	55.85	31.98
30	Cys	8.33	4.4	3.04,2.97	59.01	26.19
31	Leu	7.73	4.22	1.67,1.61	58	41.31
32	Phe	7.73	4.34	3.17	60.2	38.03
33	Leu	8	4.22	1.82	57.12	41.29
34	Ser	7.88	4.27	4.15,3.98	57.44	62.41
35	Leu	7.94	4.28	1.75,1.66	57.44	41.35
36	Phe	8.38	4.34	3.09,3.03	60.2	38.3
37	Ser	7.98	4.27	4.12,3.98	57.19	62.42
38	Phe	7.68	4.37	3.28	60.05	38.44
39	Leu	8.05	3.95	1.86	57.55	40.91
40	Ile	7.91	3.78	1.94	64.87	36.42
41	Val	7.63	3.63	2.21	66.57	30.76
42	Leu	8.32	3.97	1.63,1.49	58.03	40.9
43	Leu	8.62	4.07	1.86,1.75	58.34	41.04
44	Leu	8.88	4.11	1.95	57.86	41.03
45	Thr	8.5	3.99	4.33	66.64	68.5
46	Thr	8.19	3.92	4.54	67.49	68.09
47	Leu	8.5	4.1	1.83,1.88	61.58	41.08
48	Phe	8.56	4.16	3.37,3.48	61.91	38.24
49	Cys	8.51	4.18	2.97,3.38	63.94	25.82
50	Leu	8.71	4.1	1.98,1.89	56.56	41.31
51	Leu	8.43	4.1	1.70,1.75	58.05	41.37
52	His	7.82	4.24	2.54,2.85	58.1	27.64
53	Phe	8.26	4.67	3.19,3.32	-	38.54
54	Gly	7.99	3.97	-	45.22	-
55	Val	7.6	4.1	2.18	62.66	32.03
56	Ile	7.51	4.26	1.91	60.68	38.52
57	Gly	7.68	3.99,4.10	-	43.84	-
58	Pro	-	4.4	2.19,2.00	62.75	31.03
59	Gln	8.02	4.31	2.01,2.17	55.42	28.69
60	Arg	7.59	4.25	1.74,1.89	56.38	31.01

Table A.7 Chemical shift assignment of TNFαS34P$_{28-60}$. Resonance assignment of ^{1}H-^{1}H NOESY, ^{1}H-^{1}H TOCSY and ^{1}H-^{13}C HSQC spectra.

		H_N	H_α	H_β	C_α	C_β
28	Arg	-	3.78	1.79,1.93	58.09	34.55
29	Arg	7.94	3.78	1.93,1.79	58.09	34.55
30	Cys	8.06	4.46	2.96,2.88	60.33	29.47
31	Leu	7.76	4.28	1.46,1.55	57.77	44.34
32	Phe	7.59	4.46	3.00,3.14	59.1	41.19
33	Leu	7.59	4.12	1.63,1.73	64.6	42.9
34	Pro	-	4.31	2.30,2.04	67.4	32.78
35	Leu	7.14	4.29	1.77,1.68	59.43	44.18
36	Phe	7.98	4.41	3.18,3.14	62.24	40.69
37	Ser	8.13	4.11	3.99,3.94	63.98	64.83
38	Phe	7.66	4.29	3.29	63.05	40.75
39	Leu	8.07	3.95	1.96	60.02	43.84
40	Ile	7.95	3.79	1.99	66.44	39.35
41	Val	7.82	3.68	2.11	68.6	33.62
42	Ala	8.88	3.99	1.21	57.39	19.03
43	Gly	8.37	3.93,3.80	-	49.16	-
44	Ala	8.53	4.15	1.53	57.44	19.6
45	Thr	8.4	3.99	4.32	68.7	71.1
46	Thr	8.06	3.94	4.45	69.83	70.67
47	Leu	8.15	4.11	1.82,1.77	64.59	43.45
48	Phe	8.41	4.12	3.47,3.34	60.56	40.91
49	Cys	8.5	4.17	3.36,2.97	66.46	28.35
50	Leu	8.66	4.1	1.98,1.88	59.06	43.44
51	Leu	8.39	4.1	1.76,1.67	60.58	43.91
52	His	7.82	4.23	2.81,2.50	60.53	30.02
53	Phe	8.26	4.68	3.18,3.32	-	41.12
54	Gly	7.98	3.96,3.98	-	47.78	-
55	Val	7.61	4.09	2.17	65.15	34.62
56	Ile	7.51	4.25	1.9	63.17	41.07
57	Gly	7.69	3.99,4.11	-	46.37	-
58	Pro	-	4.41	2.20,1.99	65.29	33.59
59	Gln	8.05	4.31	2.00,2.16	57.89	31.28
60	Arg	7.61	4.22	1.88,1.75	59	33.51

B Hydrogen Deuterium Exchange Rates

Table B.1 Exchange rate constants of Notch1$_{1734-1757}$.WT. Exchange rate constants of Notch1$_{1734-1757}$ WT determined at pD 4.5 and pD 5.5 are scaled to pD 5 as $k_{ex,s}$. The error of scaled $k_{ex,s}$ $\Delta k_{ex,s}$ accounts for the error in the fitted parameter k_{ex} and the inaccuracy of the pH electrode.

		$k_{ex,s}$ [min^{-1}]	Δ $k_{ex,s}$ [min^{-1}]	log($k_{ex,s}$) [min^{-1}]	Δ log($k_{ex,s}$) [min^{-1}]
1731	Lys				
1732	Lys				
1733	Lys				
1734	Leu				
1735	His	0.00962	0.00404	-2.01672	0.42001
1736	Phe	0.00317	0.00076	-2.49901	0.23835
1737	Met				
1738	Tyr	0.05023	0.01568	-1.29906	0.31225
1739	Val	0.03485	0.00803	-1.45780	0.23053
1740	Ala	0.05248	0.01384	-1.28003	0.26367
1741	Ala	0.04891	0.01198	-1.31062	0.24505
1742	Ala	0.02333	0.00496	-1.63208	0.21271
1743	Ala	0.01783	0.00372	-1.74884	0.20867
1744	Phe	0.00713	0.00152	-2.14705	0.21362
1745	Val	0.00069	0.00014	-3.16091	0.20902
1746	Leu	0.00060	0.00013	-3.21840	0.20838
1747	Leu	0.00026	0.00006	-3.58948	0.22428
1748	Phe	0.00127	0.00027	-2.89627	0.21528
1749	Phe	0.00246	0.00051	-2.60959	0.20747
1750	Val	0.00093	0.00020	-3.02969	0.21059
1751	Gly	0.01355	0.00287	-1.86821	0.21205
1752	Cys				
1753	Gly				
1754	Val	0.02754	0.00584	-1.55996	0.21219
1755	Leu	0.03239	0.00727	-1.48959	0.22459
1756	Leu	0.00854	0.00181	-2.06874	0.21151
1757	Ser				
1758	Lys				
1759	Lys				
1760	Lys				

Table B.2 Exchange rate constants of Notch1L$_{1740-1743}$. Exchange rate constants of Notch1L$_{1740-1743}$ determined at pD 4.5 and pD 5.5 are scaled to pD 5 as $k_{ex,s}$. The error of scaled $k_{ex,s}$ $\Delta k_{ex,s}$ accounts for the error in the fitted parameter k_{ex} and the inaccuracy of the pH electrode.

		$k_{ex,s}$ [min^{-1}]	$\Delta k_{ex,s}$ [min^{-1}]	log($k_{ex,s}$) [min^{-1}]	Δ log($k_{ex,s}$) [min^{-1}]
1731	Lys				
1732	Lys				
1733	Lys				
1734	Leu				
1735	His	0.00838	0.00244	-2.07670	0.00244
1736	Phe	0.00229	0.00051	-2.63970	0.00051
1737	Met	0.01354	0.00355	-1.86829	0.00355
1738	Tyr				
1739	Val	0.03059	0.00844	-1.51438	0.00844
1740	Leu	0.01102	0.00230	-1.95794	0.00230
1741	Leu	0.00416	0.00088	-2.38044	0.00088
1742	Leu	0.00033	0.00007	-3.47644	0.00007
1743	Leu	0.00017	0.00004	-3.76293	0.00004
1744	Phe	0.00006	0.00001	-4.22185	0.00001
1745	Val	0.00002	0.00000	-4.80980	0.00000
1746	Leu	0.00003	0.00001	-4.50996	0.00001
1747	Leu	0.00002	0.00000	-4.79358	0.00000
1748	Phe	0.00014	0.00003	-3.84633	0.00003
1749	Phe	0.00076	0.00016	-3.11912	0.00016
1750	Val	0.00098	0.00020	-3.00939	0.00020
1751	Gly	0.01712	0.00371	-1.76646	0.00371
1752	Cys	0.01993	0.00579	-1.70050	0.00579
1753	Gly				
1754	Val	0.03400	0.00979	-1.46855	0.00979
1755	Leu	0.01703	0.00642	-1.76879	0.00642
1756	Leu	0.01771	0.00961	-1.75189	0.00961
1757	Ser				
1758	Lys				
1759	Lys				
1760	Lys				

Table B.3 Exchange rate constants of Notch1G$_{1740\text{-}1743}$. Exchange rate constants of Notch1G$_{1740\text{-}1743}$ determined at pD 3.5 are scaled to pD 5 as $k_{ex,s}$. The error of scaled $k_{ex,s}$ $\Delta k_{ex,s}$ accounts for the error in the fitted parameter k_{ex} and the inaccuracy of the pH electrode.

		$k_{ex,s}$ [min^{-1}]	$\Delta k_{ex,s}$ [min^{-1}]	log($k_{ex,s}$) [min^{-1}]	Δ log($k_{ex,s}$) [min^{-1}]
1731	Lys				
1732	Lys				
1733	Lys				
1734	Leu				
1735	His	0.02172	0.00467	-1.66305	0.21482
1736	Phe				
1737	Met				
1738	Tyr	0.01471	0.00398	-1.83241	0.27047
1739	Val	0.14897	0.05945	-0.82691	0.39911
1740	Gly				
1741	Gly	0.35456	0.17689	-0.45031	0.49889
1742	Gly				
1743	Gly	0.26330	0.09324	-0.57955	0.35414
1744	Phe	0.20629	0.05233	-0.68553	0.25366
1745	Val	0.02885	0.00600	-1.53981	0.20791
1746	Leu	0.01230	0.00256	-1.91001	0.20788
1747	Leu	0.00325	0.00072	-2.48771	0.22242
1748	Phe	0.00721	0.00152	-2.14199	0.21088
1749	Phe	0.00918	0.00193	-2.03695	0.20982
1750	Val	0.00306	0.00066	-2.51423	0.21728
1751	Gly	0.02203	0.00471	-1.65699	0.21373
1752	Cys	0.04321	0.01005	-1.36442	0.23270
1753	Gly	0.05148	0.01263	-1.28840	0.24532
1754	Val	0.01308	0.00273	-1.88346	0.20846
1755	Leu	0.01698	0.00355	-1.77004	0.20909
1756	Leu	0.00498	0.00110	-2.30242	0.22092
1757	Ser	0.02176	0.00544	-1.66226	0.24974
1758	Lys				
1759	Lys				
1760	Lys				

Table B.4 Exchange rate constants of Notch3$_{1642\text{-}1665}$. Exchange rate constants of Notch3$_{1642\text{-}1665}$ determined at pD 3.5, pD 5.5 and pD 6.5 are scaled to pD 5 as $k_{ex,s}$. The error of scaled $k_{ex,s}$ $\Delta k_{ex,s}$ accounts for the error in the fitted parameter k_{ex} and the inaccuracy of the pH electrode.

		$k_{ex,s}$ [min^{-1}]	$\Delta k_{ex,s}$ [min^{-1}]	log($k_{ex,s}$) [min^{-1}]	Δ log($k_{ex,s}$) [min^{-1}]
1639	Lys				
1640	Lys				
1641	Lys				
1642	Pro				
1643	Leu	0.73407	0.17128	-0.13426	0.23332
1644	Leu	0.26658	0.06054	-0.57418	0.22710
1645	Pro				
1646	Leu	0.09252	0.01941	-1.03378	0.20984
1647	Leu	0.04218	0.00875	-1.37487	0.20752
1648	Val	0.03145	0.00652	-1.50242	0.20737
1649	Ala	0.03145	0.00652	-1.50244	0.20731
1650	Gly	0.06130	0.01280	-1.21252	0.20881
1651	Ala	0.03405	0.00706	-1.46789	0.20733
1652	Val	0.00810	0.00168	-2.09133	0.20743
1653	Leu	0.00385	0.00080	-2.41418	0.20835
1654	Leu	0.00051	0.00011	-3.29335	0.22552
1655	Leu	0.00120	0.00025	-2.92007	0.21058
1656	Val	0.00008	0.00002	-4.08685	0.23840
1657	Ile	0.00007	0.00002	-4.14431	0.20929
1658	Leu	0.00013	0.00003	-3.89995	0.21504
1659	Val	0.00010	0.00002	-3.99344	0.21101
1660	Leu	0.00016	0.00004	-3.80431	0.22447
1661	Gly	0.00666	0.00138	-2.17656	0.20739
1662	Val	0.00557	0.00115	-2.25433	0.20733
1663	Met	0.01625	0.00338	-1.78923	0.20776
1664	Val	0.00632	0.00131	-2.19945	0.20756
1665	Ala	0.02509	0.00520	-1.60050	0.20737
1666	Lys				
1667	Lys				
1668	Lys				

Table B.5 Exchange rate constants of TNFα$_{28-60}$ WT. Exchange rate constants of TNFα$_{28-60}$ WT determined at pD 3.5 and pD 4.5 are scaled to pD 5 as $k_{ex,s}$. The error of scaled $k_{ex,s}$ $\Delta k_{ex,s}$ accounts for the error in the fitted parameter k_{ex} and the inaccuracy of the pH electrode.

		$k_{ex,s}$ [min^{-1}]	$\Delta k_{ex,s}$ [min^{-1}]	log($k_{ex,s}$) [min^{-1}]	Δ log($k_{ex,s}$) [min^{-1}]
28	Arg				
29	Arg				
30	Cys				
31	Leu	0.00116	0.00013	-1.33379	0.23541
32	Phe			--	--
33	Leu	0.00176	0.00031	-1.15501	0.27324
34	Ser	0.00088	0.00022	-1.45770	0.32848
35	Leu	0.00287	0.00088	-0.94173	0.37094
36	Phe	0.00129	0.00025	-1.28923	0.28306
37	Ser	0.00113	0.00008	-1.34697	0.21872
38	Phe	0.00354	0.00019	-0.85060	0.21385
39	Leu	0.00018	0.00001	-2.13582	0.21149
40	Ile	0.00026	0.00001	-3.16884	0.20857
41	Val	0.00019	0.00001	-3.30187	0.20927
42	Ala	0.00038	0.00001	-3.00581	0.20961
43	Gly	0.00050	0.00001	-1.70130	0.20929
44	Ala	0.00039	0.00001	-1.81038	0.20841
45	Thr	0.00040	0.00001	-1.80185	0.20777
46	Thr	0.00039	0.00001	-1.80390	0.20828
47	Leu	0.00099	0.00014	-2.58641	0.24932
48	Phe	0.00021	0.00003	-3.26011	0.24132
49	Cys	0.00111	0.00002	-1.35482	0.20821
50	Leu	0.00011	0.00001	-2.36436	0.23464
51	Leu	0.00022	0.00001	-2.05633	0.20961
52	His	0.00737	0.00078	-0.53279	0.23292
53	Phe	0.00585	0.00044	-0.63251	0.22036
54	Gly	0.00790	0.00068	-0.50225	0.22443
55	Val	0.02196	0.00538	-0.05832	0.32103
56	Ile	0.01884	0.00213	-0.12481	0.23600
57	Gly	0.01682	0.00197	-0.17424	0.23817
58	Pro				
59	Gln				
60	Arg				

Table B.6 Exchange rate constants of TNFαAGA/LLL$_{28-60}$. Exchange rate constants of TNFαAGA/LLL$_{28-60}$ determined at pD 4.5 and pD 5.5 are scaled to pD 5 as $k_{ex,s}$. The error of scaled $k_{ex,s}$ $\Delta k_{ex,s}$ accounts for the error in the fitted parameter k_{ex} and the inaccuracy of the pH electrode.

		$k_{ex,s}$ [min^{-1}]	$\Delta k_{ex,s}$ [min^{-1}]	log($k_{ex,s}$) [min^{-1}]	Δ log($k_{ex,s}$) [min^{-1}]
28	Arg				
29	Arg				
30	Cys				
31	Leu				
32	Phe	0.00797	0.00407	-1.53873	0.55179
33	Leu				
34	Ser	0.00202	0.00021	-2.13570	0.23234
35	Leu			--	--
36	Phe	0.00965	0.00296	-1.45526	0.37009
37	Ser			--	--
38	Phe	0.01481	0.00213	-1.26932	0.25238
39	Leu	0.00103	0.00005	-2.42727	0.21219
40	Ile	0.00054	0.00001	-3.70913	0.20876
41	Val	0.00003	0.00000	-4.91244	0.23264
42	Leu	0.00014	0.00001	-4.30033	0.22293
43	Leu	0.00013	0.00002	-4.34194	0.24475
44	Leu				
45	Thr	0.00005	0.00000	-4.75662	0.22816
46	Thr	0.00043	0.00002	-3.81155	0.21189
47	Leu	0.00030	0.00003	-3.96430	0.22452
48	Phe	0.00023	0.00002	-4.07456	0.22746
49	Cys	0.00369	0.00007	-1.87291	0.20820
50	Leu	0.00037	0.00001	-2.87641	0.20802
51	Leu	0.00025	0.00001	-3.04396	0.20912
52	His	0.01225	0.00506	-1.35201	0.46220
53	Phe	0.01165	0.00234	-1.37375	0.28878
54	Gly	0.00649	0.00093	-1.62743	0.25225
55	Val	0.01186	0.00777	-1.36606	0.68710
56	Ile	0.01069	0.00384	-1.41095	0.41453
57	Gly	0.00927	0.0031	-1.47296	0.39378
58	Pro				
59	Gln				
60	Arg				

Table B.7 Exchange rate constants of TNFαS34P$_{28-60}$. Exchange rate constants of TNFαS34P$_{28-60}$ determined at pD 3.5 and pD 4.5 are scaled to pD 5 as $k_{ex,s}$. The error of scaled $k_{ex,s}$ $\Delta k_{ex,s}$ accounts for the error in the fitted parameter k_{ex} and the inaccuracy of the pH electrode.

		$k_{ex,s}$ [min^{-1}]	$\Delta k_{ex,s}$ [min^{-1}]	log($k_{ex,s}$) [min^{-1}]	Δ log($k_{ex,s}$) [min^{-1}]
28	Arg				
29	Arg				
30	Cys				
31	Leu				
32	Phe				
33	Leu				
34	Pro				
35	Leu				
36	Phe	0.00943	0.00069	-0.67530	0.21979
37	Ser	0.00566	0.00218	-0.89686	0.43778
38	Phe	0.01181	0.00223	-0.57772	0.28060
39	Leu	0.00045	0.00001	-1.99699	0.20909
40	Ile	0.00097	0.00002	-2.59178	0.20820
41	Val	0.00038	0.00000	-3.00310	0.20752
42	Ala	0.00138	0.00005	-2.44154	0.21032
43	Gly	0.00092	0.00004	-1.68593	0.21285
44	Ala	0.00064	0.00003	-1.84696	0.21133
45	Thr	0.00059	0.00002	-1.87626	0.20938
46	Thr	0.00055	0.00002	-1.91260	0.20989
47	Leu	0.00113	0.00005	-2.52851	0.21177
48	Phe	0.00042	0.00001	-2.95315	0.20934
49	Cys	0.00114	0.00006	-1.59234	0.21489
50	Leu	0.00013	0.00001	-2.55260	0.21599
51	Leu	0.00018	0.00000	-2.38713	0.20813
52	His	0.00462	0.00070	-0.98490	0.25650
53	Phe	0.00405	0.00054	-1.04307	0.24698
54	Gly	0.00488	0.00089	-0.96166	0.27596
55	Val	0.01336	0.00113	-0.52416	0.22386
56	Ile	0.01196	0.00046	-0.57238	0.21082
57	Gly	0.00049	0.00003	-1.95791	0.21906
58	Pro				
59	Gln				
60	Arg	0.00288	4.86E-04	-1.19013	0.26716

C Structure Statistics

Table C.1 Structure statistics of Notch structure calculation. Structure statistics of $Notch1_{1734-1757}$, $Notch1L_{1740-1743}$, $Notch1G_{1740-1743}$ and $Notch3_{1642-1665}$. The values refer to the ensemble of 40 structures with the lowest energy from 400 calculated structures. * residues (1732:1740, 1743:1758). # residues (1641:1667).

	Notch1 WT	**Notch1 L1740-1743**	**Notch1 G1740-1743**	**Notch3**
Total restraints used				
Unambiguous NOE restraints	498	422	379	339
Intraresidue	200	196	184	174
Interresidue	298	226	195	165
Sequential (|i-j|=1)	128	106	95	90
Medium range (1 < |i-j|< 4)	128	91	91	52
Long range (|i-j|≥ 4)	42	29	9	23
Ambiguous NOE restraints	0	0	0	0
Statistics of structure calculations				
RMSD of bonds [A]	0.001 ± 0.0001	0.001± 0.00005	0.001 ± 0.0002	0.001 ± 0.0001
RMSD of bond angles [°]	0.338 ± 0.006	0.329 ± 0.004	0.320 ± 0.013	0.382 ± 0.008
RMSD of improper torsions [°]	0.204 ± 0.014	0.133 ± 0.011	0.172 ± 0.024	0.253 ± 0.019
Final Energies [kcal·mol^{-1}]				
E_{total}	-943 ± 45	-967 ± 45	-918 ± 39	-950 ± 39
E_{bonds}	1.06 ± 0.08	0.52 ± 0.05	0.76 ± 0.20	1.32 ± 0.17
E_{angles}	16.2 ± 0.6	16.63 ± 0.43	14.2 ± 1.2	21.5 ± 0.9
$E_{impropers}$	1.69 ± 0.23	0.75 ± 0.13	1.20 ± 0.31	2.15 ± 0.32
E_{dihed}	136.8 ± 1.5	140.8 ± 1.4	123.3 ± 2.8	131.9 ± 2.7
E_{VdW}	-242.5 ± 2.9	-258.2± 3.3	-226.0 ± 4.3	-241.9 ± 2.7
E_{elec}	-856.5 ± 44.73	-867.4 ± 45.4	-831.7 ± 39.1	-864.7 ± 38.4
Coordinate precision [A]				
RMSD of backbone (N, CA, C, O) of all residues	1.42 ± 0.65	1.72 ± 0.57	2.88 ± 0.76	1.91 ± 0.78
RMSD of all heavy atoms of all residues	2.00 ± 0.67	2.37 ± 0.62	3.96 ± 0.93	2.56 ± 0.78
RMSD of backbone (N, CA, C, O) of ordered residues (1732:1758)	1.16 ± 0.54	1.41 ± 0.57	2.62 ± 0.67*	1.43 ± 0.59#
RMSD of all heavy atoms of ordered residues (1732:1758)	1.49 ± 0.50	1.75 ± 0.54	3.64 ± 0.86*	1.77 ± 0.57#

Table C.2 Structure statistics of TNFα structure calculation. Structure statistics of $TNF\alpha_{28-60}$, $TNF\alpha AGA/LLL_{28-60}$ and $TNF\alpha S34P_{28-60}$. The values refer to the ensemble of 40 structures with the lowest energy from 400 calculated structures.

	TNFα WT	**TNFα AGA/LLL**	**TNFα S34P**
Total restraints used			
Unambiguous NOE restraints	420	467	423
Intraresidue	198	225	217
Interresidue	222	242	206
Sequential (|i-j|=1)	121	120	120
Medium range (1 < |i-j|< 4)	79	89	69
Long range (|i-j|≥ 4)	22	33	17
Ambiguous NOE restraints	0	0	0
Statistics of structure calculations			
RMSD of bonds [A]	0.0026 ± 0.0002	0.0027 ± 0.0002	0.0022 ± 0.0001
RMSD of bond angles [°]	0.447 ± 0.018	0.403 ± 0.017	0.411 ± 0.017
RMSD of improper torsions [°]	0.309 ± 0.024	0.233 ± 0.024	0.256 ± 0.037
Final Energies [kcal·mol^{-1}]			
E_{total}	-1021 ± 21	-1028 ± 19	-1028 ± 26
E_{bonds}	3.82 ± 0.67	4.07 ± 0.68	2.80 ± 0.30
E_{angles}	29.97 ± 2.47	24.64 ± 2.02	26.9 ± 2.2
$E_{impropers}$	4.32 ± 0.68	2.49 ± 0.50	3.12 ± 0.92
E_{dihed}	168.3 ± 5.1	155.6 ± 3.1	164.9 ± 3.3
E_{VdW}	-253.7 ± 2.9	-253.5 ± 5.4	-276.8 ± 4.5
E_{elec}	-973.6 ± 19.7	-961.4 ± 16.2	-948.6 ± 25.9
Coordinate precision [A]			
RMSD of backbone (N, CA, C, O) of all residues	2.42 ± 0.69	1.59 ± 0.47	2.39 ± 0.74
RMSD of all heavy atoms of all residues	3.13 ± 0.07	2.55 ± 0.55	3.11 ± 0.82
RMSD of backbone (N, CA, C, O) of ordered residues (29:56)	1.57 ± 0.52	1.22 ± 0.39	1.07 ± 0.45
RMSD of all heavy atoms of ordered residues (29:56)	1.89 ± 0.50	1.87 ± 0.46	1.59 ± 0.56

Danksagung

An dieser Stelle möchte ich allen danken, die mich in der letzten Zeit und während der Anfertigung dieser Arbeit betreut, unterstützt und ermutigt haben.

Prof. Dr. Burkhard Luy für die Aufnahme in seinem Arbeitskreis und Einführung in die NMR.

PD Dr. Claudia Muhle-Goll für die Betreuung und Einblicke in die wundervolle Welt der Intramembran-Proteasen und der NMR.

Der Forschergruppe FOR 2290 für den wissenschaftlichen Austausch und die Zusammenarbeit.

Dem IBG-2 für die Nutzung des Biochemielabors und Unterstützung bei den CD Messungen.

Den Mitgliedern des Arbeitskreises für eine schöne und interessante Zeit.

Basti für die ausgiebigen Gespräche nicht nur die Wissenschaft betreffend.

Meinen Freunden und meiner Familie, darunter meinen Eltern und meiner Schwester, besonders für die Unterstützung meiner Mama in der letzten Zeit.

Aber vor allem Artur und Frieda!